OBSERVATIONS OF METAL CONCENTRATIONS IN *E*-REGION SPORADIC THIN LAYERS USING INCOHERENT-SCATTER RADAR

A

THESIS

Presented to the Faculty

of the University of Alaska Fairbanks

in Partial Fulfillment of the Requirements

for the Degree of

DOCTOR OF PHILOSOPHY

By

Nobuhiro Suzuki, M.S.E.E.

Fairbanks, Alaska

December 2006

INFORMATION TO USERS

The quality of this reproduction is dependent upon the quality of the copy submitted. Broken or indistinct print, colored or poor quality illustrations and photographs, print bleed-through, substandard margins, and improper alignment can adversely affect reproduction.

In the unlikely event that the author did not send a complete manuscript and there are missing pages, these will be noted. Also, if unauthorized copyright material had to be removed, a note will indicate the deletion.

ProQuest Information and Learning Company
300 North Zeeb Road
P.O. Box 1346
Ann Arbor, MI 48106-1346

OBSERVATIONS OF METAL CONCENTRATIONS IN *E*-REGION SPORADIC THIN LAYERS USING INCOHERENT-SCATTER RADAR

By

Nobuhiro Suzuki, MSEE

RECOMMENDED:

Advisory Committee Chair

Chair, Department of Physics

APPROVED:

Dean, College of Natural Science and Mathematics

Dean of the Graduate School

December 19, 2006

Date

Abstract

This thesis has used incoherent-scatter radar data from the facility at Søndrestrøm, Greenland to determine the ion mass values inside thin sporadic-E layers in the lower ionosphere. Metallic positively-charged ions of meteoric origin are deposited in the earth's upper atmosphere over a height range of about 85-120 km. Electric fields and neutral-gas (eg N_2, O, O_2) winds at high latitudes may produce convergent ion dynamics that results in the re-distribution of the background altitude distribution of the ions to form thin (1-3 km) high-density layers that are detectable with radar.

A large database of experimental radar observations has been processed to determine ion mass values inside these thin ion layers. The range resolution of the radar was 600 meters that permitted mass determinations at several altitude steps within the layers. Near the lower edge of the layers the ion mass values were in the range 20-25 amu while at the top portion of the layers the mass values were generally in the range 30-40 amu. The numerical values are consistent with in-situ mass spectrometer data obtained by other researchers that suggest these layers are mainly composed of a mixture of Mg^+, Si^+, and Fe^+ ions. The small tendency for heavier ions to reside at the top portion of the layers is consistent with theory. The results have also found new evidence for the existence of complex-shaped multiple layers; the examples studied suggest similar ion mass values in different layers that in some cases are separated in altitude by several km.

Table of Contents

List of Figures

List of Tables

List of Appendices

Acknowledgements

First of all, I would like to express my great appreciation to my supervisor, Prof. Brenton Watkins. He has given to me advice and guidance day by day not only for research but also with other concerns; I think it has sometimes been challenging because of my language. I believe that this research could not have been completed without his great guidance. He also invited me to parties held with his family and friends.

I also would like to express appreciation to members of my advisory committee, Prof. Bill Bristow, Prof. Joe Hawkins, and Prof. Vikas Sonwalkar. They gave me a lot of useful advice in committee meetings.

Prof. Bill Bristow is a specialist in the incoherent-scatter radar technique and he was most helpful on the many occasions I visited his office asking for suggestions about my research. I also enjoyed talking with him in general about radar systems since I am also a radar engineer in Japan.

Prof. Joe Hawkins, a professor of electrical and computer engineering, not only provided advice in committee meetings, but his class was quite practical and useful for me to further understand RF systems.

Prof. Vikas Sonwalkar, also a professor of electrical and computer engineering, has given me a careful and precise review on my thesis.

I also would like to express appreciation to Prof. Syun-Ichi Akasofu who is a director of International Arctic Research Center. His encouragement to Japanese institutions and companies has made it possible for me to visit Alaska. He has also helped many other researchers and students from Japan.

I also would like to mention that I have been supported by a lot of other people, such as class instructors, classmates, officemates, Japanese friends, and so on.

I also have to mention that this research has been supported by Mitsubishi Electric Corporation. The company has supported not only for university tuition but also living expenses and alternative human resources during my stay in Fairbanks. I would like to express great appreciation to Dr. Ryugo Nishii, who is the General Manager of the

Information Technology R&D Center, and Dr. Shuso Wadaka, who is the General Manager of the Electro-Optics & Microwave Systems Lab., for giving me a chance to visit to Alaska and study at University of Alaska Fairbanks.

I also would like to express appreciation to Dr. Hiroyuki Miyata who is the Senior Manager of Electronic Systems Technology Dept., and Dr. Isamu Chiba, who is the former Senior Manager of the Dept. and the present General Manager of the Communication Lab. I believe that I could not have continued this research without their great assistance and strong encouragement.

I also would like to express appreciation to Dr. Toshiyuki Hirai who is the Chief Engineer of Kamakura Works, and Prof. Yoshio Kosuge, who is a professor of Nagasaki University, for their guidance and encouragement to me.

I also would like to express my thanks to Dr. Atsushi Okamura, who is the Manager of Passive Sensor Systems Team. He has been my supervisor since I entered the company and I have often made him worry in certain aspects of my work.

I also would like to express my thanks to Prof. Takahiko Fujisaka who is the former Manager of the Team and present associate professor of Tokyo University of Marine Science and Technology.

Finally, I would like to say thank you again to many people, and I hope this research may make a small contribution, not only to research of the ionosphere but also to other fields of science, engineering, business, and, ..., peace of the world.

CHAPTER 1
INTRODUCTION AND OBJECTIVES OF THE THESIS

1.1 Introduction

This thesis deals with the use of radar signals to probe small-scale structures in the ionosphere, the portion of the upper atmosphere that is ionized. The discovery of the ionosphere itself is closely tied to development of electromagnetic wave communications during the early twentieth century. Pioneer radio engineers discovered the reflection of high frequency (HF) waves in the upper atmosphere and inferred the existence of an electrically-charged atmospheric region, now called the ionosphere. The reflections of HF radio signals were found to be quite variable, suggesting variability of the ionospheric layer. This ionospheric variability was also observed to affect other radio frequencies such as medium frequency (MF) and very high frequency (VHF) ranges. This thesis deals specifically with thin enhanced layers of ionization that occur as a result of the accumulation of long-lived metal ions that arise from meteor ablation. These dense layers were inferred from the reflections of VHF radio waves during the early days of radio experiments but not fully understood until recent years. When these layers, often called sporadic-*E* layers, appear over densely populated cities, VHF radio waves are anomalously reflected, which may create interference in certain systems. Some effect on certain navigation systems may also result from small-scale irregularities and dense layered structures in the ionosphere; for example, correction data for navigation systems is distributed through FM radio in Japan. It is therefore evident that research into and monitoring of the ionosphere has potential practical applications.

In addition to possible effects on real-world systems, the study of the ionosphere is a worthy science endeavor in itself. The ionosphere is affected by radiation, particles, and the earth's magnetic field. Solar-terrestrial relations and space-weather studies have an intrinsic link to the ionosphere, and ionospheric research contributes to the further understanding of these other related disciplines.

1.2 Historical Background

Our understanding of the ionosphere was developed by Edward Appleton (the recipient of the Nobel Prize in physics in 1947), beginning in the 1920's. He postulated that the fading of radio signals might be caused by interference between two radio waves, one of which propagates directly from the transmitter along the ground, while the other propagates overhead, reflected by something in the upper atmosphere. He then conducted experimental studies on the propagation of radio waves by changing the frequency slightly while transmitting. If fading was caused by interference, the received signal power should vary periodically in response to the varying transmitter frequency. Using a simple relation defining the path differences,

$$n = \frac{D}{\lambda_1} - \frac{D}{\lambda_2} \tag{1.1}$$

where D is the path-difference, λ_1 and λ_2 are the wave lengths when received signal power is maximum, and n is an integer. Using this equation, he determined that radio waves were reflected from a height of approximately 90km.

After the discovery of this reflecting layer (the ionosphere), investigation of the ionosphere progressed explosively, beginning with the development of routine radio reflection methods to probe and monitor the ionosphere. The altitude at which radio reflections occur is the height at which the radio wave frequency matches the local plasma frequency; therefore by using a pulsed transmitter with variable HF frequency, it was possible to determine the altitude variation of the lower ionosphere. The altitude of the reflection region could be determined by measuring the time delay between transmitted and received signals. This 'ionosonde' technique remains in use today globally as a routine method to monitor the ionosphere.

During routine observations of the ionosphere using ionosondes the intermittent occurrence of anomalous strong reflecting layers was often observed, generally at altitudes of about 100 – 110 km. These sporadically-occurring echoes were from the *E*-region altitude of the ionosphere, and therefore were termed 'sporadic-*E*' layers. A mechanism for the formation of these layers was proposed by Whitehead(1961) and

Axford(1963). The natural background ions O^+ and NO^+ recombine too rapidly to support dense thin layer structures. It was therefore suggested that the majority of ions within these layers must have long chemical lifetimes, and were therefore most likely to be metallic ions produced during meteor ablation. The natural wind shear at those altitudes could produce a convergence in the vertical ion motion and therefore form thin ionization layers. This explanation remains widely accepted to explain layer formation at mid-latitudes; at high latitudes, while this mechanism is indeed important, additional ion dynamics due to the large magnitudes of high-latitude electric fields plays an additional role.

Nygren et al.(1984a) first examined the role of high-latitude electric fields in the formation of thin ionized layers. Experimental observations using the European Incoherent Scatter (EISCAT) radar system confirmed the existence of metal ions in these layers (Turunen, 1988, Huuskonen, 1988). Further modeling and experimental studies were conducted by Bristow(1991 and 1993) using data from the incoherent-scatter radar at Søndrestrøm, Greenland. Bedey and Watkins (2001) measured the latitudinal extent and time variation of electric fields and confirmed the role of high-latitude electric fields in layer formation; a westward component of the electric field is necessary for ion convergence and therefore for ion layer formation.

A limited number of case studies using incoherent-scatter radars such as the EISCAT and Søndrestrøm radars at high latitudes (Turunen, 1988, Huuskonen, 1988, Bristow,1993), and the Arecibo low-latitude facility (Behnke, 1975) confirmed the suggestion by Axford et al.(1966) that these layers are composed of metal ions. The radar technique only determines the mean ion mass and the method adopted by Behnke (1975), Turunen et al (1988) and Bristow (1993) was to assume one heavy ion Fe^+ plus a mixture of lighter ions with average mass 30amu; thus an estimate of an average fraction of Fe^+ was obtained over the width of a layer. In those three studies concentrations up to 70% Fe^+ were determined. The radar study reported by Huuskonen et al (1988) successfully demonstrated the detailed ion composition variations over the height range within sporadic-E layers and a number of cases were presented; in several instances Fe^+ was

inferred to have relative abundances of 30-80% however in one case there was no evidence for heavy Fe^+ ions.

Using in-situ rocket ion mass spectrometer methods, Narcisi(1968) first showed sporadic-*E* ionized layers were composed of Fe^+, Mg^+, Ca^+, and Na^+. A review of metal ion measurements by rocket-borne mass spectrometers is presented by Grebowsky (2002); it is evident that a wide variety of altitude structures occur with no clear behavior related to latitude, season, or time. The three major elements in terms of cosmic abundances are *Mg*, *Si*, and *Fe* (masses 24, 28, 56 respectively). All three elements are present as positive ions in the data, however Si^+ presents an experimental issue because it has the same mass as N_2^+ and CO^+, both of which may be present in the mesosphere and lower thermosphere.

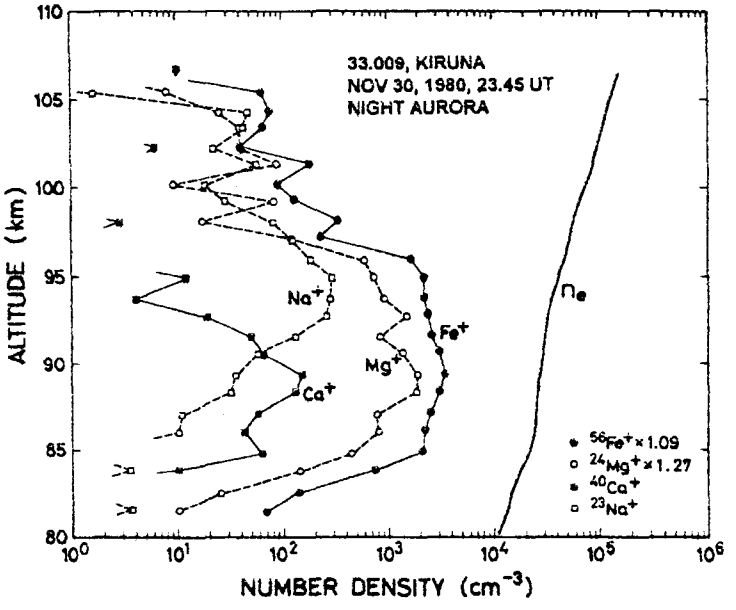

Fig. 1.1 Altitude profile of metal ions obtained from mass spectrometer data. In this case Fe^+ is the major metal ion species. (from Kopp et al, 1997).

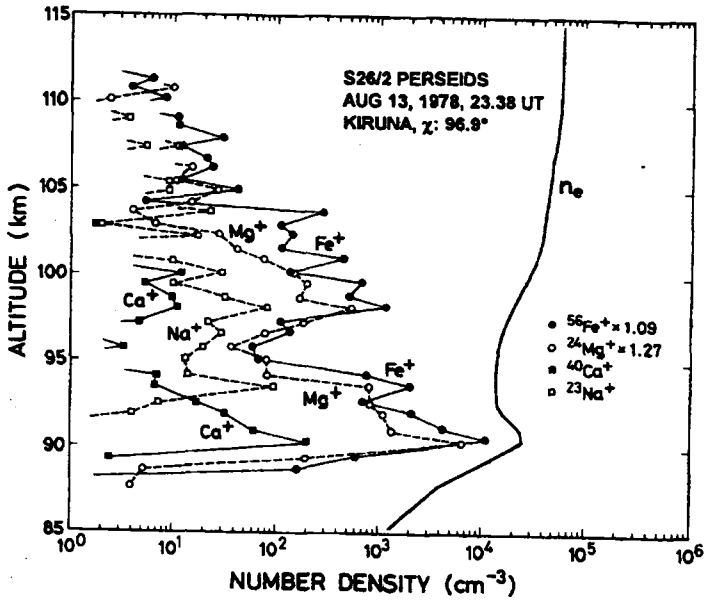

Fig 1.2 Altitude profile of metal ions obtained from mass spectrometer data. In this case Fe^+ and Mg^+ have comparable densities. (from Kopp et al, 1997).

The mass spectrometer data shown in Figures 1.1 and 1.2 illustrate fairly typical densities of Fe^+ and Mg^+. Fe^+ is often the greater density although the lighter Mg^+ ions are at times comparable. It is important to note that Si^+ ions are not presented in this data and we infer that they are not present because of experimental difficulties or ambiguities with other ions of similar masses. Zbinden et al (1975) discussed the experimental difficulties in identifying Si^+ and show data with Si^+ ions having densities exceeding Fe^+ at heights above about 100km whereas Fe^+ dominates at lower heights.

Figure 1.3 illustrates mass spectrometer data that identify a large variety of positive ions. In this case Si^+ is identified (as compared to N_2^+) because only long-lived metal ions including Si^+ are likely to form thin layered structures.

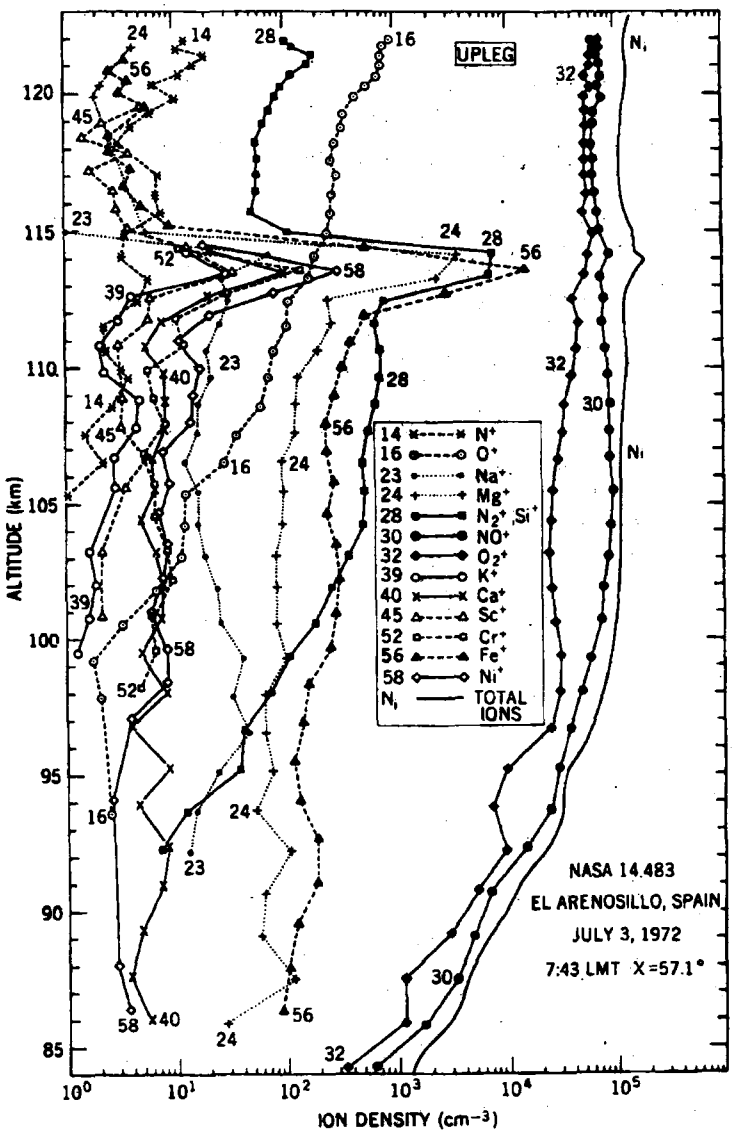

Fig. 1.3 Mass spectrometer data showing a variety of positive ion species. In this case Fe^+, Si^+ and Mg^+ have accumulated into a thin layered structure (Goldberg, 1975).

In the following Figure 1.4 the three major positive ions are shown for data gathered by Johannessen and Krankowsky (1974) for a sporadic layer where Mg^+ is the major ion and Fe^+ and Si^+ are of comparable densities. It is evident from the in-situ data that a variety of ion structures may be present; however when a layered structure forms we should expect a mixture of Fe^+, Mg^+, and Si^+ to constitute the bulk of the layer.

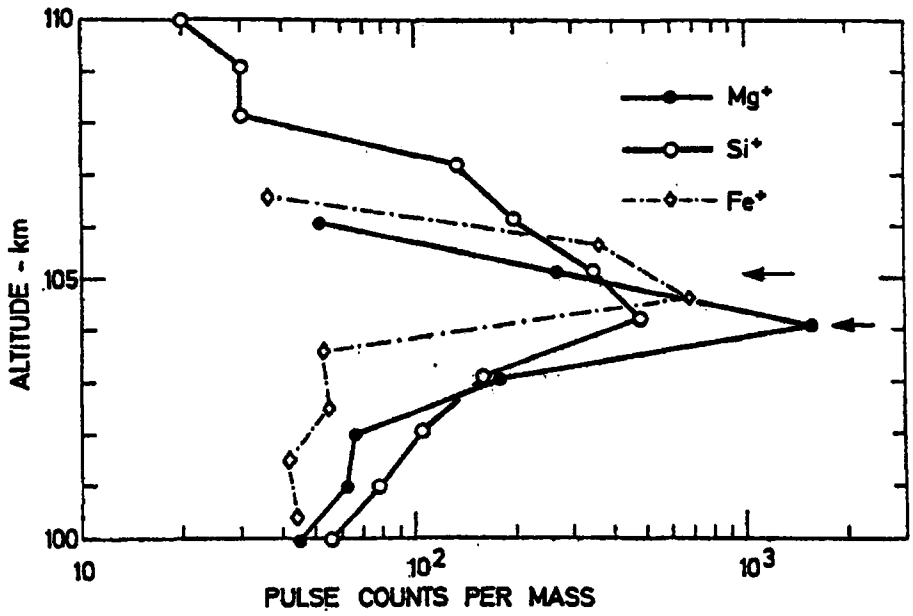

Fig. 1.4 Mass spectrometer data showing the three major positive ions in a sporadic layer. It is interesting to note that Mg^+ is dominant while Si^+ and Fe^+ densities are comparable (Johannessen and Krankowsky, 1974).

Modeling studies by Nygren et al. (1984b) showed that different ion masses formed a peak at slightly different altitudes; the heavier ions (primarily Fe^+) accumulated at the top of the sporadic-*E* layer and lighter ions such as Mg^+ accumulated at the bottom of the sporadic-*E*. Ions with different masses accumulate at different altitudes because their gyro frequencies differ from each other whereas their collision frequencies with the background neutral gas are the same. In agreement with this idea, Huuskonen et al (1988) has presented experimental evidence using the EISCAT radar that indeed there is a tendency for heavier ions to accumulate in the upper portion of a layer.

Advances in the incoherent-scatter radar technique at the Søndrestrøm, Greenland facility has permitted significant advances in experimental observations of sporadic-*E* layers and forms the basis of this thesis. Before addressing the specific goals of the thesis the next section provides a brief introduction to the experimental method.

1.3 Incoherent Scatter Radar

The incoherent-scatter radar (IS-radar) is a powerful method for obtaining various parameters of ionosphere, viz. ionization density, ion velocity, electron temperature, and ion temperature (assuming an ion mass value). In contrast to an ionosonde which is essentially an HF frequency radar, an IS-radar operates at frequencies well above the plasma frequency of the ionosphere, allowing the radar-transmitted pulse to travel through the ionosphere. A very small portion of the transmitted power is scattered by natural thermally-induced refractive index fluctuations in the ionospheric plasma.

The power of the reflected signal is proportional to the ionization density. The Doppler spectrum of the scattered signal returns contains information about thermal fluctuations of plasma; the naturally-occurring ion acoustic plasma waves in the ionosphere are responsible for a scattered spectrum with a width that depends on the ion temperature-mass ratio. The spectral shape may also be used to determine the electron temperature; ion acoustic waves undergo temperature-dependent Landau damping that affects the spectral shape. A small Doppler shift of the entire spectrum can be used to determine the ion velocity component in the direction of the antenna beam. Although the scattering is from electrons, the electrons are electrostatically bound to the ions and therefore the ion velocity (not electron velocity) is measured. We can estimate these parameters by fitting the observed spectrum to a theoretical spectrum based upon the fundamental plasma physics (Dougherty, 1960). A review of the experimental and theoretical methods are discussed by Evans (1969). From those primary data mentioned above, we can also obtain higher order information such as current, electric field, conductivities, etc. that can be computed from the primary data alone or perhaps in conjunction with a model.

In this thesis, we use data from the Søndrestrøm IS-radar operated by SRI International and the National Science Foundation. This radar is located on Søndrestrøm Fjord (Kangerlussuaq) in Greenland, 67N 309E, just north of the Arctic Circle. It is situated in a narrow valley to minimize ground-clutter signals and undesirable artificial noise. The radar antenna is a 32m-diameter fully steerable Cassegrain antenna, and the final Klystron tube amplifier produces 3MW (typical) peak power with a 3% (max) duty

cycle. The receiver has a quadrature detector that makes it possible to obtain spectra. The detected signals are digitized, auto-correlated by a real time processor, integrated in several seconds, and stored on a PC. For this analysis, we used data stored on 4mm-tapes or CD-Roms. The specifications of the Søndrestrøm IS-radar are shown on Table 1.1 below.

Table 1.1 Specification of Søndrestrøm IS-radar.

Location	67N 309E
Transmit frequency	1290 MHz
Transmit peak power	3MW(typ.), 5MW(max.)
Duty cycle	3%(max.)
Transmit polarization	Right-handed circularly
Receive polarization	Left-handed circularly
Antenna diameter	32 m
Receiver system noise	110 K
Pulse length	Long pulse mode: 320 us Multiple pulse mode: 5 x 28us
Receiver bandwidth (Base band)	Long pulse mode: 31.3 kHz Multiple pulse mode: 125 kHz

1.4 Objectives of this Thesis

An extensive database of experimental data has been used to study ion composition within thin sporadic-*E* layers; from this database a number of selected case studies have been chosen as the basis for the thesis. The thesis seeks to address the question of how the ion composition might vary within different types of layers, viz. with altitude, thickness, time, etc. A second goal is to address the relative concentrations of heavy ions, viz. Fe^+, and light ions, viz. Mg^+, Si^+, Na^+, etc. Numerous rocket experiments have consistently established that Fe^+ is often the major metal ion and Mg^+ and Si^+ are normally the second most abundant ion species in the sporadic-*E* layers, however there is also evidence that light ions may at times be dominant (for example see Figure 1.4). Iron (56 AMU) has a mass approximately double that of other abundant metal ions (Mg^+, Si^+, Ca^+, Na^+). Although the radar method only determines the mean ion mass (with certain

assumptions), it is feasible to use this method to examine individual layers to determine the possible mixture of heavy and light ions, and specifically to determine if the ion composition varies with altitude through an individual layer. In addition we frequently observe two layers stacked one above the other separated by 1-5 km; we have attempted in this thesis to determine if both layers contain mainly heavy ions (Fe^{+}), or if one layer contains mainly heavy ions and the other light ions, or if there is no significant difference. It is noteworthy to mention that except for one case presented by Huuskonen et al (1988) we are not aware of such double layers being routinely observed at other radar sites; however there have been relatively few experiments specifically designed to study such events at sites other than Søndrestrøm.

CHAPTER 2
INCOHERENT SCATTER THEORY

2.1 Introduction

The basic concept of incoherent-scatter theory was developed in the 1960's from two approaches. One such approach is the macroscopic method proposed by Dougherty and Farley(1960), based on Nyquist's theorem and plasma density fluctuation theory. The other is a microscopic method proposed by Fejer (1960) based on plasma kinetic theory. Both obtained the same results, but the former approach is more often referenced and we will therefore review the incoherent-scatter theory using the former approach.

2.2 Scattering from Density Fluctuation

Scattering from a single electron is so weak that we can take the Born approximation that regards scattering from plasma fluctuation to be the same as scattering from refractive index variations. The back scattered signal from electron density fluctuations is:

$$E_s(t) = -\frac{r_e E_o e^{i\omega_0 t}}{R_0} \int_{V_s} \Delta N(\mathbf{r},t) e^{-2ik_0 z} dV , \tag{2.1}$$

where ΔN is the deviation of electron density from a mean value, r_e is the classical electron radius ($= e^2/4\pi\varepsilon_0 m_e c^2$ in MKS units $= 2.82\times10^{-15}$m), ω_0 is the carrier frequency, R_0 is the mean distance between scattering volume (V_s) and the receiver, and k_0 is the wave number of the radio wave ($= 2\pi f_0/c$).

Assuming electron density has periodic fluctuation with a period of L,

$$\Delta N(x,y,z,t) = \Delta N(x+L, y+L, z+L, t) . \tag{2.2}$$

The above equation can be written as

$$\Delta N(\mathbf{r},t) = \sum_{\mathbf{k}} \Delta N(\mathbf{k},t) e^{-i\mathbf{k}\cdot\mathbf{r}} \tag{2.3}$$

where $\mathbf{k} = \frac{2\pi}{L}(l,m,n)$. (2.4)

Substituting (2.3) into (2.1), we obtain the following equation describing the received signal:

$$\begin{aligned} E_s(t) &= -\frac{r_e E_o e^{i\omega_0 t}}{R_0}\int_{V_s}\sum_{\mathbf{k}}\Delta N(\mathbf{k},t)e^{-i\mathbf{k}\cdot\mathbf{r}}e^{-2ik_0 z}dV \\ &= -\frac{r_e E_o e^{i\omega_0 t}}{R_0}\sum_{\mathbf{k}}\Delta N(\mathbf{k},t)\int_{V_s}e^{-i(\mathbf{k}\cdot\mathbf{r}+2k_0 z)}dV \\ &= -\frac{r_e E_o e^{i\omega_0 t}}{R_0}\sum_{\mathbf{k}}\Delta N(\mathbf{k},t)\int_{-\frac{d}{2}}^{\frac{d}{2}}e^{-ik_x x}dx\int_{-\frac{d}{2}}^{\frac{d}{2}}e^{-ik_y y}dy\int_{R_0-\frac{d}{2}}^{R_0+\frac{d}{2}}e^{-i(k_z+2k_0)z}dz \\ &= -\frac{r_e E_o e^{i(\omega_0 t-2k_0R_0)}}{R_0}\sum_{\mathbf{k}}\Delta N(\mathbf{k},t)\frac{\sin\frac{k_x d}{2}\sin\frac{k_y d}{2}\sin\frac{(k_z+2k_0)d}{2}}{k_x k_y\left(k_z+2k_0\right)} \end{aligned} \quad (2.5)$$

where $d = V_s^{-3}$.

In order to obtain the spectrum of the received signal, we will calculate the auto-correlation function (ACF):

$$\begin{aligned} \rho(\tau) &= \left\langle E_s(t)E_s^*(t+\tau)\right\rangle \\ &= \frac{r_e^2\left|E_o\right|^2 e^{-i\omega_0\tau}}{R_0^2}\left\{\sum_{\mathbf{k}}\left\langle\Delta N(\mathbf{k},t)\Delta N^*(\mathbf{k},t+\tau)\right\rangle\frac{\sin^2\frac{k_x d}{2}\sin^2\frac{k_y d}{2}\sin^2\frac{(k_z+2k_0)d}{2}}{k_x^2k_y^2\left(k_z+2k_0\right)^2}\right. \\ &\left. + \sum_{\mathbf{k},\mathbf{k}',\mathbf{k}\neq\mathbf{k}'}\left\langle\Delta N(\mathbf{k},t)\Delta N^*(\mathbf{k}',t+\tau)\right\rangle\frac{\sin\frac{k_x d}{2}\sin\frac{k'_x d}{2}\sin\frac{k_y d}{2}\sin\frac{k'_y d}{2}\sin\frac{(k_z+2k_0)d}{2}\sin\frac{(k'_z+2k_0)d}{2}}{k_x k'_x k_y k'_y\left(k_z+2k_0\right)\left(k'_z+2k_0\right)}\right\}. \end{aligned} \quad (2.6)$$

Since $\Delta N(\mathbf{k},t)$ is independent of $\Delta N(\mathbf{k}',t)$ when $\mathbf{k}\neq\mathbf{k}'$, the second term should be zero, yielding the following equation describing ACF:

$$\rho(\tau) = \frac{r_e^2\left|E_o\right|^2 e^{-i\omega_0\tau}}{R_0^2}\sum_{\mathbf{k}}\left\langle\Delta N(\mathbf{k},t)\Delta N^*(\mathbf{k},t+\tau)\right\rangle\frac{\sin^2\frac{k_x d}{2}\sin^2\frac{k_y d}{2}\sin^2\frac{(k_z+2k_0)d}{2}}{k_x^2k_y^2\left(k_z+2k_0\right)^2} \quad (2.7)$$

Because the spectrum spread by fluctuation is much narrower than the carrier frequency, $\mathbf{k}$ is not sufficiently different from $-2k_0$ that we can assume $\Delta N(\mathbf{k},t)$ to be a constant of $\mathbf{k}$. Evaluating the summation term as an integral, we obtain the following equation:

$$\rho(\tau)=\frac{r_e^2|E_o|^2 e^{-i\omega_0\tau}}{R_0^2}\left\langle \Delta N(-2\mathbf{k}_0,t)\Delta N^*(-2\mathbf{k}_0,t+\tau)\right\rangle \sum_{\mathbf{k}} \frac{\sin^2\frac{k_x d}{2}\sin^2\frac{k_y d}{2}\sin^2\frac{(k_z+2k_0)d}{2}}{k_x^2 k_y^2\left(k_z+2k_0\right)^2}$$

$$=\frac{r_e^2|E_o|^2 V_s L^3 e^{-i\omega_0\tau}}{R_0^2}\left\langle \Delta N(-2\mathbf{k}_0,t)\Delta N^*(-2\mathbf{k}_0,t+\tau)\right\rangle. \tag{2.8}$$

Applying $\left\langle f(t)f^*(t+\tau)\right\rangle = \int\left\langle |f(\omega)|^2\right\rangle e^{-i\omega\tau}d\omega$ to both sides of the above equation,

$$\int\left\langle |E_s(\omega)|^2\right\rangle e^{-i\omega\tau}d\omega=\frac{r_e^2|E_o|^2 V_s L^3 e^{-i\omega_0\tau}}{R_0^2}\int\left\langle |\Delta N(-2\mathbf{k}_0,\omega')|^2\right\rangle e^{-i(\omega_0+\omega')\tau}d\omega' \tag{2.9}$$

and we obtain the following equation:

$$\left\langle |E_s(\omega)|^2\right\rangle d\omega=\frac{r_e^2|E_o|^2 V_s L^3}{R_0^2}\left\langle |\Delta N(-2\mathbf{k}_0,\omega)|^2\right\rangle d\omega. \tag{2.10}$$

Finally, the radar scattering cross section per unit frequency and unit scattering volume becomes the following:

$$\sigma_b(\omega_0\pm\omega)d\omega=r_e^2L^3\left\langle |\Delta N(2\mathbf{k}_0,\omega)|^2\right\rangle d\omega. \tag{2.11}$$

With this equation, we can apply plasma density fluctuation to the incoherent scatter radar spectrum.

2.3 Density Fluctuation in Plasma

The following equations express the dynamics of ions and electrons in plasma:

$$N_0\mathbf{u}_i=e\mathbf{Y}_i\cdot\mathbf{E} \tag{2.12}$$

$$N_0\mathbf{u}_e=\mathbf{Y}_e\cdot\left(\mathbf{F}-e\mathbf{E}\right) \tag{2.13}$$

$$\mathbf{j}=N_0e\left(\mathbf{u}_i-\mathbf{u}_e\right) \tag{2.14}$$

and

$$\mathbf{j}=\boldsymbol{\Gamma}\cdot\mathbf{E} \tag{2.15}$$

where $\mathbf{u}_i$ is the flow vector of ions, $\mathbf{u}_e$ is the flow vector of electrons, $\mathbf{Y}_i$ is the admittance tensor of ions, $\mathbf{Y}_e$ is the admittance tensor of electrons, $\mathbf{\Gamma}$ is the conductance tensor, and $\mathbf{F}$ is a fictitious force introduced to derive the force that affects electrons.

Eliminating $\mathbf{E}$, $\mathbf{u}_i$, and $\mathbf{j}$,

$$N_0\mathbf{u}_e = \mathbf{Y}'\cdot\mathbf{F} \tag{2.16}$$

where

$$\mathbf{Y}' = \left(\mathbf{Y}_i - \mathbf{\Gamma}/e^2\right)\left(\mathbf{Y}_i + \mathbf{Y}_e - \mathbf{\Gamma}/e^2\right)^{-1}\mathbf{Y}_e. \tag{2.17}$$

If both the force and the electron flow are regard as one dimensional along the z axis, the admittance tensor is diagonal and (2.17) becomes

$$Y' = \frac{\left(Y_i - \Gamma/e^2\right)Y_e}{Y_i + Y_e - \Gamma/e^2}. \tag{2.18}$$

Now, remember Nyquist's theorem. Consider generalized force V_0 and response I_0 to the force. If the complex amplitude of the response has a linear relationship to the complex amplitude of the force, we can define generalized admittance $Y(\omega)$ by

$$I_0 = Y(\omega)V_0. \tag{2.19}$$

Nyquist's theorem says that when the system is in thermal equilibrium and disconnected from any disturbing force, the response becomes a stochastic function of time, and its spectrum becomes:

$$\left\langle \left|I(\omega)\right|^2 \right\rangle d\omega = \frac{KT}{\pi}\Re[Y(\omega)]d\omega, \tag{2.20}$$

while the spectrum of the force, which is exerted by spontaneous thermal fluctuation is:

$$\left\langle \left|V(\omega)\right|^2 \right\rangle d\omega = \frac{KT}{\pi}\frac{\Re[Y(\omega)]}{\left|Y(\omega)\right|^2}d\omega \tag{2.21}$$

where K is Boltzmann's constant and T is the system temperature.

Applying this theorem to (2.16) and rewriting $L^3N_0\mathbf{u}$ as the response I,

$$\left\langle \left|N_0\mathbf{u}(\mathbf{k},\omega)\right|^2 \right\rangle d\omega = \frac{KT}{\pi L^3}\Re[Y'(\omega)]d\omega. \tag{2.22}$$

The particles' flow, $N_0\mathbf{u}$, and density fluctuation are described by

$$\frac{dN}{dt} = -\nabla \cdot (N_0 \mathbf{u}) \tag{2.23}$$

Considering that the number density and flow are both periodic along the z-axis in the form of $e^{j(\omega t - kz)}$,

$$\begin{aligned} \left\langle \left|\Delta N(\mathbf{k},\omega)\right|^2 \right\rangle d\omega &= (k/\omega)^2 \left\langle \left|N_0 u_z(\mathbf{k},\omega)\right|^2 \right\rangle d\omega \\ &= \frac{KTk^2}{\pi L^3 \omega^2} \mathrm{Re}(Y'_{zz}) d\omega \end{aligned} \tag{2.24}$$

Substituting (2.24) into (2.11),

$$\sigma_b(\omega_0 \pm \omega) d\omega = \frac{r_e^2 KTk^2}{\pi\omega^2} \mathrm{Re}(Y'_{zz}) d\omega \tag{2.25}$$

where $Y' = \left(Y_i - \Gamma/e^2\right) Y_e \Big/ \left(Y_i + Y_e - \Gamma/e^2\right)$ if all tensors are diagonal.

The next step in obtaining the spectrum is considering the admittance tensor $\mathbf{Y}'$.

2.4 Admittance Tensor and Spectrum

The conductivity tensor Γ can be derived from Maxwell's equations by eliminating the magnetic field term and transforming the equation to the form of $\mathbf{j} = \boldsymbol{\Gamma} \cdot \mathbf{E}$. Each element becomes

$$\Gamma_{pq} = \left(ic^2/4\pi\omega\right)\left[\left(k^2 - \omega^2/c^2\right)\delta_{pq} - k_p k_q\right] \quad \text{in cgs units} \tag{2.26a}$$

or

$$\Gamma_{pq} = \left(i\varepsilon_0 c^2/\omega\right)\left[\left(k^2 - \omega^2/c^2\right)\delta_{pq} - k_p k_q\right] \quad \text{in MKS units.} \tag{2.26b}$$

When $\mathbf{k} = (0,\ 0,\ k)$, Γ is diagonal and the zz-element is

$$\Gamma_{zz} = \omega/(4\pi i) \qquad \text{in cgs units} \tag{2.27a}$$

or

$$\Gamma_{zz} = -i\varepsilon_0 \omega \qquad \text{in MKS units.} \tag{2.27b}$$

The admittance tensor is more complicated to derive, but Dougherty and Farley(1960) did it by starting from the Boltzmann equation. We employ their results.

In the collisionless case,

$$\begin{cases} Y_{xx} = Y_{yy} = \dfrac{N_0}{m\omega}\left[R_x(\theta) - iI_x(\theta)\right] \\ Y_{zz} = \dfrac{N_0}{m\omega}\left[R_z(\theta) - iI_z(\theta)\right] \end{cases} \tag{2.28}$$

where $R_x = \sqrt{\pi}\theta e^{-\theta^2}$, $I_x = 2\theta e^{-\theta^2}\int_0^{\theta} e^{p^2}dp$, $R_z = 2\theta^2 R_x$, $I_z = 2\theta^2\left(I_x - 1\right)$, and $\theta = \left(\omega/k\right)\sqrt{m/2KT}$.

At this point we only lack the zz-element, which is

$$Y_{zz} = \frac{N_0\omega}{KTk^2}\left[\pi^{\frac{1}{2}}\theta e^{-\theta^2} + i\left(1 - I(\theta)\right)\right] \tag{2.29}$$

where $I(\theta) = 2\theta e^{-\theta^2}\int_0^{\theta} e^{p^2}dp$.

Next, we introduce a new dimensionless normalized admittance tensor **y** to simplify the following equations:

$$\frac{KTk^2}{N_0\omega}\mathbf{Y} \equiv \mathbf{y} . \tag{2.30}$$

The spectrum becomes simply

$$\sigma_b(\omega_0 \pm \omega)d\omega = \frac{r_e^2 N_0}{\pi\omega}\mathrm{Re}(y'_{zz})d\omega \tag{2.31}$$

where

$$y'_{zz} = \frac{\left(y_{zzi} + i\lambda_D^2 k^2\right)y_{zze}}{y_{zze} + y_{zzi} + i\lambda_D^2 k^2} \tag{2.32}$$

when the electron temperature and ion temperature are the same. λ_D is the Debye length of electrons ($= \sqrt{KT/4\pi N_0 e^2}$ in cgs units or $\sqrt{\varepsilon_0 KT/N_0 e^2}$ in MKS units).

The admittance tensor is simplified to

$$y_{zz} = \pi^{\frac{1}{2}}\theta e^{-\theta^2} + i\left(1 - I(\theta)\right). \tag{2.33}$$

When $\theta \ll 1$, we can use the following approximation:

$$y_{zz} = \pi^{\frac{1}{2}}\theta + i. \tag{2.34}$$

This approximation is useful for expressing the electron term because $\theta_e = (\omega/k)\sqrt{m_e/2KT_e} \ll \theta_i \simeq 1$.

Now, we will calculate the spectrum for several cases.

Case1: Temperature is at equilibrium ($T_e = T_i$) and collision is not the dominant phenomenon.

Substituting (2.33) for y_{zzi} and (2.34) for y_{zze} in (2.32) and making the assumptions that $\lambda_D^2 k^2 \ll 1$ and $\theta_i e^{-\theta_i^2} \gg \theta_e$,

$$\mathrm{Re}(y'_{zz}) = \frac{\pi^{\frac{1}{2}}\theta_i e^{-\theta_i^2}}{\pi\theta_i^2 e^{-2\theta_i^2} + \left(2 - I(\theta_i)\right)^2}. \tag{2.35}$$

Replacing θ_i with θ and substituting (2.35) into (2.31), the spectrum becomes

$$\boxed{\sigma_b(\omega_0 \pm \omega)d\omega = \frac{r_e^2 N_0}{\pi^{\frac{1}{2}}} \frac{\theta e^{-\theta^2}}{\pi\theta^2 e^{-2\theta^2} + \left(2 - I(\theta)\right)^2} \frac{d\omega}{\omega}.} \tag{2.36}$$

Case2: Temperature is not at equilibrium ($T_e \neq T_i$) and collision is not the dominant phenomenon.

In this case, where ion temperature and electron temperature are different, we must return to (2.18):

$$\begin{aligned} Y'_{zz} &= \frac{\left(Y_{zzi} - \Gamma_{zz}/e^2\right)Y_{zze}}{Y_{zzi} + Y_{zze} - \Gamma_{zz}/e^2} \\ &= \frac{N_0\omega}{KT_e k^2} \frac{\left[\mu y_{zzi} + i\lambda_D^2 k^2\right] y_{zze}}{y_{zze} + \mu y_{zzi} + i\lambda_D^2 k^2} \end{aligned} \tag{2.37}$$

where μ is the electron-ion temperature ratio($= T_e/T_i$).

If we define y'_{zz} as

$$y'_{zz} \equiv \frac{KT_i k^2}{N_0 \omega} Y'_{zz} = (1/\mu) \cdot \frac{\left[\mu y_{zzi} + i\lambda_D^2 k^2\right] y_{zze}}{y_{zze} + \mu y_{zzi} + i\lambda_D^2 k^2} \tag{2.38}$$

we can use (2.31) again. Substituting (2.33) and (2.34) into (2.38) and using the same assumptions as in Case1, we obtain

$$\mathrm{Re}(y'_{zz}) = \frac{\pi^{\frac{1}{2}} \theta e^{-\theta^2}}{\mu^2 \pi \theta^2 e^{-2\theta^2} + \left[1 + \mu\left(1 - I(\theta)\right)\right]^2}. \tag{2.39}$$

The spectrum is

$$\boxed{\sigma_b(\omega_0 \pm \omega) d\omega = \frac{r_e^2 N_0}{\pi^{\frac{1}{2}}} \frac{\theta e^{-\theta^2}}{\mu^2 \pi \theta^2 e^{-2\theta^2} + \left[1 + \mu\left(1 - I(\theta)\right)\right]^2} \frac{d\omega}{\omega}} \tag{2.40}$$

Case3: Temperature is not at equilibrium ($T_e \neq T_i$) and collision cannot be neglected

For the case where collisions between ions and neutrals, as well as collisions between the electron and neutral gas, cannot be neglected, the zz-element of the normalized admittance tensor is a function of both Doppler frequency and collision frequency and the following equation from Dougherty and Farley(1963) is applicable:

$$y_{zz} = i \frac{1 - (\theta - i\psi) G(\theta - i\psi)}{1 + i\psi G(\theta - i\psi)} \tag{2.41}$$

where ψ is the normalized collision frequency $\psi = (\nu/k)\sqrt{m/2KT}$ and ν is the collision frequency.

$G(x)$ is called the plasma dispersion function. The sign of x is opposite to the sign of the function mentioned in Fried and Conte (1961):

$$G(x) = 2e^{-x^2} \int_{-i\infty}^{x} e^{p^2} dp \,. \tag{2.42}$$

In the same way as (2.38), the zz-element of y' is

$$y'_{zz}(\theta_i, \theta_e, \psi_i, \psi_e) = (1/\mu) \frac{\left(\mu y_{zzi}(\theta_i, \psi_i) + i\lambda_D^2 k^2\right) y_{zze}(\theta_e, \psi_e)}{y_{zze}(\theta_e, \psi_e) + \mu y_{zzi}(\theta_i, \psi_i) + i\lambda_D^2 k^2} \,. \tag{2.43}$$

The spectrum is

$$\boxed{\sigma_b(\omega_0 \pm \omega) d\omega = N_0 r_e^2 \,\mathrm{Re}\left[(1/\mu) \frac{\left(\mu y_{zzi} + i\lambda_D^2 k^2\right) y_{zze}}{y_{zze} + \mu y_{zzi} + i\lambda_D^2 k^2} \right] (d\omega / \pi\omega)} \tag{2.44}$$

θ_i and θ_e are $(\omega/k)\sqrt{m_i/2KT_i}$ and $(\omega/k)\sqrt{m_e/2KT_e}$ respectively; therefore the spectrum is a function of ion temperature T_i, electron temperature T_e or electron-ion temperature ratio μ, ion mass m_i, ion collision frequency ν_i, and electron collision frequency ν_e.

In order to estimate these parameters from the shape of the spectrum, the practical approach is to generate theoretical spectra based upon the above theory and to compare them with measured spectra. Varying parameters in the theoretical spectrum to obtain a best fit with the measured spectrum yields the ionosphere parameters appropriate to the measured spectrum. Although we derived the three special cases above for the purposes of illustration, it is possible to apply a general fitting procedure to generate the theoretical spectrum from the most general form of case 3 using computers. The calculation of the plasma dispersion function is computationally challenging because of complex integration; however an approximate function which delivers faster calculation is usually employed.

Examples of a spectrum calculated by Equation (2.44) are shown in Fig. 2.1 and Fig. 2.2. In Fig. 2.1, electron to ion temperature ratio T_e/T_i is taken as a variable parameter and both of ion and collision frequencies, ψ_i and ψ_e are set to zero. In Fig 2.2,

normalized ion collision frequency ψ_i is taken as a variable parameter and normalized electron collision frequency ψ_e is set as $\psi_i/10$, and electron to ion temperature ratio T_e/T_i is set to 1.

In the lower ionosphere (<150km) that is applicable to all the analysis for this thesis, the temperature ratio can be assumed to be unity. Therefore, temperature ratio is not an important variable parameter in the fitting procedure for data presented in later chapters. By contrast, the collision frequency strongly affects the spectrum, especially at the bottom of the ionosphere (<120km). In the upper ionosphere, the electron temperature becomes significantly higher than the ion temperature and the temperature ratio needs to be taken into account, whereas the collision frequency is almost zero and collision effects are negligible.

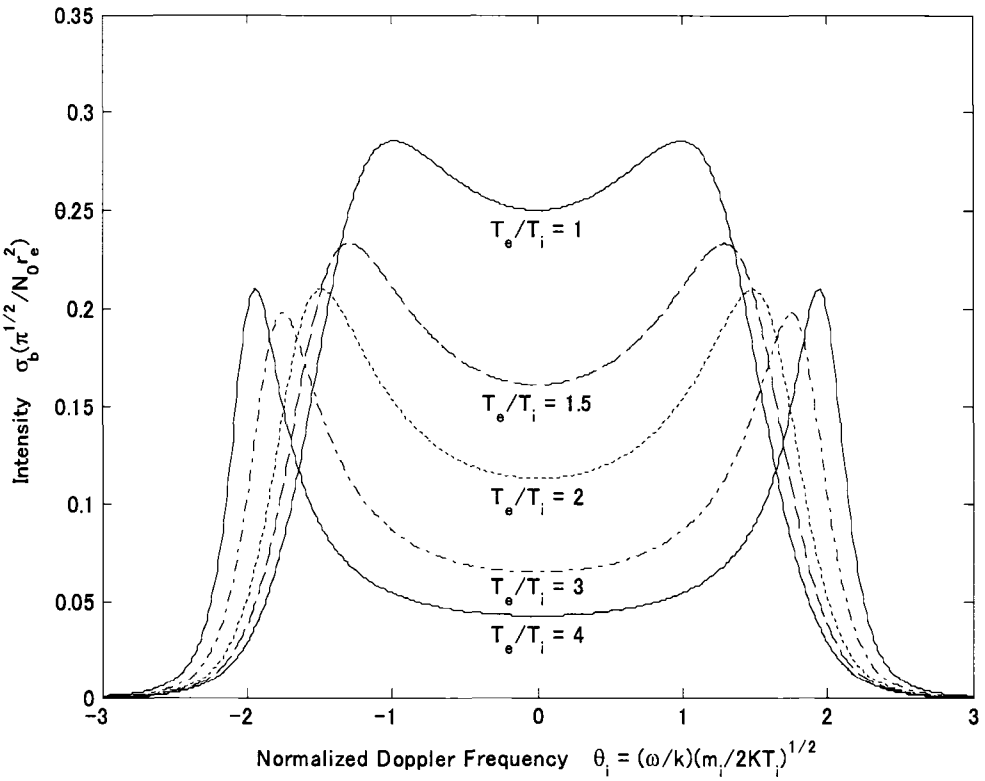

Fig. 2.1 Incoherent scattering spectrum varying with the electron to ion temperature ratio. Both ion and collision frequencies are set to zero.

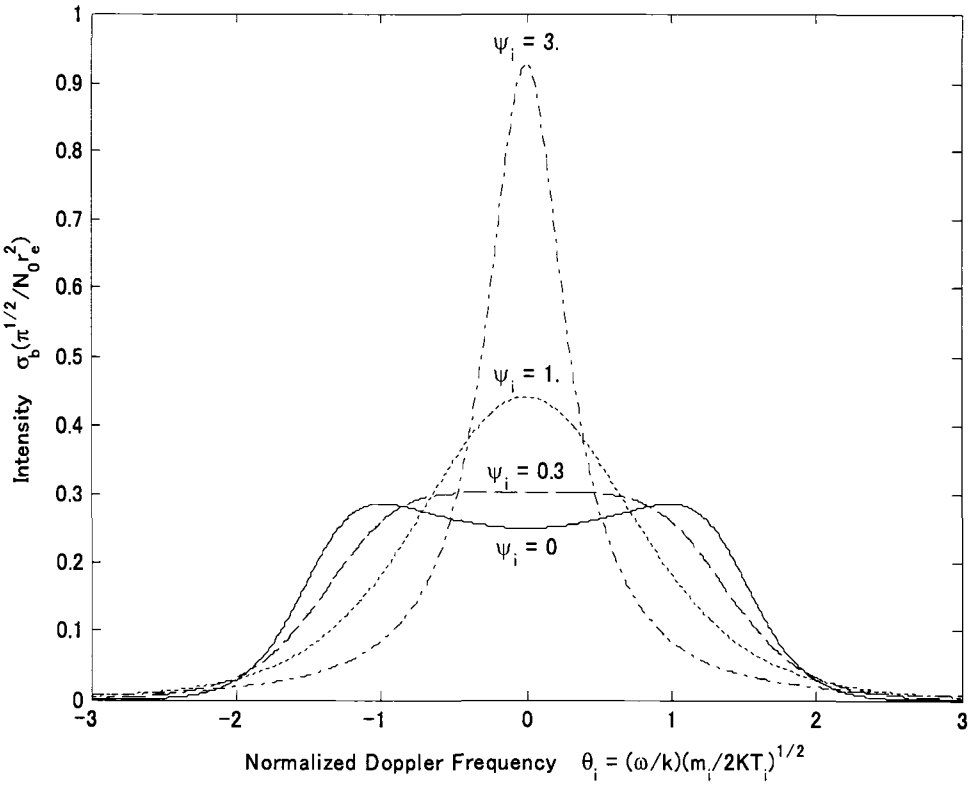

Fig. 2.2 Incoherent scattering spectrum varying with the normalized ion collision frequency. The normalized electron collision frequency is set as $\psi_e = \psi_i/10$ and electron to ion temperature ratio is set to 1.

2.5 Total Scattering Cross Section

The basic procedure used to obtain the total scattering cross section is integrating the spectrum, i.e. adding signals over the frequency band that contains the received spectrum:

$$\begin{aligned}\sigma_{\text{total}} &= \int_{-\infty}^{\infty} \sigma_d(\omega_0+\omega)d\omega \\ &= N_0 r_e^2 \,\text{Re}\int_{-\infty}^{\infty} y'_{zz}\frac{d\omega}{\pi\omega}.\end{aligned} \tag{2.45}$$

Dougherty and Farley(1960) evaluated the total cross section as the following:

$$\frac{\sigma_{\text{total}}}{N_0 r_e^2} = \left(\frac{\lambda_D^2 k^2}{1+\lambda_D^2 k^2} + \frac{1}{\left(1+\mu+\lambda_D^2 k^2\right)\left(1+\lambda_D^2 k^2\right)}\right). \tag{2.46}$$

In the case of $\lambda_D^2 k^2 \ll 1$ (i.e. the radar wavelength is much larger than the plasma Debye length), the right side of the equation approaches $(1+T_e/T_i)^{-1}$. For example, using typical ionospheric values, $T_e = 200\text{K}$, $N_e = 10^{12} m^{-3}$, and the radar carrier frequency is $f_0 = 1290\text{MHz}$, $\lambda_D^2 k^2$ is 2.8×10^{-3} and the following approximation is valid:

$$\sigma_{\text{total}} = N_0 r_e^2 \frac{1}{1+T_e/T_i} \tag{2.47}$$

Fig. 2.3 below shows the numerical integration results of (2.45) and approximation results of $(1+T_e/T_i)^{-1}$. It shows that we can use the approximation results in practical situations.

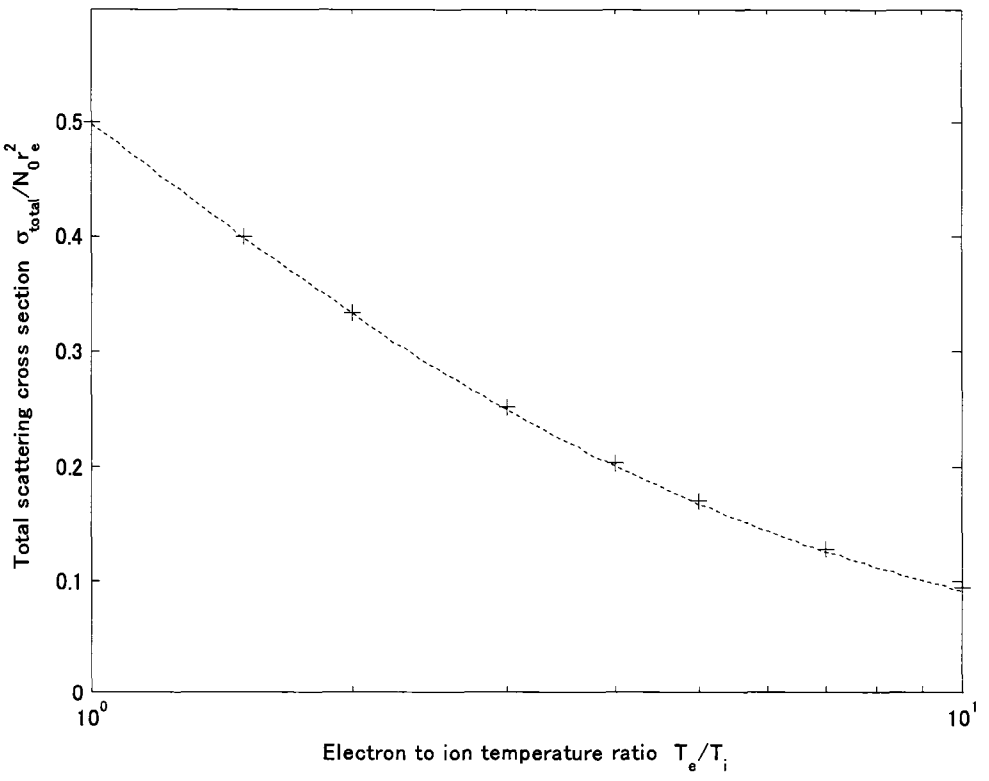

Fig. 2.3 Total scattering cross section versus electron to ion temperature ratio. '+' is calculated by numerical integration of the spectrum and broken line is $1/(1+T_e/T_i)$ curve, which approximates the total scattering cross section well.

CHAPTER 3
RADAR TECHNIQUE

3.1 Introduction

In the previous chapter we discussed the radar scattering cross section resulting from thermally-induced fluctuations in the refractive index. In this chapter we consider the radar techniques required to detect those weak signals scattered from the ionosphere. The radar equation that defines the received power for a given radar system is first presented, and then modulation methods that permit us to obtain a high resolution signal from a long transmitter pulse are discussed.

3.2 Radar Equation

The general radar equation to calculate the received power from a point target is the following (eg. Skolnik(editor), 1990):

$$P_r = \frac{P_t G^2 \lambda^2 \sigma}{(4\pi)^2 R^4 L} \tag{3.1}$$

where P_r is the received signal power, P_t is the transmitted signal power, G is the antenna gain($= 4\pi A_e / \lambda^2$; A_e is the effective area of the antenna), λ is the wave length, σ is the radar cross section of the pinpoint target, R is the range distance of the target, and L is the total power loss including propagation loss, transmitter to antenna loss, and antenna to receiver loss.

For the incoherent-scatter radar(and also meteorological radars), scattering occurs in the entire volume created by the antenna beam. The beam-filling scattering volume is also determined by the pulse length; therefore the total radar cross section becomes the following:

$$\begin{aligned} \sigma &= \sigma_0 V \\ &= \sigma_0 R^2 \Omega \frac{c\tau}{2} \end{aligned} \tag{3.2}$$

where σ_0 is the radar cross section per unit volume which is expressed as the Equation (2.47) in chapter 2, V is the target volume, Ω is the solid angle of antenna beam($=\lambda^2/A_e$), c is the speed of light, and τ is the pulse length. This equation tells us that for a given volume of scatter, the received power is inversely proportional to R^2 (as compared to a point target with an R^4 dependence).

A most important parameter for designing radars is the signal to noise ratio (SNR), described by

$$SNR = \frac{P_r}{N} = \frac{P_r}{KT_{sys}B} \tag{3.3}$$

where K is Boltzman's constant, T_{sys} is the system noise temperature, and B is the bandwidth of the receiver.

In the next we will evaluate the SNR using typical ionospheric parameters and the Søndrestrøm IS radar parameters shown in Table 1.1 as a specific example.

1) Solid angle of antenna beam Ω and antenna gain G

Using the antenna diameter of 32m and the frequency of 1290MHz in the Søndrestrøm IS radar and assuming an antenna efficiency of 70 %, the solid angle of the antenna beam is

$$\Omega = \frac{\lambda^2}{A_e} = \frac{\left(3\times10^8[\mathrm{ms^{-1}}]/1290\times10^6[\mathrm{Hz}]\right)^2}{\pi\left(32[\mathrm{m}]/2\right)^2\times0.7} = 9.61\times10^{-5}[\mathrm{sr}] \tag{3.4}$$

and the antenna gain becomes

$$G = \frac{4\pi}{\Omega} = \frac{4\pi}{9.61\times10^{-5}[\mathrm{sr}]} = 1.31\times10^5 = 51.2\ [\mathrm{dB}]. \tag{3.5}$$

2) Radar Cross Section σ_0, σ

We now assume ionospheric parameters to be $T_e = T_i$ and $N_0 = 10^{11}\mathrm{m}^{-3}$. From Equation (2.47), the radar cross section per unit volume expressed with the classical electron radius $r_e = e^2/4\pi\varepsilon_0 m_e c^2 = 2.82\times10^{-15}$, is

$$\begin{aligned}\sigma_0 &= N_0 r_e^2 \frac{1}{1+T_e/T_i} \\ &= 10^{11}[\mathrm{m}^{-3}]\times\left(2.82\times10^{-15}[\mathrm{m}]\right)^2\times0.5 = 3.98\times10^{-19}[\mathrm{m}^{-1}].\end{aligned} \tag{3.6}$$

The target volume depends on the solid angle of antenna beam, target distance and pulse length. In the long pulse mode, of which observation target is mainly F-region, the target distance is 200-500km and pulse length is 320 us in the Søndrestrøm IS radar. In the short pulse mode, of which observation target is the fine structures in lower ionosphere, the target distance is approximately 100km and pulse length is 28us.

Assuming that the target distance R is 500km and pulse length τ is 320 us, the radar cross section for the long pulse mode is

$$\begin{aligned}\sigma_{LP} &= \sigma_0 R^2 \Omega \frac{c\tau}{2} \\ &= 3.98\times10^{-19}[\mathrm{m}^{-1}]\times\left(500\times10^3[\mathrm{m}]\right)^2\times9.61\times10^{-5}\times\frac{3\times10^8[\mathrm{m}\cdot\mathrm{s}^{-1}]\times320\times10^{-6}[s]}{2} \\ &= 4.59\times10^{-7}[\mathrm{m}^2].\end{aligned} \tag{3.7}$$

Also assuming that target distance R is 100km and pulse length τ is 28 us, the total radar cross section for the short pulse mode is

$$\begin{aligned}\sigma_{SP} &= 3.98\times10^{-19}[\mathrm{m}^{-1}]\times\left(100\times10^3[\mathrm{m}]\right)^2\times9.61\times10^{-5}\times\frac{3\times10^8[\mathrm{m}\cdot\mathrm{s}^{-1}]\times28\times10^{-6}[s]}{2} \\ &= 1.61\times10^{-9}[\mathrm{m}^2].\end{aligned} \tag{3.8}$$

3) Received signal power P_r

Assuming that the transmitted power P_t is 3MW and total loss L is 5dB, the received signal power for long pulse mode is

$$P_{r\_LP} = \frac{P_t G^2 \lambda^2 \sigma_{LP}}{(4\pi)^2 R^4 L}$$

$$= \frac{3\times10^6[\mathrm{W}]\times(1.31\times10^5)^2\times\left(\frac{3\times10^8[\mathrm{m\cdot s^{-1}}]}{1290\times10^6[\mathrm{Hz}]}\right)^2\times4.59\times10^{-7}[\mathrm{m^2}]}{(4\pi)^2\times(500\times10^3[\mathrm{m}])^4\times10^{0.5}} \quad (3.9)$$

$$= 4.10\times10^{-17}[\mathrm{W}],$$

and for short pulse mode is

$$P_{r\_SP} = \frac{P_t G^2 \lambda^2 \sigma_{SP}}{(4\pi)^2 R^4 L}$$

$$= \frac{3\times10^6[\mathrm{W}]\times(1.31\times10^5)^2\times\left(\frac{3\times10^8[\mathrm{m\cdot s^{-1}}]}{1290\times10^6[\mathrm{Hz}]}\right)^2\times1.61\times10^{-9}[\mathrm{m^2}]}{(4\pi)^2\times(100\times10^3[\mathrm{m}])^4\times10^{0.5}} \quad (3.10)$$

$$= 8.98\times10^{-17}[\mathrm{W}].$$

4) Noise power N and signal to noise ratio SNR

The receiver bandwidth B is 31.3 kHz for the long pulse mode and 125kHz for the short pulse mode in base-band stage. Those should be doubled to calculate noise power because the band width in IF(intermediate frequency) stage is twice larger than in the base-band stage. Assuming that the system noise temperature T_{sys} is 110K, noise power for the long pulse mode is calculated as

$$N_{LP} = KT_{sys}B_{LP}$$

$$= 1.38\times10^{-23}[\mathrm{J\cdot K^{-1}}]\times110[\mathrm{K}]\times2\times31.3\times10^3[\mathrm{Hz}] \quad (3.11)$$

$$= 9.50\times10^{-17}[\mathrm{W}],$$

and for the short pulse mode is

$$N_{SP} = KT_{sys}B_{LP}$$

$$= 1.38\times10^{-23}[\mathrm{J\cdot K^{-1}}]\times110[\mathrm{K}]\times2\times125\times10^3[\mathrm{Hz}] \quad (3.12)$$

$$= 3.80\times10^{-16}[\mathrm{W}].$$

The SNR for the long pulse mode becomes

$$SNR_{LP} = \frac{P_{r\_LP}}{N_{LP}} = \frac{4.10\times10^{-17}[\mathrm{W}]}{9.50\times10^{-17}[\mathrm{W}]} = 0.432 = -3.65[\mathrm{dB}], \tag{3.13}$$

and for the short pulse mode becomes

$$SNR_{SP} = \frac{P_{r\_SP}}{N_{SP}} = \frac{8.98\times10^{-17}[\mathrm{W}]}{3.80\times10^{-16}[\mathrm{W}]} = 0.236 = -6.27[\mathrm{dB}]. \tag{3.14}$$

In both cases of long pulse mode and short pulse mode, the SNR is less than 0dB, which means the received signal power is less than the noise power. However the SNR can be effectively improved by integrating the received signal for a number of pulses. The improvement factor yielded by such integration is given as

$$IMF = \frac{SNR_{\text{integrated}}}{SNR_{\text{single\_hit}}} = N. \tag{3.15}$$

where N is the number of pulses to integrate.

In practice the integration times typically vary from a few seconds to several tens of minutes depending on the particular application.

The above illustrates how the SNR (and therefore the target electron density) may be calculated from the basic radar parameters. In practice it is often useful to additionally calibrate an incoherent-scatter radar by using an independent measurement of the electron density in the ionosphere such as can be obtained from ionosondes.

3.3 Pulse Compression Technique

Although a longer pulse maximizes the detection capability, it reduces the range resolution of the radar. For example, the long pulse mode of Søndrestrøm radar, which uses a pulse length of 320 μs, is used to probe the main F-region ionosphere. This pulse length produces 48km range resolution, which is enough for many ionosphere observing missions; however, it is not sufficient to reveal small-scale structures, such as those that

are the objective of this thesis. However, simple shortening of pulse length to attain the desired range resolution is not practical because the energy of a short pulse will typically make the target undetectable.

A solution for this issue is modulating pulses. Modulation achieves higher range resolution while retaining sufficient total pulse energy to detect small-scale structures. This modulation technique is called "pulse compression". The basic idea of pulse compression is transmitting modulated long pulses, and demodulating the received pulses in order to make the demodulated pulse length shorter than the transmitted pulse.

In order to achieve this technique, frequency modulation, which is simply decreasing or increasing frequency, was used at first. This type of frequency modulated radar is often called "chirp" radar. In early radar systems, analog anomalous dispersion devices, which have special group delay characteristics varying with frequency, were used to compress pulses in the receiver, whereas modern radars use equivalent digital techniques.

This particular pulse-compression technique provides superior range resolution compared to an equivalent length of unmodulated pulse; however, there is a problem with this chirp pulse. When a target is moving toward (or away from) the radar, the received signals exhibit a Doppler frequency; in consequence, the measured target range becomes incorrect. The linear FM chirp radar cannot distinguish Doppler shift from range shift; this uncertainty or "ambiguity" can be visualized by cross-correlating a function that defines the transmitted pulse with the phased lagged pulse simulating the received signals.

Fig 3.1 and Fig.3.2 show the ambiguity function of an unmodulated pulse and that of a linear FM chirp pulse, respectively. The ridge of the ambiguity function shown in Fig.3.1 lies along the time axis on zero Doppler frequency, which means that the unmodulated pulse radar has less range resolution, whereas it has high frequency resolution. However, in the chirp pulse radar shown in Fig. 3.2, the ridge of the ambiguity function is tilted from the zero Doppler frequency axis, which means that if the target does not move along the radial direction to/from the radar, the chirp pulse radar has higher range resolution than does the unmodulated pulse radar. However if the target has a non-zero Doppler frequency, it is possible to make an erroneous range detection.

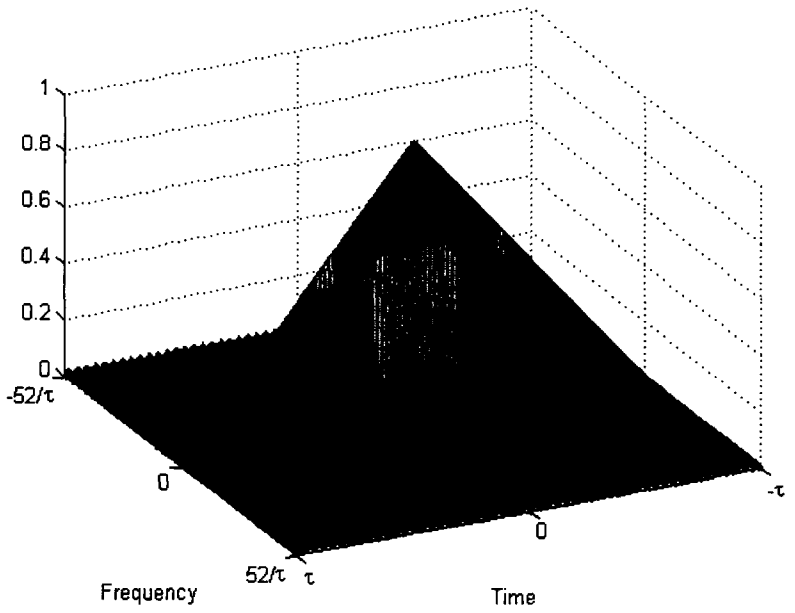

(a) 3D view

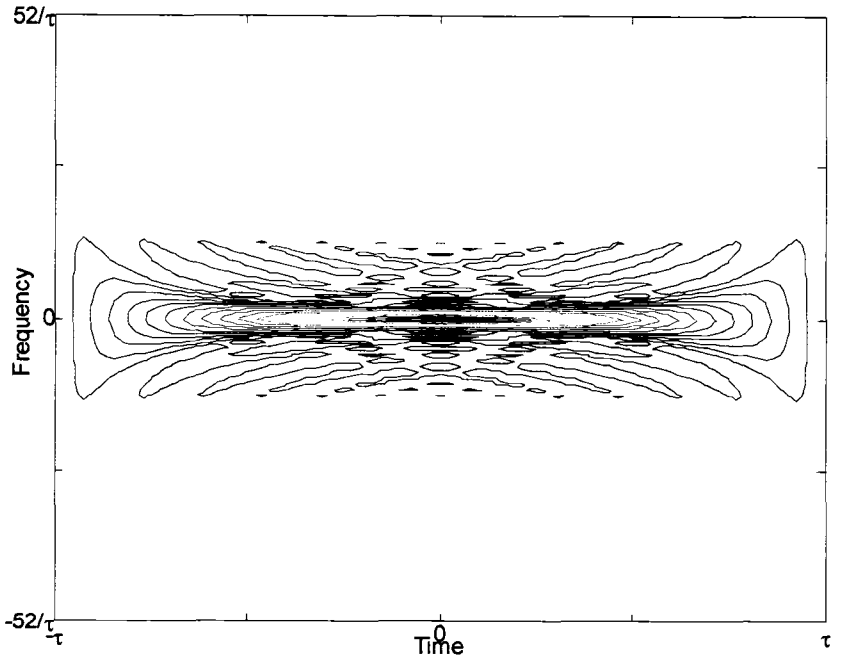

(b) Top view

Fig 3.1 Ambiguity function of unmodulated rectangular pulse. The unmodulated rectangular pulse delivers high Doppler frequency resolution but less range resolution.

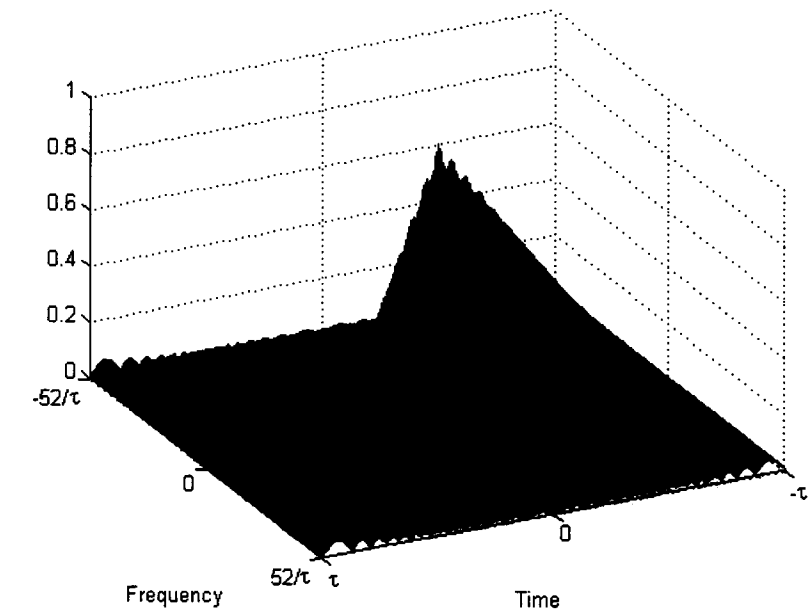

(a) 3D view

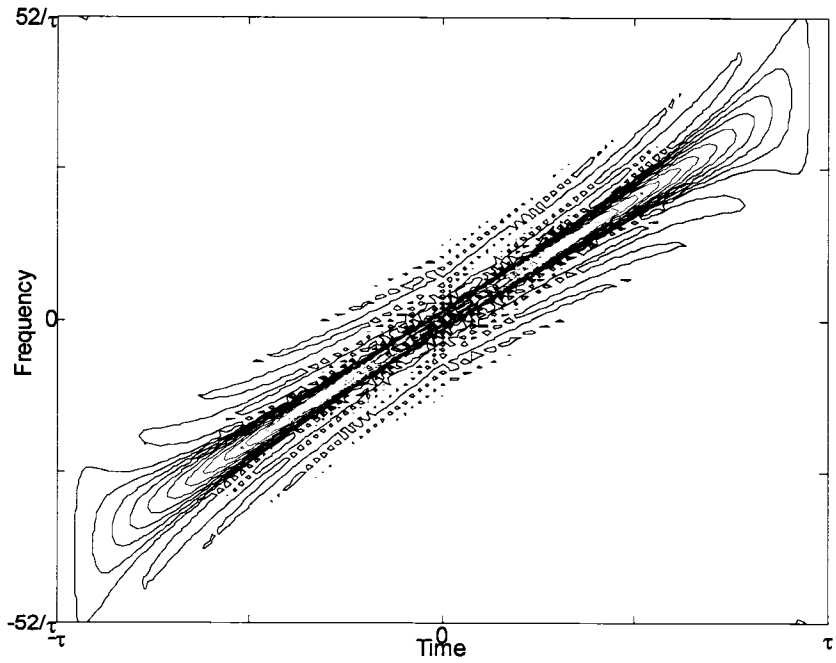

(b) Top view

Fig 3.2 Ambiguity function of linear FM chirp pulse. The linear FM chirp pulse produces high range resolution, but cannot avoid range-frequency ambiguity.

Other pulse compression methods have been developed, one of which is the family of Barker codes (Barker, 1953), which was used to accumulate data in the experiments described in this thesis. Table 3.1 shows bi-phase Barker codes up to 13 bits in length. Transmitted pulses are modulated with the particular codes shown in Table 3.1, and received signals are de-modulated with the same codes. For example, the 5-bit Barker coded pulse is

$$S_t(t) = \delta(t) + \delta(t-T) + \delta(t-2T) - \delta(t-3T) + \delta(t-4T) \tag{3.16}$$

where T is the unit time length of the modulation and

$$\delta(t) = \begin{cases} 1 & \text{when } -T/2 \le t \le T/2, \\ 0 & \text{else.} \end{cases} \tag{3.17}$$

The de-modulated signal is

$$S'_r(t) = S_r(t) - S_r(t-T) + S_r(t-2T) + S_r(t-3T) + S_r(t-4T) \tag{3.18}$$

where $S_r(t)$ is the received signal.

For the case where the received signal is simply the transmitted pulse signal delayed by T_d, the demodulated signal is

$$\begin{aligned} S'_r(t) = {} & \delta(t') + \delta(t'-T) + \delta(t'-2T) - \delta(t'-3T) + \delta(t'-4T) \\ & -\delta(t'-T) - \delta(t'-2T) - \delta(t'-3T) + \delta(t'-4T) - \delta(t'-5T) \\ & +\delta(t'-2T) + \delta(t'-3T) + \delta(t'-4T) - \delta(t'-5T) + \delta(t'-6T) \\ & +\delta(t'-3T) + \delta(t'-4T) + \delta(t'-5T) - \delta(t'-6T) + \delta(t'-7T) \\ & +\delta(t'-4T) + \delta(t'-5T) + \delta(t'-6T) - \delta(t'-7T) + \delta(t'-8T) \\ = {} & \delta(t') + \delta(t'-2T) + 5\delta(t'-4T) + \delta(t'-6T) + \delta(t'-8T) \end{aligned} \tag{3.19}$$

where $t' = t - T_d$. As shown as the above equation, the term of $t'-4T$ is integrated to 5 times larger than the transmitted pulse, as if the power of the received signal pulse is concentrated at $t'-4T$. Other relatively small terms are undesired signals called side-lobes or clutters.

Fig.3.3 shows the demodulated pulse shapes of other length codes. The transmitted pulse length, LT where L is code length and T is the unit time length of the code, seems to be reduced to T after demodulation, and the amplitude after demodulation

seems to be increased by L times larger than the amplitude transmitted in voltage, which means the signal power becomes L^2 times larger.

However, the bandwidth of the receiver filter necessary to accommodate the coded pulse must be wider by a factor of L, since the bandwidth of a coded pulse is L times wider than that of the unmodulated pulse of equivalent length. Since the noise power is proportional to the receiver bandwidth as we saw in Equation (3.3), the noise power at the receiver of the coded pulse radar becomes L times larger than the unmodulated pulse radar. In addition, since noises are summed by L times in the demodulating process as the Equation (3.18), noise power outputted from the demodulating process becomes L times larger than that of the received signal. In total, the noise power of the demodulated signal of coded pulse radar is L^2 times larger than that of the unmodulated pulse radar.

Since the magnification of the noise power by the demodulation process is equal to the magnification of the received signal power by the demodulation process, the SNR of the coded pulse radar is the same as that of unmodulated pulse radar which has the same pulse length.

Fig.3.4 shows the ambiguity function of the 13-bit Barker coded pulse. As Fig 3.4 shows, we can obtain high range resolution without a time - frequency ambiguity problem; the drawback, however, is clutters, witch is the undesired signals appeared around the main lobe. The coded pulse often has more clutters than unmodulated pulse or linear FM pulse.

The average clutter level of the demodulated signal is obtained by summing all side-lobes, and the total signal to clutter ratio (SCR) is given by

$$SCR = \frac{1}{N_c(1/SCR_1)} = \frac{L^2}{N_c} \tag{3.20}$$

where SCR_1 is the signal (main-lobe) to clutter (side-lobe) ratio of a single side-lobe and N_c is number of side-lobes at the demodulated signal shown in Fig.3.3. The average clutter levels of several code lengths are summarized in Table 3.1. In some cases which require an extra low clutter level, clutter may become a problem. However in the incoherent-scatter radar, SNR is usually so low that it is no problem to use Barker bi-

phase coding if the code length is long enough to obtain SCR better than the required final SNR. Considering that we need both better range resolution and better SNR in low electron density in the lower ionosphere, the pulse compression technique is quite useful.

Table 3.1 Barker bi-phase coding (Barker, 1953)

Code Length (L)	Code	Main-lobe to single side-lobe power ratio ($SCR_1=L^2$)	Number of side-lobes (N_c)	Total SCR ($SCR=L^2/N_c$)
2	++, +−	2^2	2	3.01 dB
3	++−	3^2	2	6.53 dB
4	++−+, +++−	4^2	4	6.02 dB
5	+++−+	5^2	4	7.96 dB
7	+++−−+−	7^2	6	9.12 dB
11	+++−−−+−−+−	11^2	10	10.83 dB
13	+++++−−++−+−+	13^2	12	11.49 dB

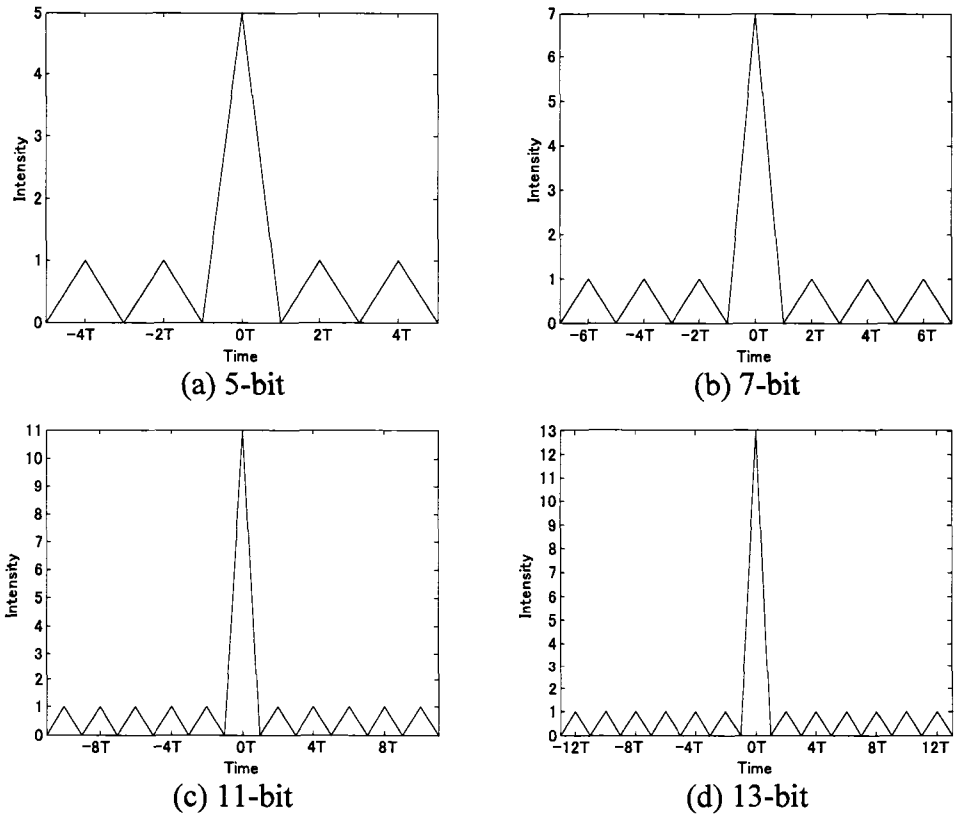

(a) 5-bit (b) 7-bit

(c) 11-bit (d) 13-bit

Fig.3.3 Demodulated pulse shapes of Barker bi-phase coding. T is the unit time period of the code.

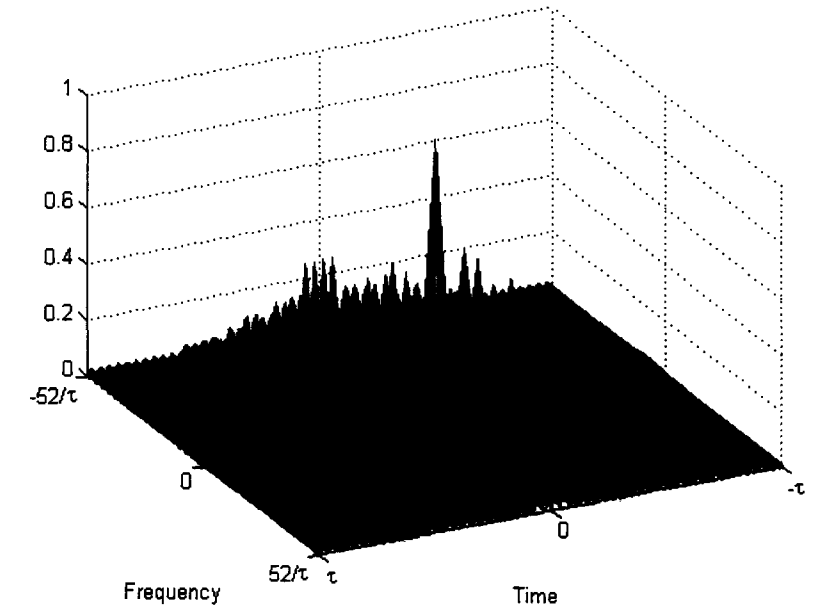

(a) 3D view

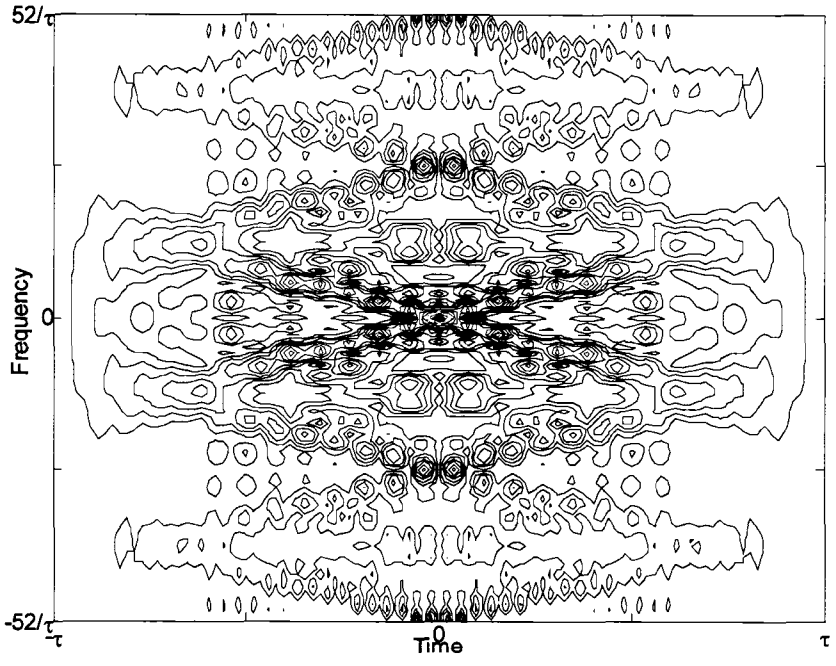

(b) Top view

Fig. 3.4 Ambiguity function of the 13-bit Barker coded pulse. The coded pulse produces both high range resolution and high frequency resolution at the same time without ambiguity, but there are many clutters. However, clutters are not a significant problem in the case of poor SNR.

3.4 Multiple-Pulse Technique

The multiple-pulse technique is an extremely useful approach for obtaining the signal power spectrum using incoherent-scatter radars without any degradation in range resolution.

To obtain the Doppler frequency of the target with short pulses, a paired pulse method was first developed (Rummler, 1968). The principle of paired pulse is that two pulses are transmitted during a single transmit cycle, and the auto correlation function (ACF) of received signal, lagged with the same duration of the two transmitted pulses, is calculated. The spacing between the two pulses is varied for a successive number of transmitted pulse cycles. The frequency resolution depends on the number of transmitted paired pulses; actually, the same number of transmit cycles is required to obtain the spectrum shape if only two pulses are used for each transmit cycle.

The multiple pulse technique is an extension of this two-pulse method. It transmits a number of pulses per transmit cycle (instead of just two). The number of spectrum points depends on the number of lags obtained. To obtain as many lags as possible, the pulse spacing must be carefully determined. The practical spacing of pulses given by Farley(1972) is shown in Table 3.2.

Table 3.2 Possible multiple pulse schemes (Farley, 1972)

Number of pulses	Number of lags	Pulse positions	Lags	Missing lags
3	3	0, 1, 3	1, 2, 3	--
4	6	0, 1, 4, 6	1-6	--
		0, 1, m-2, m	1, 2, m-3 to m	--
5	10	0, 3, 4, 9, 11	1-9, 11	10
		0, 1, 4, 9, 11	1-5, 7-11	6
6	15	0, 1, 8, 11, 13, 17	1-13, 16, 17	14, 15
		0, 1, 8, 12, 15, 17	1-9, 11-14, 16, 17	10, 15
		0, 1, 4, 10, 15, 17	1-7, 9-11, 13-17	8, 12
7	21	0, 1, 4, 10, 18, 23, 25	1-10, 13-15, 17-19, 21-25	11, 12, 16, 20
		0, 2, 3, 10, 16, 21, 25	1-11, 13-16, 18-19, 21-23, 25	12, 17, 20, 24
		0, 1, 11, 16, 19, 23, 25	1-12, 14-16, 18-19, 22-25	13, 17, 20, 21
		0, 1, 7, 11, 20, 23, 25	1-7, 9-14, 16, 18-20, 22-25	8, 15, 17, 21

For example, the range time diagram of the 5-pulse scheme multiple pulse is shown in Fig. 3.5. In the 5-pulse scheme, ten combinations of lagged ACFs can be obtained. Those at altitude h are

$$\begin{aligned}
&\rho(h,\tau) = S_r(t+3\tau)S_r^*(t+4\tau)\\
&\rho(h,2\tau) = S_r(t+9\tau)S_r^*(t+11\tau)\\
&\rho(h,3\tau) = S_r(t)S_r^*(t+3\tau)\\
&\rho(h,4\tau) = S_r(t)S_r^*(t+4\tau)\\
&\rho(h,5\tau) = S_r(t+4\tau)S_r^*(t+9\tau)\\
&\rho(h,6\tau) = S_r(t+3\tau)S_r^*(t+9\tau)\\
&\rho(h,7\tau) = S_r(t+4\tau)S_r^*(t+11\tau)\\
&\rho(h,8\tau) = S_r(t+3\tau)S_r^*(t+11\tau)\\
&\rho(h,9\tau) = S_r(t)S_r^*(t+9\tau)\\
&\rho(h,11\tau) = S_r(t)S_r^*(t+11\tau)
\end{aligned} \tag{3.21}$$

where $S_r(t)$ is the received signal at t, τ is the unit lag time, and * denotes a conjugate complex. We should note that lag 10 is missing.

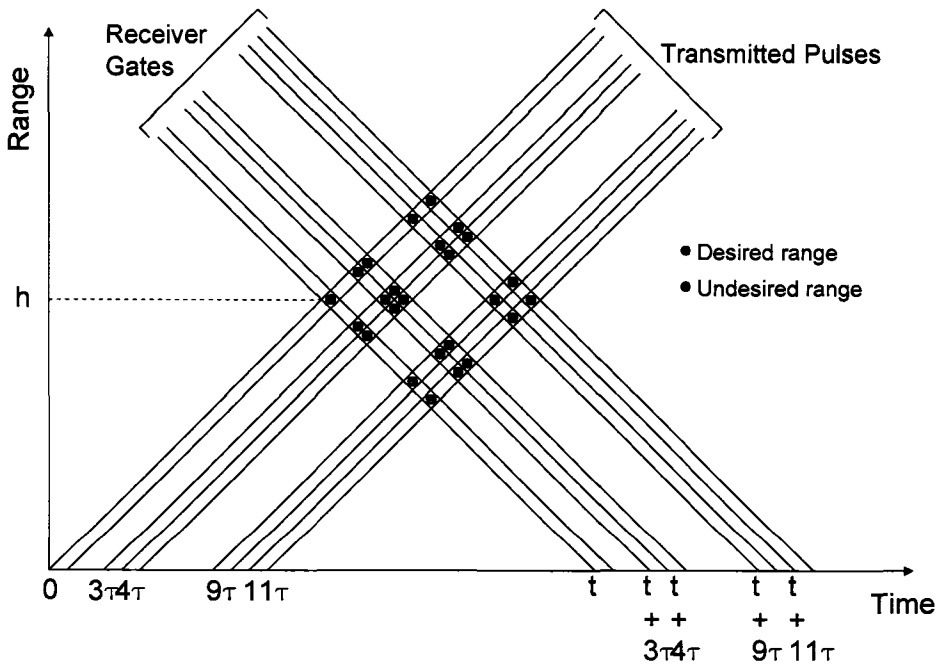

Fig. 3.5 Range time diagram of 5-pulse scheme multiple pulse.

The spectrum is obtained from ACFs by calculating the next equation.

$$F(h,\omega) = \mathrm{DFT}[\ \langle \rho^*(h,11)\rangle,\ 0,\ \langle \rho^*(h,9)\rangle,\ \langle \rho^*(h,8)\rangle,\ \cdots,\langle \rho^*(h,1)\rangle,\ 0,\ \langle \rho(h,1)\rangle,\ \langle \rho(h,2)\rangle,\ \cdots,\ \langle \rho(h,9)\rangle,\ 0,\ \langle \rho(h,11)\rangle\ ] \tag{3.22}$$

where $\langle . \rangle$ denotes averaging or integrating, and DFT[.] denotes Distributed Fourier Transforming.

In the above equation, we have substituted zero into the lag 0 term, but if we need to take care the power of the returned signal, we should input lag 0 term. Every ACF includes clutters that come from undesired ranges (see Figure 3.5), however, the signals returned from these undesired ranges do not have the correlation with the desired range h and it will be reduced by integration.

In order to obtain adequate SNR, appropriate integration time is required in the multiple-pulse radar. Increasing the number of pulses in the multi-pulse sequence helps define the ACF but has the disadvantage of resulting in increased clutter which is reflected from undesired ranges, and longer integration time is required to compensate. Therefore in practice a compromise must be made to determine the optimum number of pulses in a multi-pulse scheme. In the next, the effectiveness of integration is shown.

The accuracy of the received signal ACF given by Farley(1969) is

$$\left\langle (\rho - \hat{\rho})^2 \right\rangle \propto \left[(S + C + N)/S \right]^2 K^{-1} \tag{3.23}$$

where ρ is true auto correlation, $\hat{\rho}$ is estimated auto correlation, S is signal power, C is clutter power, N is noise power, and K is the number of independent samples to integrate. To increase estimation accuracy, K must be increased and integration time becomes longer.

Assuming the scattering target is homogeneous, the clutter power is

$$C \approx (n_p - 1)S \tag{3.24}$$

where n_p is the number of pulses in a 'multi-pulse' sequence. Equation (3.23) becomes

$$\left\langle (\rho - \hat{\rho})^2 \right\rangle \propto (n_p + N/S)^2 K^{-1}. \tag{3.25}$$

To obtain a particular accuracy,

$$K \propto \left(n_p + N/S\right)^2 . \tag{3.26}$$

If the number of pulses n_p increases, clutter increases also; therefore the number of independent samples to integrate must also be increased to obtain the same accuracy. But if n_p is decreased to reduce clutter, the number of lags decreases and we will need additional pulse hit cycles with different pulse spacing to obtain enough number of lags. The required number of lags is concerned with the spectrum resolution.

The number of lags we can obtain from the n_p pulse scheme is

$$n_d = n_p\left(n_p - 1\right)/2 . \tag{3.27}$$

We want to reduce the number of independent samples K per single lag to reduce the total time required to obtain the spectrum. The number of samples normalized by the number of lags is given by

$$K/n_d \propto \frac{\left(n_p + N/S\right)^2}{n_p\left(n_p - 1\right)} \equiv R . \tag{3.28}$$

Table 3.3 shows the relationship between SNR, n_p, and the normalized sample number calculated with the above equation. The most notable thing is that, for a given SNR, R decreases with increasing n_p. This means n_p should simply be increased to reduce the total time required to obtain the spectrum. It also shows that the poorer the SNR, the greater the advantage of increasing n_p. In the incoherent-scatter radar, SNR of the received signal tends to be poor, and a complex multi-pulse scheme will therefore confer a great advantage. But, of course, we don't need more lags than required to define the spectral resolution; therefore the actual number of pulses should be determined from the desired number of frequency points in the spectrum.

In practical, the multi-pulse scheme and the Barker codes are often combined in use in the incoherent-scatter radar(e.g. Zamlutti, 1980). The experiments at the Søndrestrøm radar that were used to obtain data for this thesis used a 5-pulse Barker-coded multiple scheme which produces 10 lags and 22 points of frequency resolution.

Table 3.3 Normalized sample number to obtain a certain accuracy of ACF

S/N n_p	-20 dB	-10 dB	0 dB	10 dB
2	5202	72.0	4.50	2.21
3	1768	28.17	2.67	1.60
5	551	11.25	1.80	1.30
7	273	6.88	1.52	1.20
10	134	4.44	1.34	1.13

CHAPTER 4
LAYER FORMATION MECHANISMS

4.1 Introduction

It is known that high density ionized layers occasionally appear in the E-region of the ionosphere and sometimes affect short-wave communication. As discussed in the introduction to this thesis, these layers are now known to be primarily composed of long-lived metallic ions that originate from meteor ablation. The composition has been confirmed by numerous in-situ rocket experiments using mass spectrometers (Young et al., 1967; Narcisi et al., 1968; Johannesen and Krankowsky, 1972; Aikin and Goldberg, 1973). Incoherent-scatter radar experiments (Behnke and Vickrey, 1975; Huuskonen, et al., 1988; Turunen, et al., 1988; Bristow and Watkins, 1993) have also been able to determine mean ion masses in the layers; however this measurement has not been carried out routinely since it requires special geophysical conditions as well as appropriate experimental and analysis methods. Due to the difficulty in making these measurements only a limited number of special case studies have been possible to date. Analysis of a unique large database from experiments specifically designed to measure thin metal ion layers using the Søndrestrøm, Greenland radar is the topic of this thesis. Before discussing the data itself this chapter next briefly reviews the physical process responsible for layer formation, in particular the altitude distribution of masses expected within layers that is relevant to the analysis and results.

Metal ions have quite long chemical lifetimes in the lower ionosphere where meteors ablate and therefore dense layers, once formed, do not readily dissipate. The background density of metal ions is considerably lower that can be detected via incoherent-scatter radar. Under the action of electric fields and in response to neutral gas motions the vertical component of the ion motion, under appropriate circumstances, results in a convergence that in turn produces enhanced metal ion densities that are detectable via radar.

4.2 Wind Shear Mechanism

The first attempt to explain the layer formation mechanism, which was named the "wind shear mechanism", was made by Dungey (1959) and others (Whitehead, 1961; Axford, 1963;). According to this mechanism, neutral wind and geomagnetic field play the main roles. Fig 4.1 illustrates this mechanism simply. Two neutral winds at different altitudes and flowing in opposite directions, and a magnetic field which has a dip angle, are required to form ionized layers. Ions are pushed horizontally by neutral winds, but they are forced to move along the magnetic field because of electro-magnetic dynamics. Under the condition that neutral wind flows northward at high altitude and flows southward at low altitude in the northern hemisphere, ions are concentrated in the altitude where horizontal neutral velocity is zero, and the layer forms there.

However, those neutral wind conditions are not necessary in order to form layers. Under the assumption of uniform electric field, no mean current flow but currents flowing in different directions and at different heights to southward or northward are allowed. Whitehead (1961) showed that a rapid change in the height of westward or eastward neutral winds may cause vertical movement of ions and layer formation.

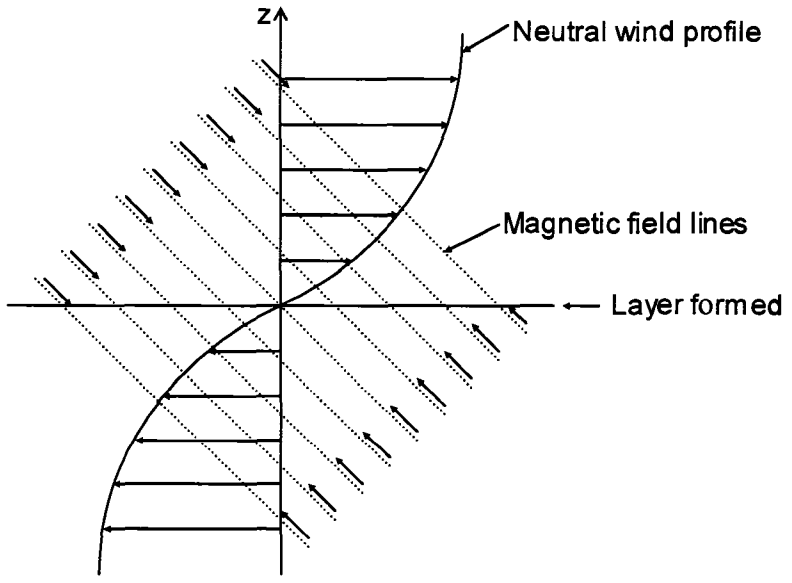

Fig 4.1. Explanation of wind shear layer formation mechanism. Figure is after Axford, 1963.

4.3 Electric Field Dominated Mechanism

The wind shear mechanism has been widely accepted to explain layer formation at mid-latitudes. However, at high latitudes the ion motions are frequently controlled by strong electric fields. These electric fields have been shown to result in ion convergence (and hence layer formation) when the electric fields have a westward directed component. Nygren et al. (1984a) and others (e.g. Bristow,1991) have presented a theory describing layer formation under the influence of strong electric fields that is applicable to the work presented in this thesis. The vertical component of the ion motion is

$$v_{iz} = \frac{\cos I}{B\left(1+\rho_i^2\right)}\left[\rho_i\left(E_{N\perp} - Bu_W\right) - \left(E_W + Bu_N \sin I\right)\right] \tag{4.1}$$

where B is the geomagnetic field, I is the dip angle of the field, $\rho_i = \nu_i/\omega_i$ is the ratio of ion collision frequency and gyro frequency ($=|q_i|B/m_i$), $E_{N\perp}$ and E_W are the northward perpendicular component and the westward component of the electric field, respectively, and u_W and u_N are the westward component and the northward component of wind velocity, respectively.

In the special case of zero electric field the condition for zero vertical ion velocity is

$$\rho_i = -\cot\Psi \cdot \sin I \tag{4.2}$$

where Ψ is azimuth angle of the wind ($=\tan^{-1} u_W/u_N$). This condition is equivalent to the conventional wind shear theory that is applicable at mid-latitudes.

On the other hand, when the electric field is strong enough to neglect geomagnetic and wind flow terms, the next equation also satisfies the condition of zero vertical ion velocity:

$$\rho_i = \tan\phi \tag{4.3}$$

where ϕ is the directional angle of the electric field ($=\tan^{-1} E_W/E_{N\perp}$). This condition is more likely to occur in the polar region where a strong electric field exists.

In both cases, the occurrence depends on the ratio of ion collision frequency and gyro frequency. The gyro frequency depends on ion mass and geomagnetic field. The geomagnetic field does not vary very much with the altitude over the ionospheric region

of interest and therefore gyro frequency is almost constant with the altitude for a given ion mass. For example, taking the value of the geomagnetic field to be approximately $B = 50,000\text{nT}$, and given masses of magnesium ($M_i = 24$) or iron ($M_i = 56$) ions, both of which exist abundantly in the lower ionosphere as a result of meteor ablation, the gyro frequencies are 200 Hz for magnesium and 85.5 Hz for iron.

The collision frequency varies rapidly with altitude due mainly to the neutral gas density that decreases with increasing altitude. Fig. 4.2 shows a plot of collision and gyro frequencies versus altitude. Assuming Equations (4.2) or (4.3) are satisfied when $\omega_i \approx \nu_i$, heavy ions (Fe^+) will concentrate a few kilometers above the region where light ions (Mg^+) concentrate. Since iron and magnesium (and other light ions comparable in mass to magnesium) are dominant, this suggests that the accumulation of metal ions might result in two distinct layers with the heavier ion layer above the second layer of light ions. Alternatively, in a single layer of metals, a greater concentration of heavy ions should be found at the top of the layer.

Experimental observations of layer heights show a wide variation from about 95 to 125 km (eg Turunen, 1988; Huuskonen, 1988; Bristow,1993). In practice the altitudes of layer formation are controlled by both the ion and neutral gas dynamics. A westward component of an applied electric field, for example, will result in a thin ion layer; however, the altitude at which the layer forms is dependent on the azimuth direction of the applied electric field, as well as on the vertical profile of the neutral gas. It is not the goal of this thesis to discuss the formation mechanisms as this has been addressed elsewhere. We wish to simply point out that the actual altitudes at which layers form depends on the ion and neutral dynamics; however, in all cases the heavy ions tend to accumulate at heights slightly higher than the height at which lighter ions accumulate.

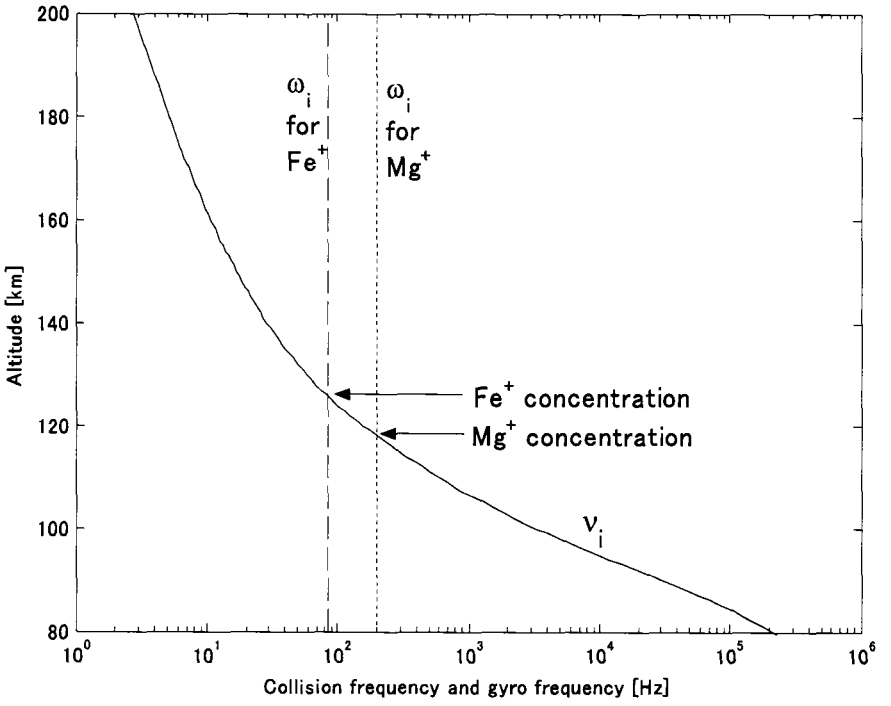

Fig. 4.2 Collision and gyro frequencies versus altitude. Heavy ions (Fe^+) will concentrate a few kilometers above the region where light ions (Mg^+) concentrate.

Fig 4.3 and Fig. 4.4 (Min and Watkins, personal communication, 1994) result from a numerical simulation of a multi-species ionosphere, including two metal ions Fe^+ and Mg^+. Initially the metal ions are present at low concentrations that are uniform with altitude. Fig 4.3 (left side plot) shows the results 300 seconds after the application of a 50 mV/m electric field in a direction 45 degrees west of north with zero neutral wind; two metal layers Fe^+ and Mg^+ are evident, while the total ion density shows a broad single peak. The right hand side plot in Fig 4.3 shows the results after 600 seconds; at this time two distinct peaks in the total ion density are evident, and the individual metal ion layers become sharper. The point here is that the expected experimental structures will have shapes that depend on the prior duration of the applied electric field.

Fig 4.4 illustrates the additional effects of a neutral wind on layer heights. Both plots in Fig 4.4 were derived using a 50mV/m electric field directed to the west. The left and right hand side plots in this figure show neutral winds 200 m/s to the north and south,

respectively. The altitudes, and layer shapes, of the ion layers are greatly affected by the winds.

The purpose of the above discussion is to briefly summarize the complexity of layer formation dynamics and to illustrate how layers form. It is also important to note that all models and simulations to date of metal ion layer formation predict two closely spaced metal layers with the heavier ions on top.

The goal of this thesis is not to address the layer formation mechanisms but to determine the relative abundances of ions within a single layer and, in the case of double layers, to determine if there are composition differences between layers. The incoherent-scatter radar method does not permit us to determine specific ions but only the mean ion mass. Fortunately, since Fe^+ is the major metal ion, and other metal ions are substantially lighter, we are able to estimate relative abundances of the heavy Fe^+ ions.

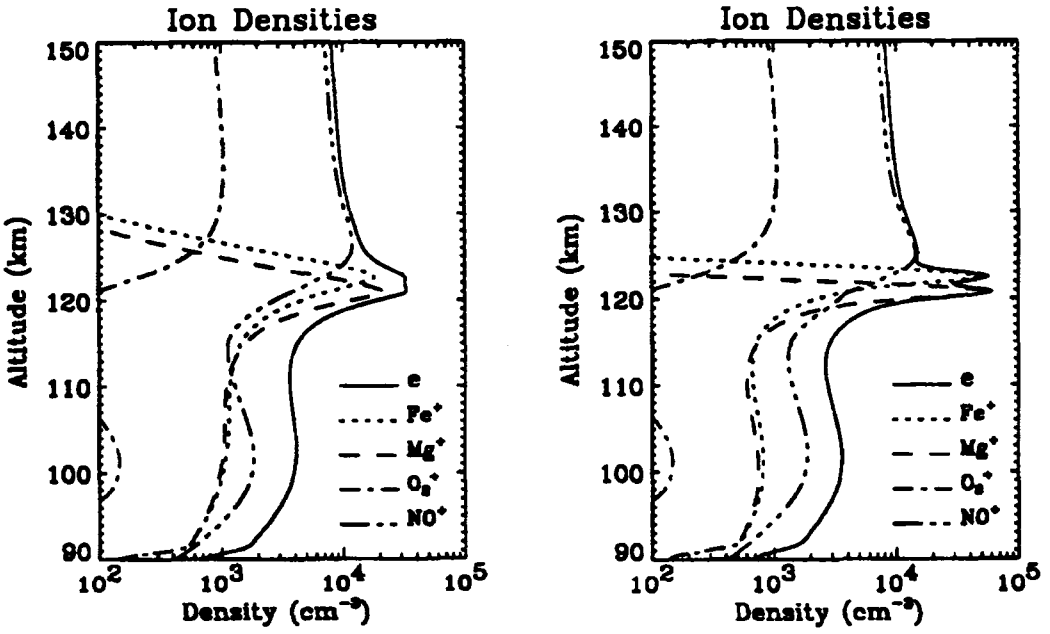

Fig.4.3 Ion densities computed from a model simulation. The left hand plot shows the results of metal ion layers that form 300 seconds after the application of a 50 mV/m electric field directed 45 degrees west of north. The right hand plot is the same simulation after 600 seconds.

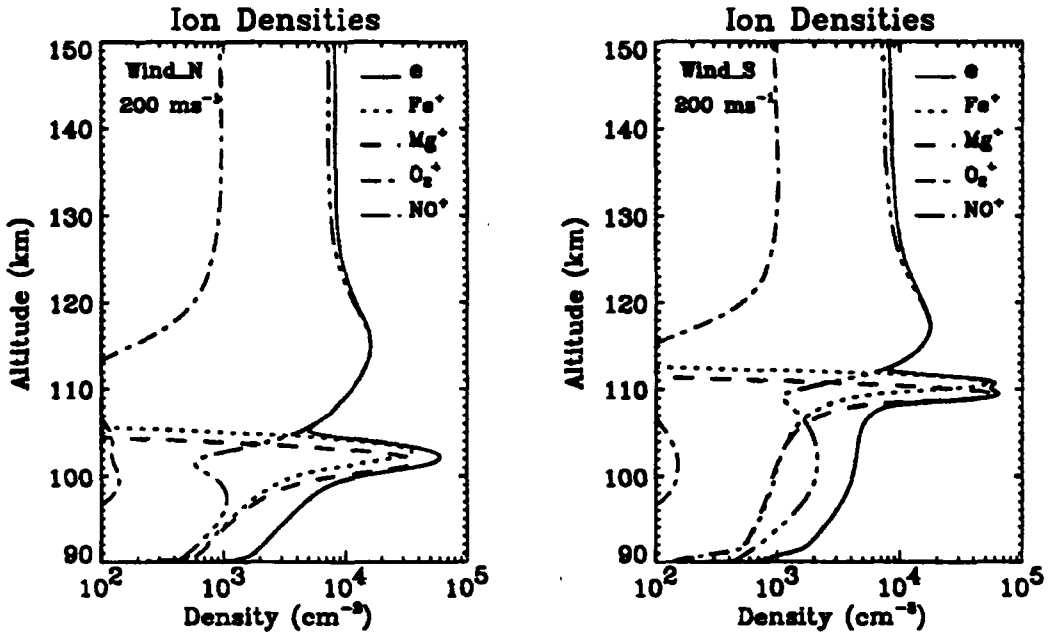

Fig 4.4 Ion densities computed from a model simulation after the equilibrium. The applied electric field is 50mV/m directed to the west. The left and right plots have the neutral wind of 200 m/s directed to the north and south respectively.

CHAPTER 5
ANALYSIS PROCEDURES

5.1 Outline of Procedure for Ion Mass Estimation in Sporadic Layers

This chapter explains the procedure used in this thesis to estimate ion masses in sporadic layers. As mentioned in chapter 2, the scattered power spectrum of ISR includes information about ion temperature, electron temperature, ion collision frequency, and the ratio of ion mass to ion temperature. However, all this information cannot be obtained independently. We wish to estimate ion masses in sporadic layers; the lack of any ability to estimate ion temperature and mass independently is our primary issue. The width of the power spectrum depends primarily on both the ion temperature and the ion mass. A higher ion temperature, or a lower ion mass, will result in a wider spectrum. Since the spectral width depends on the ratio of ion temperature to ion mass, the procedure is to estimate the ion temperature within the layer using other radar data from outside the layer, then to compute the ion mass using the independently computed temperature.

The outline of procedure followed for this experiment is shown in Fig.5.1. At first, ion temperatures at several points were estimated in the upper region of sporadic layers, assuming a mean ion mass of a background composed of a mixture of O^+, NO^+, and O_2^+ ions. The mixture ratio of those ions was obtained from the IRI (International Reference Ionosphere) model (http://nssdc.gsfc.nasa.gov/space/model/ionos/iri.html), as well as from the ion electron temperature ratio, which was required to generate the theoretical spectrum. Ion-neutral and electron-neutral collision frequencies were also required to generate the theoretical spectrum, and those were calculated from number densities of neutral gases obtained from the MSIS-E (Mass Spectrometer & Incoherent Scatter Extended) atmospheric model (http://nssdc.gsfc.nasa.gov/space/model/atmos/msise.html).

The next step was extending the ion temperature profile to the height of the sporadic layers. Since the IRI model did not provide an ion temperature profile for the lower ionosphere in which sporadic layers exist, a neutral temperature profile from the MSIS-E model was used as the basic shape of the temperature profile. The basic shape of the

temperature profile was deformed with several fitting parameters, which were determined using ion temperatures obtained as described above. This seems reasonable because the shape of the ion temperature profile should be similar to the shape of the neutral temperature profile in the lower ionosphere.

Finally, using the obtained ion temperature profile, the ion mass was calculated by fitting the observed spectra to a theoretical spectrum with the ion mass as a free parameter. The actual calculations were carried out with a PC using the Matlab software package.

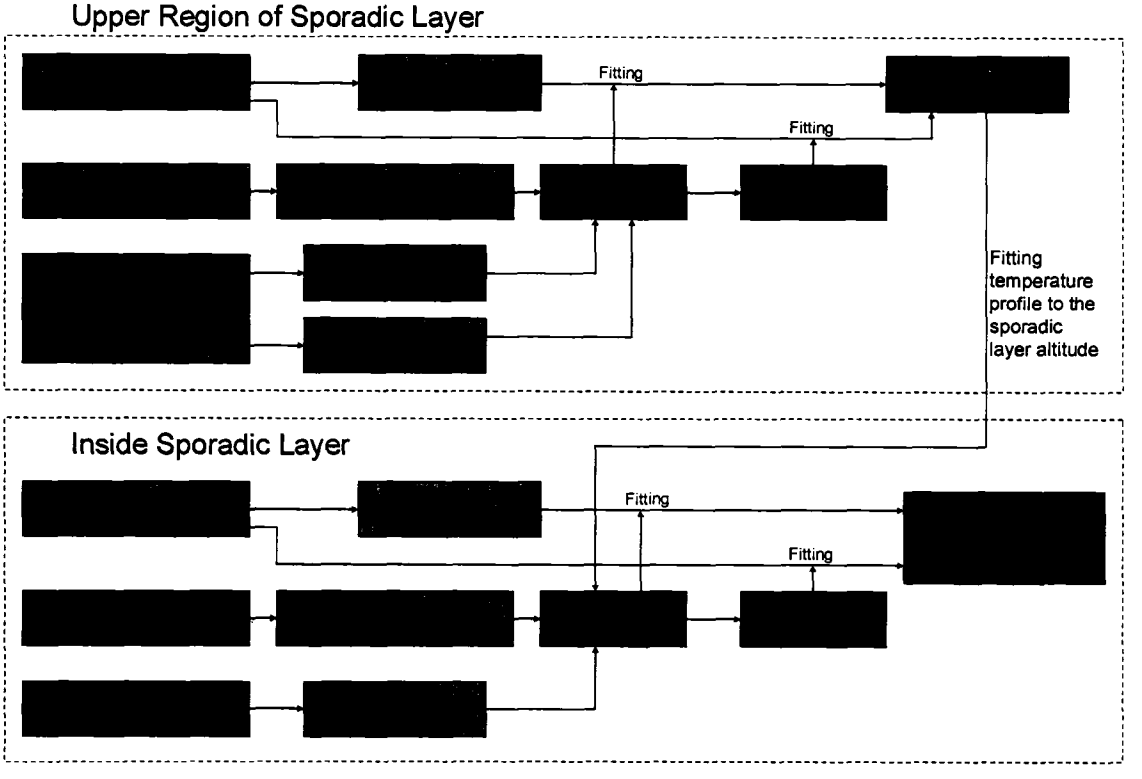

Fig.5.1 Procedure chart for sporadic layer ion mass estimation.

5.2 Generating the Theoretical Spectrum

Following the procedure shown in Fig 5.1, we need ion-neutral gas collision frequency ν_i, electron-neutral gas collision frequency ν_e, and electron and ion temperature ratio T_e/T_i to generate the theoretical spectrum.

Ion-neutral and electron-neutral collision frequencies were calculated by

$$\nu_i = 2.38\times10^{-10}[\mathrm{O}] + 4.18\times10^{-10}[\mathrm{O}_2] + 4.23\times10^{-10}[\mathrm{N}_2] \quad (5.1)$$

and

$$\begin{aligned}\nu_e = {} & 8.9\times10^{-10}[\mathrm{O}]\times\left(1+5.7\times10^{-4}T_e\right)\sqrt{T_e} \\ & +1.86\times10^{-10}[\mathrm{O}_2]\times\left(1+3.6\times10^{-2}\sqrt{T_e}\right)\sqrt{T_e} \\ & +2.33\times10^{-11}[\mathrm{N}_2]\times\left(1-1.21\times10^{-4}T_e\right)T_e\end{aligned} \quad (5.2)$$

where $[\mathrm{O}]$ is the number density of oxygen atoms in m^{-3}, $[\mathrm{O}_2]$ is the number density of oxygen molecules, and $[\mathrm{N}_2]$ is the number density of nitrogen molecules. Number density of neutral gases can be obtained from the MSIS-E atmospheric model. Electron temperature T_e can be obtained from ionospheric models such as the IRI model, but that model does not give the electron temperature at the lowest end of the ionosphere where collision frequency actually affects the spectrum. Therefore, we will use the neutral gas temperature given by the MSIS-E atmospheric model. In the lower ionosphere, the electron temperature is almost same as neutral gas temperature. Fig.5.2 shows an example of a neutral gas density profile, and Fig 5.3 shows a collision frequency profile calculated using the neutral gas density.

The electron/ion temperature ratio T_e/T_i can be determined from the IRI model. Actually, values of T_e and T_i provided by the IRI model are sometimes different from observed values. However, for the purpose of generating a spectrum it is sufficiently precise to calculate T_e/T_i. Especially in the lower ionosphere, T_e/T_i is approximately one and there is no need to focus particular attention on it. Fig. 5.4 shows an example of ion and electron temperature profiles given by the IRI model.

The IRI model also yields a mean ion mass with which to calculate ion temperature in the upper region of the sporadic layer. Fig.5.5 shows an example of ion compositions from IRI model and Fig. 5.6 shows mean ion mass.

Substituting those parameters into (2.44), we obtain our spectrum. By far, the most difficult part of the spectrum-generating calculation is the calculation of the plasma dispersion function given by Eq. (2.42). Even though it has recently gotten easier to calculate integration directly due to recent increases in computational power, an approximate function given by Martin et al. (1980) is still useful for calculating the plasma dispersion function. The approximate function requires a much shorter calculation time than the direct integration and also is sufficiently precise. Direct integration was only used for a performance test comparing direct integration with the approximation function. The direct integration method is shown in the Appendix.

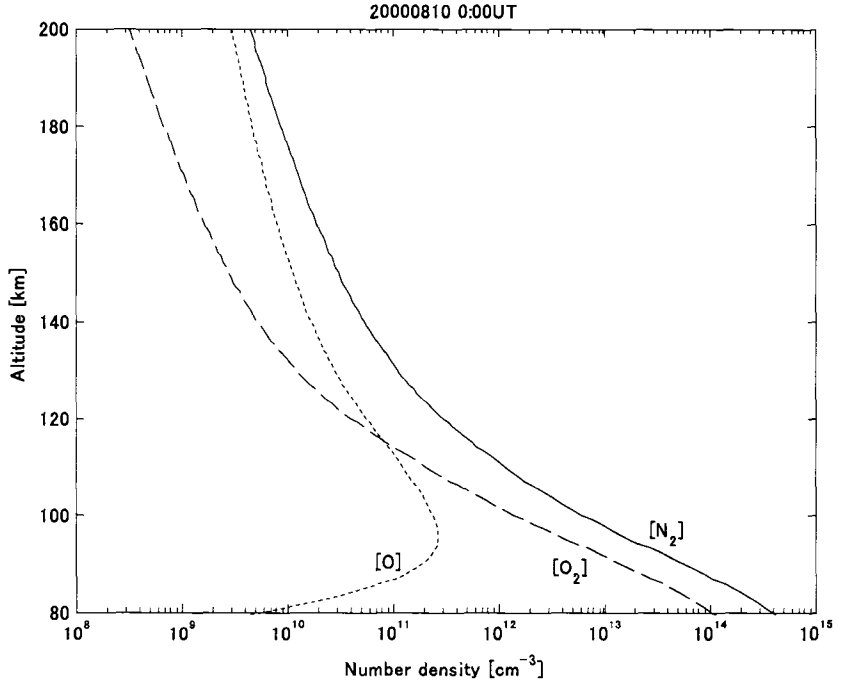

Fig. 5.2 Neutral gas density profile given by the MSIS-E model.

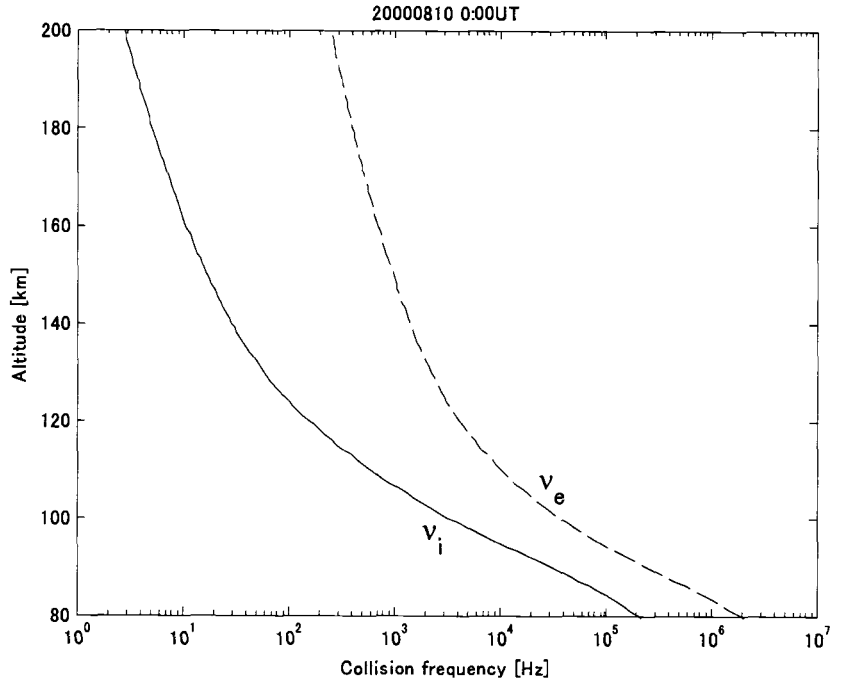

Fig. 5.3 Collision frequency calculated from neutral gas density.

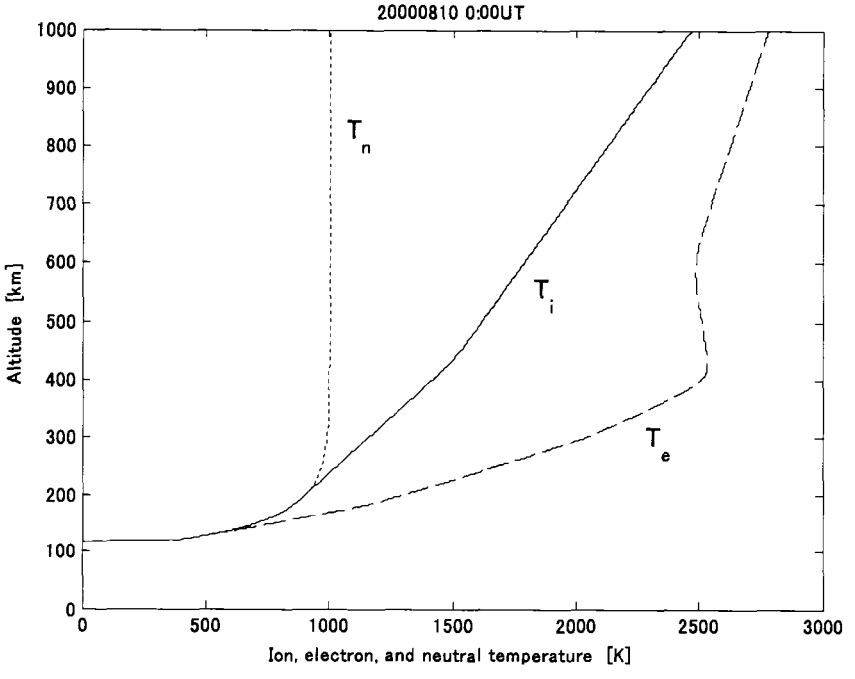

Fig. 5.4 Temperature profiles of ions, electrons, and neutral gas given by the IRI model.

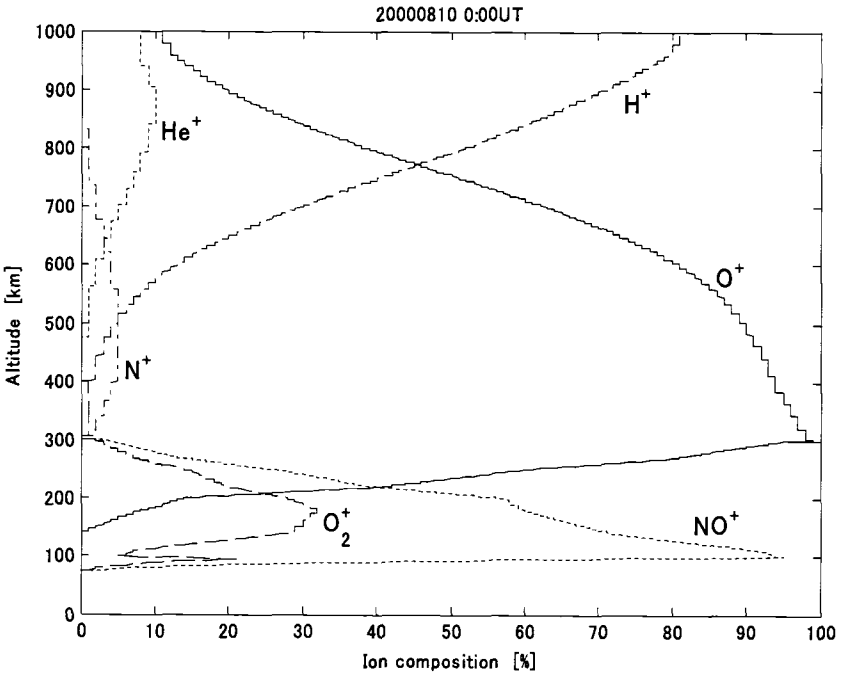

Fig. 5.5 Ion composition given by the IRI model.

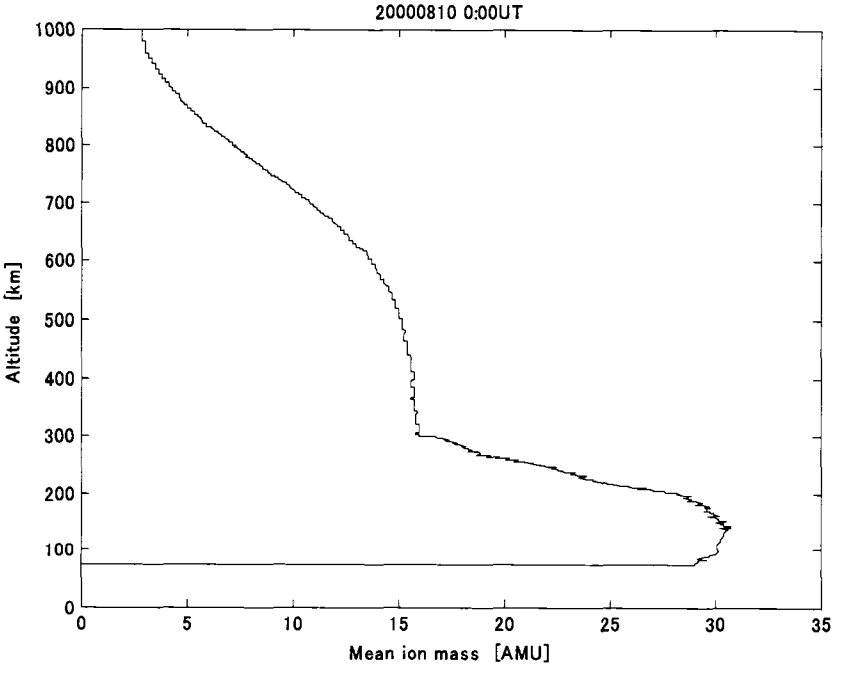

Fig. 5.6 Mean ion mass from the IRI ion composition model.

5.3 Spectrum Fitting and Ion Temperature Mass Ratio Estimation

Raw data from the Søndrestrøm IS-Radar were obtained in the form of an ACF, which is the inverse Fourier transform of a spectrum. In contrast, the theoretical spectrum is obtained as it is. Therefore, there are two ways to fit data to calculate ion temperature mass ratio. One is fitting in the frequency domain, which means calculating the Fourier transformation of the observed ACFs and fitting them to the theoretical spectra. The other is fitting in the time domain, which means calculating the inverse Fourier transformation of the theoretical spectra and fitting them to the observed ACFs. There are advantages and disadvantages to both methods.

When the spectrum distribution is relatively narrow, which is very often the case, particularly at lower altitude, it is difficult to fit in the frequency domain because only 22 spectrum points can be observed in short-coded multi-pulse mode. Occasionally only a few points of the spectrum distribution can be observed, and fitting them leads to excessive error in such cases. For those cases, fitting in the time domain is better because the ACF distribution is wider when the spectrum is narrow. On the other hand, in the case of a wider spectrum distribution, fitting in the spectrum is better because the ACF distribution is narrower in such cases. For these reasons, we will use both spectrum fitting and ACF fitting using a weighted least square error method.

To begin with, the observed spectrum was calculated from the observed ACF using Fourier transformation:

$$\begin{aligned} P_m &= \sum_{n=-N}^{N-1} \rho_n \exp\frac{-2\pi mn}{2N} \\ &= \sum_{n=0}^{N-1} \rho_n \exp\frac{-2\pi mn}{2N} + \sum_{n=1}^{N-1} \rho_n^{*} \exp\frac{2\pi mn}{2N} \qquad (5.3) \\ &\qquad (m = -N, -N+1, \ldots, N-2, N-1) \end{aligned}$$

where ρ_n is the observed ACF, n is the ACF time index, m is the frequency index of the spectrum, and N is the number of observed ACF points . Since only plus-lagged ACFs were provided from the Søndrestrøm facility, minus-lagged ACFs were recovered as the complex conjugate of plus-lagged in the above equation. In the obtained spectrum,

the range of frequency is $-1/(2\tau)$ to $(N-1)/(2N\tau)$ with interval of $1/(2N\tau)$, where τ is the unit lag time of the ACF.

In order to fit the theoretical spectrum with the observed spectrum, the theoretical spectrum was deformed by the following method:

$$\hat{\mathrm{P}}_m(\alpha,\beta,\gamma) = \alpha\, F(\beta(m/N+\gamma)) \qquad (m=-N,-N+1,...,N-2,N-1) \qquad (5.4)$$

where $\hat{\mathrm{P}}_m(\alpha,\beta,\gamma)$ is the deformed theoretical spectrum, $F(\theta)$ is the normalized theoretical spectrum as a continuous function expressed by Eq.(2.44) in the Chapter 2, and α, β, and γ are fitting parameters: α is the amplitude parameter, β is the width parameter corresponding to ion temperature mass ratio, and γ is the shift parameter corresponding to mean velocity.

The theoretical ACF was also deformed using the same fitting parameters in order to fit the observed ACF by the following method:

$$\begin{aligned}\hat{\rho}_n(\alpha,\beta,\gamma) &= \frac{1}{2N}\sum_{m=-N}^{N-1}\hat{\mathrm{P}}_m(\alpha,\beta,\gamma)\exp\frac{2i\pi\, mn}{2N} \\ &= \frac{1}{2N}\sum_{m=-N}^{N-1}\alpha\, F(\beta(m/N+\gamma))\exp\frac{2i\pi\, mn}{2N} \\ &= \alpha\, f(n/\beta)\exp(-i\pi\gamma\, n) \qquad (n=0,\,1,...,N-1)\end{aligned} \qquad (5.5)$$

where $\hat{\rho}_n(\alpha,\beta,\gamma)$ is the deformed ACF, and $f(x)$ is the normalized theoretical ACF as a continuous function.

For the next procedure, the least square method was used to fit the ACF and the spectrum by finding parameters α, β, and γ such that the next equation is minimized:

$$\chi^2(\alpha,\beta,\gamma) = \sum_{n=0}^{N-1}\left|\rho_n - \hat{\rho}_n(\alpha,\beta,\gamma)\right|^2 + W\frac{\sigma_\rho^2}{\sigma_{\mathrm{P}}^2}\sum_{m=-N}^{N-1}\left|\mathrm{P}_m - \hat{\mathrm{P}}_m(\alpha,\beta,\gamma)\right|^2 \qquad (5.6)$$

where σ_ρ^2 is the error variance of ρ_n, σ_{P}^2 is the error variance of P_m, and W is the parameter defining the weight ratio of ACF fitting to spectrum fitting.

Using Parseval's Theorem, which is

$$\sum_{n=-N}^{N-1}|f_n|^2 = \frac{1}{2N}\sum_{m=-N}^{N-1}|F_m|^2\,, \qquad (5.7)$$

the next relationship is derived:

$$\sigma_{\mathrm{P}}^2 = 2N\sigma_\rho^2. \tag{5.8}$$

Then, Eq.(5.6) can be rewritten as

$$\chi^2(\alpha,\beta,\gamma) = \sum_{n=0}^{N-1}\left|\rho_n - \hat{\rho}_n(\alpha,\beta,\gamma)\right|^2 + \frac{W}{2N}\sum_{m=-N}^{N-1}\left|\mathrm{P}_m - \hat{\mathrm{P}}_m(\alpha,\beta,\gamma)\right|^2. \tag{5.9}$$

In order to minimize χ^2, α can be optimized analytically by differentiating χ^2, as shown in the following equation:

$$\begin{aligned}
\frac{\partial\chi^2}{\partial\alpha} &= \frac{\partial}{\partial\alpha}\sum_{n=0}^{N-1}\left|\rho_n - \alpha\, f(n/\beta)\exp(-i\pi\gamma\, n)\right|^2 + \frac{W}{2N}\frac{\partial}{\partial\alpha}\sum_{m=-N}^{N-1}\left|\mathrm{P}_m - \alpha\, F(\beta(m/N+\gamma))\right|^2 \\
&= -\sum_{n=0}^{N-1} f(n/\beta)\exp(-i\pi\gamma\, n)\left\{\rho_n^* - \alpha\, f^*(n/\beta)\exp(i\pi\gamma\, n)\right\} \\
&\quad -\sum_{n=0}^{N-1} f^*(n/\beta)\exp(i\pi\gamma\, n)\left\{\rho_n - \alpha\, f(n/\beta)\exp(-i\pi\gamma\, n)\right\} \\
&\quad -\frac{W}{2N}\sum_{m=-N}^{N-1} F(\beta m/N+\gamma)\left\{\mathrm{P}_m^* - \alpha\, F^*(\beta(m/N+\gamma))\right\} \\
&\quad -\frac{W}{2N}\sum_{m=-N}^{N-1} F^*(\beta m/N+\gamma)\left\{\mathrm{P}_m - \alpha\, F(\beta(m/N+\gamma))\right\} \\
&= 2\alpha\sum_{n=0}^{N-1}\left|f(n/\beta)\right|^2 - 2\sum_{n=0}^{N-1}\mathrm{Re}\left[f(n/\beta)\rho_n^*\exp(-i\pi\gamma\, n)\right] \\
&\quad +\frac{2\alpha W}{2N}\sum_{m=-N}^{N-1}\left|F(\beta(m/N+\gamma))\right|^2 - \frac{2W}{2N}\sum_{m=-N}^{N-1}\mathrm{Re}\left[F(\beta(m/N+\gamma))\mathrm{P}_m^*\right]
\end{aligned} \tag{5.10}$$

When χ^2 is minimized, $\partial\chi^2/\partial\alpha$ should be zero, therefore, optimized α is given by

$$\alpha_{opt} = \frac{\sum_{n=0}^{N-1}\mathrm{Re}\left[f(n/\beta)\rho_n^*\exp(-i\pi\gamma\, n)\right] + \frac{W}{2N}\sum_{m=-N}^{N-1}\mathrm{Re}\left[F(\beta(m/N+\gamma))\mathrm{P}_m^*\right]}{\sum_{n=0}^{N-1}\left|f(n/\beta)\right|^2 + \frac{W}{2N}\sum_{m=-N}^{N-1}\left|F(\beta(m/N+\gamma))\right|^2}. \tag{5.11}$$

In contrast to α can be optimized analytically as the above, β and γ cannot be optimized by analytical methods; therefore the Newton-Rahpson numerical optimization

method was used. In this method, β and γ are updated to the optimum by the following recurrence equation:

$$\begin{bmatrix} \beta_{k+1}-\beta_k \\ \gamma_{k+1}-\gamma_k \end{bmatrix} = -\begin{bmatrix} \dfrac{\partial^2\chi^2(\alpha_{opt},\beta_k,\gamma_k)}{\partial\beta^2} & \dfrac{\partial^2\chi^2(\alpha_{opt},\beta_k,\gamma_k)}{\partial\beta\partial\gamma} \\ \dfrac{\partial^2\chi^2(\alpha_{opt},\beta_k,\gamma_k)}{\partial\beta\partial\gamma} & \dfrac{\partial^2\chi^2(\alpha_{opt},\beta_k,\gamma_k)}{\partial\gamma^2} \end{bmatrix}^{-1} \begin{bmatrix} \dfrac{\partial\chi^2(\alpha_{opt},\beta_k,\gamma_k)}{\partial\beta} \\ \dfrac{\partial\chi^2(\alpha_{opt},\beta_k,\gamma_k)}{\partial\gamma} \end{bmatrix}. \tag{5.12}$$

In this thesis, partial differentiations in the above equation were calculated by numerical differentiation as shown in the following equations:

$$\frac{\partial\chi^2(\alpha,\beta,\gamma)}{\partial\beta} = \frac{\chi^2(\alpha,\beta+\Delta_\beta,\gamma)-\chi^2(\alpha,\beta-\Delta_\beta,\gamma)}{2\Delta_\beta}, \tag{5.13}$$

$$\frac{\partial\chi^2(\alpha,\beta,\gamma)}{\partial\gamma} = \frac{\chi^2(\alpha,\beta,\gamma+\Delta_\gamma)-\chi^2(\alpha,\beta,\gamma-\Delta_\gamma)}{2\Delta_\gamma}, \tag{5.14}$$

$$\frac{\partial^2\chi^2(\alpha,\beta,\gamma)}{\partial\beta^2} = \frac{\chi^2(\alpha,\beta+\Delta_\beta,\gamma)-2\chi^2(\alpha,\beta,\gamma)+\chi^2(\alpha,\beta-\Delta_\beta,\gamma)}{\Delta_\beta^{\,2}}, \tag{5.15}$$

$$\frac{\partial^2\chi^2(\alpha,\beta,\gamma)}{\partial\gamma^2} = \frac{\chi^2(\alpha,\beta,\gamma+\Delta_\gamma)-2\chi^2(\alpha,\beta,\gamma)+\chi^2(\alpha,\beta,\gamma-\Delta_\gamma)}{\Delta_\gamma^{\,2}}, \tag{5.16}$$

and

$$\begin{aligned} \frac{\partial^2\chi^2(\alpha,\beta,\gamma)}{\partial\beta\partial\gamma} = & \frac{\chi^2(\alpha,\beta+\Delta_\beta,\gamma+\Delta_\gamma)-\chi^2(\alpha,\beta-\Delta_\beta,\gamma+\Delta_\gamma)}{4\Delta_\beta\Delta_\gamma} \\ & -\frac{\chi^2(\alpha,\beta+\Delta_\beta,\gamma-\Delta_\gamma)-\chi^2(\alpha,\beta-\Delta_\beta,\gamma-\Delta_\gamma)}{4\Delta_\beta\Delta_\gamma}. \end{aligned} \tag{5.17}$$

Initial values of β and γ were set to be 5 and 0 respectively, which correspond to the supposed ion temperature mass ratio and zero mean velocity. In most cases, this recursive calculation was converged without a problem when the peak of the spectrum was clear; however, in noisy cases, β and γ were often divergent. In order to avoid divergence, the

recursive calculation was restarted from other initial values when the updated β and/or γ went too far.

After the optimum α , β , and γ were found, ion temperature mass ratio was estimated from optimized β. Remembering that the normalized Doppler frequency is expressed as $\theta = (\omega/k)\sqrt{M_i/2KT_i}$ in the theoretical spectrum of Eq.(2.44) and $\theta = \beta(m/N + \gamma)$ ($\gamma = 0$ when mean velocity is zero) in the fitting function of Eq.(5.4), measured Doppler frequency is $\omega = 2\pi m/(2N\tau)$, and wave number is $k = 4\pi f_0/c$, the temperature mass ratio is calculated as:

$$\begin{aligned}\frac{T_i}{M_i} &= \frac{1}{2K}\left(\frac{\omega}{k\theta}\right)^2 \\ &= \frac{1}{2K}\left\{\frac{2\pi m/(2N\tau)}{(4\pi f_0/c)(\beta m/N)}\right\}^2 \\ &= \frac{1}{2K}\left\{\frac{c}{4\beta f_0\tau}\right\}^2\end{aligned} \tag{5.18}$$

where c is the speed of light, f_0 is the carrier frequency of the radar, and τ is the unit lag time of the ACF.

Mean velocity was also estimated by the following equation:

$$\bar{v} = \frac{c}{4f_0\tau}\gamma \tag{5.19}$$

5.4 Error Estimation of Spectrum Fitting

In order to evaluate estimation errors of the fitting parameters α, β, and γ, let us define the spectrum-ACF error vector as the following form:

$$\boldsymbol{\varepsilon} \equiv \hat{\boldsymbol{\rho}}(\hat{\alpha},\hat{\beta},\hat{\gamma}) - \boldsymbol{\rho}$$

or $$\boldsymbol{\rho} = \hat{\boldsymbol{\rho}}(\hat{\alpha},\hat{\beta},\hat{\gamma}) + \boldsymbol{\varepsilon}, \tag{5.20}$$

where

$$\boldsymbol{\rho} = \left[\rho_0, \rho_1, ..., \rho_{N-1}, \sqrt{\frac{W}{2N}}\mathrm{P}_{-N}, \sqrt{\frac{W}{2N}}\mathrm{P}_{-N+1}, ..., \sqrt{\frac{W}{2N}}\mathrm{P}_{N-1} \right]^T, \tag{5.21}$$

$$\hat{\boldsymbol{\rho}}(\hat{\alpha},\hat{\beta},\hat{\gamma}) = \left[\hat{\rho}_0(\hat{\alpha},\hat{\beta},\hat{\gamma}), ..., \hat{\rho}_{N-1}(\hat{\alpha},\hat{\beta},\hat{\gamma}), \sqrt{\frac{W}{2N}}\hat{\mathrm{P}}_{-N}(\hat{\alpha},\hat{\beta},\hat{\gamma}), ..., \sqrt{\frac{W}{2N}}\hat{\mathrm{P}}_{N-1}(\hat{\alpha},\hat{\beta},\hat{\gamma}) \right]^T$$

. (5.22)

In the above equations, $\boldsymbol{\rho}$ is the observed spectrum-ACF vector, and $\hat{\boldsymbol{\rho}}(\hat{\alpha},\hat{\beta},\hat{\gamma})$ is the theoretical spectrum-ACF vector as a function of estimated parameters $\hat{\alpha}$, $\hat{\beta}$, and $\hat{\gamma}$. Expanding $\hat{\boldsymbol{\rho}}(\alpha,\beta,\gamma)$ into a Taylor series around $(\hat{\alpha},\hat{\beta},\hat{\gamma})$ and taking the first term,

$$\hat{\boldsymbol{\rho}}(\alpha,\beta,\gamma) = \hat{\boldsymbol{\rho}}(\hat{\alpha},\hat{\beta},\hat{\gamma}) + \frac{\partial\hat{\boldsymbol{\rho}}(\hat{\alpha},\hat{\beta},\hat{\gamma})}{\partial\alpha}\varepsilon_\alpha + \frac{\partial\hat{\boldsymbol{\rho}}(\hat{\alpha},\hat{\beta},\hat{\gamma})}{\partial\beta}\varepsilon_\beta + \frac{\partial\hat{\boldsymbol{\rho}}(\hat{\alpha},\hat{\beta},\hat{\gamma})}{\partial\gamma}\varepsilon_\gamma \tag{5.23}$$

where $\varepsilon_\alpha = \alpha - \hat{\alpha}$, $\varepsilon_\beta = \beta - \hat{\beta}$, and $\varepsilon_\gamma = \gamma - \hat{\gamma}$ are estimation errors of fitting parameters. Comparing Eq. (5.23) with Eq.(5.20), the spectrum-ACF error vector should be

$$\boldsymbol{\varepsilon} = \frac{\partial\hat{\boldsymbol{\rho}}(\hat{\alpha},\hat{\beta},\hat{\gamma})}{\partial\alpha}\varepsilon_\alpha + \frac{\partial\hat{\boldsymbol{\rho}}(\hat{\alpha},\hat{\beta},\hat{\gamma})}{\partial\beta}\varepsilon_\beta + \frac{\partial\hat{\boldsymbol{\rho}}(\hat{\alpha},\hat{\beta},\hat{\gamma})}{\partial\gamma}\varepsilon_\gamma . \tag{5.24}$$

Multiplying conjugate transpositions of themselves to both side of the above equation, and performing the expectation operation on them, the following equation is obtained:

$$
E[\boldsymbol{\varepsilon}\cdot\boldsymbol{\varepsilon}^H]=\begin{bmatrix}
\sigma_\rho^2 & 0 & \cdots & 0 & & & & \\
0 & \sigma_\rho^2 & \ddots & \vdots & & & & \\
\vdots & \ddots & \ddots & 0 & & \mathbf{0}_{N\times 2N} & & \\
0 & \cdots & 0 & \sigma_\rho^2 & & & & \\
 & & & & \frac{W}{2N}\sigma_{\mathrm{P}}^2 & 0 & \cdots & 0 \\
 & \mathbf{0}_{N\times 2N} & & & 0 & \frac{W}{2N}\sigma_{\mathrm{P}}^2 & \ddots & \vdots \\
 & & & & \vdots & \ddots & \ddots & 0 \\
 & & & & 0 & \cdots & 0 & \frac{W}{2N}\sigma_{\mathrm{P}}^2
\end{bmatrix}
$$

$$
=E\left[\begin{bmatrix}\frac{\partial\hat{\boldsymbol{\rho}}(\hat{\alpha},\hat{\beta},\hat{\gamma})}{\partial\alpha} & \frac{\partial\hat{\boldsymbol{\rho}}(\hat{\alpha},\hat{\beta},\hat{\gamma})}{\partial\beta} & \frac{\partial\hat{\boldsymbol{\rho}}(\hat{\alpha},\hat{\beta},\hat{\gamma})}{\partial\gamma}\end{bmatrix}\begin{bmatrix}\varepsilon_\alpha\\ \varepsilon_\beta\\ \varepsilon_\gamma\end{bmatrix}\begin{bmatrix}\varepsilon_\alpha & \varepsilon_\beta & \varepsilon_\gamma\end{bmatrix}\begin{bmatrix}\frac{\partial\hat{\boldsymbol{\rho}}(\hat{\alpha},\hat{\beta},\hat{\gamma})}{\partial\alpha}\\ \frac{\partial\hat{\boldsymbol{\rho}}(\hat{\alpha},\hat{\beta},\hat{\gamma})}{\partial\beta}\\ \frac{\partial\hat{\boldsymbol{\rho}}(\hat{\alpha},\hat{\beta},\hat{\gamma})}{\partial\gamma}\end{bmatrix}\right]
$$

$$
=\mathbf{A}\begin{bmatrix}\sigma_\alpha^2 & \sigma_{\alpha\beta} & \sigma_{\gamma\alpha}\\ \sigma_{\alpha\beta} & \sigma_\beta^2 & \sigma_{\beta\gamma}\\ \sigma_{\gamma\alpha} & \sigma_{\beta\gamma} & \sigma_\gamma^2\end{bmatrix}\mathbf{A}^H. \tag{5.25}
$$

In the above equation, spectrum-ACF errors are assumed to be uncorrelated. $E[\ ]$ and H denote the expectation operation and the conjugate transposition of the matrix, respectively, and:

$$
\mathbf{A}=\left[\frac{\partial\hat{\boldsymbol{\rho}}(\hat{\alpha},\hat{\beta},\hat{\gamma})}{\partial\alpha},\frac{\partial\hat{\boldsymbol{\rho}}(\hat{\alpha},\hat{\beta},\hat{\gamma})}{\partial\beta},\frac{\partial\hat{\boldsymbol{\rho}}(\hat{\alpha},\hat{\beta},\hat{\gamma})}{\partial\gamma}\right], \tag{5.26}
$$

$$
\begin{bmatrix}\sigma_\alpha^2 & \sigma_{\alpha\beta} & \sigma_{\gamma\alpha}\\ \sigma_{\alpha\beta} & \sigma_\beta^2 & \sigma_{\beta\gamma}\\ \sigma_{\gamma\alpha} & \sigma_{\beta\gamma} & \sigma_\gamma^2\end{bmatrix}\equiv E\left[\begin{bmatrix}\varepsilon_\alpha\\ \varepsilon_\beta\\ \varepsilon_\gamma\end{bmatrix}\begin{bmatrix}\varepsilon_\alpha & \varepsilon_\beta & \varepsilon_\gamma\end{bmatrix}\right]. \tag{5.27}
$$

Letting the weight $W=1$ and substituting Eq.(5.8) into Eq.(5.25),

$$E[\boldsymbol{\varepsilon}\cdot\boldsymbol{\varepsilon}^H]=\begin{bmatrix}\sigma_\rho^2 & 0 & \cdots & 0\\ 0 & \sigma_\rho^2 & \ddots & \vdots\\ \vdots & \ddots & \ddots & 0\\ 0 & \cdots & 0 & \sigma_\rho^2\end{bmatrix}=\mathbf{A}\cdot\begin{bmatrix}\sigma_\alpha^2 & \sigma_{\alpha\beta} & \sigma_{\gamma\alpha}\\ \sigma_{\alpha\beta} & \sigma_\beta^2 & \sigma_{\beta\gamma}\\ \sigma_{\gamma\alpha} & \sigma_{\beta\gamma} & \sigma_\gamma^2\end{bmatrix}\mathbf{A}^H. \tag{5.28}$$

Multiplying the pseudo-inverse matrix of $\mathbf{A}$ from both sides, the error covariance matrix of fitting parameters is obtained thus:

$$\begin{bmatrix}\sigma_\alpha^2 & \sigma_{\alpha\beta} & \sigma_{\gamma\alpha}\\ \sigma_{\alpha\beta} & \sigma_\beta^2 & \sigma_{\beta\gamma}\\ \sigma_{\gamma\alpha} & \sigma_{\beta\gamma} & \sigma_\gamma^2\end{bmatrix}=\mathbf{A}^+\begin{bmatrix}\sigma_\rho^2 & 0 & \cdots & 0\\ 0 & \sigma_\rho^2 & \ddots & \vdots\\ \vdots & \ddots & \ddots & 0\\ 0 & \cdots & 0 & \sigma_\rho^2\end{bmatrix}\left(\mathbf{A}^+\right)^H \tag{5.29}$$

where $\mathbf{A}^+$ is the pseudo-inverse matrix of $\mathbf{A}$ $(=(\mathbf{A}^H\cdot\mathbf{A})^{-1}\mathbf{A}^H)$.

In this thesis, the spectrum error variance σ_ρ^2 was evaluated from the residual square error $\chi^2_{\min}$ using the following equation:

$$\sigma_\rho^2\approx\frac{\chi^2_{\min}}{M-k} \tag{5.30}$$

where M is the number of observed values and k is the number of parameters, which are $3N$ and 3 respectively in this case.

The first column of matrix $\mathbf{A}$ was calculated from Eq.(5.4) and Eq.(5.5) as the following equations:

$$\frac{\partial\hat{\rho}_n(\alpha,\beta,\gamma)}{\partial\alpha}=f(n/\beta)\exp(-i\pi\gamma\, n)\qquad(n=0,\,1,\ldots,N-1) \tag{5.31}$$

$$\frac{\partial\hat{\mathrm{P}}_m(\alpha,\beta,\gamma)}{\partial\alpha}=F(\beta(m/N+\gamma))\qquad(m=-N,-N+1,\ldots,N-2,N-1). \tag{5.32}$$

However, the second column and the third column of matrix $\mathbf{A}$ can not be calculated easily, therefore a numerical approach was taken:

$$\frac{\partial\hat{\boldsymbol{\rho}}(\alpha,\beta,\gamma)}{\partial\beta}\approx\frac{\hat{\boldsymbol{\rho}}(\alpha,\beta+\Delta_\beta,\gamma)-\hat{\boldsymbol{\rho}}(\alpha,\beta-\Delta_\beta,\gamma)}{2\Delta_\beta} \tag{5.33}$$

$$\frac{\partial\hat{\boldsymbol{\rho}}(\alpha,\beta,\gamma)}{\partial\gamma}\approx\frac{\hat{\boldsymbol{\rho}}(\alpha,\beta,\gamma+\Delta_\gamma)-\hat{\boldsymbol{\rho}}(\alpha,\beta,\gamma-\Delta_\gamma)}{2\Delta_\gamma}. \tag{5.34}$$

Substituting Eq.(5.30) through (5.34) into Eq.(5.29), error variances of the fitting parameters were evaluated. the standard deviation of the ion temperature mass ratio was calculated from the error variance of β, as shown:

$$\begin{aligned}\sigma_{\frac{T}{M}} &= \left|\frac{\partial(T_i/M_i)}{\partial\beta}\right|\sigma_\beta \\ &= \frac{1}{K\beta^3}\left\{\frac{c}{4f_0\tau}\right\}^2\sigma_\beta .\end{aligned} \tag{5.35}$$

5.5 Ion Temperature Profile Estimation

Before evaluation of ion mass in the sporadic layers, the ion temperature profile was estimated from ion temperatures at several points in the upper regions of the layers. In order to estimate ion temperatures in the upper region, two radar modes were used on a case by case basis; an unmodulated long pulse mode and a coded multiple pulse mode. The transmitted pulse schemes of both are shown in Fig 5.7.

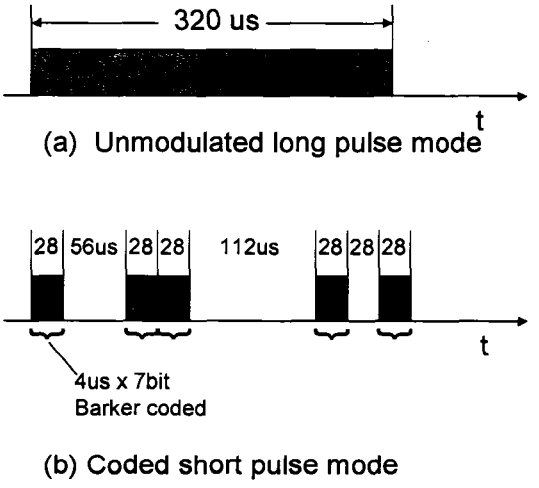

Fig. 5.7 Transmitted pulse scheme of Søndrestrøm IS-radar.

The unmodulated long pulse mode produces better SNR but less range resolution, and the coded short pulse mode produces a lower SNR but high resolution. The range resolution was 48 km in the long pulse mode, and 0.6km in the short pulse mode.

In order to estimate ion temperature immediately above the layer, the high resolution provided by the short pulse mode was useful. However, the SNR of the short pulse mode was often too low to calculate ion temperature in the background. In those cases, the long pulse mode was used, avoiding strong reflections from layers.

To determine the ion temperature profile curve, the shape of the temperature profile was assumed to be the same as the neutral temperature calculated with the MSIS atmospheric model. It is reasonable to assume that the ion temperature profile is similar to the neutral temperature profile in this region. In order to fit the neutral temperature profile with the estimated ion temperatures, logarithm linear approximation of the following form was used:

$$\log[T_i(z)] = a\log[T_{MSIS}(z)] + b \tag{5.36}$$

or

$$T_i(z) = \exp(b)\cdot T_{MSIS}^{a}(z) \tag{5.37}$$

where T_{MSIS} is neutral temperature from the MSIS atmospheric model, T_i is the ion temperature profile that we need, and a and b are fitting parameters. The temperature profile is an approximately exponential function of the height in this region, which means this approximation can adjust the height of the temperature profile and the rate of temperature increase with height. This approximation also ensures that ion temperature is positive, whereas the antilogarithm linear approximation does not.

The optimum fitting parameters were calculated using the least square method:

$$\begin{bmatrix} a_{opt} \\ b_{opt} \end{bmatrix} = \left(\begin{bmatrix} x_1 & \cdots & x_N \\ 1 & \cdots & 1 \end{bmatrix} \begin{bmatrix} x_1 & 1 \\ \vdots & \vdots \\ x_N & 1 \end{bmatrix} \right)^{-1} \begin{bmatrix} x_1 & \cdots & x_N \\ 1 & \cdots & 1 \end{bmatrix} \begin{bmatrix} y_1 \\ \vdots \\ y_N \end{bmatrix} = \frac{1}{\Delta} \begin{bmatrix} N\sum x_n y_n - \sum x_n \sum y_n \\ \sum x_n^2 \sum y_n - \sum x_n \sum x_n y_n \end{bmatrix} \tag{5.38}$$

where

$$x_n = \log[T_{MSIS}(z_n)], \tag{5.39}$$

$$y_n = \log[T_{sp}(z_n)], \tag{5.40}$$

$$\Delta = N\sum x_n^2 - \left(\sum x_n\right)^2, \tag{5.41}$$

and $T_{sp}(z_n)$ is the ion temperature estimated from spectra at altitude z_n. Those optimum fitting parameters a_{opt} and b_{opt} minimize $(y_n - ax_n - b)^2$.

5.6 Error Estimation of Temperature Profile

The uncertainty of the logarithmic ion temperature estimated from spectra becomes the following:

$$\sigma_{\log Tsp}^2 = \frac{1}{N-2}\sum\left(y_n - a_{opt}x_n - b_{opt}\right)^2. \tag{5.42}$$

This value, which reflects estimation errors of ion temperatures when those were calculated from spectra, of course, causes fitting parameter errors. The error sensitivities from the estimated ion temperatures to fitting parameters are calculated by taking derivatives of Eq.(5.38):

$$\frac{\partial a}{\partial y_n} = \frac{1}{\Delta}\left(Nx_n - \sum x_n\right) \tag{5.43}$$

$$\frac{\partial b}{\partial y_n} = \frac{1}{\Delta}\left(\sum x_n^2 - x_n\sum x_n\right). \tag{5.44}$$

Uncertainties of the fitting parameters are given by:

$$\begin{aligned}
\sigma_a^2 &= \sum\left[\left(\frac{\partial a}{\partial y_n}\right)^2 \sigma_{\log Tsp}^2\right] \\
&= \frac{\sigma_{\log Tsp}^2}{\Delta^2}\sum\left(Nx_n - \sum x_n\right)^2 \\
&= \frac{\sigma_{\log Tsp}^2}{\Delta^2}\sum\left[N^2x_n^2 - 2Nx_n\sum x_n + \left(\sum x_n\right)^2\right] \\
&= \frac{\sigma_{\log Tsp}^2}{\Delta^2}\left[N^2\sum x_n^2 - N\left(\sum x_n\right)^2\right] \\
&= \frac{\sigma_{\log Tsp}^2}{\Delta}N,
\end{aligned} \tag{5.45}$$

and

$$\begin{aligned}\sigma_b^2 &= \sum\left[\left(\frac{\partial b}{\partial y_n}\right)^2 \sigma_{\log Tsp}^2\right] \\ &= \frac{\sigma_{\log Tsp}^2}{\Delta^2}\sum\left(\sum x_n^2 - x_n\sum x_n\right)^2 \\ &= \frac{\sigma_{\log Tsp}^2}{\Delta^2}\sum\left[\left(\sum x_n^2\right)^2 - 2x_n\sum x_n^2\sum x_n + x_n^2\left(\sum x_n\right)^2\right] \\ &= \frac{\sigma_{\log Tsp}^2}{\Delta^2}\left[N\left(\sum x_n^2\right)^2 - \sum x_n^2\left(\sum x_n\right)^2\right] \\ &= \frac{\sigma_{\log Tsp}^2}{\Delta}\sum x_n^2.\end{aligned} \tag{5.46}$$

It follows that the uncertainty of the logarithm of the ion temperature at a particular altitude becomes

$$\begin{aligned}\sigma_{\log T}^2(z) &= \sigma_a^2\left(\log[T_{MSIS}(z)]\right)^2 + \sigma_b^2 \\ &= \frac{\sigma_{\log Tsp}^2}{\Delta}N\left(\log[T_{MSIS}(z)]\right)^2 + \frac{\sigma_{\log Tsp}^2}{\Delta}\sum x_n^2 \\ &= \frac{\sigma_{\log Tsp}^2}{\Delta}\left\{N\left(\log[T_{MSIS}(z)]\right)^2 + \sum\left(\log[T_{MSIS}(z_n)]\right)^2\right\}\end{aligned} \tag{5.47}$$

The true value of the ion temperature $T_i(z)$ will exist in the following range with a probability of 1σ =68%:

$$\exp\left\{a\log[T_{MSIS}(z)] + b - \sigma_{\log T}(z)\right\} \le T_i(z) \le \exp\left\{a\log[T_{MSIS}(z)] + b + \sigma_{\log T}(z)\right\}. \tag{5.48}$$

CHAPTER 6
EXPERIMENTAL RESULTS

6.1 Overview

Abundant data exist from several years of observations collected at the Søndrestrøm facility, as shown in Table 6.1. However, data which have enough significant layers to be useful in calculating ion mass are not so abundant. Several notable results, which are indicated with shading in Table 6.1, are shown in this chapter.

Table 6.1 Data set collected at Søndrestrøm facility during May 1995-Aug. 2000.

Date	Time of layer appearance	Peak electron density [m^{-3}]	Description
8/9/2000	**0:09(8/10)-0:25(8/10), 0:37(8/10)-2:32(8/10), 3:05(8/10)-3:16(8/10)**	**3.14e+012@97.5km(0:59-)**	**Extraordinarily strong, narrow spaced double layer(1:26-1:31), wide spaced double layer(1:59-2:10), shown in Fig.6.1-6.20.**
8/5/2000	23:54-0:11(8/6)	5.47e+011@ 99.5km(23:54-)	Weak, short-lived.
2/27/2000	0:44(2/28)-0:49(2/28)	4.16e+011@114.3km(0:44-)	Weak, short-lived.
2/3/2000	20:59-21:14	3.22e+011@103.3km(21:4-)	Weak, short-lived.
8/6/1999	23:57-0:18(8/7)	5.32e+011@103.4km(0:12-)	Weak, short-lived.
7/29/1999	0:45(7/30)-1:45(7/30), 1:57(7/30)-2:13(7/30), 2:25(7/30)-2:36(7/30)	4.16e+011@110.3km (1:18-)	Weak, long-lasting.
7/21/1999	23:58-0:09(7/22)	9.30e+011@116.9km(0:04-)	Fair, short-lived.
5/21/1999	**1:18-3:09, 3:37-3:43,**	**5.30e+011@96.1km(2:03-)**	**Fair, double layers(2:30-2:46), shown in Fig.6.21-6.28.**
8/23/1998	23:58-0:21(8/24)	7.47e+011@109.3km(0:04-)	Weak, short-lived.
7/24/1998	23:38-1:17(7/25)	6.00e+011@104.0km (0:56-)	Weak, but long-lasting.
11/16/1997	22:10-22:43	6.14e+011@117.7km(22:10-)	Weak, short-lived.
8/12/1997	1:32(8/13)-2:00(8/13)	3.10e+011@107.7km(1:32-)	Weak, short-lived.
7/21/1997	22:19-23:09, 23:38-23:49, 1:20(7/22)-1:25(7/22)	5.37e+011@104.3km(22:25-)	Weak, but long-lasting.
7/16/1997	**22:11-22:45, 0:01(7/17)-1:20(7/17), 1:48(7/17)-2:39(7/17)**	**9.36e+011@113.1km (0:35-)**	**Several scans show a strong, double layer with tilted upper layer(0:41-0:57), shown in Fig.6.29-6.34.**

Table 6.1 Continued

5/12/1997	23:17-23:39, 0:31(5/13)-0:36(5/13), 1:27(5/13)-1:32(5/13), 2:52(5/13)-2:57(5/13), 3:03(5/13)-3:08(5/13)	3.28e+011@112.2km(1:27-)	Weak, several short-lived appearances.
8/19/1996	22:22-22:28, 22:39-23:01, 1:45(8/20)-1:50(8/20)	7.06e+011@105.9km(22:45-)	Mostly weak but one scan is fair.
8/12/1996	22:21-22:49, 23:47-23:51, 0:03(8/13)-0:09(8/13), 2:11(8/13)-3:01(8/13)	6.74e+011@105.4km(22:38-) 4.56e+011@109.5km(0:03-) 4.00e+011@ 94.6km(2:56-)	Mostly weak but several scans are fair, long-lasting.
7/22/1996	23:54-0:16(7/23)	4.23e+011@104.8km(0:05-)	Weak, thin, short-lived.
7/19/1996	**22:32- 22:37, 22:49-23:45, 23:57-0:41(7/20), 0:53(7/20)-1:04(7/20)**	**1.22e+012@103.8km (23:23-)**	**Several scans are fair to strong, long-lasting, shown in Fig.6.35-6.43.**
7/17/1996	22:08-22:30	9.18e+011@104.7km (22:25-)	Only one scan fair, short-lived.
7/14/1996	21:57-0:21(7/15)	4.76e+011@95.3km(22:50-)	Weak, long-lasting.
7/8/1996	**0:14(7/9)-0:36(7/9), 1:05(7/9)-3:03(7/9).**	**9.70e+011@103.8km (2:19-) 1.12e+012@100.4km (2:58-)**	**Double layer(2:30-2:35), hown in Fig.6.44-6.52.**
6/13/1996	22:26-22:54	1.16e+012@112.2km(22:26-)	Several scans are fair to strong, short-lived.
6/12/1996	23:16-23:32	3.75e+011@107.1km(23:27-)	Very weak, short-lived.
3/28/1996	21:42-21:52	3.67e+011@116.3km(21:42-)	Very weak, short-lived.
2/9/1996	23:22-23:27	2.65e+011@100.5km(23:22)	Very weak, short-lived.
8/15/1995	23:30-0:10(8/16), 0:21(8/16)-1:18(8/16), 2:37(8/16)-2:42(8/16)	1.20e+012@103.1km(23:30-)	Mostly weak but one scan is strong.
8/14/1995	21:58-22:43	7.19e+011@110.1km (22:09-)	Several fair scans.
8/4/1995	21:51-21:56, 22:23-22:29, 22:48-22:59	6.02e+011@117.2km(21:51-) 6.34e+011@118.4km(22:23-) 7.28e+011@119.7km(22:48-)	Weak, several short-lived appearances.
8/3/1995	22:14-22:30, 23:11-23:56	6.41e+011@114.2km(22:26-) 1.17e+012@103.3km(23:50-)	Several scans are fair but aurora overlaid.
7/20/1995	**0:17(7/21)-1:36(7/21)**	**1.18e+012@102.4km(0:57-)**	**Narrow spaced double layer(0:45-0:50), Shown in Fig.6.68-6.74.**
7/19/1995	**23:50-1:43(7/20)**	**8.53e+011@104.9km(0:02-)**	**Several strong, bending layers (0:24-0:47), shown in Fig.6.53-6.67.**
7/18/1995	**22:25-23:04, 23:21-23:53**	**1.22e+012@108.2km(22:47-) 2.16e+012@106.5km (23:38-)**	**Shown in Fig.6.53-6.61.**
5/22/1995	21:34-22:42	1.00e+012@112.2km (22:25-)	Several scans are fair.
5/10/1995	23:52-0:03(5/11), 0:48(5/11)-1:11(5/11)	2.96e+011@124.2km(23:52-) 4.97e+011@109.3km(1:00-)	Mostly weak.

6.2 Results

6.2.1 Aug. 9th, 2000

A sporadic thin layer appeared at 0:09UT on Aug. 10th 2000 and disappeared for the first time at 0:25UT . The layer appeared again at 0:37UT, and continued through 2:43UT. During this period, the double layer, made up of two thin layers that occur at the same time and same place but different altitudes, was observed from 1:26UT through 1:31UT and again from 1:59 UT through 2:10UT. The interval distance between the two thin layers was several kilometers between 1:26UT and 1:31UT as shown in Fig.6.12, and ten and several kilometers from 1:59 UT through 2:10UT as shown in Fig.6.18 through Fig.6.20. We will call the former cases "narrow spaced double layer", and the latter cases "wide spaced double layer".

In order to obtain temperature profile, the unmodulated long pulse mode was used since the SNR of the coded short pulse mode was too low to estimate the temperature outside the layer. Fig. 6.1(a) shows electron density during the temperature estimation. Spectra were integrated over five kilometer intervals between 130 and 180km. The long pulse mode has 48km resolution, so the lowest altitude in which temperature was estimated was chosen to be 130km to avoid the influence of the sporadic layer which exists around 100km.

Fig 6.1(b) shows integrated spectra and Fig. 6.1(c) shows the estimated ion temperature profile using the long pulse mode. The estimated ion temperature was 197.2K at 100km. Fig 6.2 shows electron density, spectra, and ion temperature profile estimated using the coded short pulse mode. It seems reasonable to use the long pulse mode rather than the short pulse mode since the temperature profile error of the short pulse mode is much larger than that of the long pulse mode.

Fig. 6.3 and following figures show overview images of electron density, spectra around the layers, electron density profiles, and ion masses. The coded short pulse mode, which has 600m resolution, was used to estimate ion masses. Integration was carried out horizontally choosing the nearest altitude section so that vertical resolution was not lost.

SNR of spectra seems good enough to estimate ion mass in the layer, whereas the spectra outside of the layer are buried under noise.

In the narrow-spaced double layer case shown in Fig.6.12, ion mass in the upper layer seems to be heavier than in the lower layer. This result supports Nygren's hypothesis mentioned in Chapter 4. In the single layer cases shown in Fig.6.3 through Fig.6.11 and Fig.6.13 through Fig.6.17, there is also a tendency for ion mass in the top part of the layer to be heavier than in the bottom part of the layer.

However, in the wide-spaced double layer cases shown in Fig.6.18 through Fig.6.20, it is difficult to find such a tendency. In the case that the altitude difference between two layers is relatively large, the ion temperature difference between those two layers is large as well, making it difficult to compare ion masses between two layers.

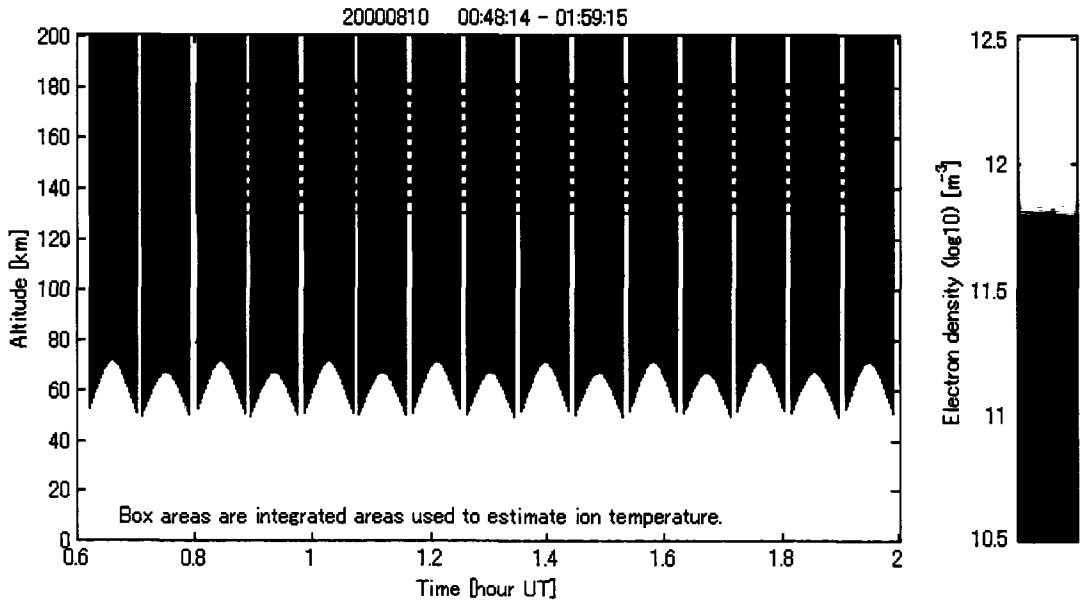

(a) Electron density

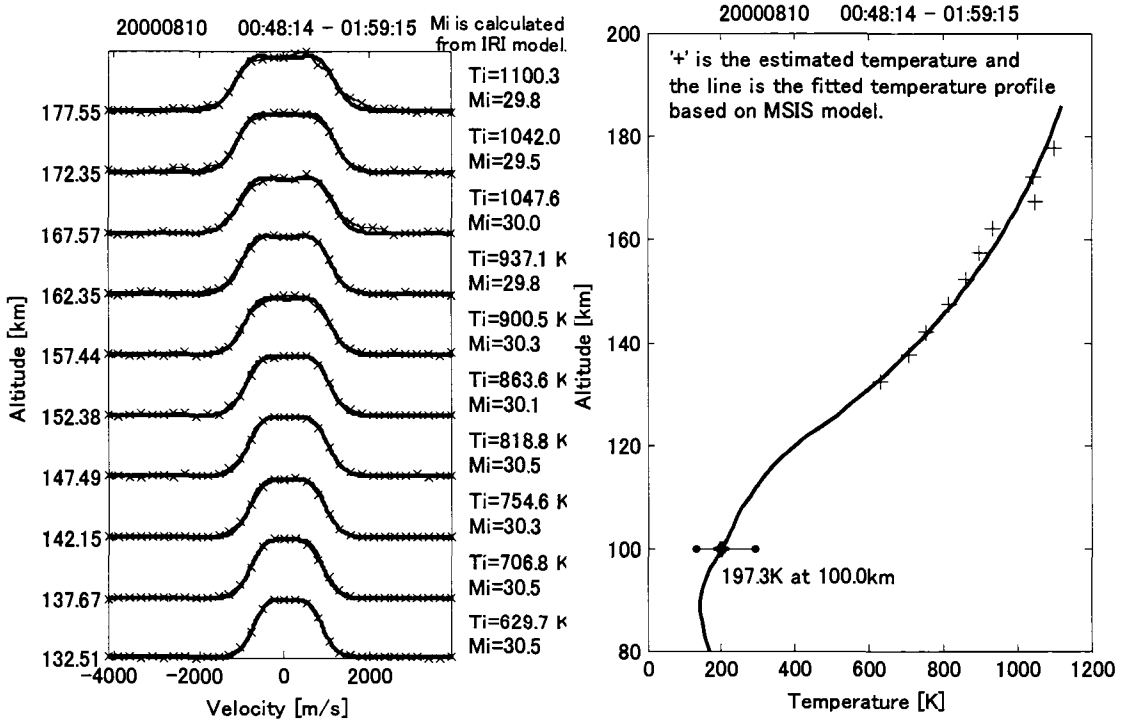

(b) Spectra (c) Ion temperature

Fig. 6.1 Ion temperature estimation using the long pulse mode on Aug. 10th 2000.

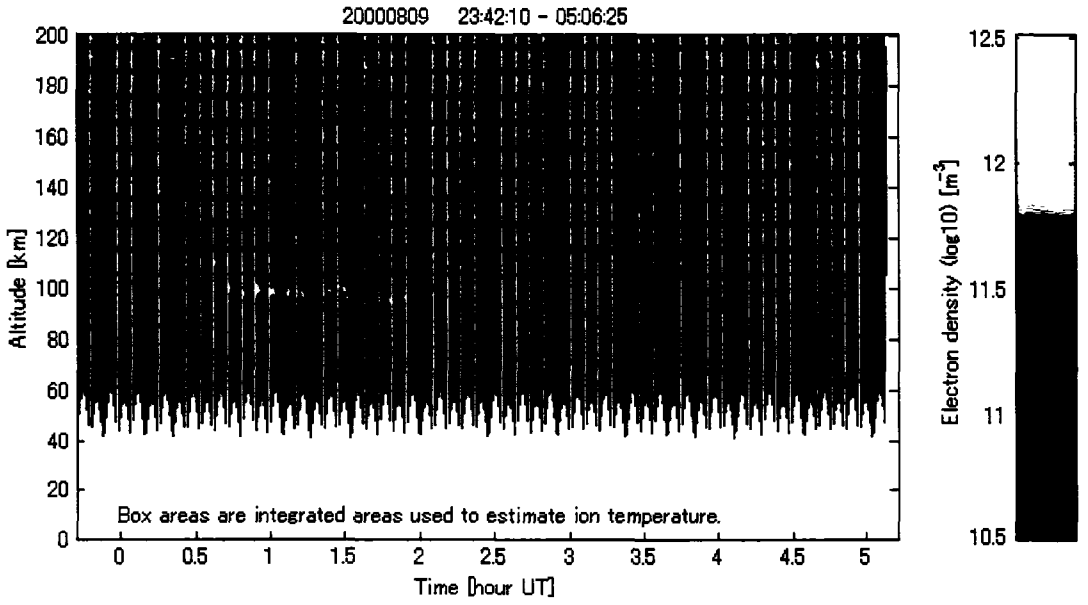

(a) Electron density

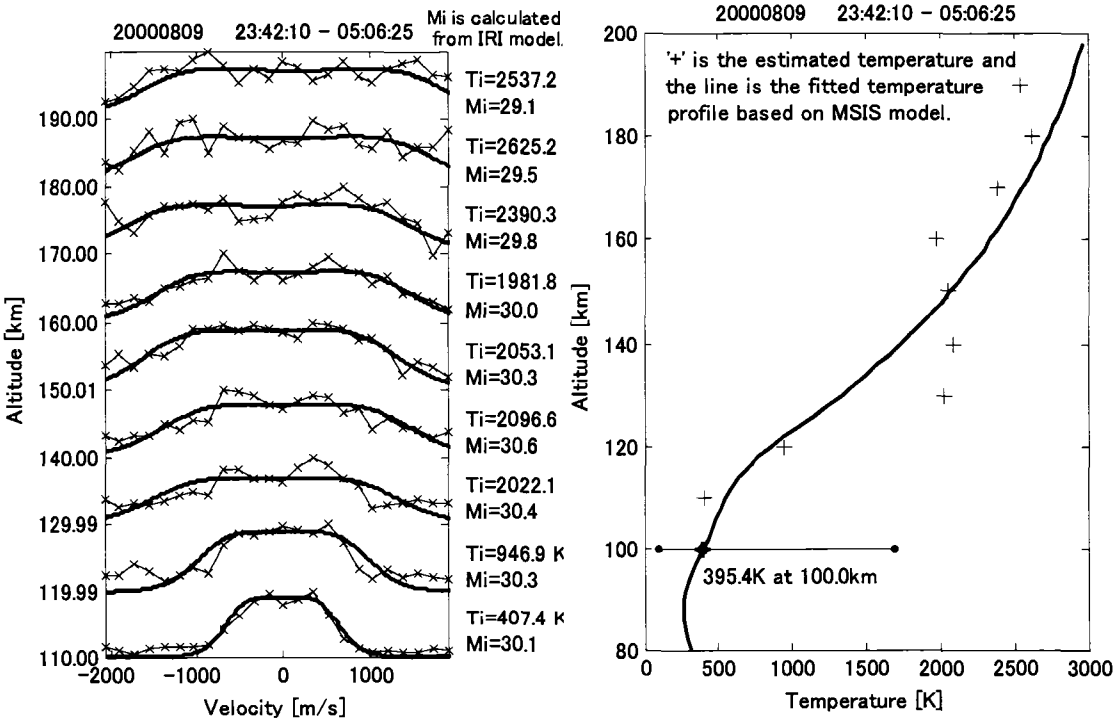

(b) Spectra (c) Ion temperature

Fig. 6.2 Ion temperature estimation using the short pulse mode on Aug. 10th 2000.

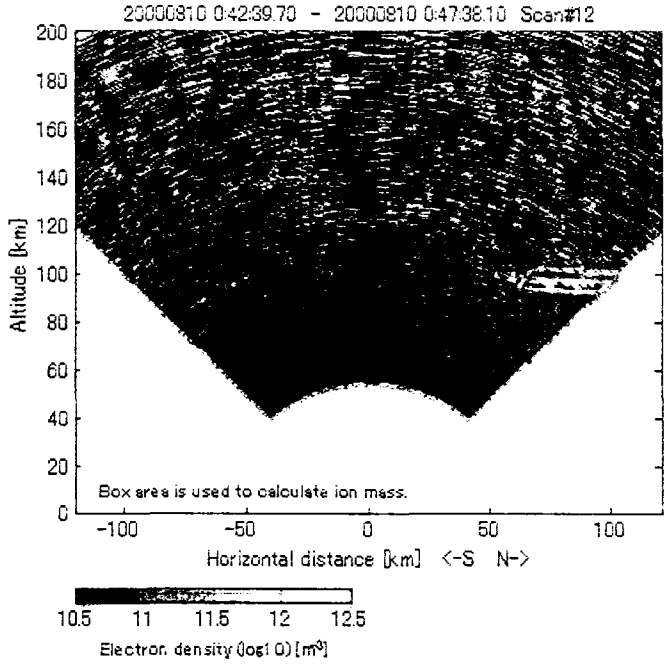

(a) Electron density

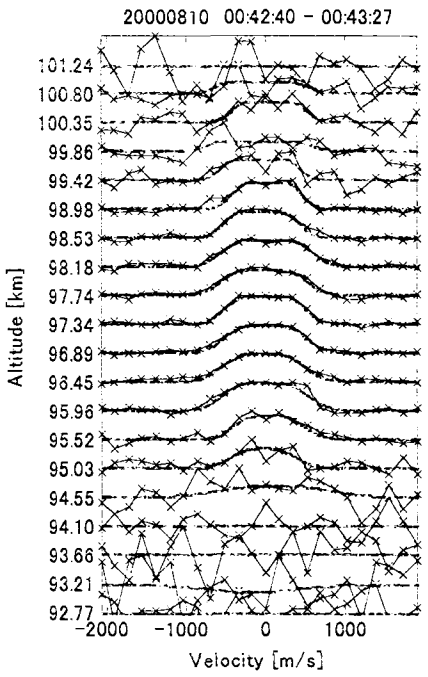

(b) Spectra

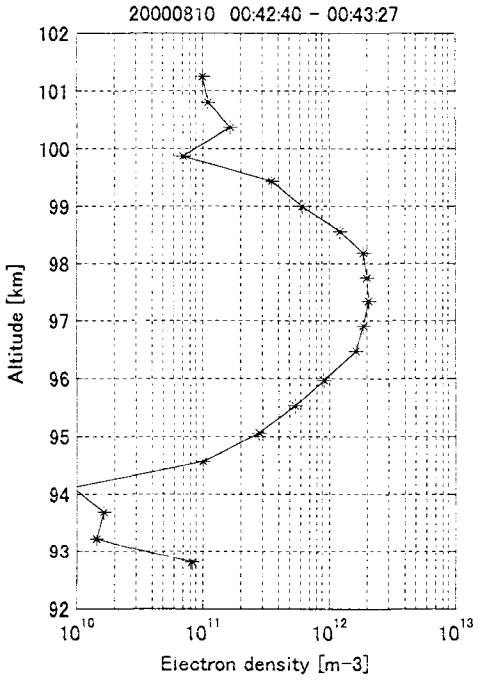

(c) Electron density in the layer

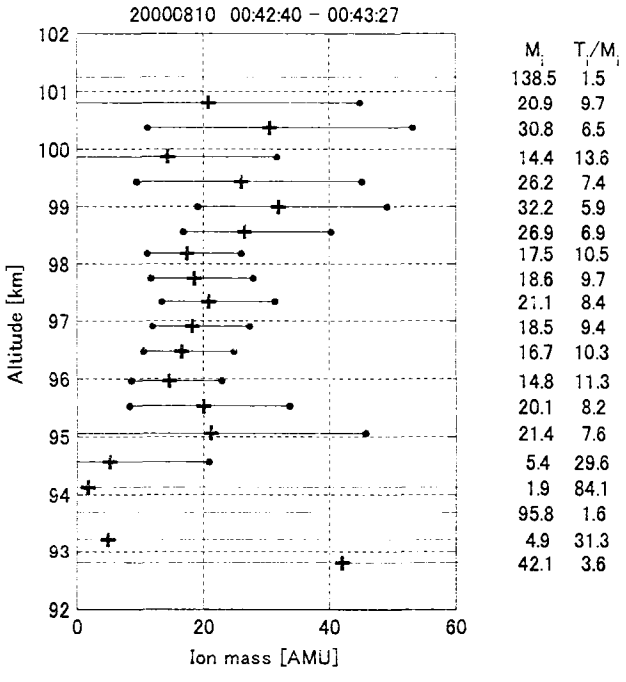

(d) Ion mass in the layer

Fig. 6.3 Ion mass estimation in the layer during 0:42-0:43UT on Aug. 10th 2000.

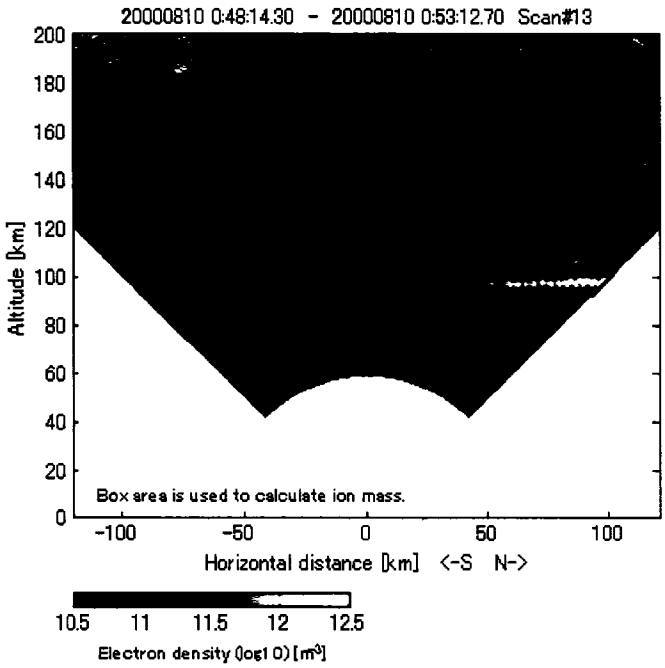

(a) Electron density

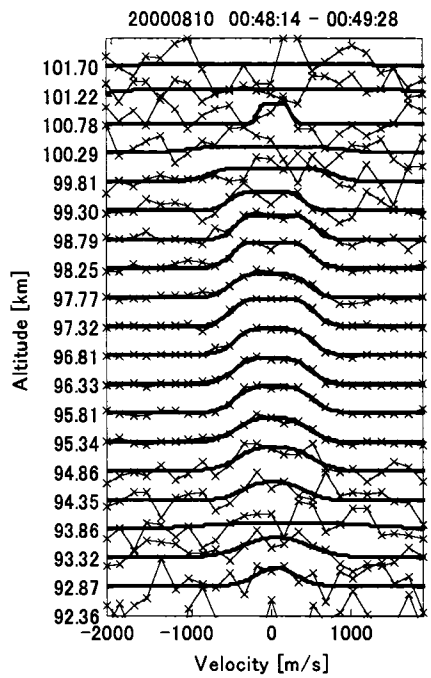

(b) Spectra

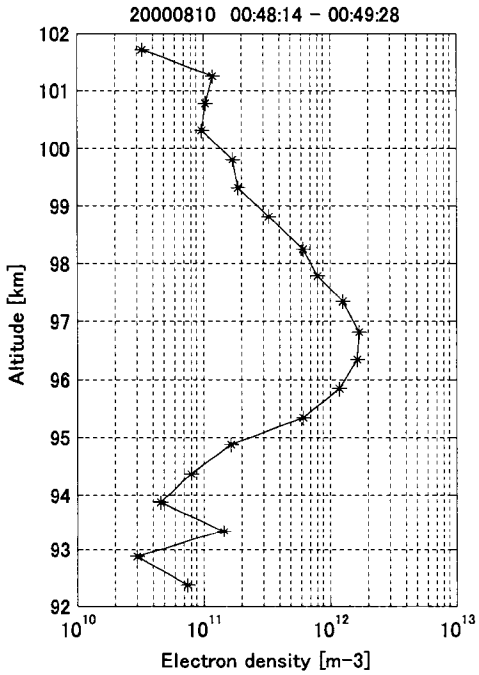

(c) Electron density in the layer

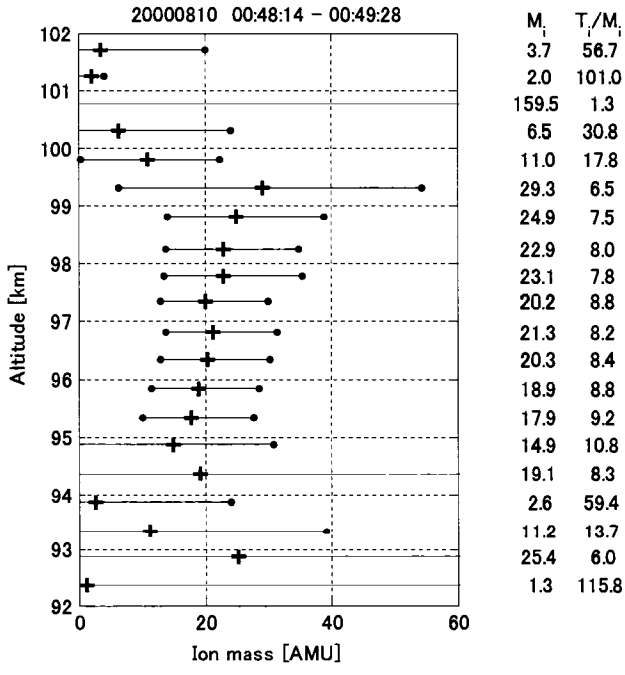

(d) Ion mass in the layer

Fig. 6.4 Ion mass estimation in the layer during 0:48-0:49UT on Aug. 10th 2000.

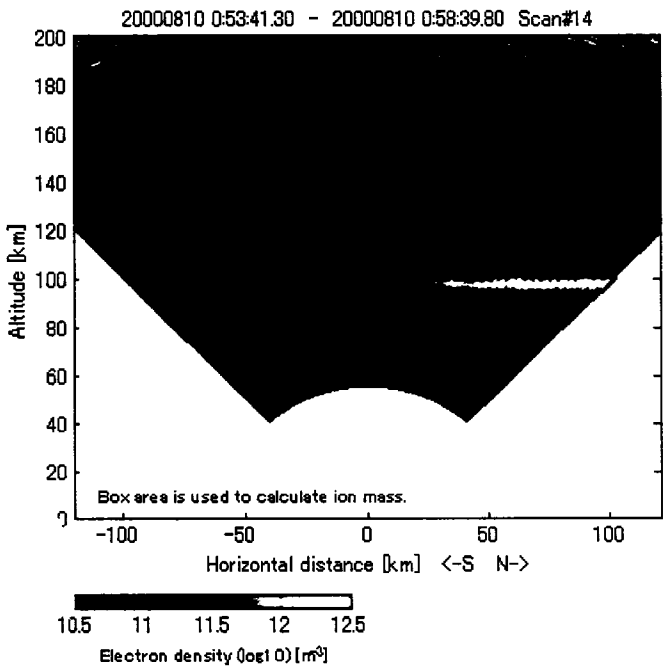

(a) Electron density

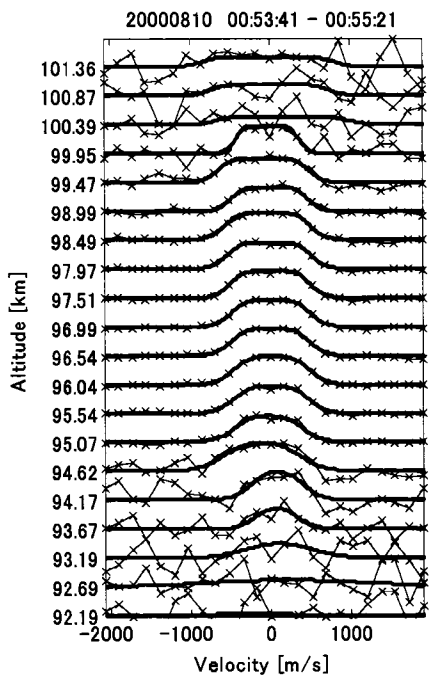

(b) Spectra

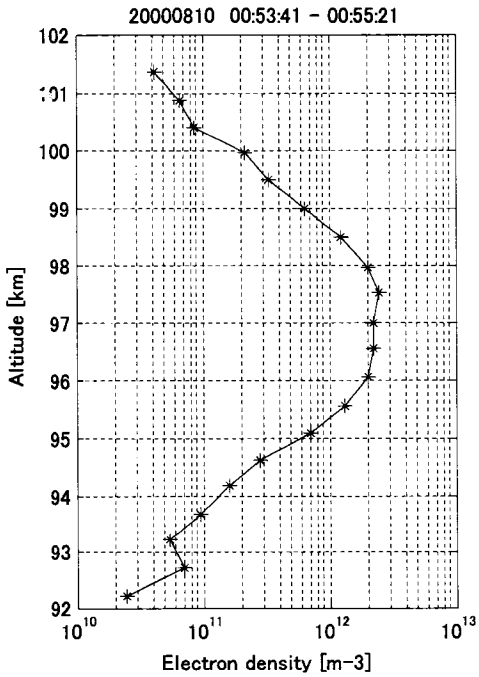

(c) Electron density in the layer

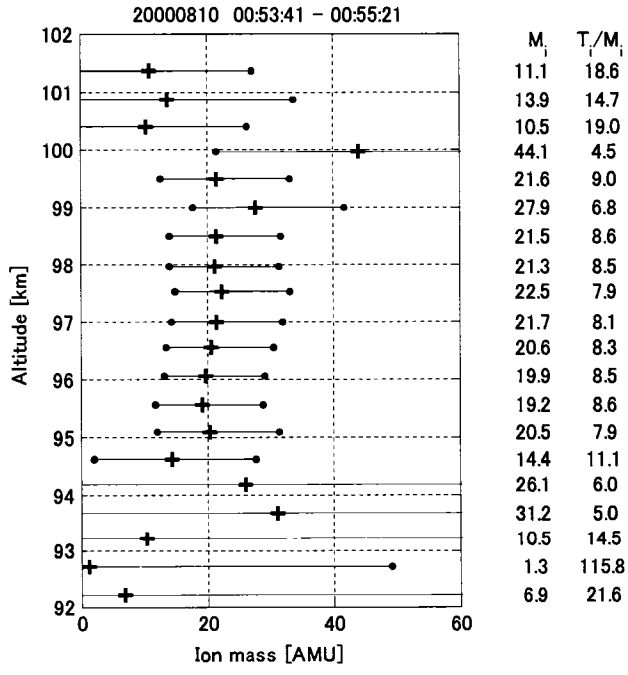

(d) Ion mass in the layer

Fig. 6.5 Ion mass estimation in the layer during 0:53-0:55UT on Aug. 10th 2000.

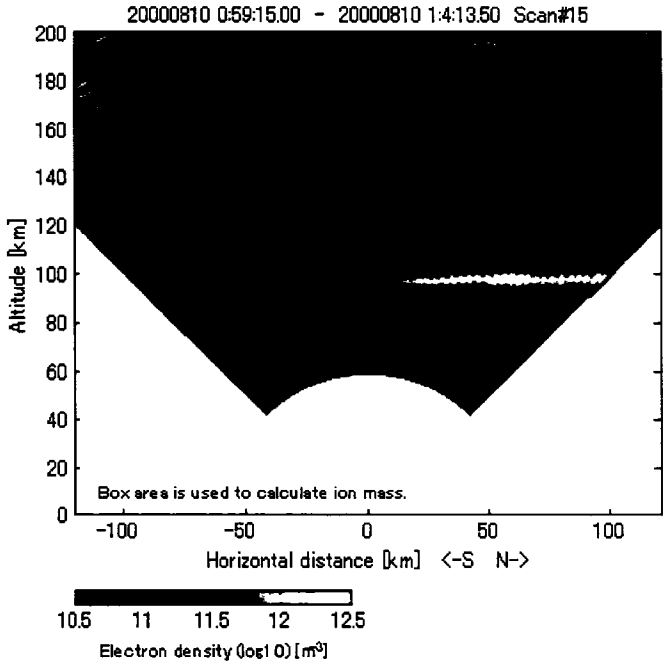

(a) Electron density

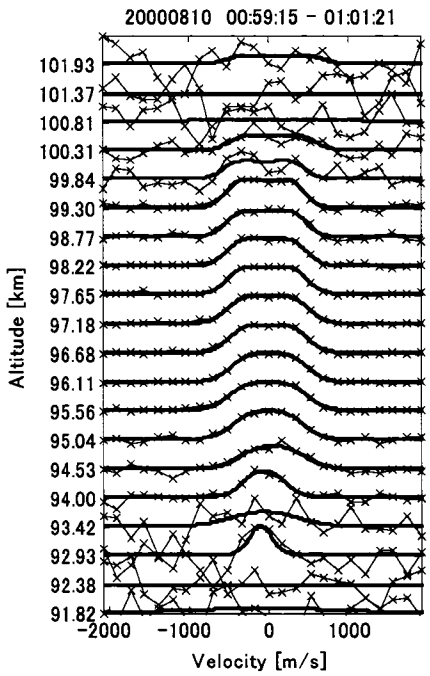

(b) Spectra

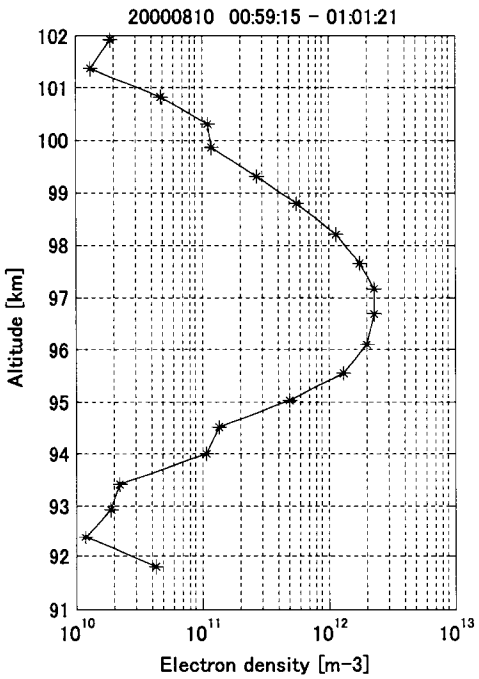

(c) Electron density in the layer

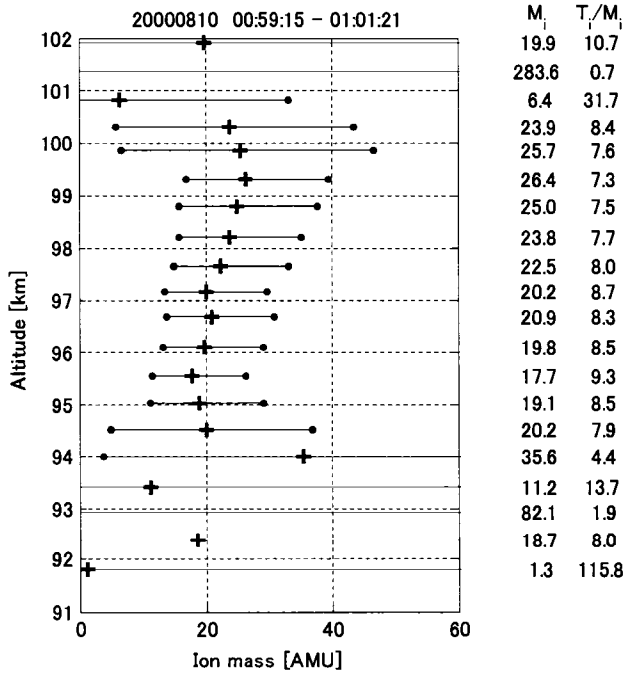

M_i	T_i/M_i
19.9	10.7
283.6	0.7
6.4	31.7
23.9	8.4
25.7	7.6
26.4	7.3
25.0	7.5
23.8	7.7
22.5	8.0
20.2	8.7
20.9	8.3
19.8	8.5
17.7	9.3
19.1	8.5
20.2	7.9
35.6	4.4
11.2	13.7
82.1	1.9
18.7	8.0
1.3	115.8

(d) Ion mass in the layer

Fig. 6.6 Ion mass estimation in the layer during 0:59-1:01UT on Aug. 10th 2000.

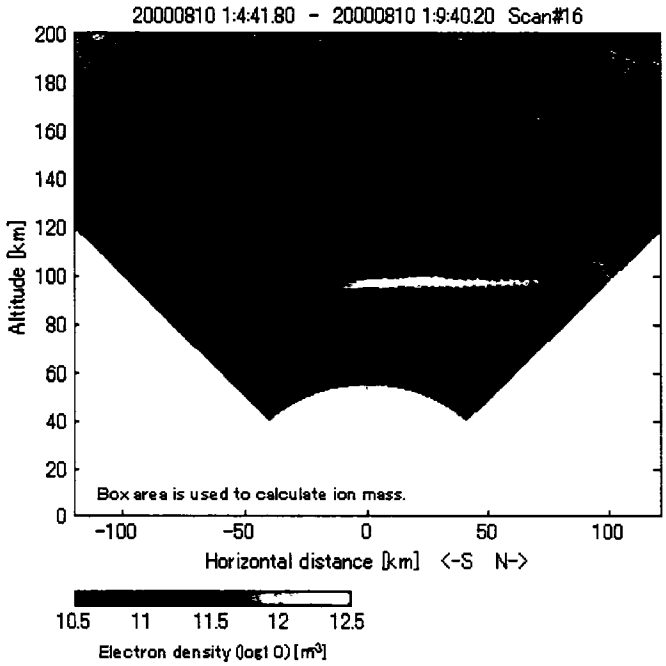

(a) Electron density

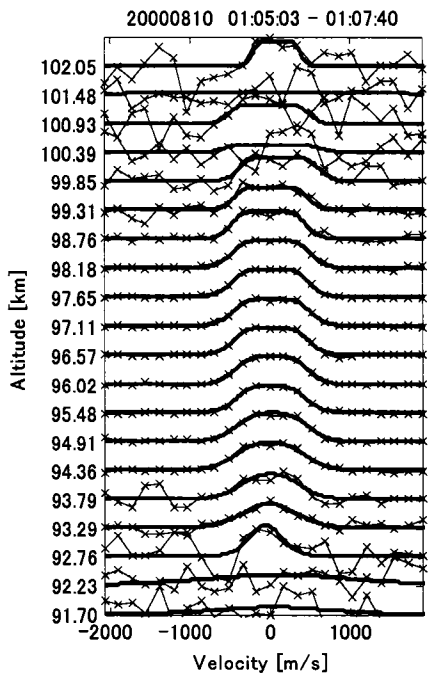

(b) Spectra

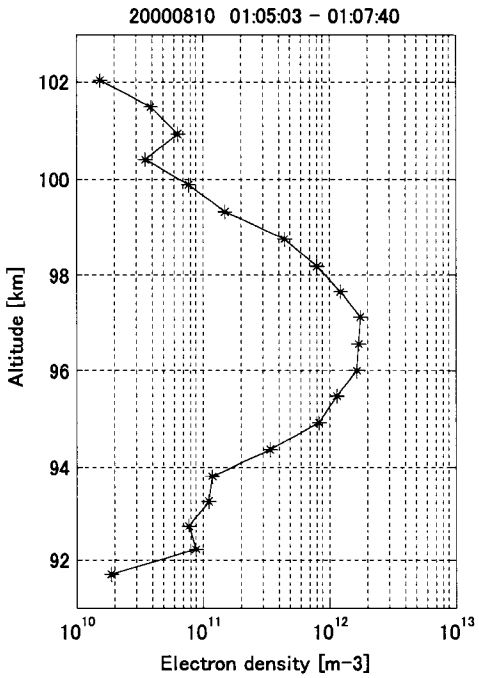

(c) Electron density in the layer

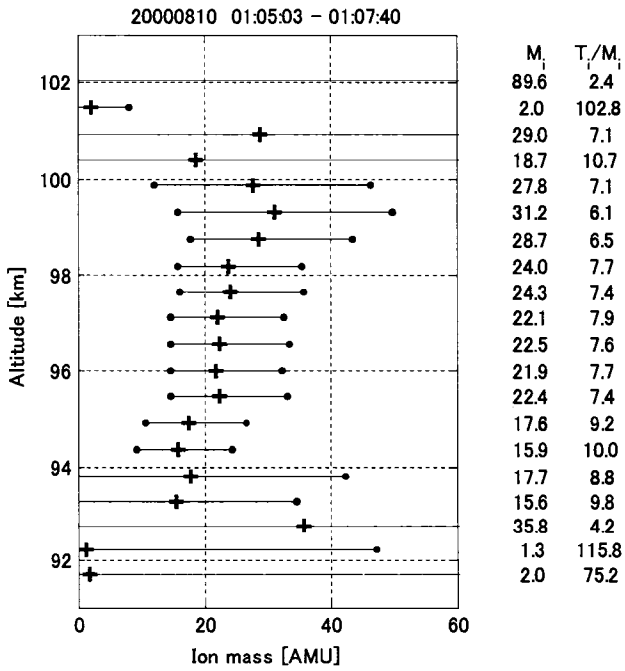

(d) Ion mass in the layer

Fig. 6.7 Ion mass estimation in the layer during 1:05-1:07UT on Aug. 10th 2000.

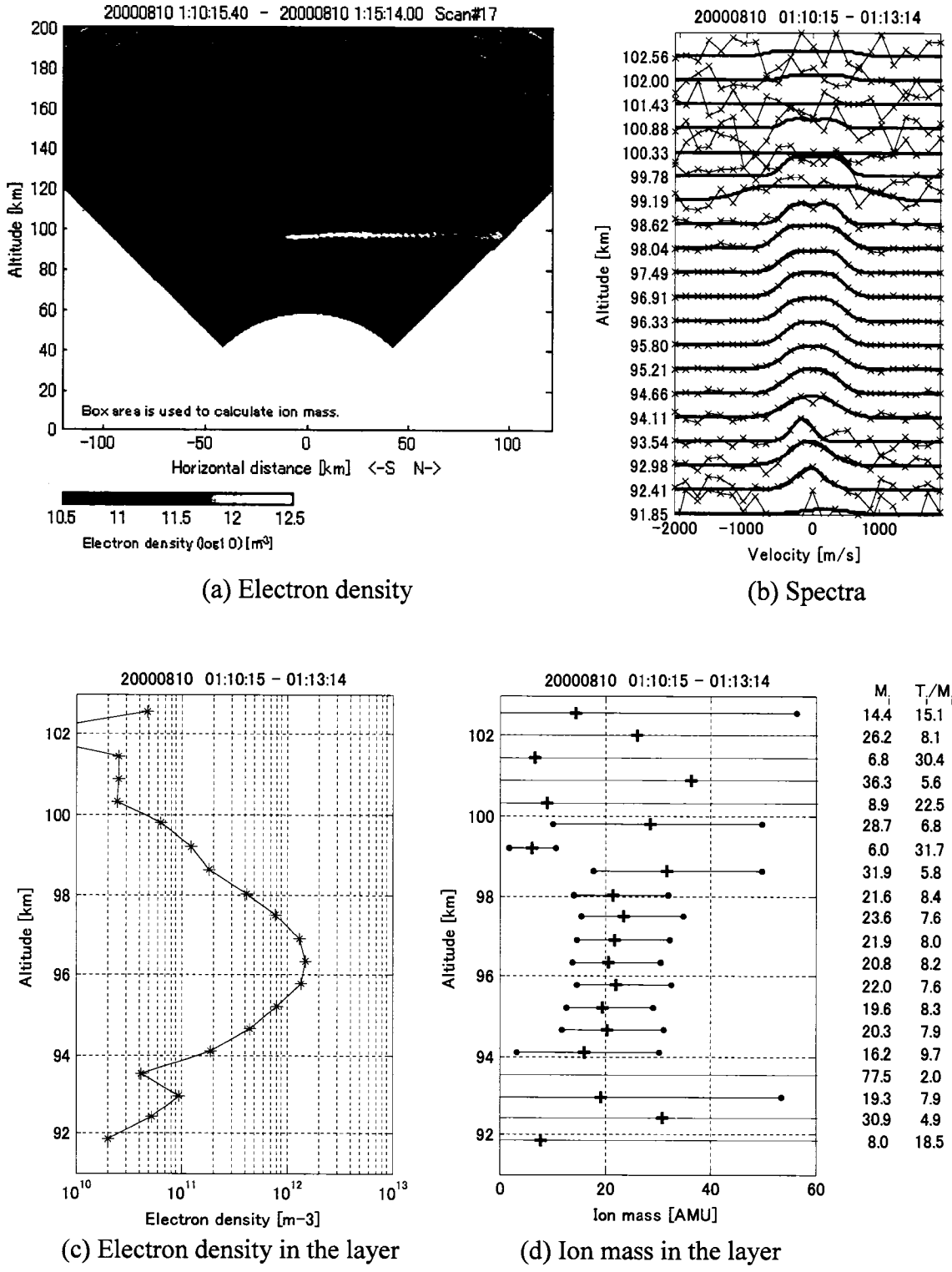

Fig. 6.8 Ion mass estimation in the layer during 1:10-1:13UT on Aug. 10th 2000.

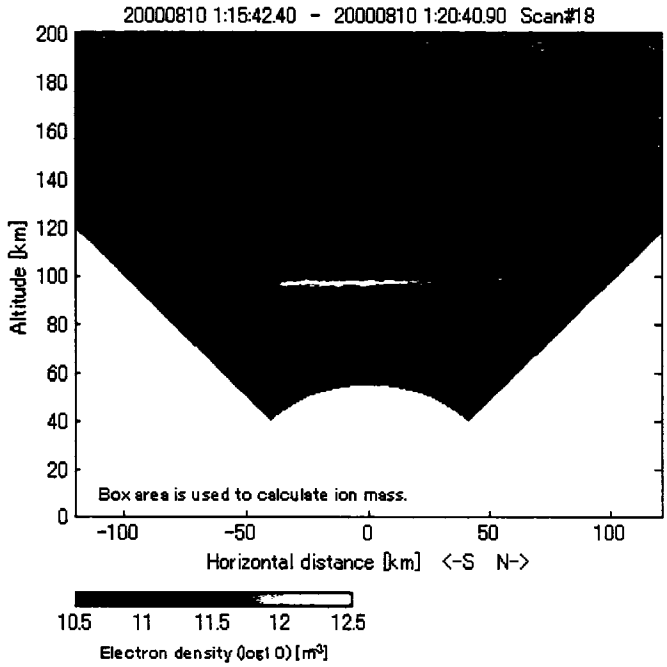

(a) Electron density

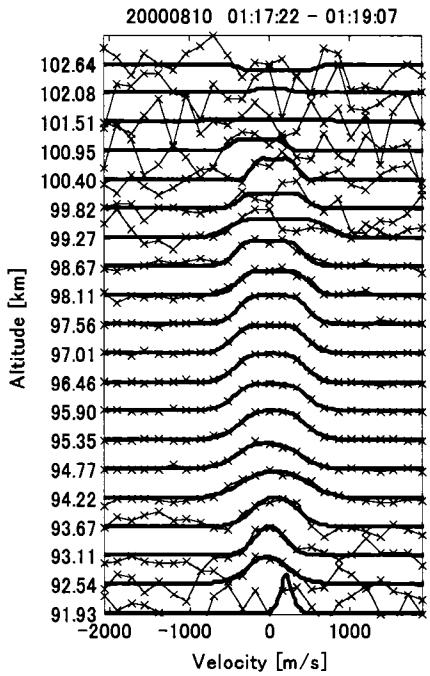

(b) Spectra

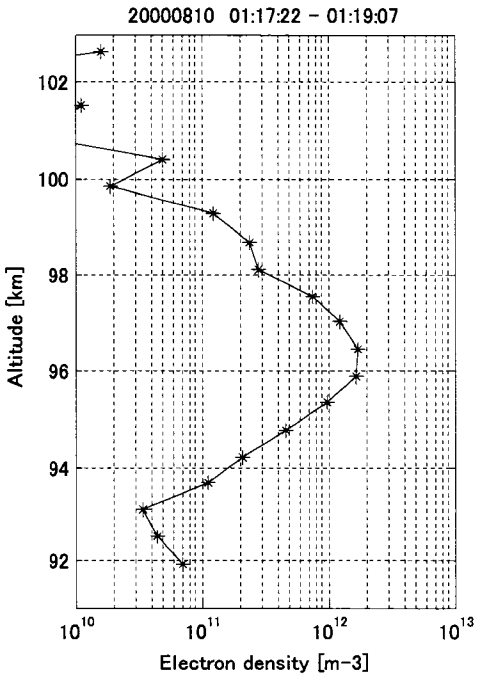

(c) Electron density in the layer

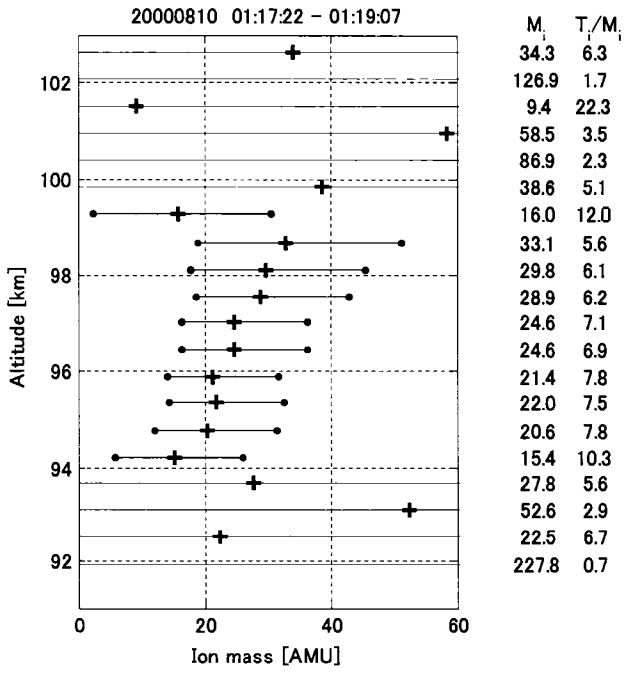

(d) Ion mass in the layer

Fig. 6.9 Ion mass estimation in the layer during 1:17-1:19UT on Aug. 10th 2000.

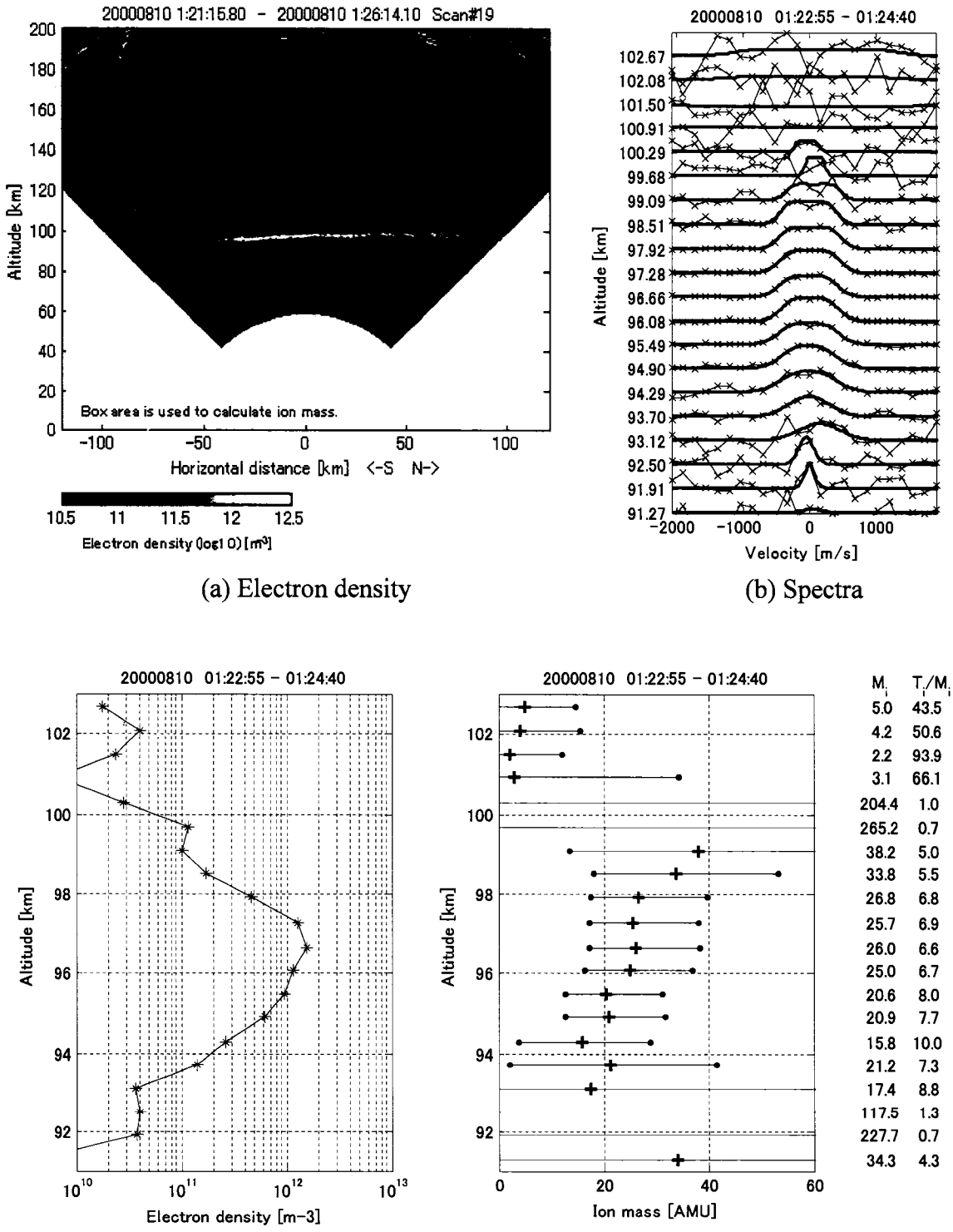

Fig. 6.10 Ion mass estimation in the layer during 1:22-1:24UT on Aug. 10th 2000.

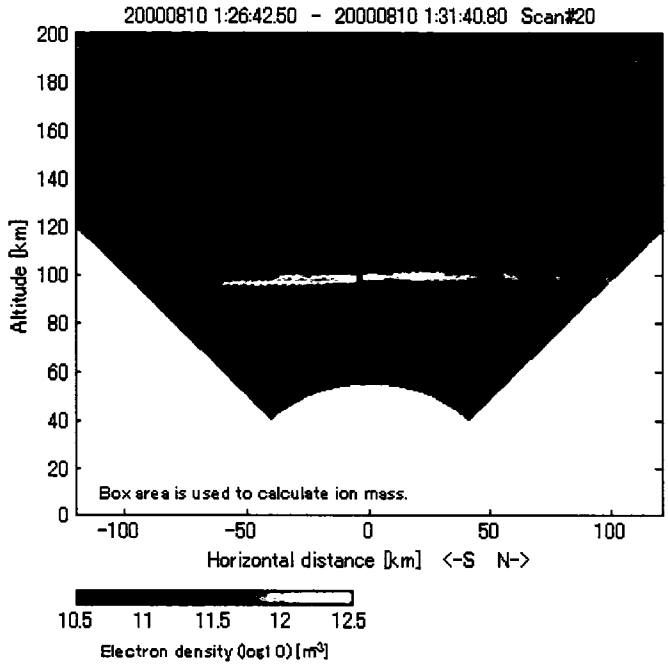

(a) Electron density

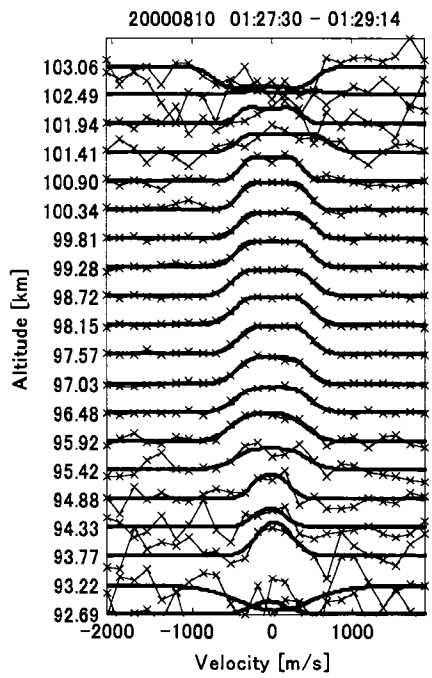

(b) Spectra

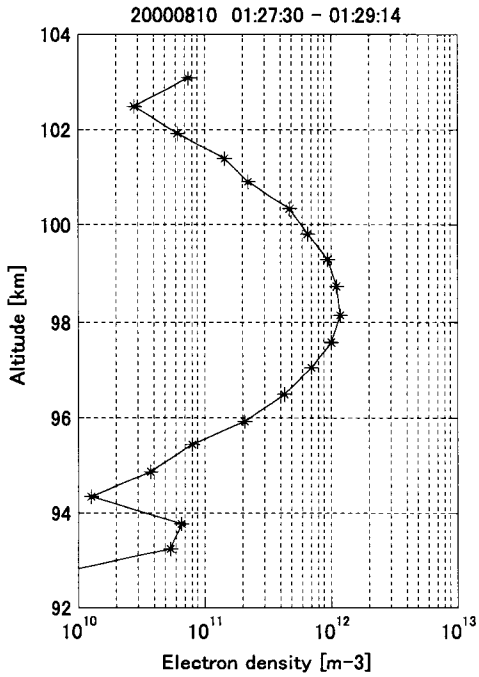

(c) Electron density in the layer

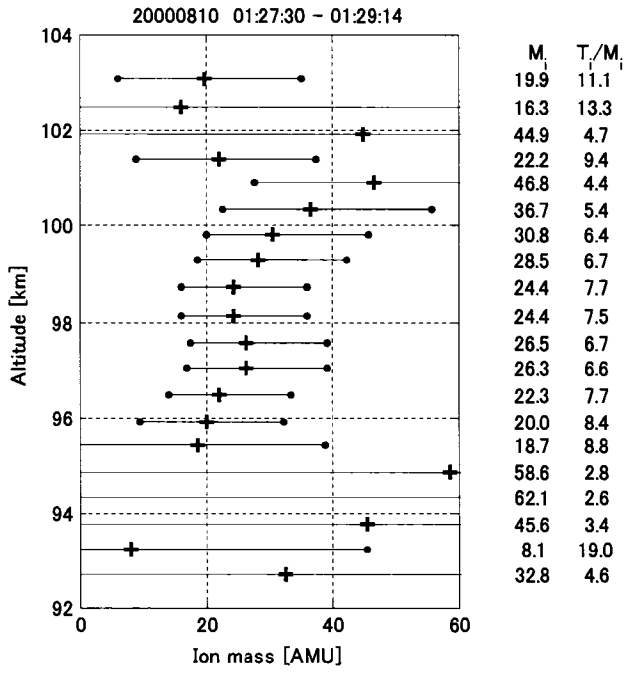

(d) Ion mass in the layer

Fig. 6.11 Ion mass estimation in the layer during 1:27-1:29UT on Aug. 10th 2000.

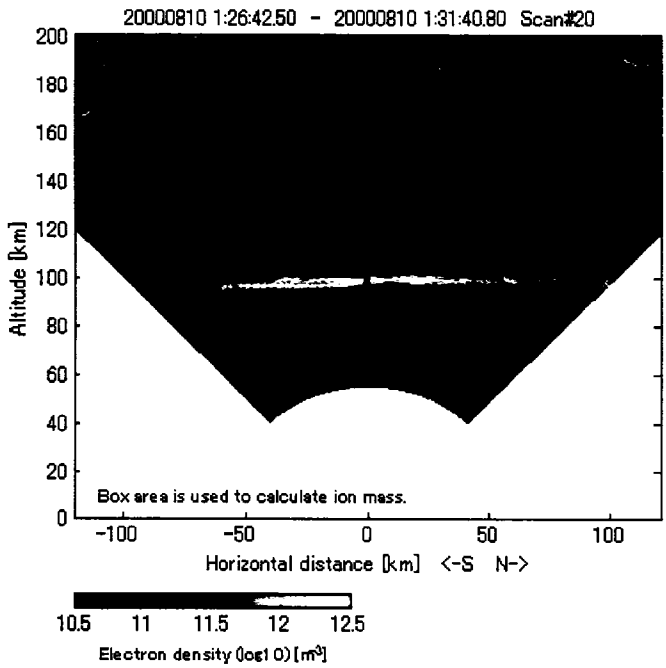

(a) Electron density

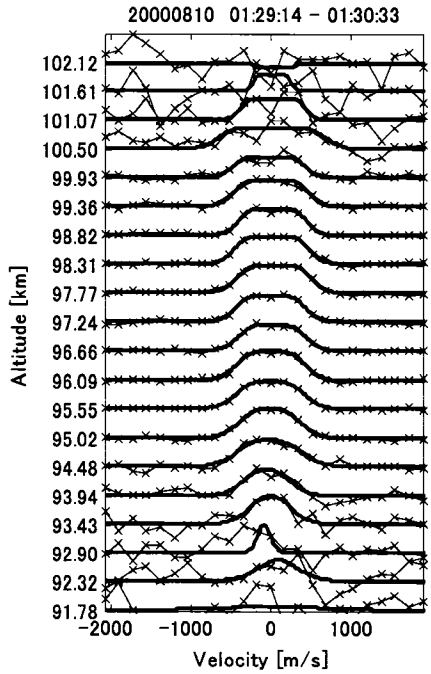

(b) Spectra

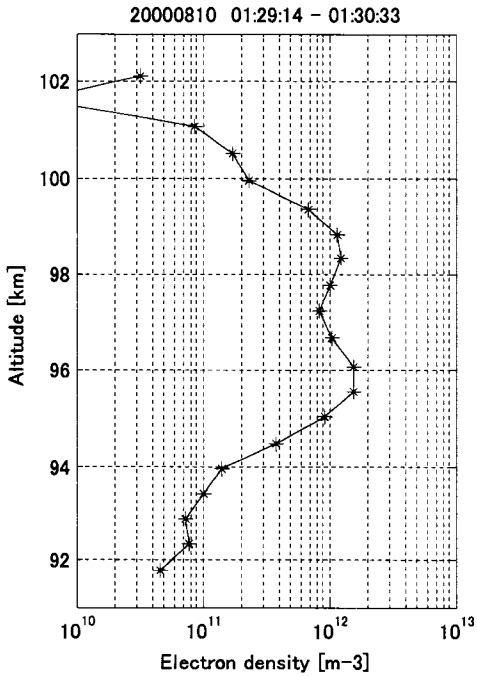

(c) Electron density in the layer

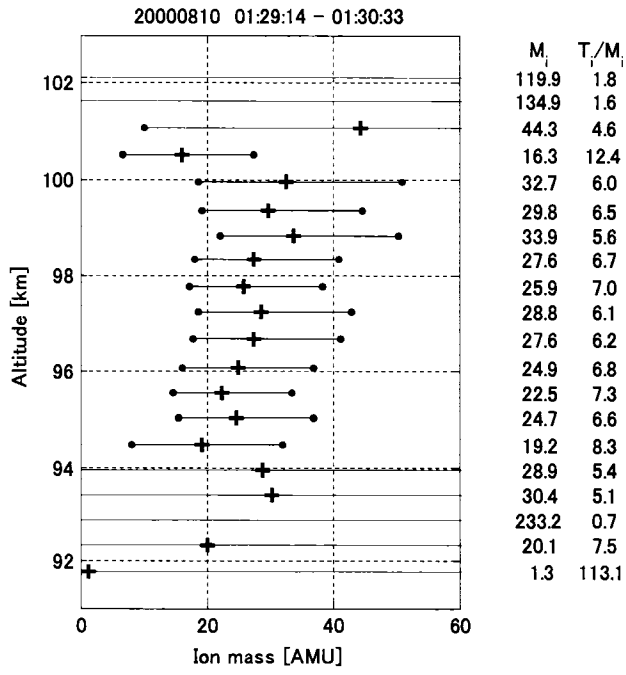

(d) Ion mass in the layer

Fig. 6.12 Ion mass estimation in the layer during 1:29-1:30UT on Aug. 10th 2000.

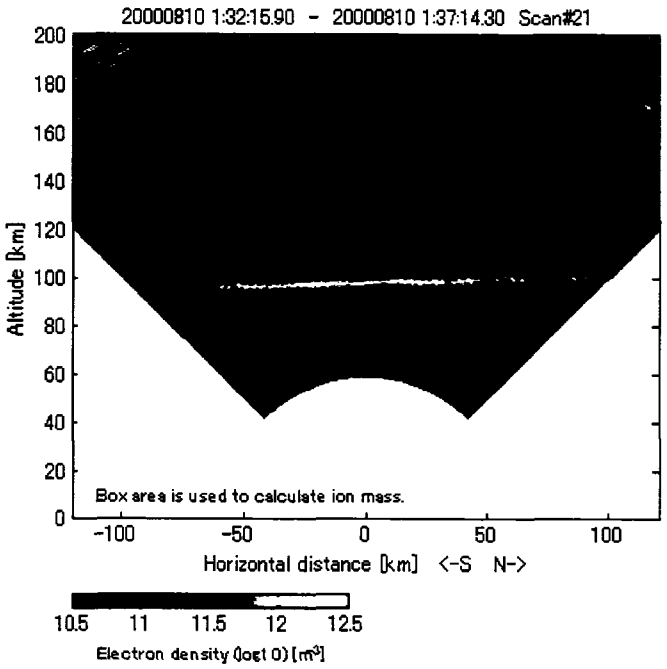

(a) Electron density

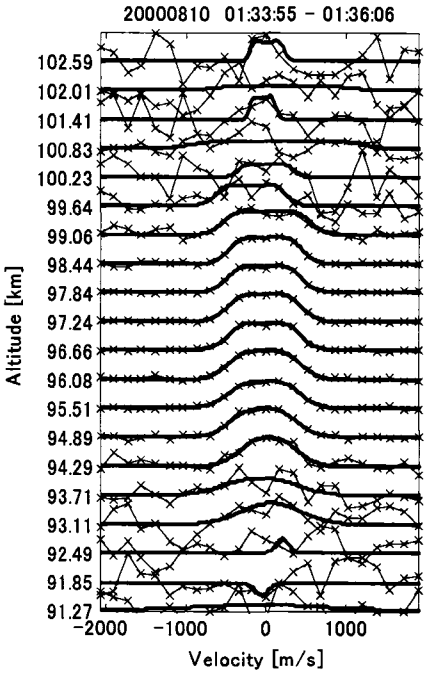

(b) Spectra

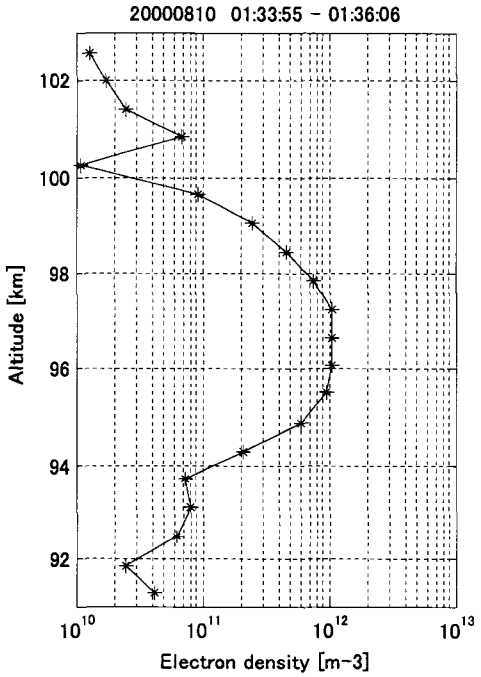

(c) Electron density in the layer

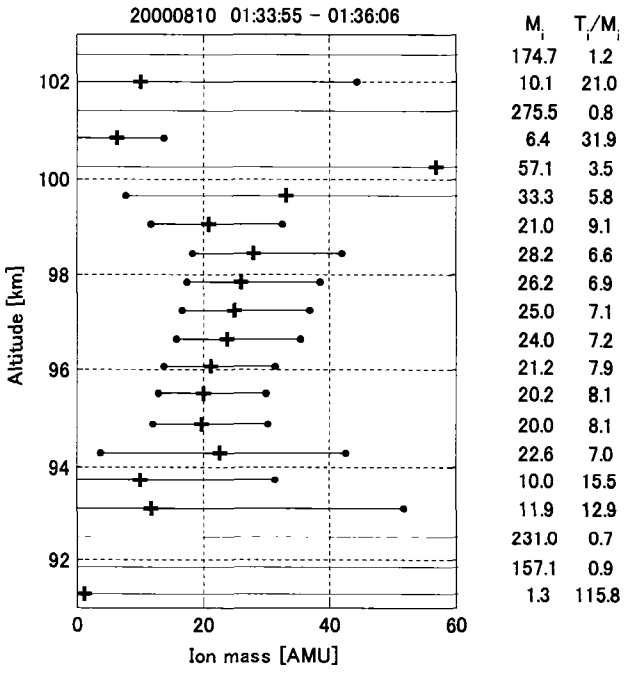

(d) Ion mass in the layer

Fig. 6.13 Ion mass estimation in the layer during 1:33-1:36UT on Aug. 10th 2000.

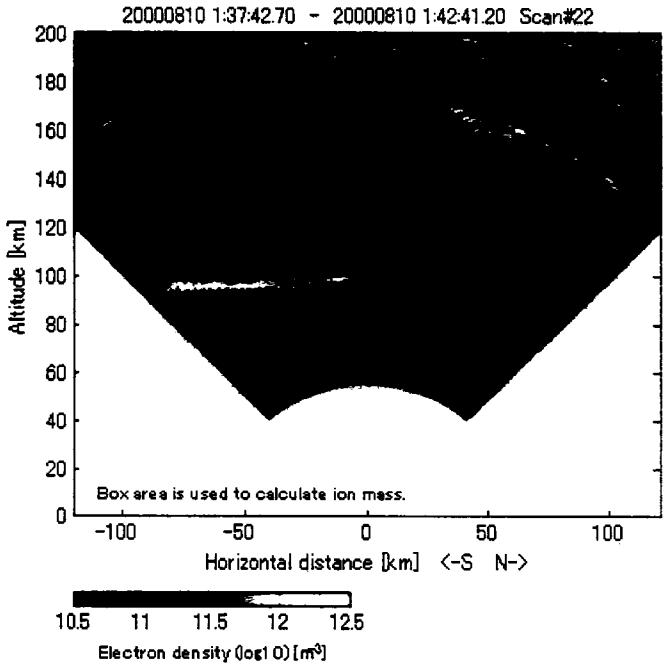

(a) Electron density

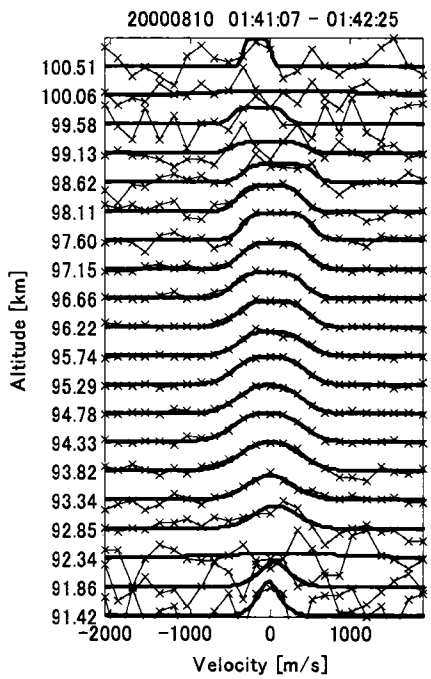

(b) Spectra

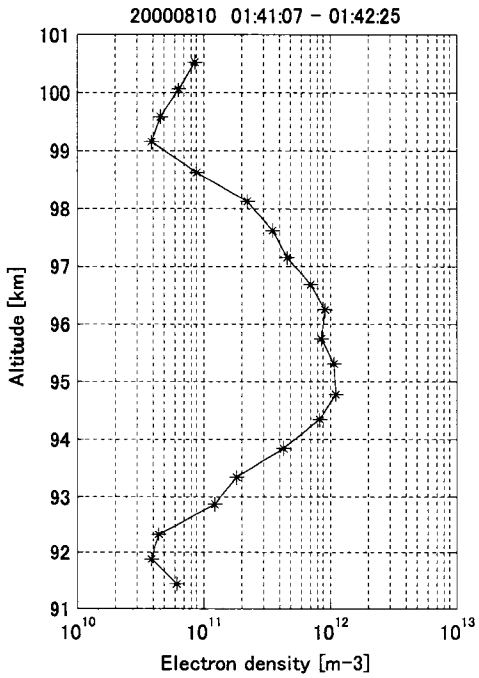

(c) Electron density in the layer

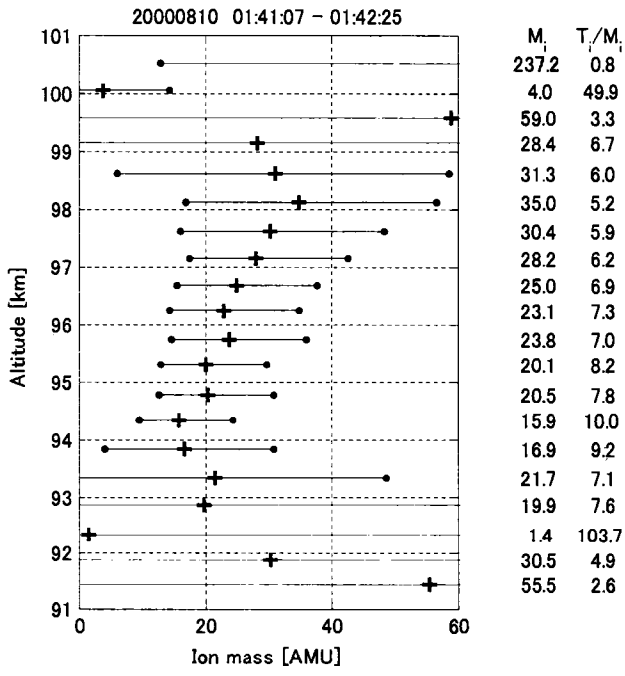

(d) Ion mass in the layer

Fig. 6.14 Ion mass estimation in the layer during 1:41-1:42UT on Aug. 10th 2000.

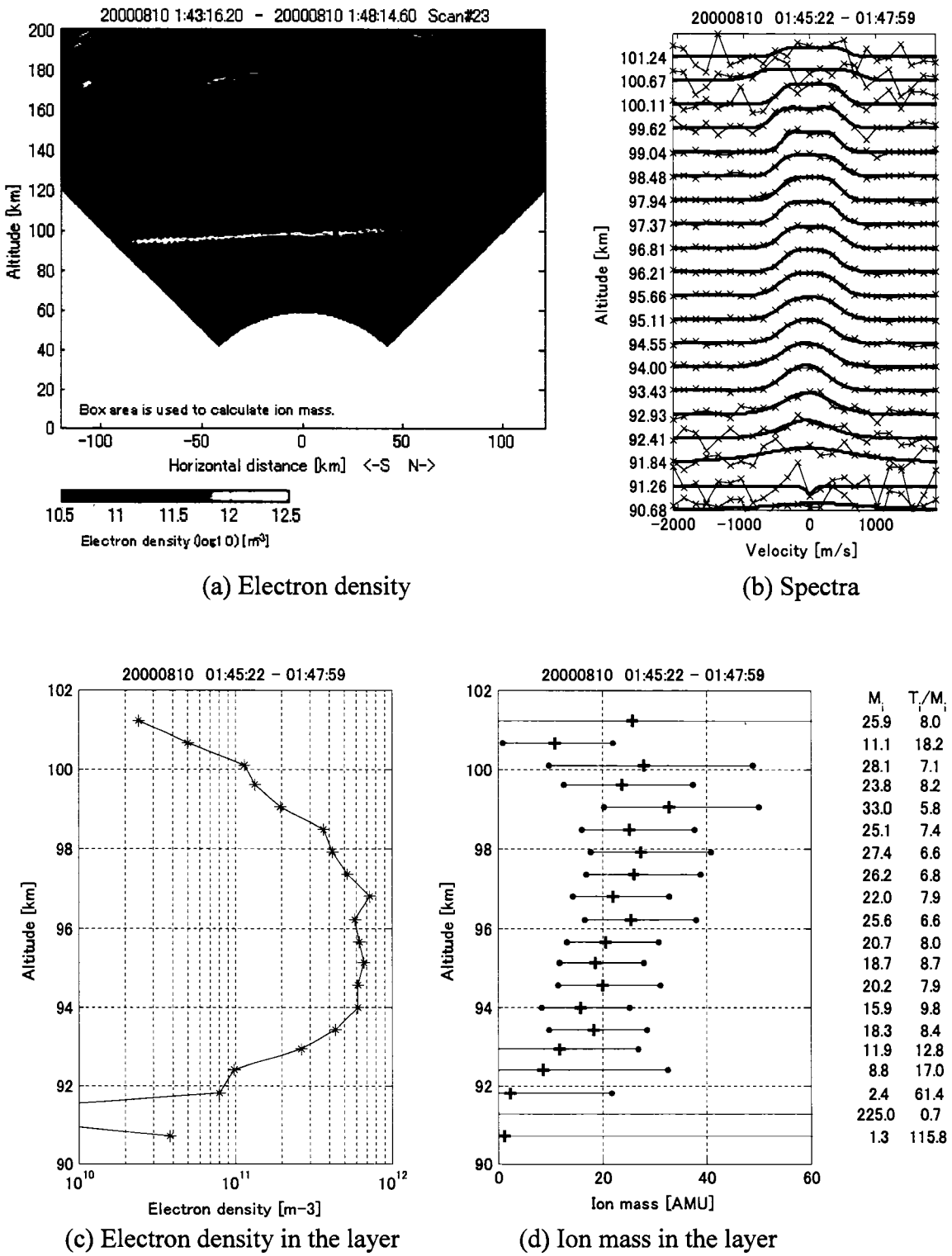

Fig. 6.15 Ion mass estimation in the layer during 1:45-1:47UT on Aug. 10th 2000.

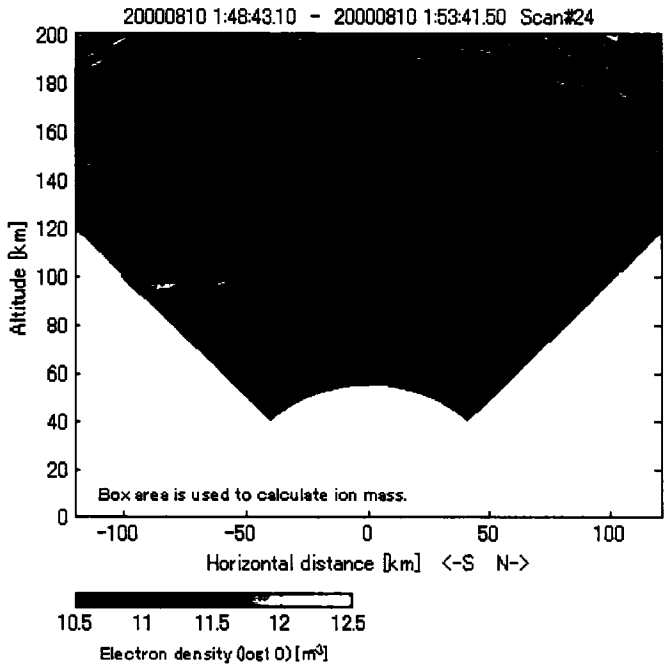

(a) Electron density

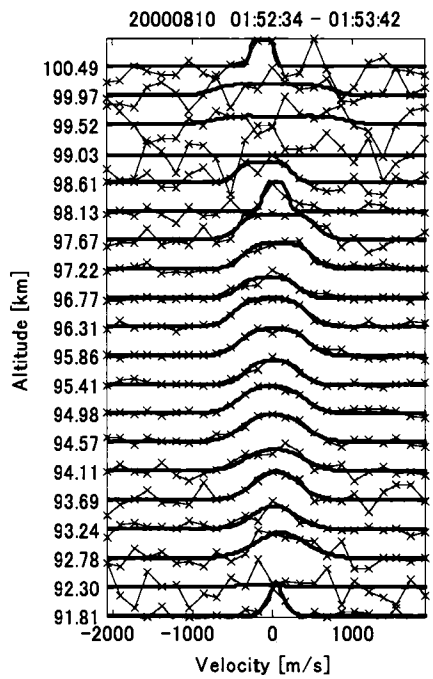

(b) Spectra

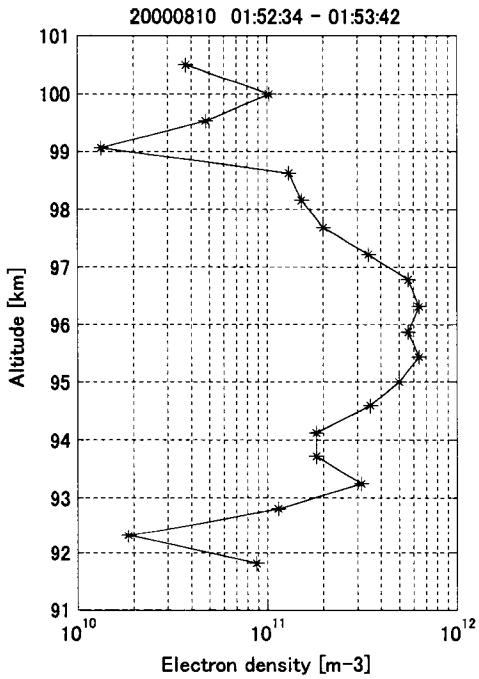

(c) Electron density in the layer

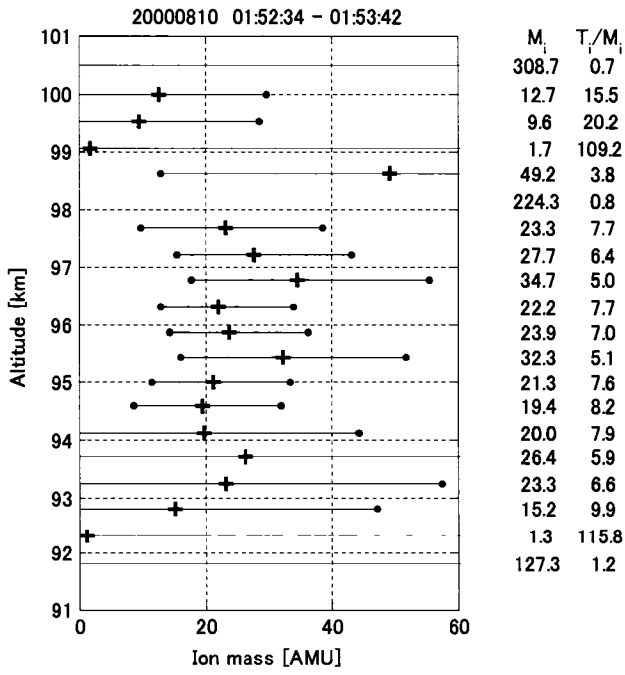

(d) Ion mass in the layer

Fig. 6.16 Ion mass estimation in the layer during 1:52-1:53UT on Aug. 10th 2000.

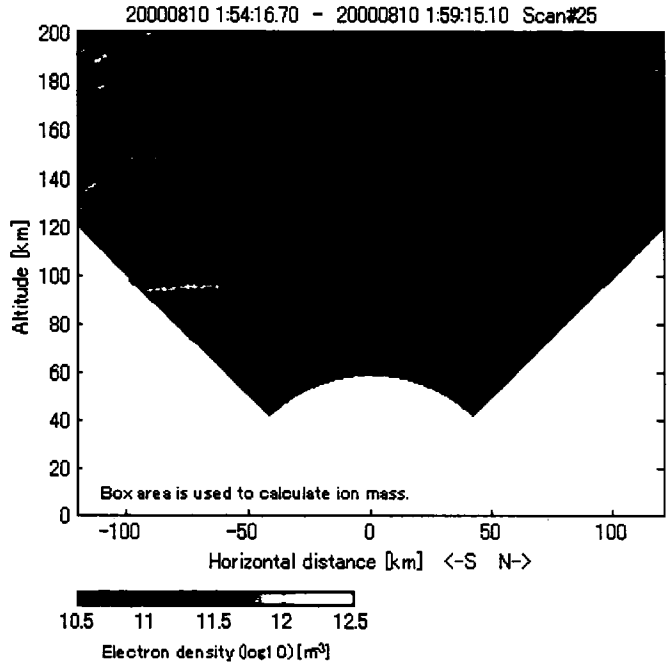

(a) Electron density

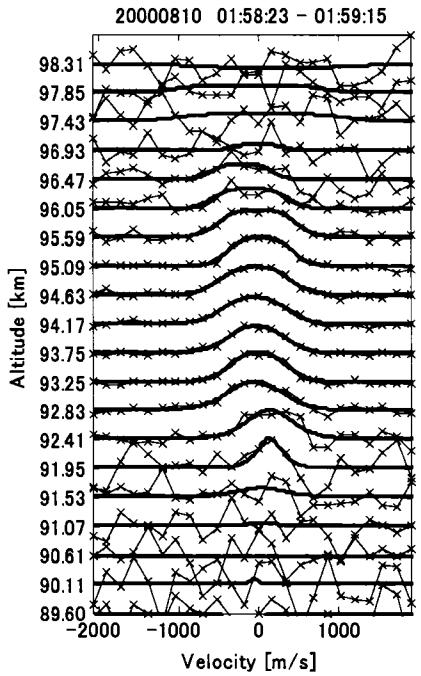

(b) Spectra

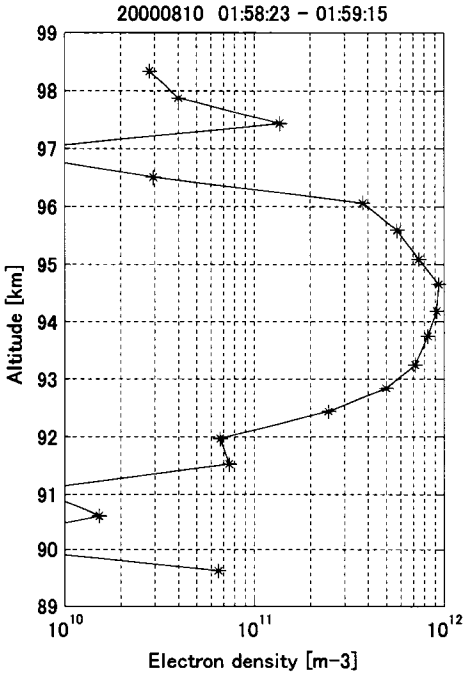

(c) Electron density in the layer

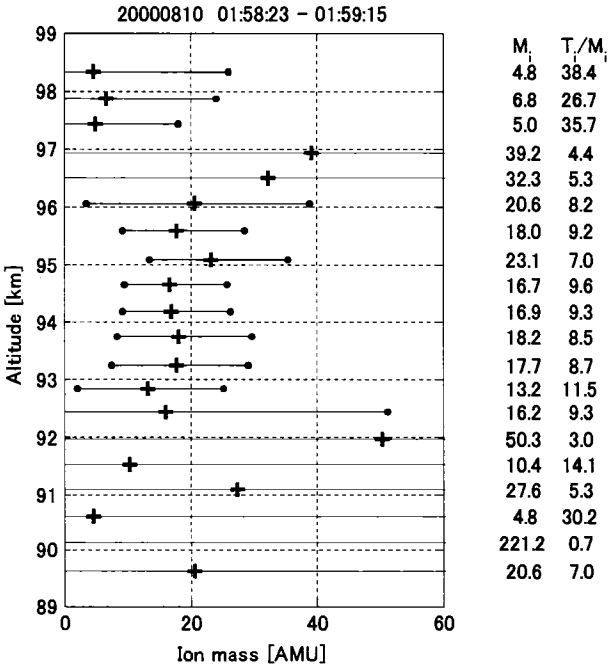

(d) Ion mass in the layer

Fig. 6.17 Ion mass estimation in the layer during 1:58-1:59UT on Aug. 10th 2000.

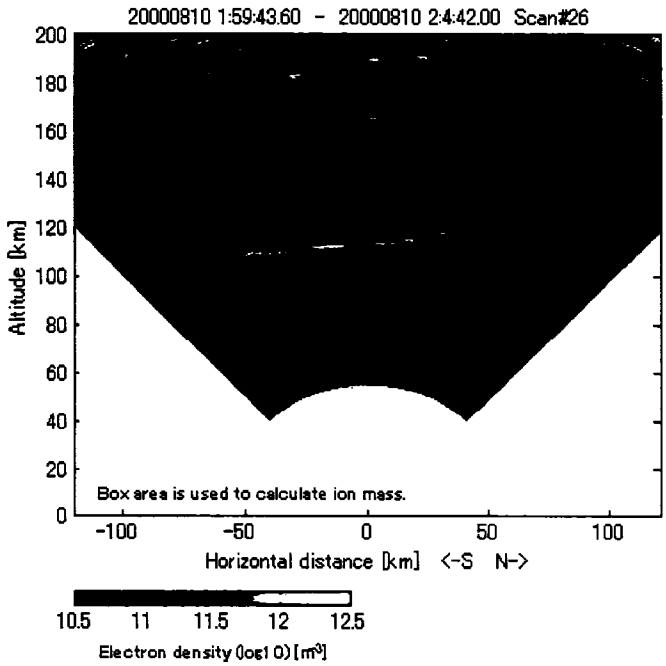

(a) Electron density

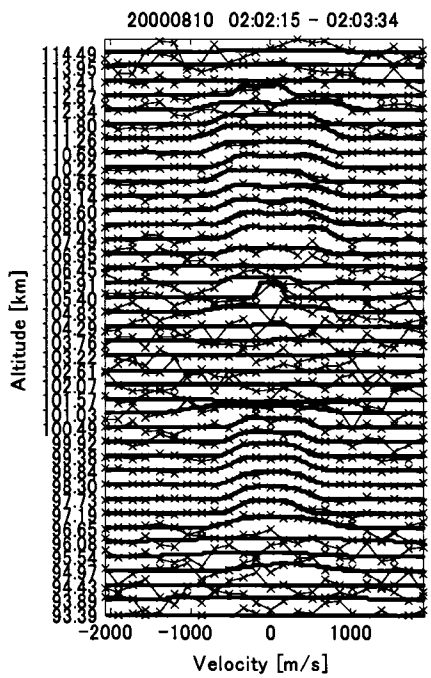

(b) Spectra

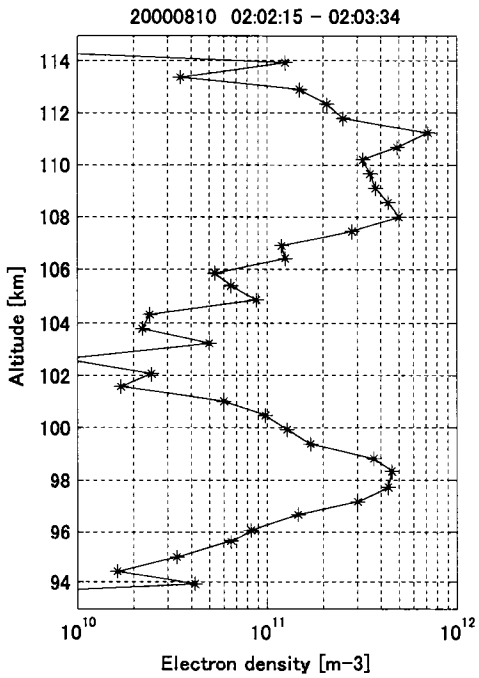

(c) Electron density in the layer

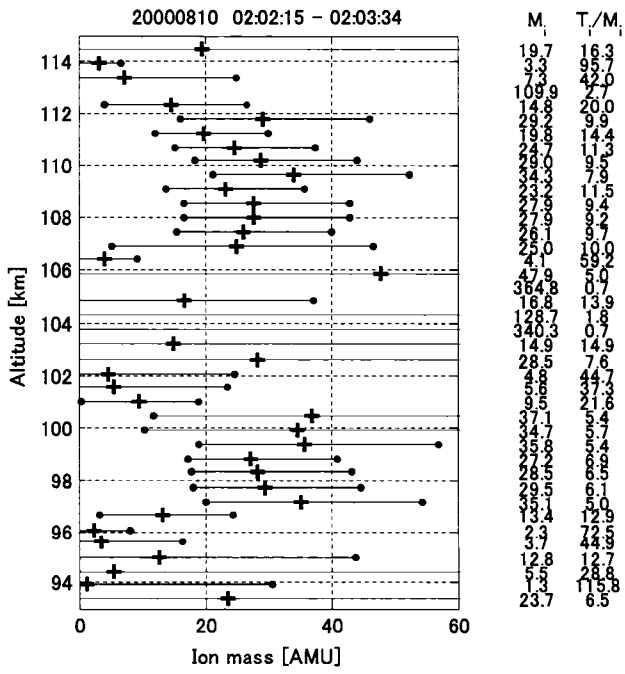

(d) Ion mass in the layer

Fig. 6.18 Ion mass estimation in the layer during 2:02-2:03UT on Aug. 10th 2000.

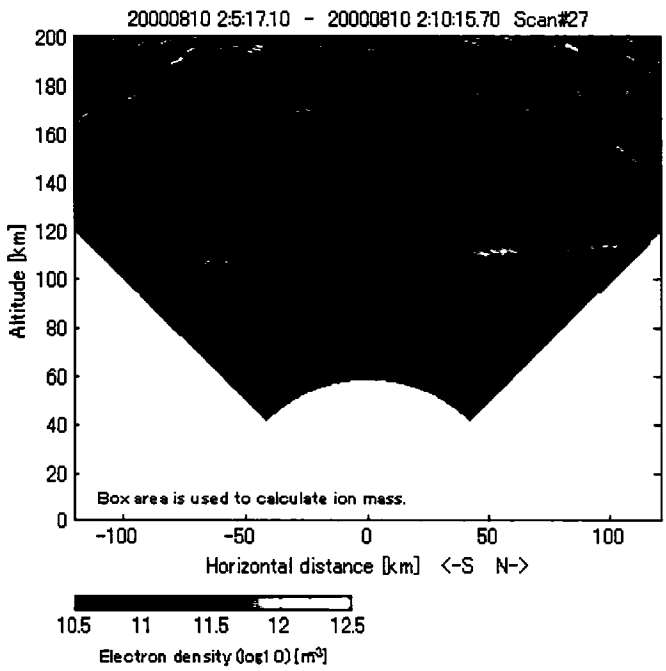

(a) Electron density

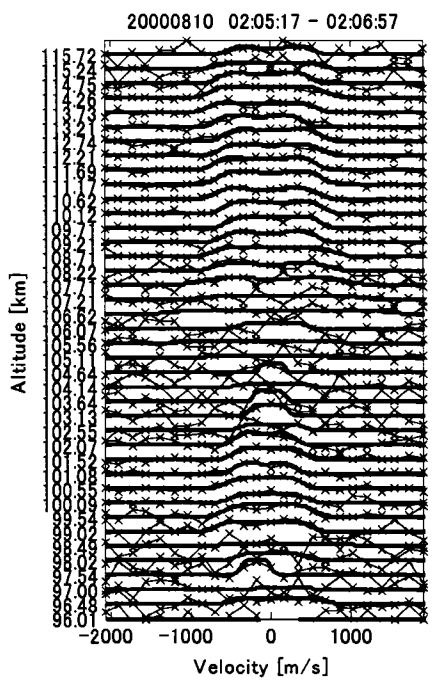

(b) Spectra

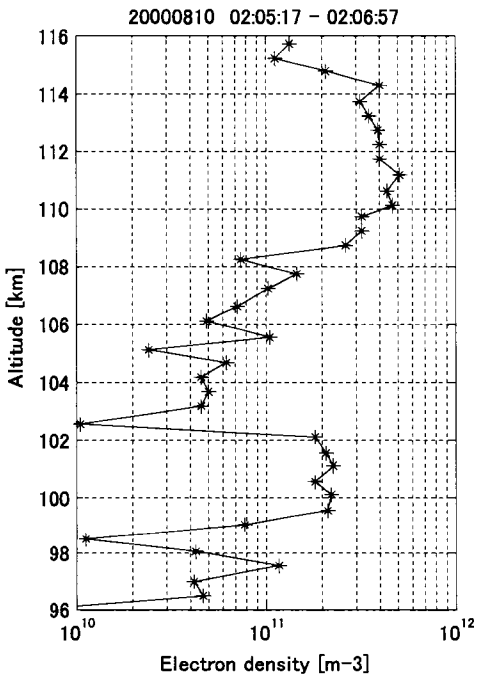

(c) Electron density in the layer

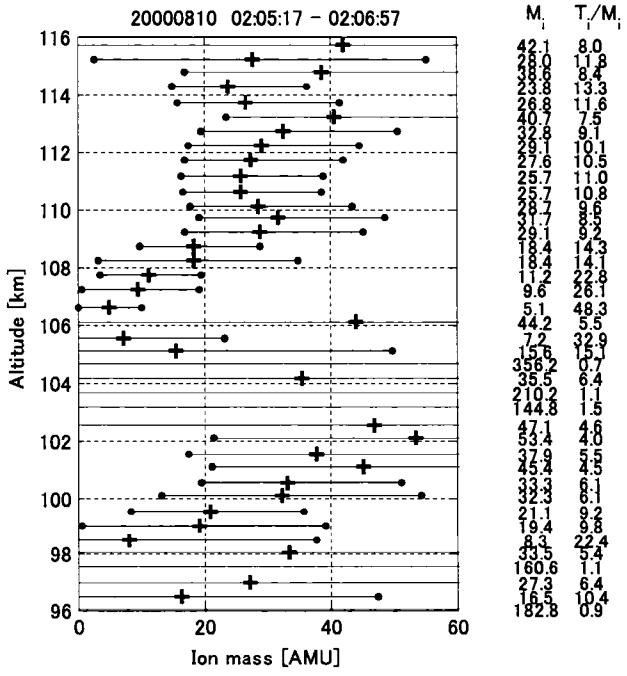

(d) Ion mass in the layer

Fig. 6.19 Ion mass estimation in the layer during 2:05-2:06UT on Aug. 10th 2000.

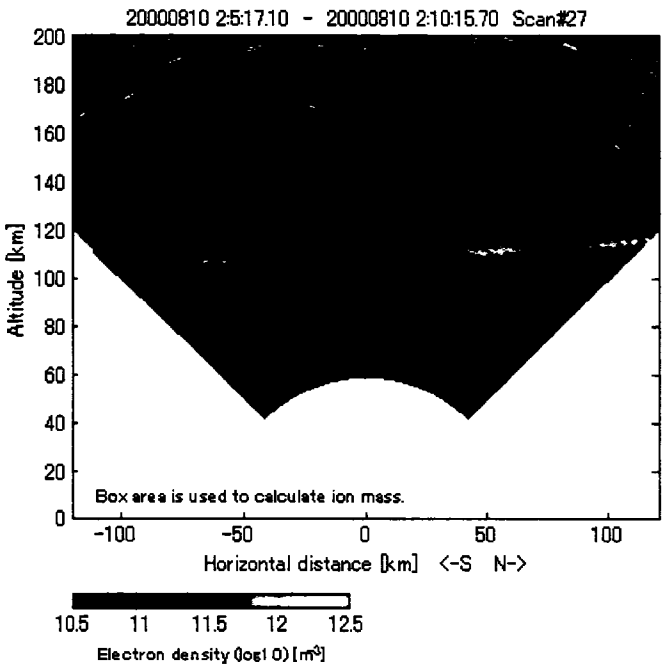

(a) Electron density

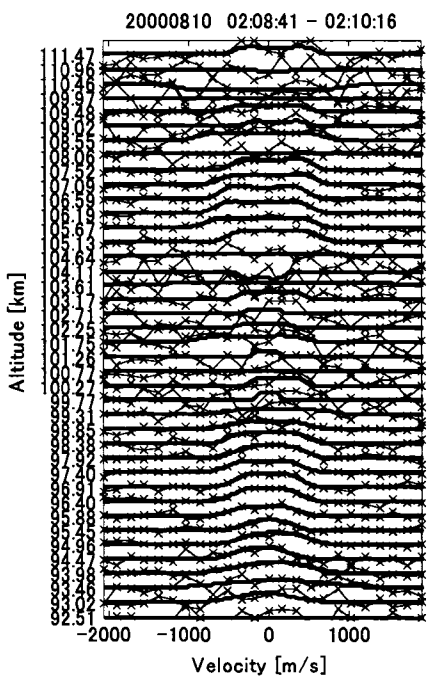

(b) Spectra

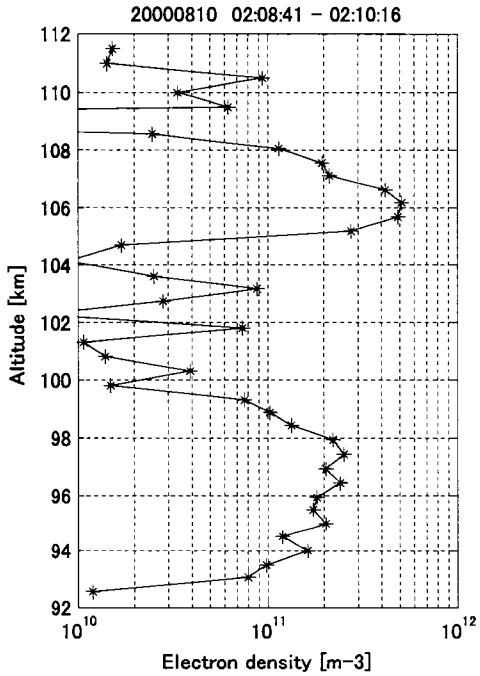

(c) Electron density in the layer

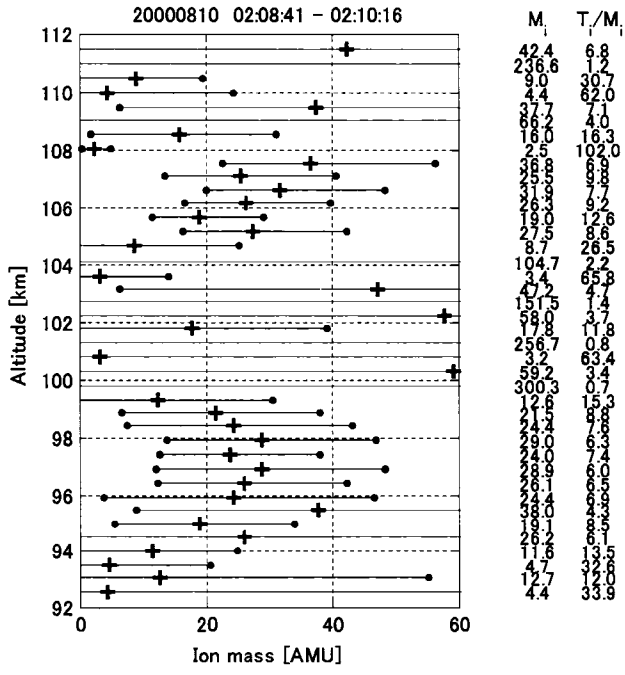

(d) Ion mass in the layer

Fig. 6.20 Ion mass estimation in the layer during 2:08-2:10UT on Aug. 10th 2000.

6.2.2 May. 21st 1999

A weak sporadic layer appeared at 1:23 UT and became stronger around 2:08 UT. A double layer, the upper layer of which was too weak to allow an estimation of ion mass, appeared at 2:19 UT and continued through 2:46 UT. Another weak layer intermittently appeared after that until 4:30 UT.

There was aurora precipitation through the whole night. The temperature profile was estimated using the unmodulated long pulse mode at first as shown in Fig.6.21. However apparently there was an influence of aurora precipitation and the estimated ion temperatures were too high. Since the long pulse mode has a poor resolution of 48km, it was impossible to avoid the influences both of the sporadic layer which existed around 100km height and the aurora which existed in the upper region.

In order to avoid the influences of both the sporadic layer and the aurora, the short pulse mode, which has 0.6km resolution, was used to estimate the temperature profile, as shown in Fig.6.22. Height was chosen carefully to be immediately above the double layers at 105km to 130 km with 5km step integration areas. Even though integration was carried out for five hours, SNR was relatively low and the temperature estimation error was certainly large.

Because the short pulse mode was used to estimate ion temperature, the temperature error is relatively large, which also causes a large error of ion mass estimation. However, the temperature error does not produce random error but rather produces bias error in ion mass estimation so that it is possible to compare ion masses if the altitude difference is relatively small, as is true inside thin layers. There are several cases for which the ion mass in the top part of the layer seems to be greater than the mass at the bottom of the layer (Fig.6.23 to Fig.6.26).

In the double layer case in Fig.6.27, ion mass in the upper layer seems to be slightly heavier than in the lower layer, however, in the next moment it is difficult to find such tendency as shown in Fig.6.28.

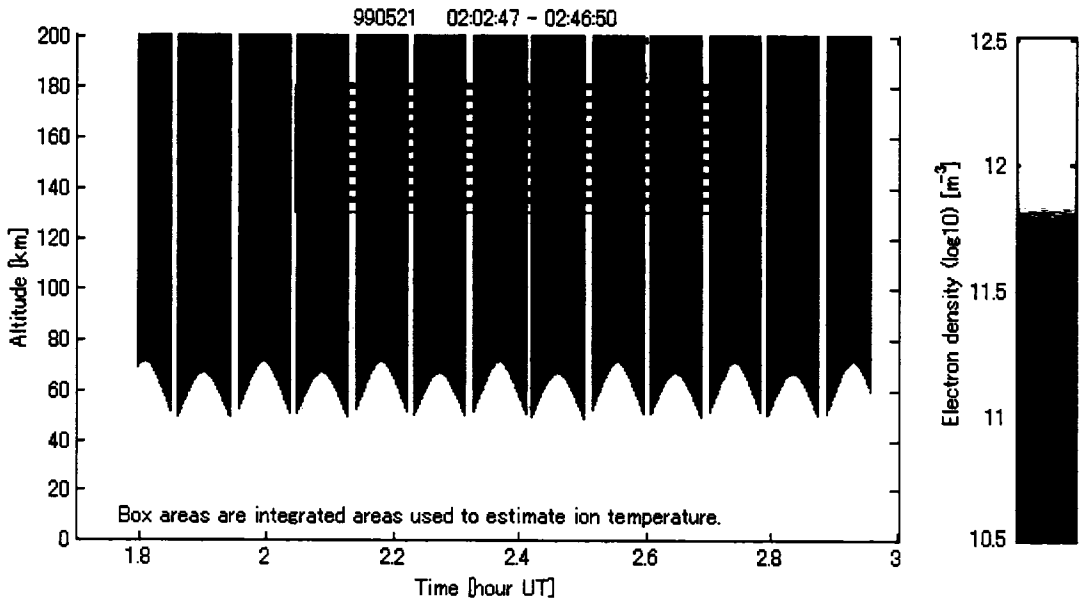

(a) Electron density

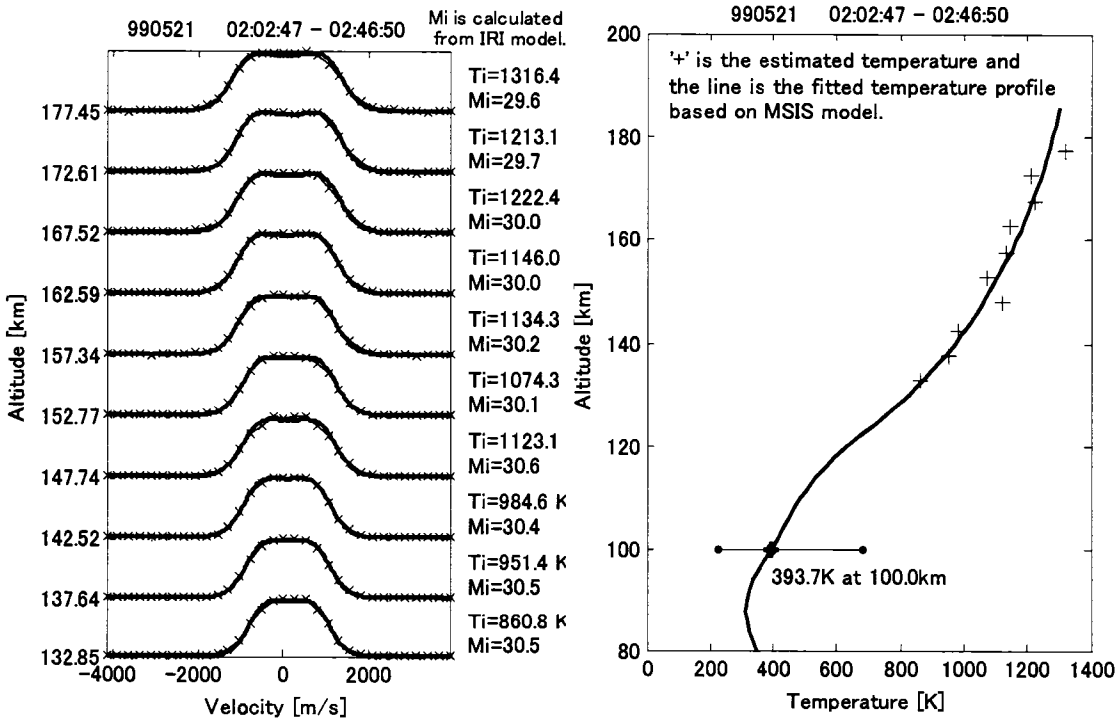

(b) Spectra (c) Ion temperature

Fig. 6.21 Ion temperature estimation using the long pulse mode on May 21st 1999.

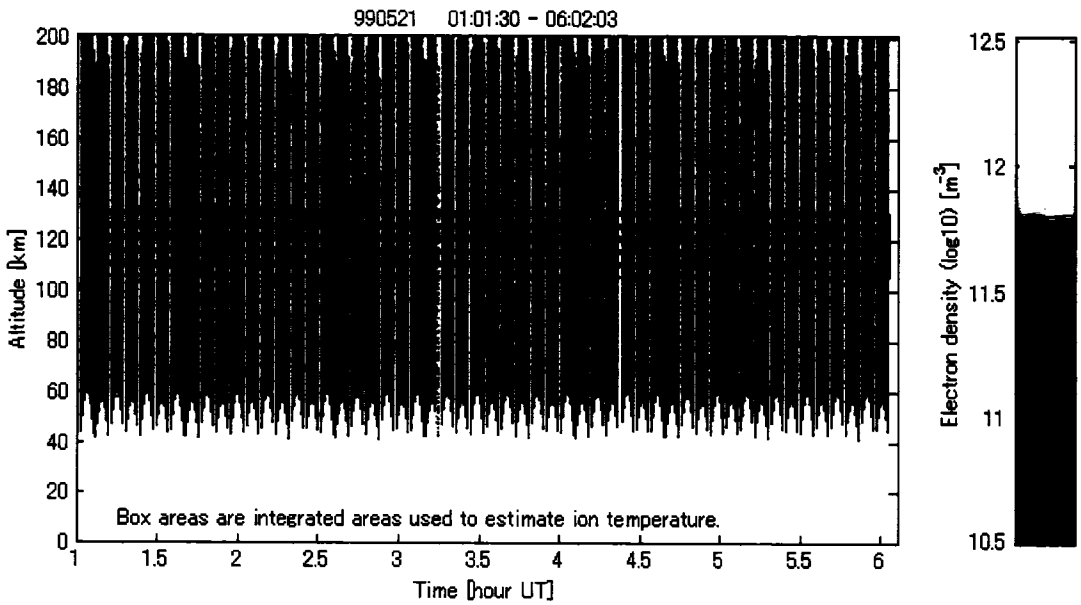

(a) Electron density

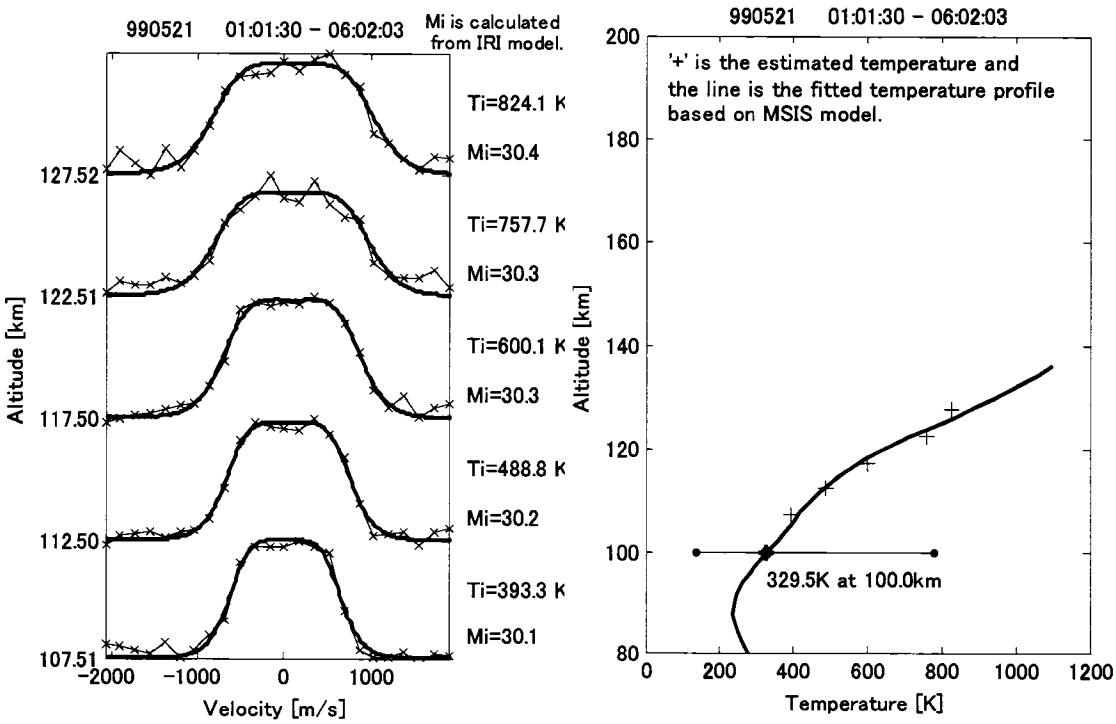

(b) Spectra (c) Ion temperature

Fig. 6.22 Ion temperature estimation using the short pulse mode on May 21st 1999.

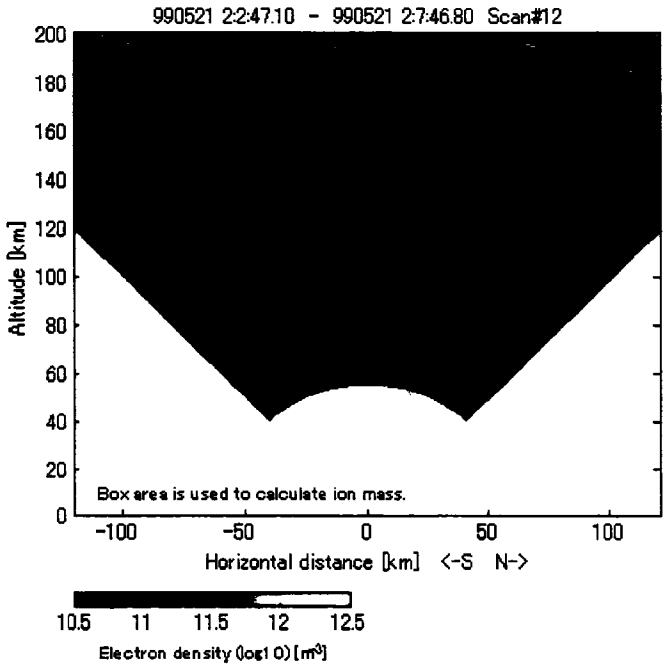

(a) Electron density

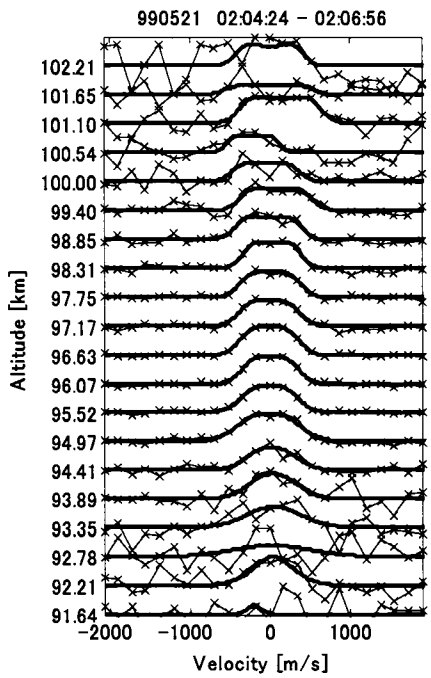

(b) Spectra

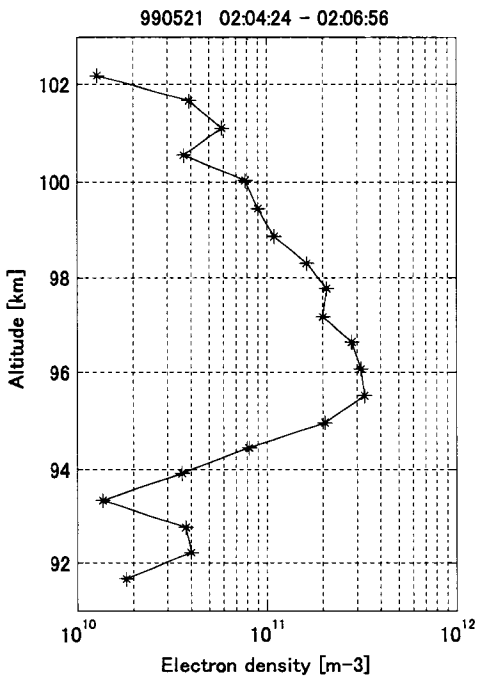

(c) Electron density in the layer

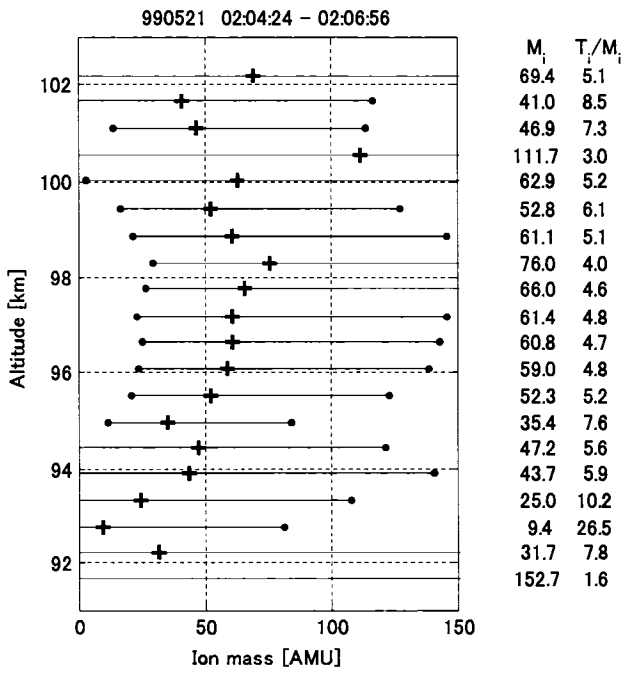

(d) Ion mass in the layer

Fig. 6.23 Ion mass estimation in the layer during 2:04-2:06UT on May 21st 1999.

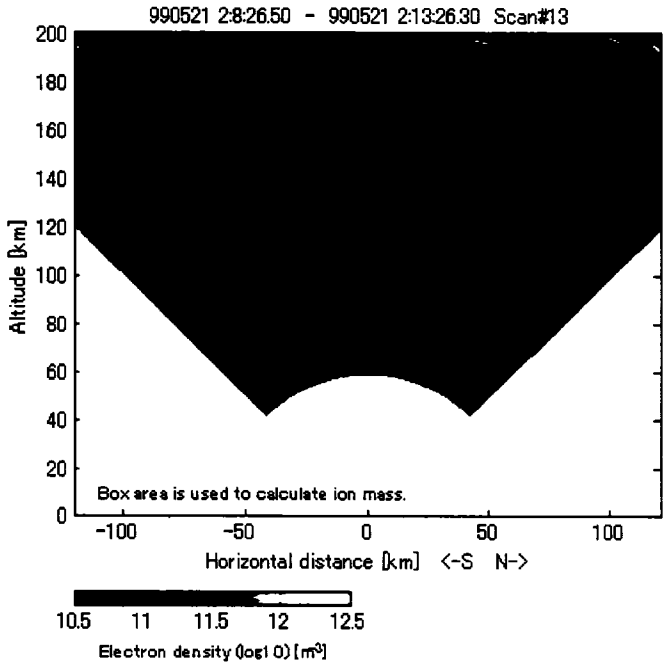

(a) Electron density

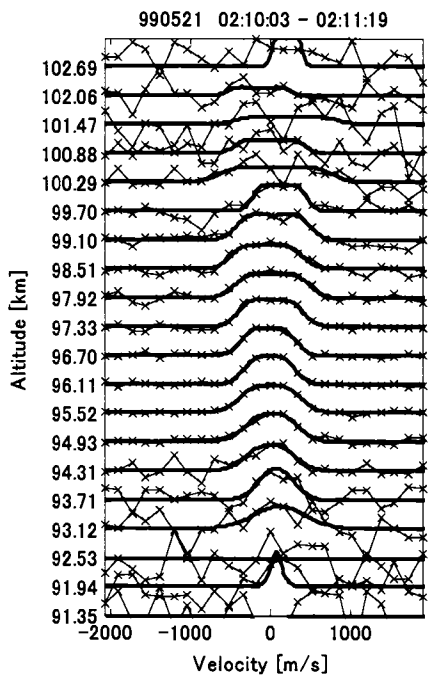

(b) Spectra

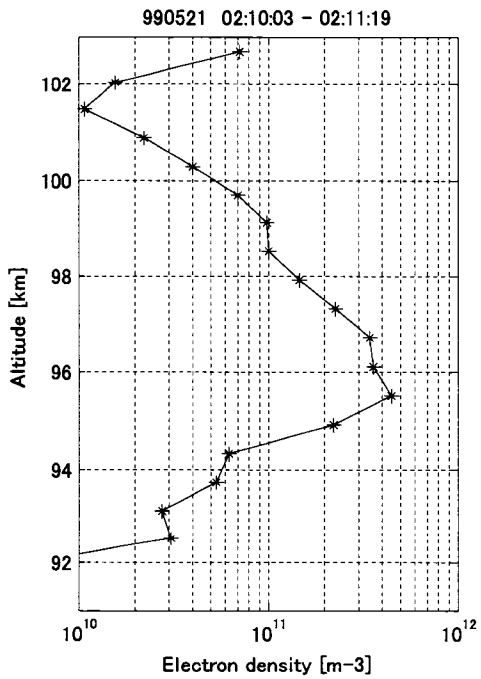

(c) Electron density in the layer

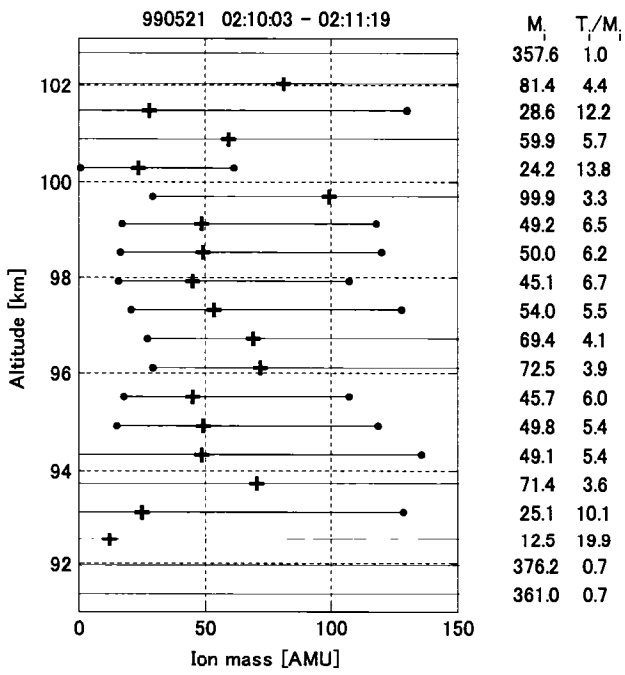

(d) Ion mass in the layer

Fig. 6.24 Ion mass estimation in the layer during 2:10-2:11UT on May 21st 1999.

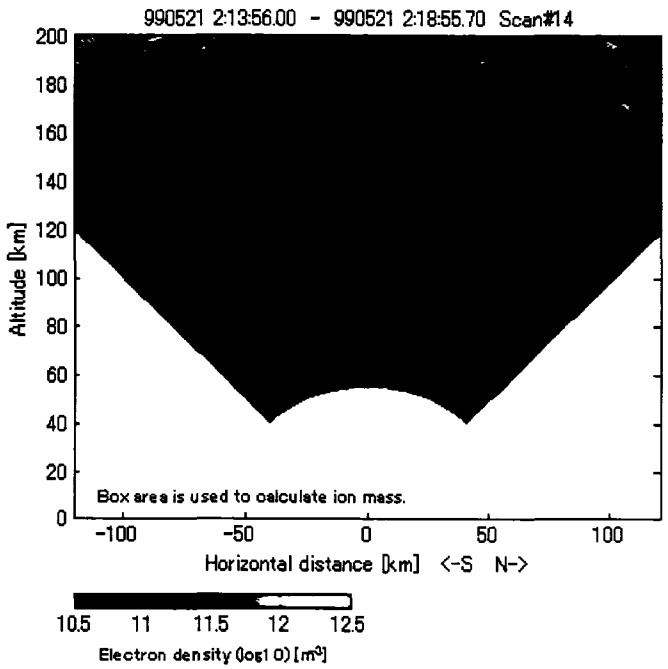

(a) Electron density

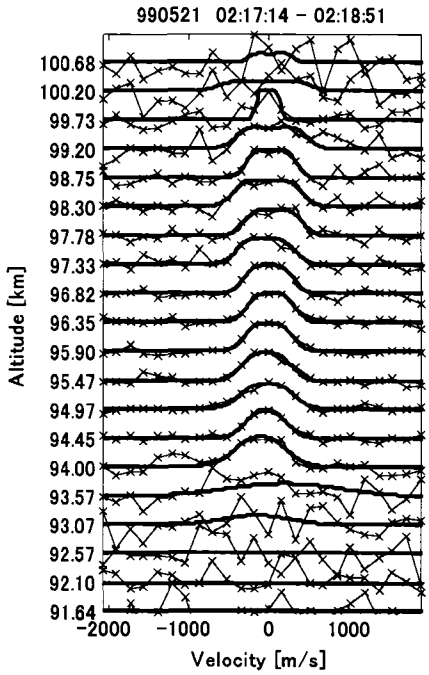

(b) Spectra

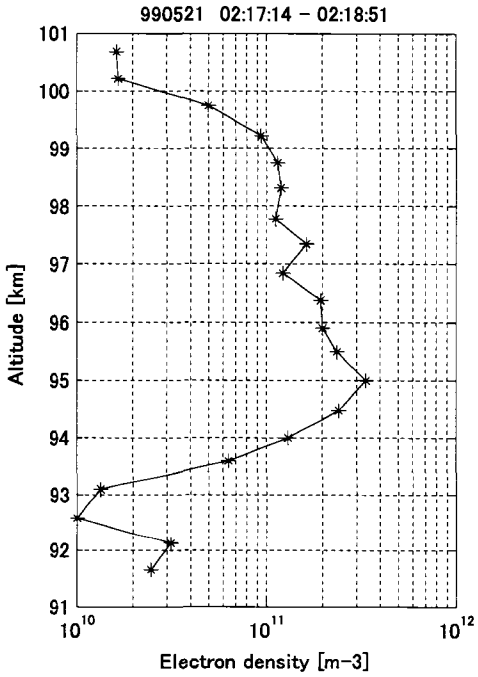

(c) Electron density in the layer

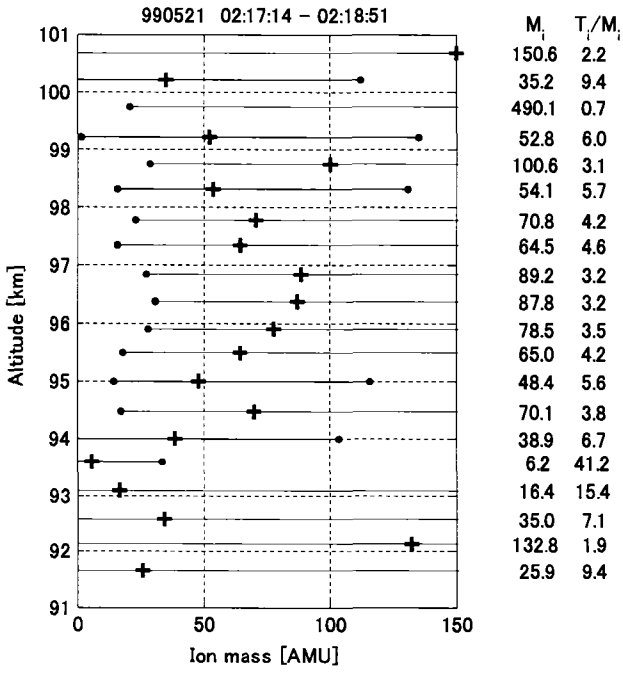

(d) Ion mass in the layer

Fig. 6.25 Ion mass estimation in the layer during 2:17-2:18UT on May 21st 1999.

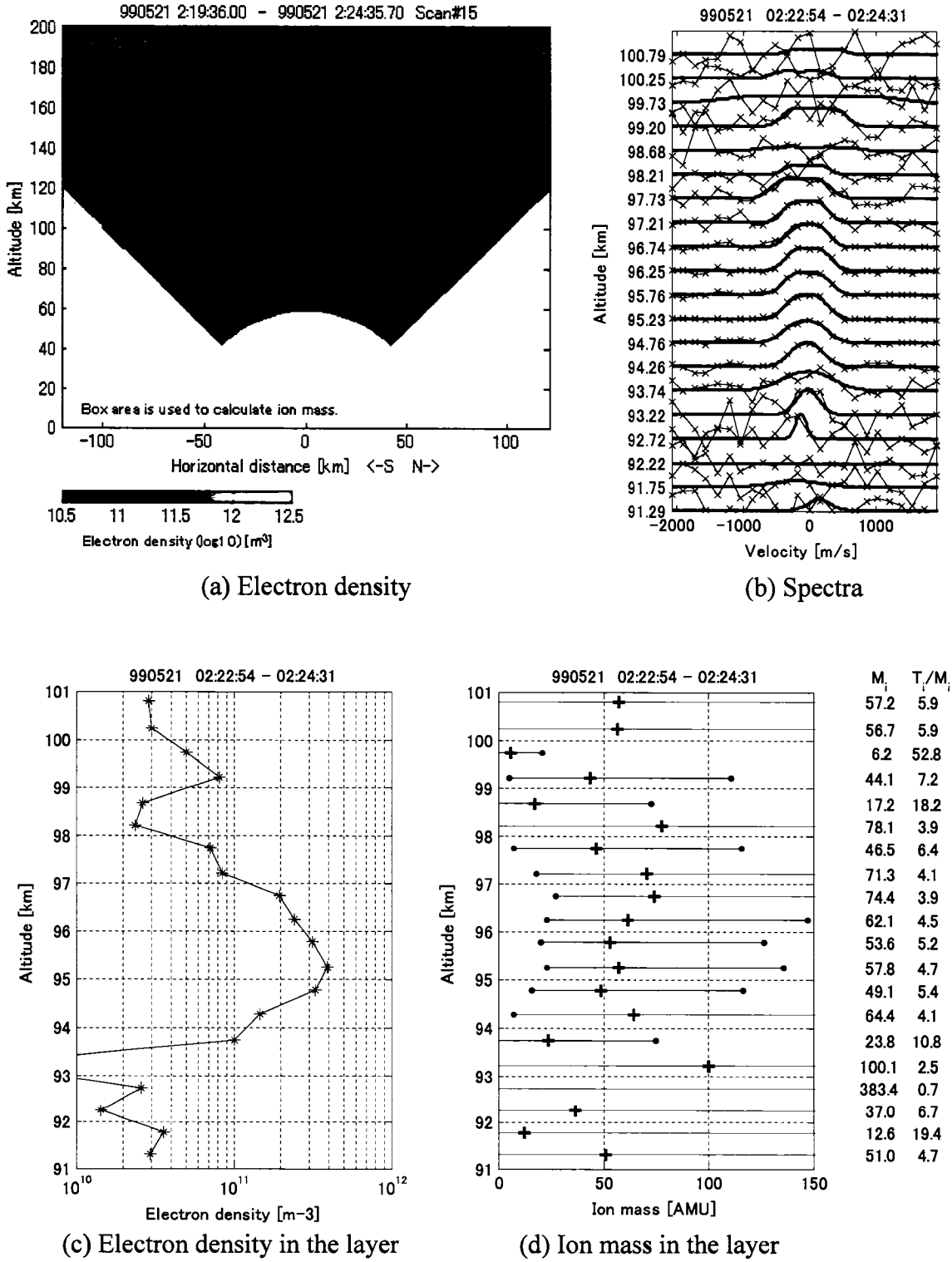

Fig. 6.26 Ion mass estimation in the layer during 2:22-2:24UT on May 21st 1999.

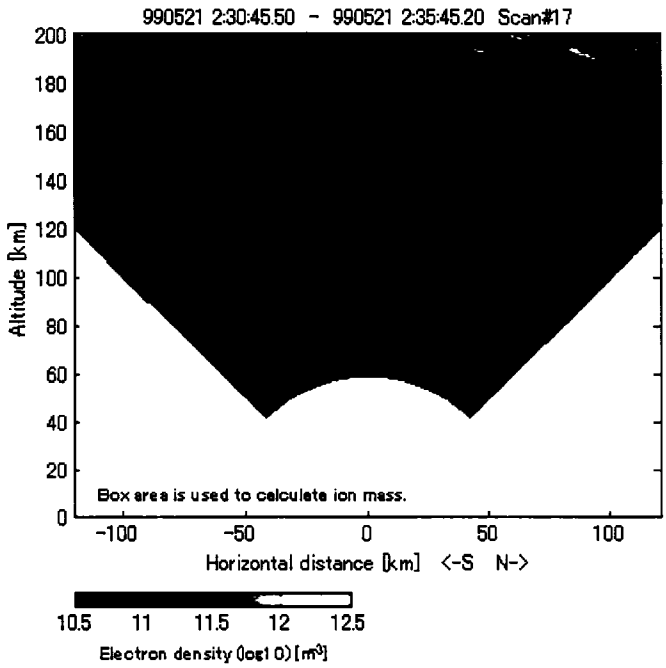

(a) Electron density

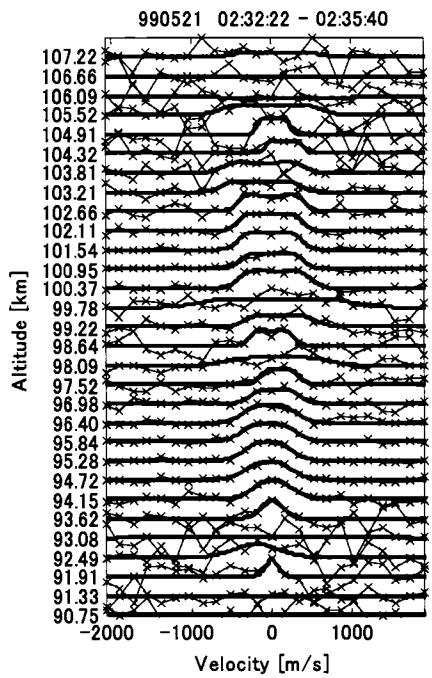

(b) Spectra

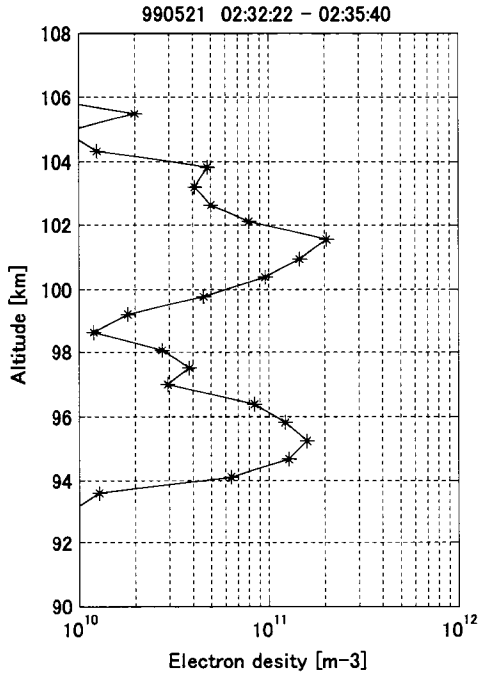

(c) Electron density in the layer

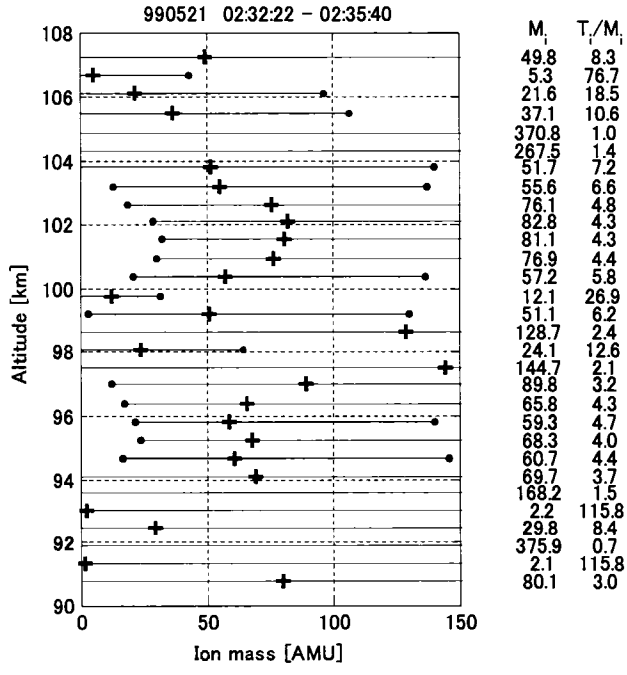

(d) Ion mass in the layer

Fig. 6.27 Ion mass estimation in the layer during 2:32-2:35UT on May 21st 1999.

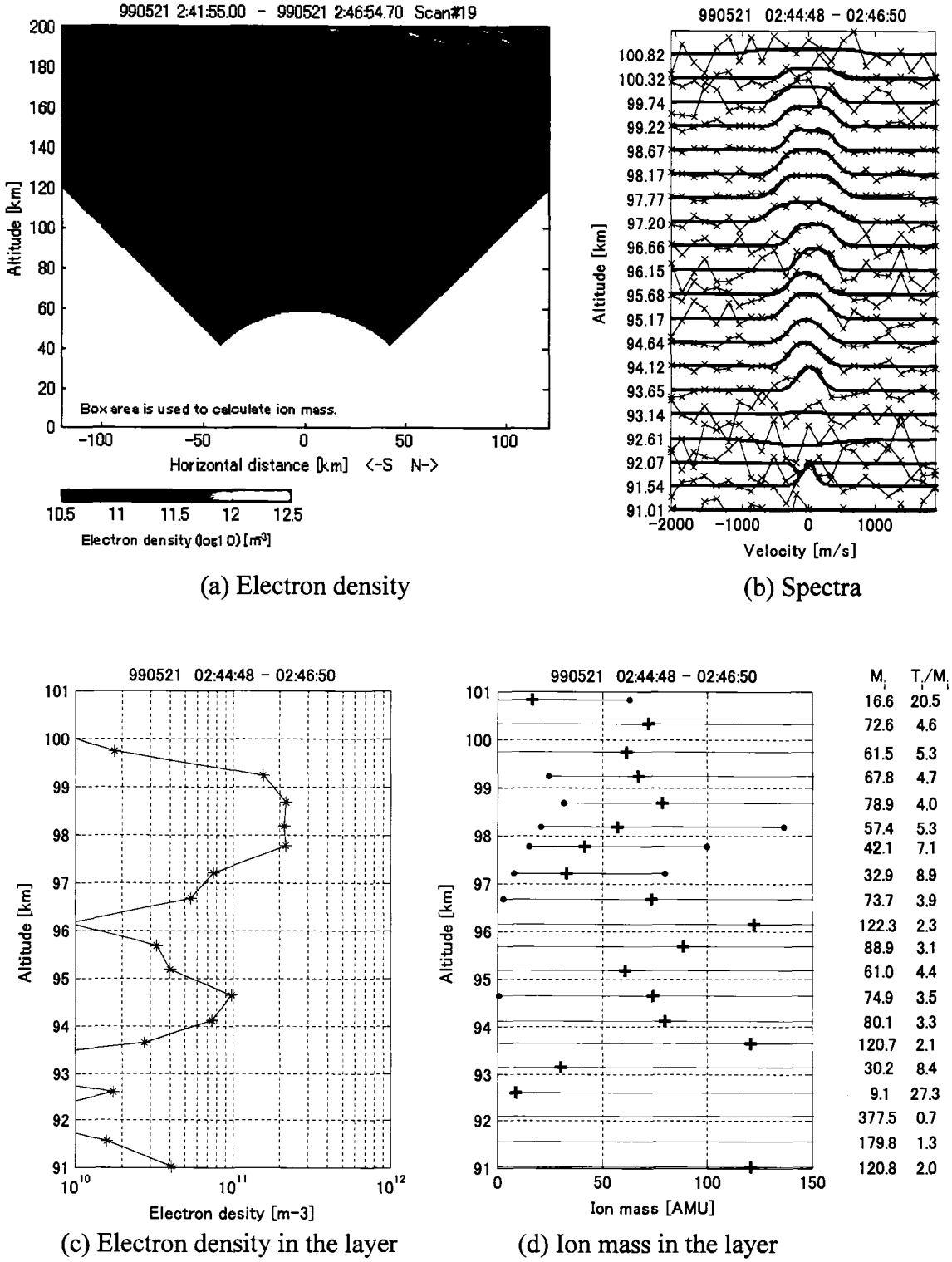

(a) Electron density (b) Spectra

(c) Electron density in the layer (d) Ion mass in the layer

Fig. 6.28 Ion mass estimation in the layer during 2:44-2:46UT on May 21st 1999.

6.2.3 Jul. 16th 1997

A weak layer first appeared at 22:11UT on Jul. 16th 1997. After several appearances and disappearances of this weak layer, a strong thick layer appeared at 0:29 UT as shown in Fig. 6.32. The electron density profile shown in Fig. 6.32(c) indicates that this strong layer seems to be a defective double layer. A significant double layer appeared at 0:41 UT as shown in Fig.6.33, of which the upper layer was "tilted". There are two explanations for this phenomenon; perhaps the tilted layer really existed, or perhaps the apparent tilt was the result of vertical movement of the layer during the observation. Since a single scan takes approximately five minutes, vertical movement of the layer may cause an apparent tilted layer on the electron density plot. If the latter explanation is true, the rate of vertical layer motion can be calculated from the tilt angle. The rate of layer motion in Fig.6.33 is about 10km/min upward. The tilted layer appeared again at 0:52 UT and soon disappeared. Temperature profile estimation was carried out using an unmodulated long pulse mode as shown in Fig.6.29, since the SNR of the coded short pulse mode was too low.

In the defective double layer presented in Fig.6.32, the ion mass of the upper part seems to be slightly heavier than that of the lower part, although the estimation error is relatively large. In the tilted layer in Fig.6.33 and Fig.6.34, the SNR was low because integration was carried out horizontally and it is therefore difficult to assess the ion mass.

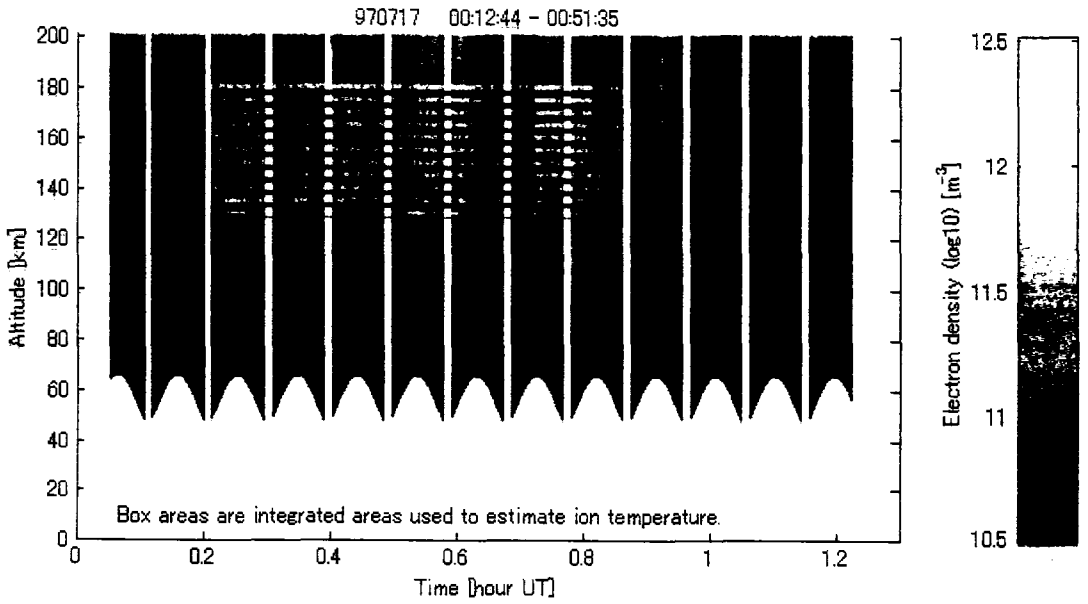

(a) Electron density

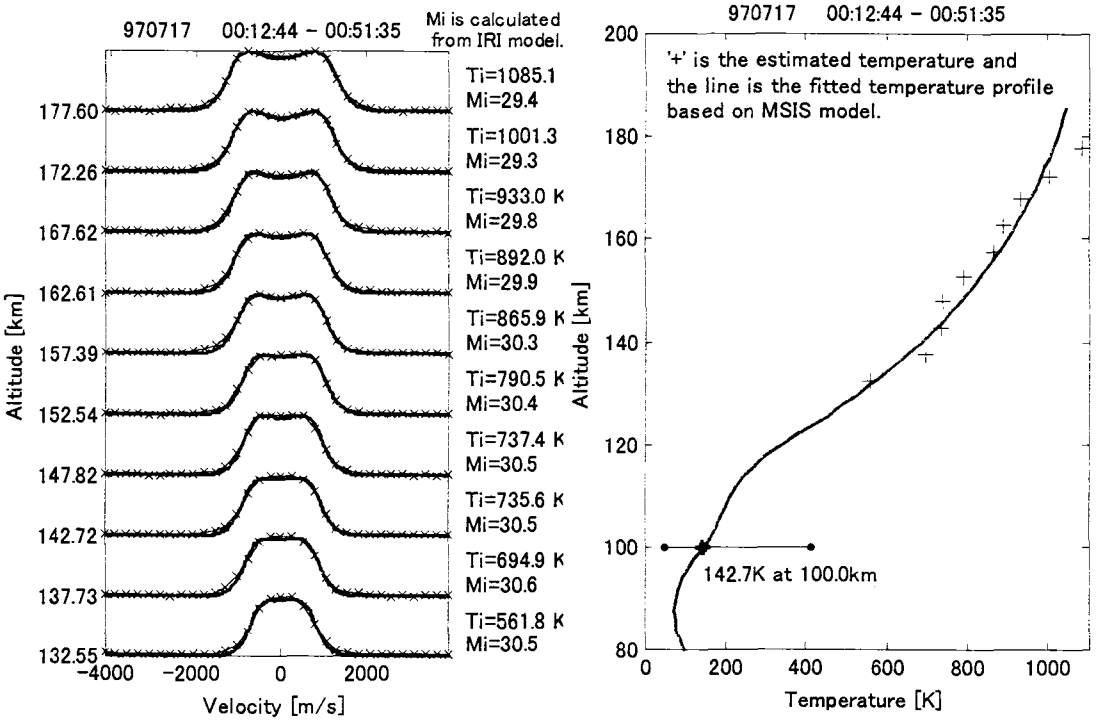

(b) Spectra (c) Ion temperature

Fig. 6.29 Ion temperature estimation using the long pulse mode on Jul. 17th 1997.

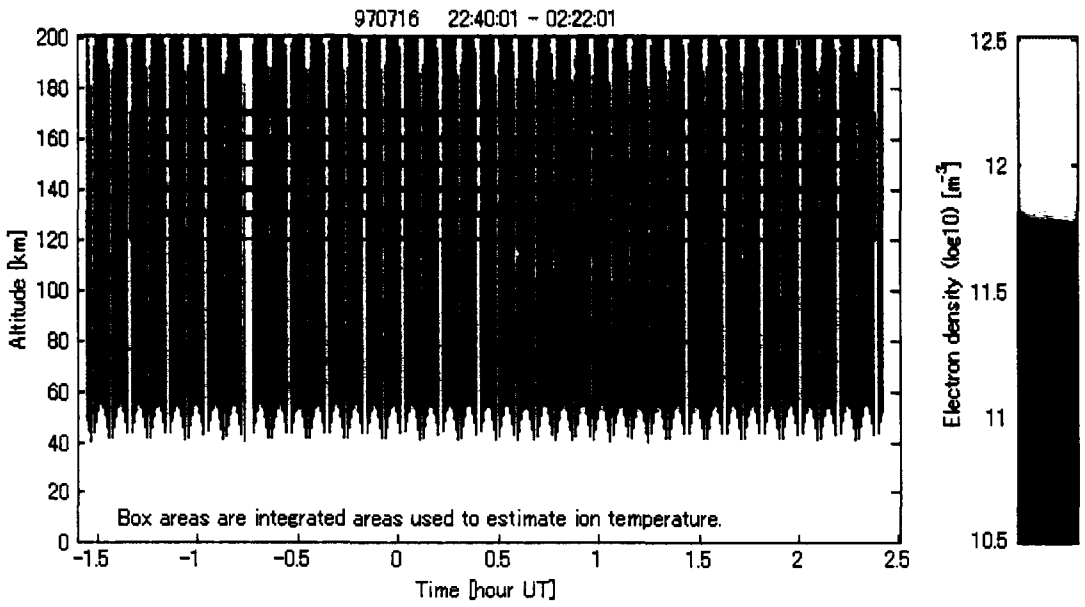

(a) Electron density

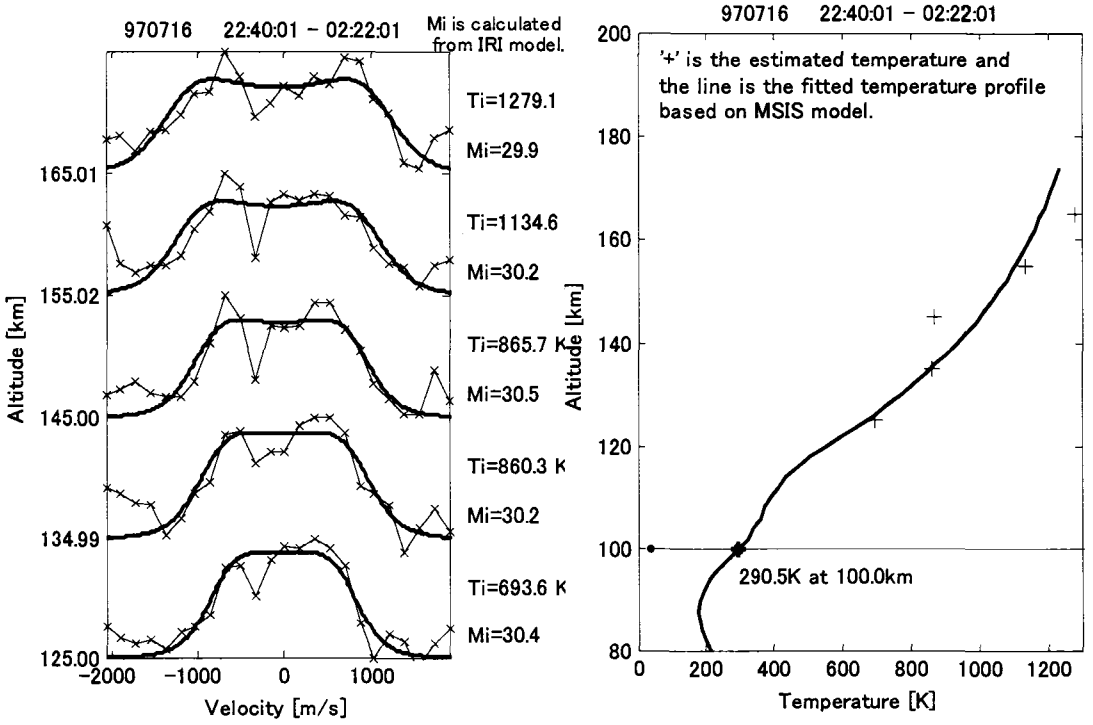

(b) Spectra (c) Ion temperature

Fig. 6.30 Ion temperature estimation using the short pulse mode on Jul. 17th 1997.

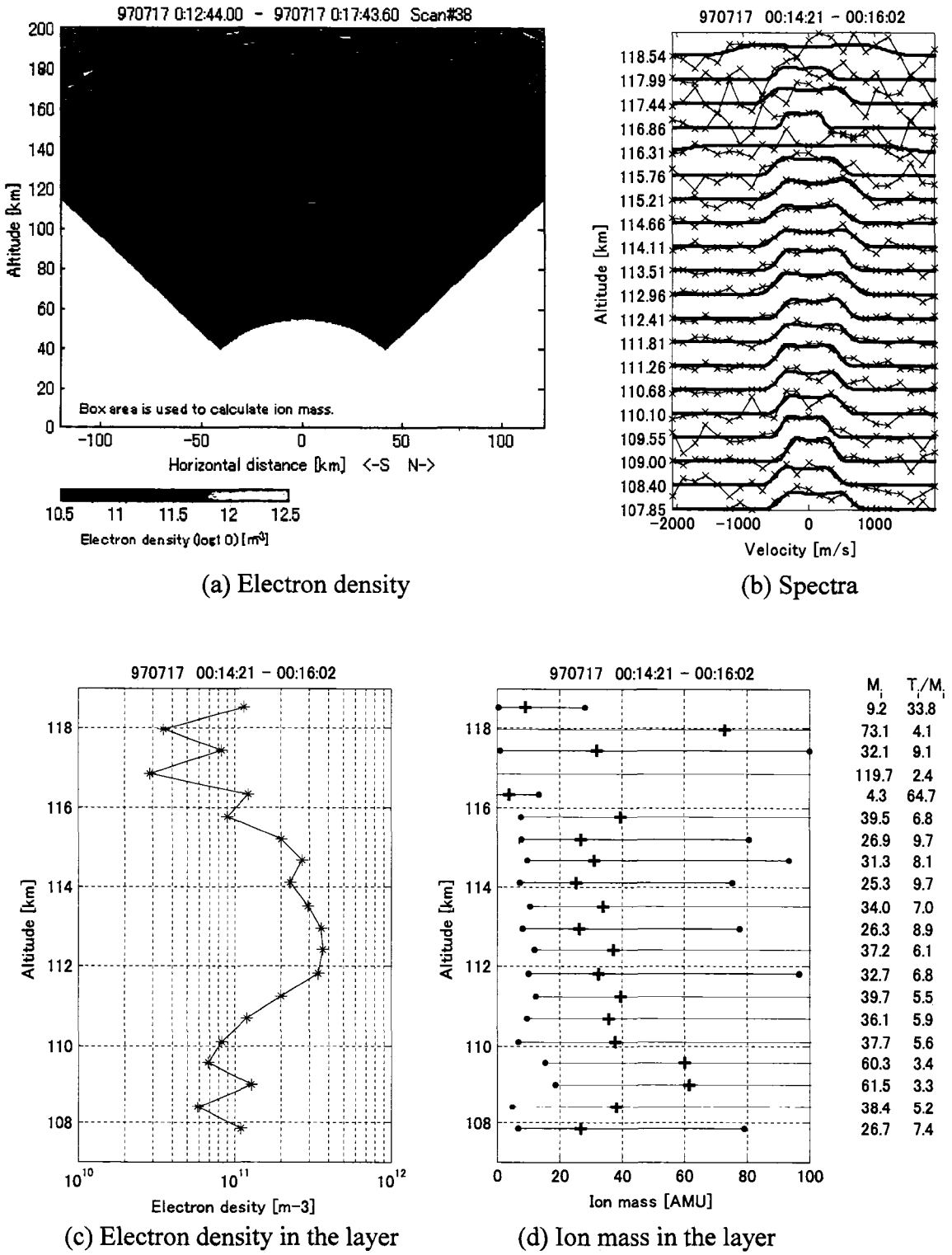

Fig. 6.31 Ion mass estimation in the layer during 0:14-0:16UT on Jul. 17th 1997.

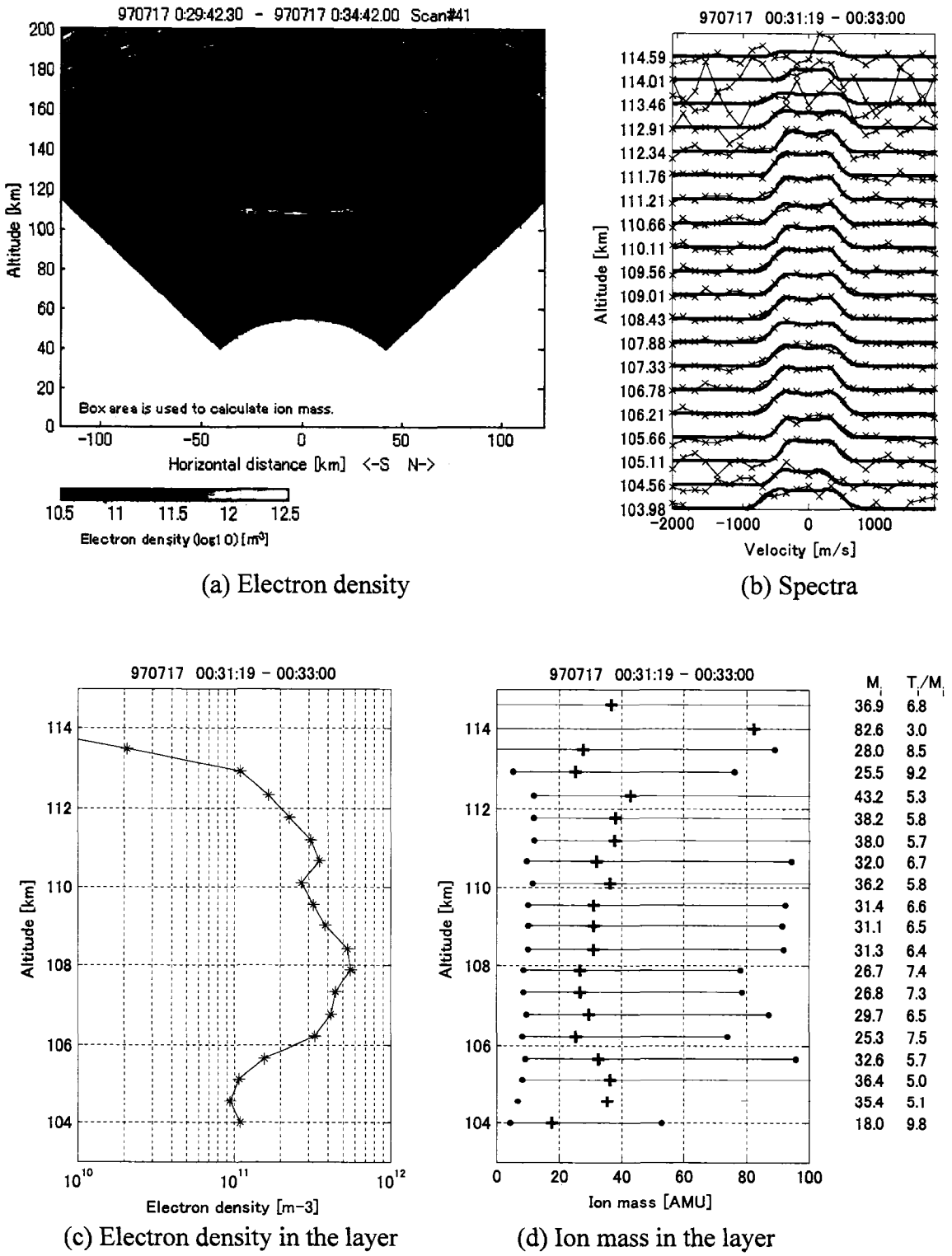

Fig. 6.32 Ion mass estimation in the layer during 0:31-0:33UT on Jul. 17th 1997.

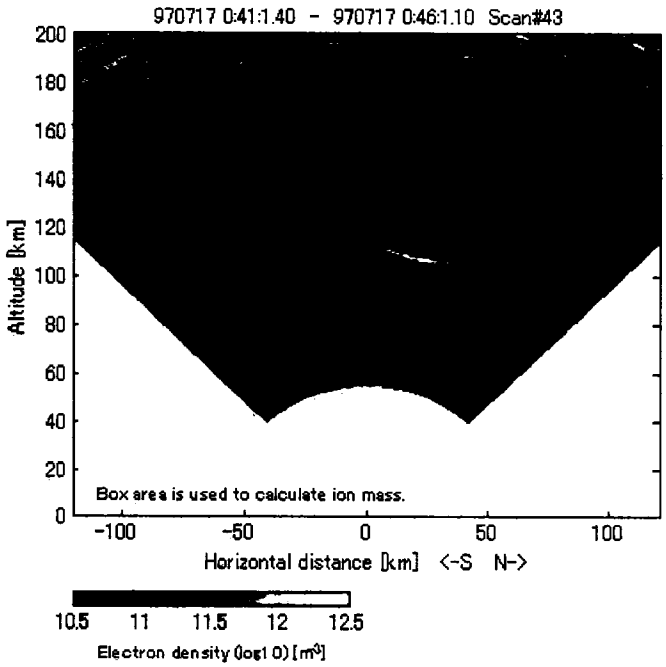

(a) Electron density

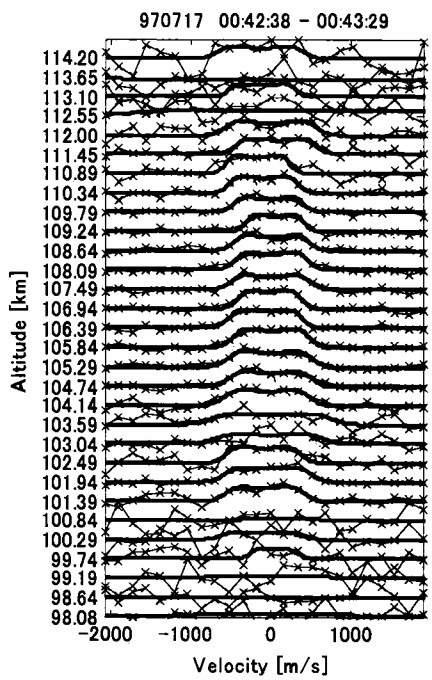

(b) Spectra

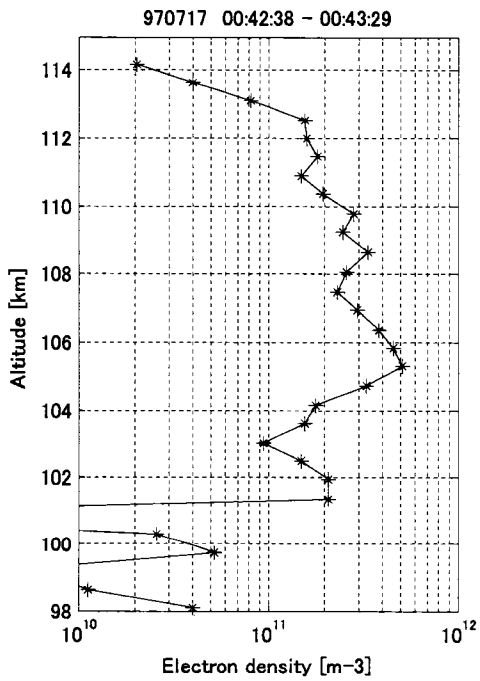

(c) Electron density in the layer

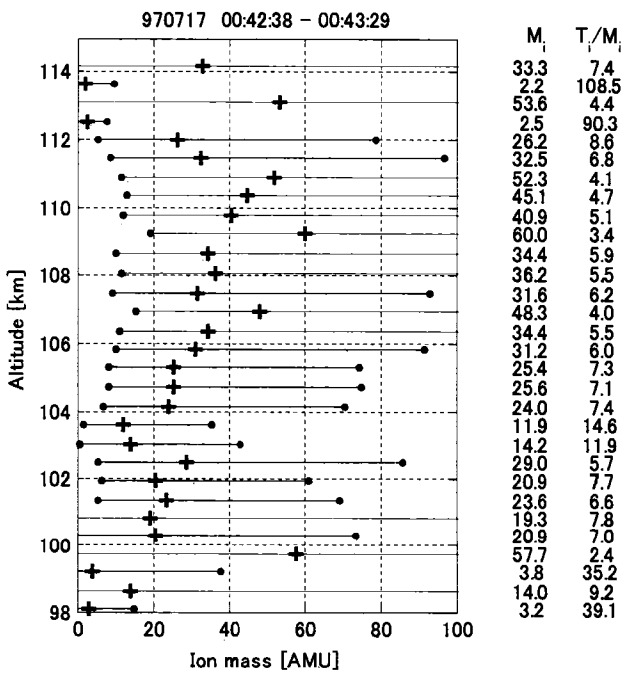

(d) Ion mass in the layer

Fig. 6.33 Ion mass estimation in the layer during 0:42-0:43UT on Jul. 17th 1997.

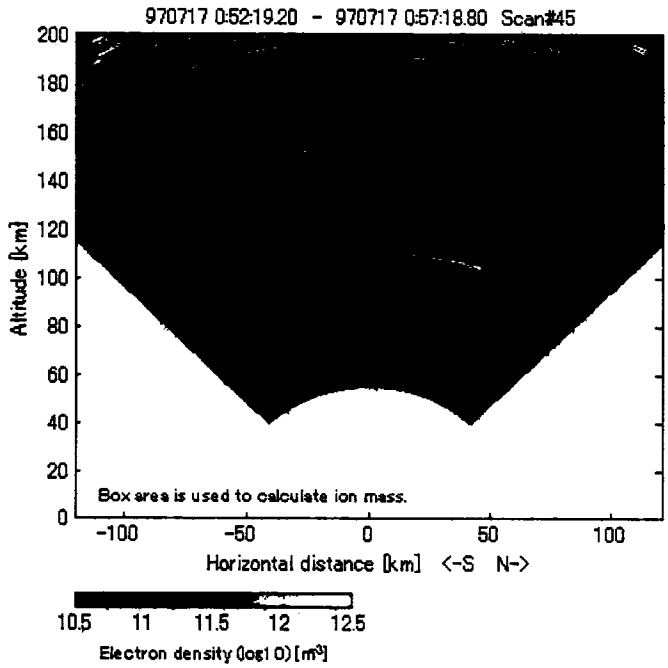

(a) Electron density

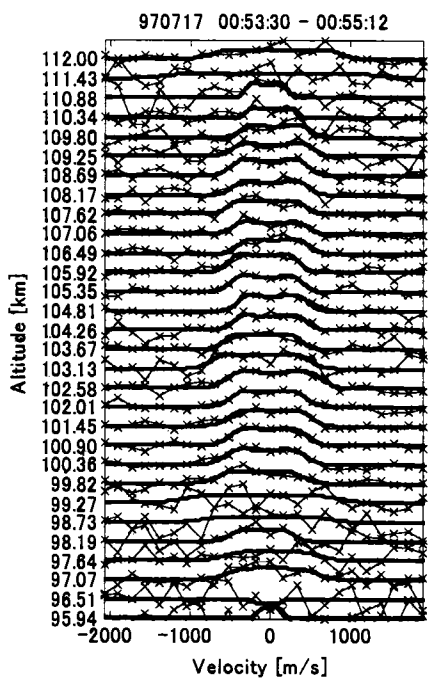

(b) Spectra

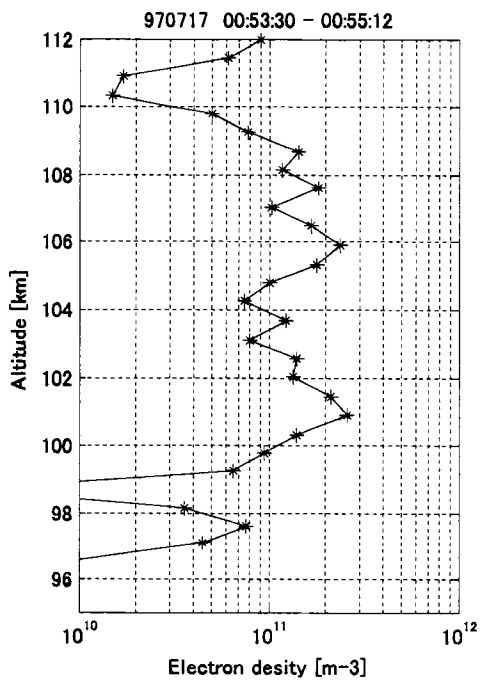

(c) Electron density in the layer

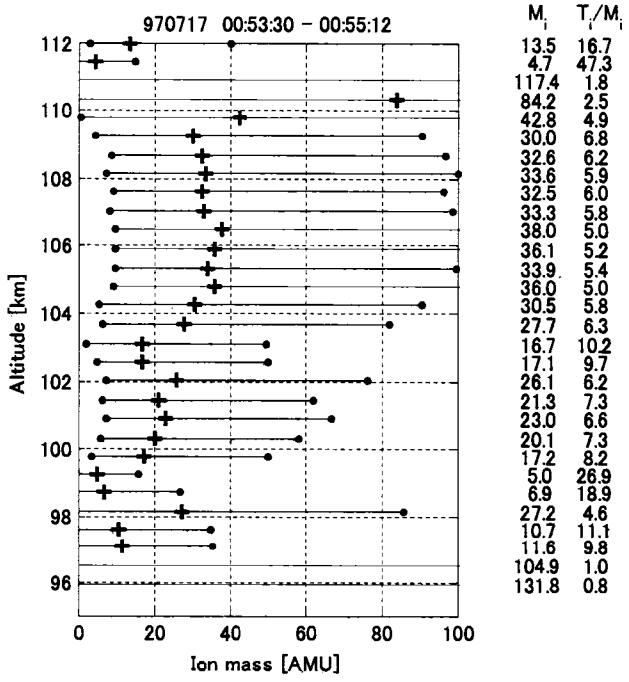

(d) Ion mass in the layer

Fig. 6.34 Ion mass estimation in the layer during 0:53-0:55UT on Jul. 17th 1997.

6.2.4 Jul. 19th 1996

A weak layer appeared at 22:32 UT on Jul. 19th 1996. This layer strengthened and weakened several times. At 23:17 UT (Fig.6.40) two layers occurred side by side at slightly different altitudes. The SNR of the coded short pulse mode was too low to allow an estimation of ion temperature so the unmodulated long pulse mode was used.

Examining the ion mass plot, several cases are evident in which ion mass in the top part of the layer is larger than in the bottom part, although in the case of the two layers in Fig.6.40, the low SNR makes it difficult to say anything about the ion mass tendency.

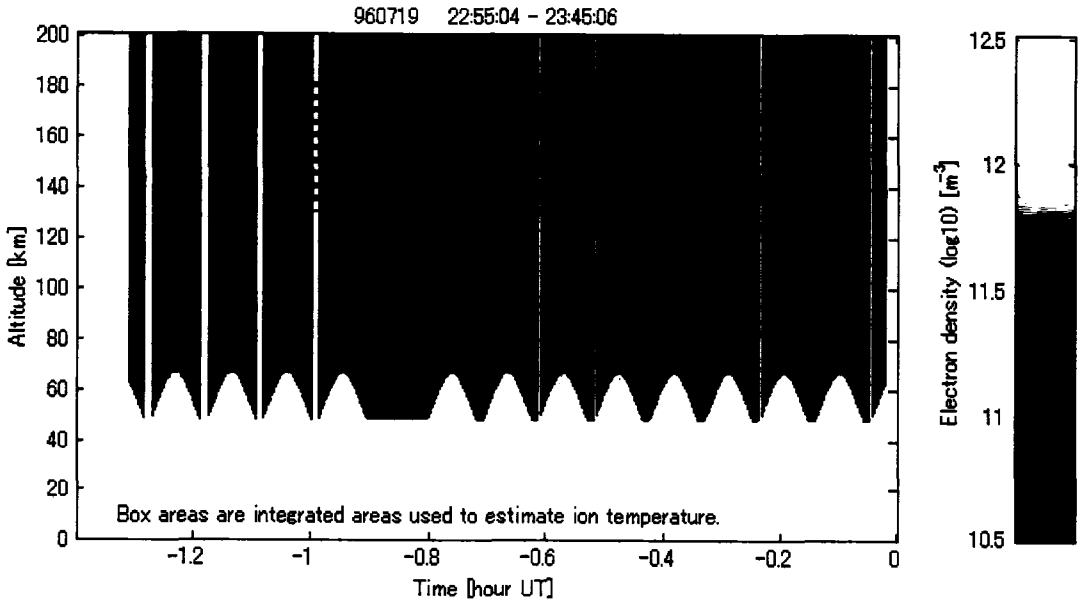

(a) Electron density

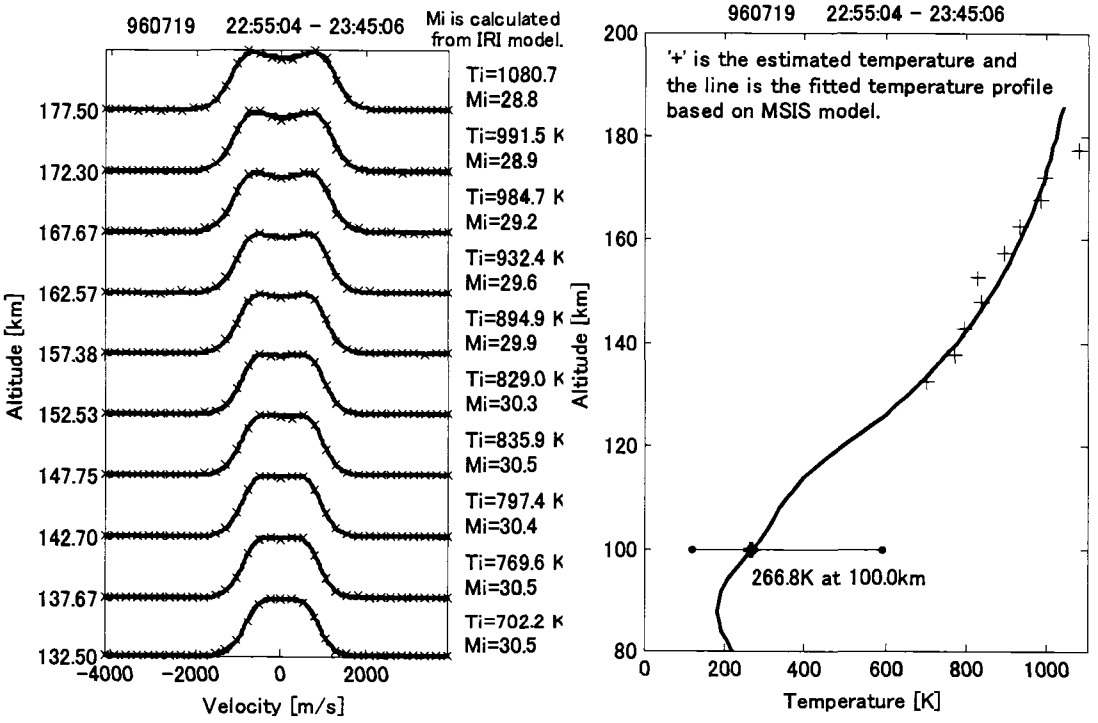

(b) Spectra

(c) Ion temperature

Fig. 6.35 Ion temperature estimation using the long pulse mode on Jul. 19th 1996.

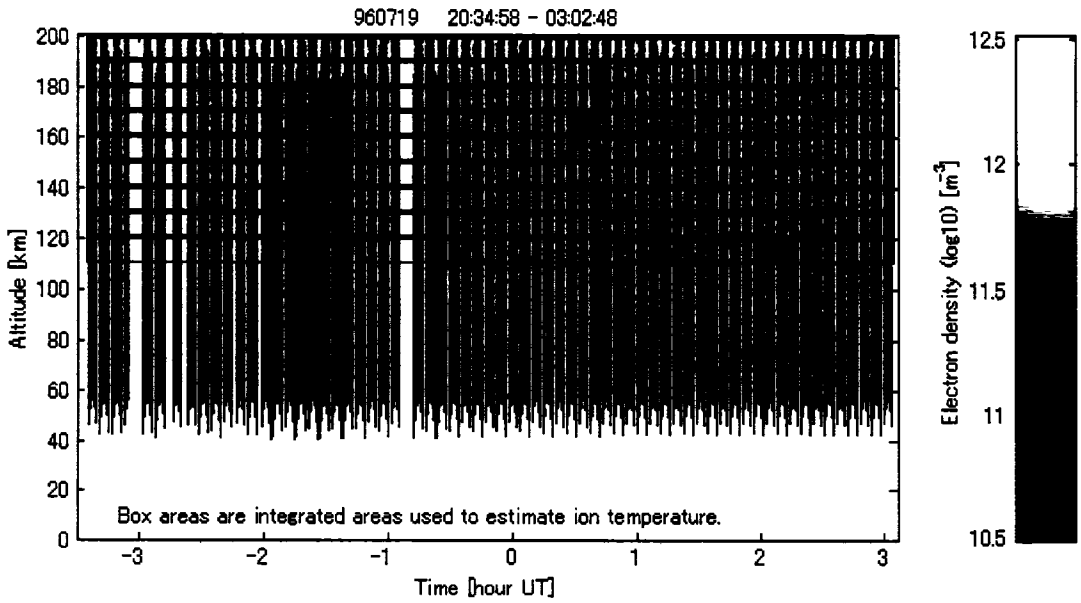

(a) Electron density

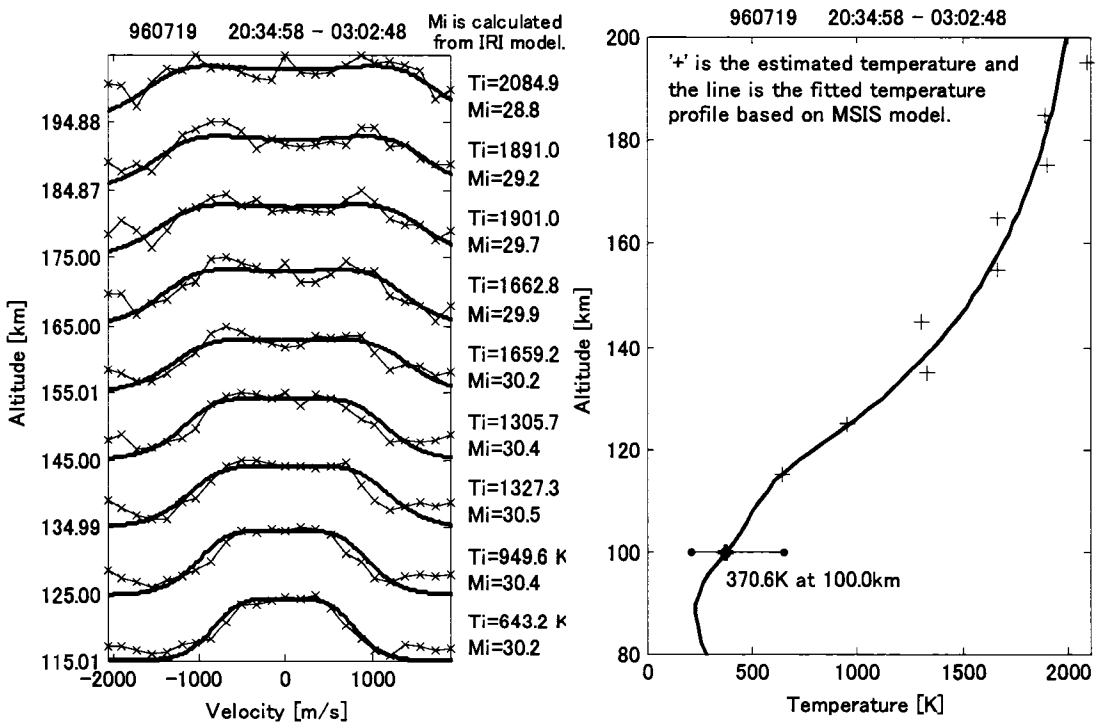

(b) Spectra (c) Ion temperature

Fig. 6.36 Ion temperature estimation using the short pulse mode on Jul. 19th 1996.

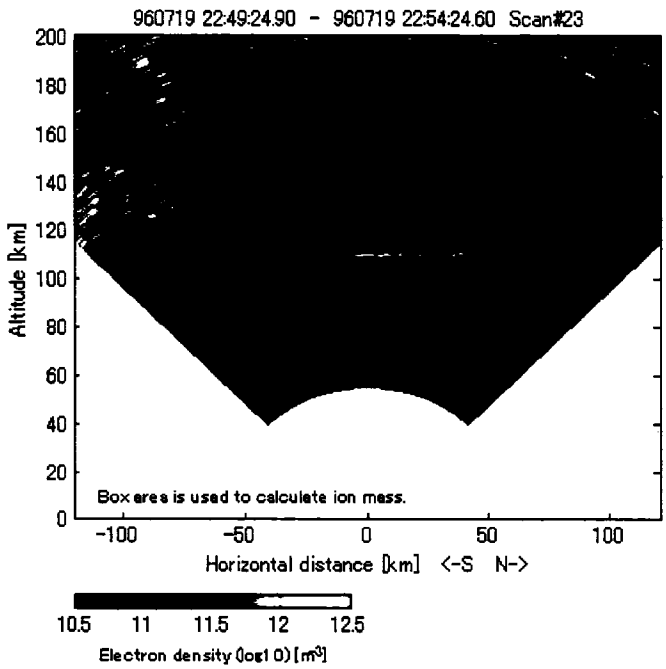

(a) Electron density

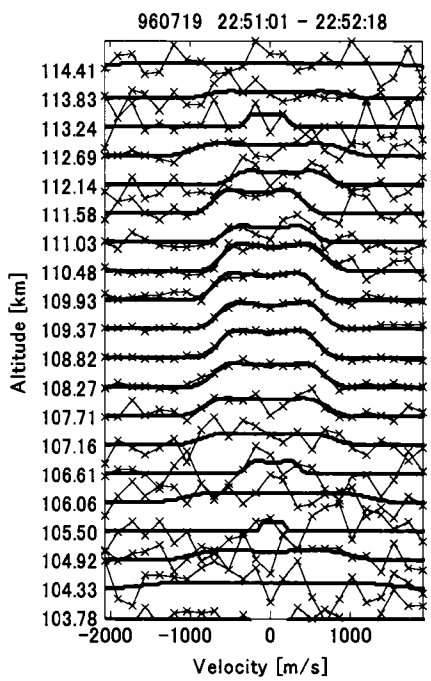

(b) Spectra

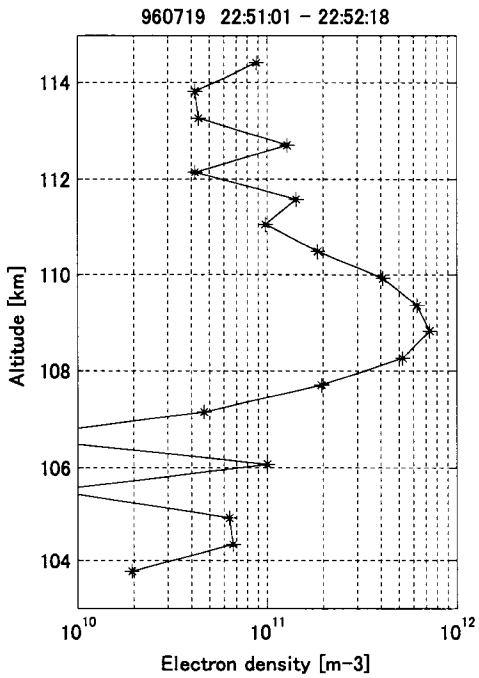

(c) Electron density in the layer

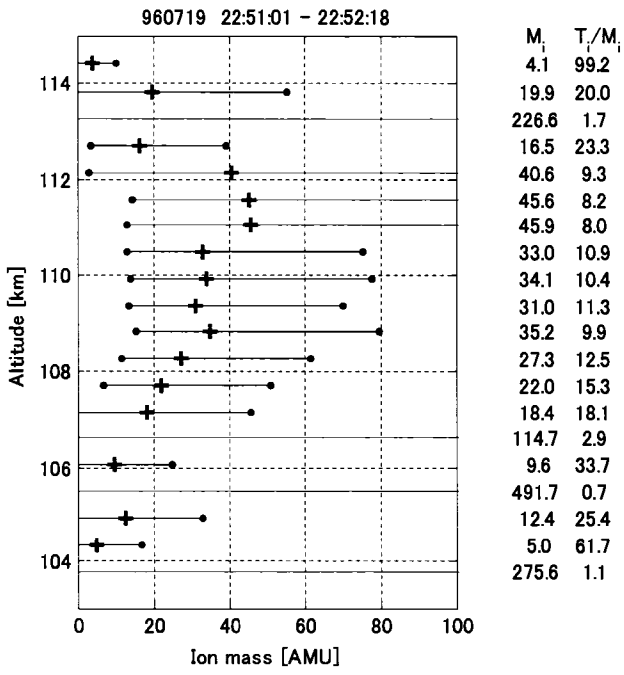

M_i	T_i/M_i
4.1	99.2
19.9	20.0
226.6	1.7
16.5	23.3
40.6	9.3
45.6	8.2
45.9	8.0
33.0	10.9
34.1	10.4
31.0	11.3
35.2	9.9
27.3	12.5
22.0	15.3
18.4	18.1
114.7	2.9
9.6	33.7
491.7	0.7
12.4	25.4
5.0	61.7
275.6	1.1

(d) Ion mass in the layer

Fig. 6.37 Ion mass estimation in the layer during 22:51-22:52UT on Jul. 19th 1996.

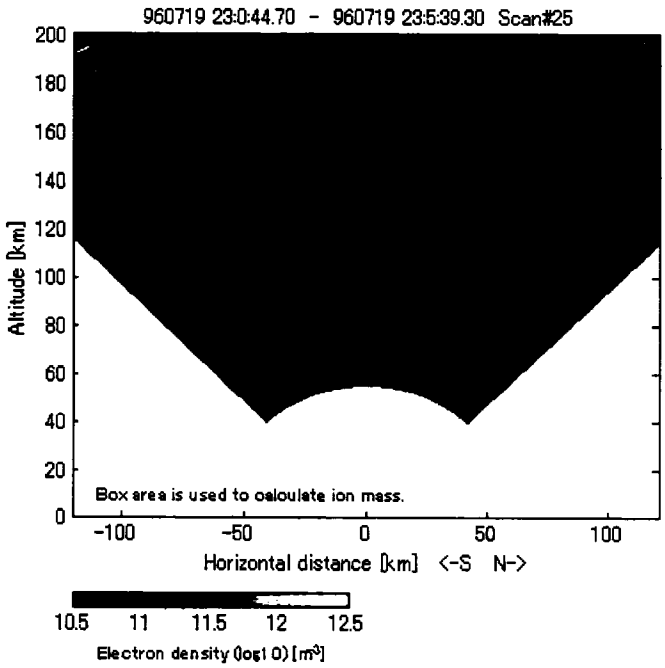

(a) Electron density

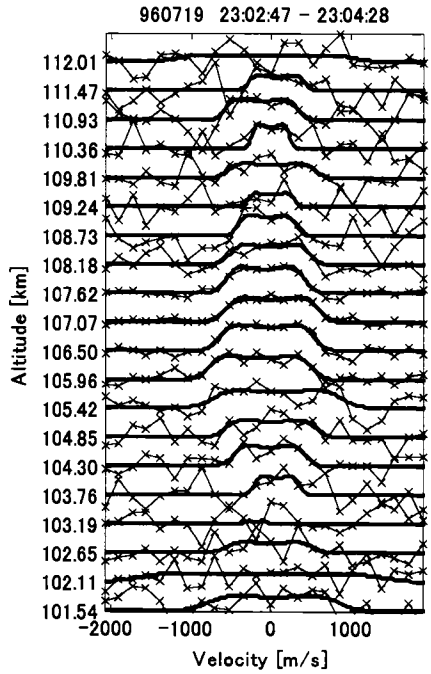

(b) Spectra

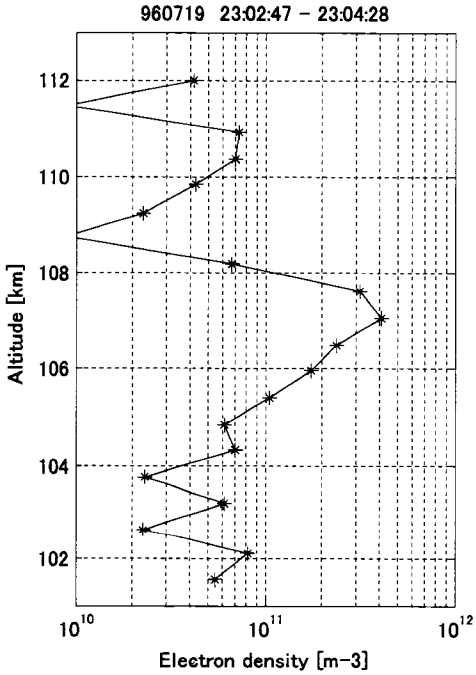

(c) Electron density in the layer

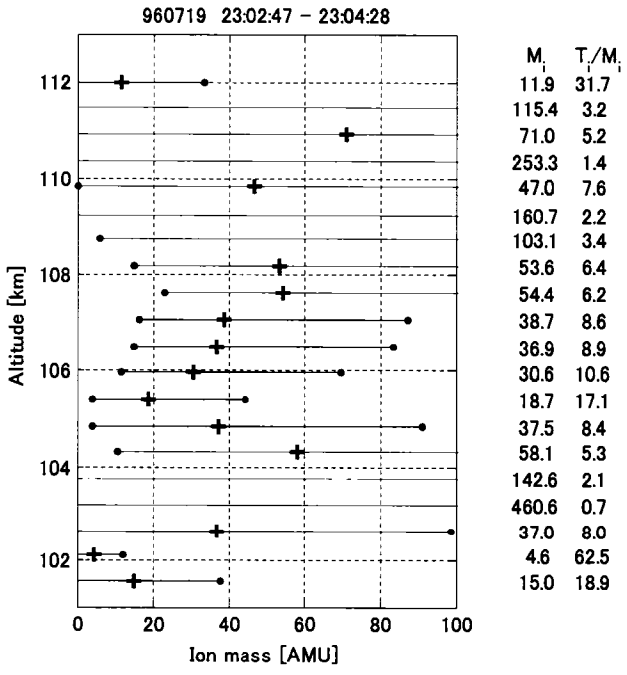

(d) Ion mass in the layer

Fig. 6.38 Ion mass estimation in the layer during 23:02-23:04UT on Jul. 19th 1996.

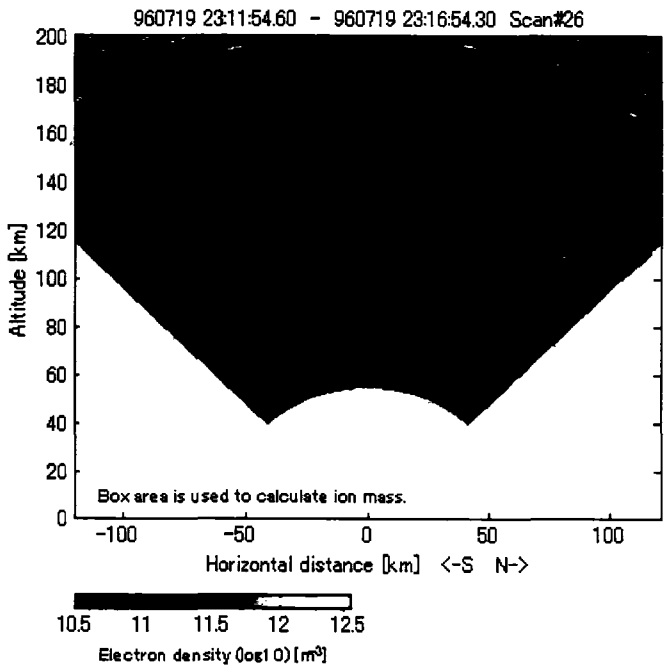

(a) Electron density

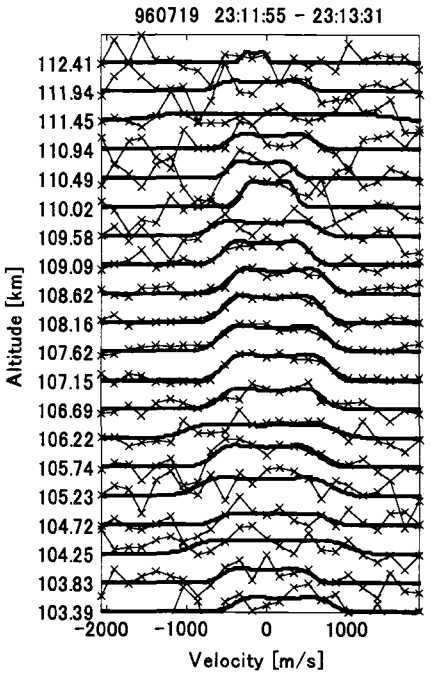

(b) Spectra

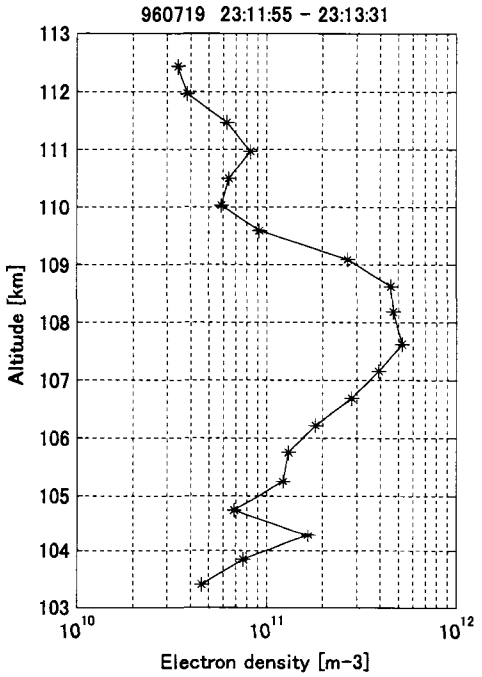

(c) Electron density in the layer

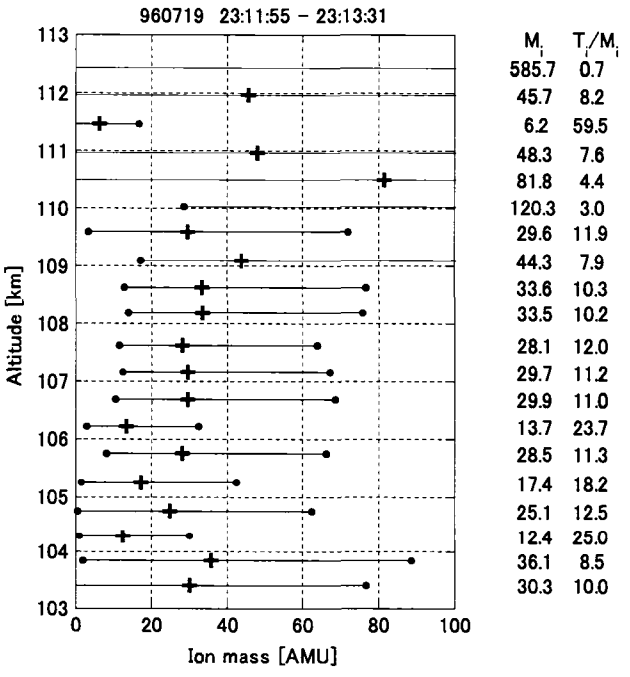

(d) Ion mass in the layer

Fig. 6.39 Ion mass estimation in the layer during 23:11-23:13UT on Jul. 19th 1996.

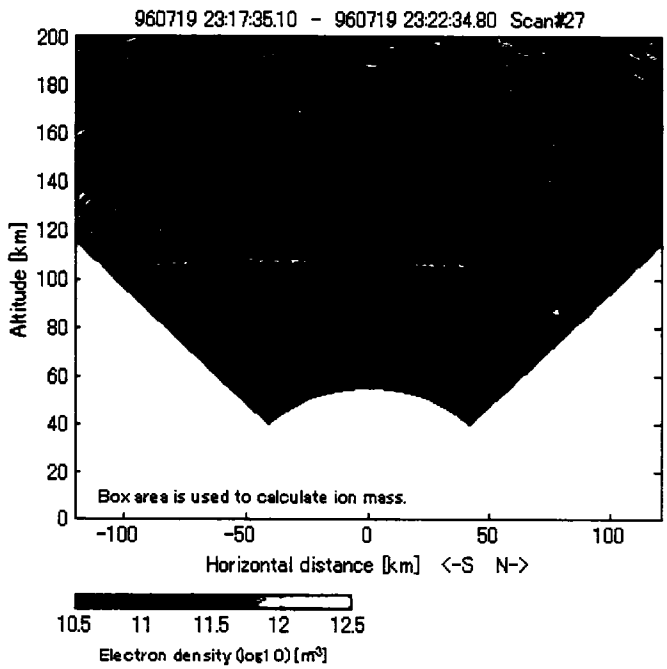

(a) Electron density

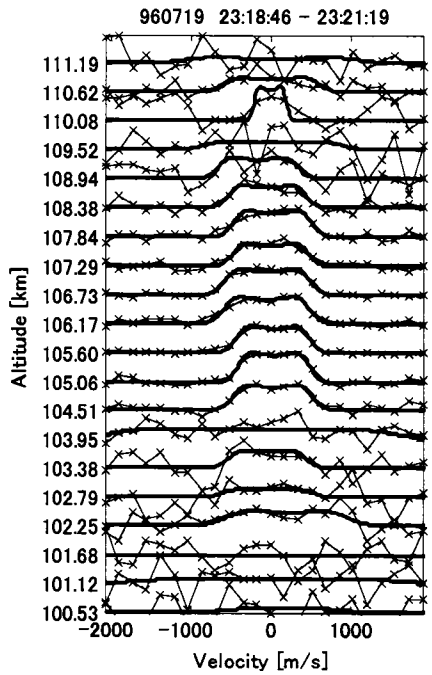

(b) Spectra

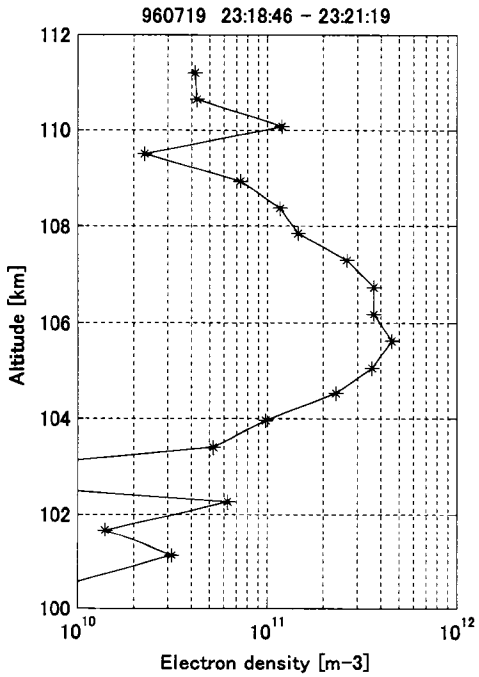

(c) Electron density in the layer

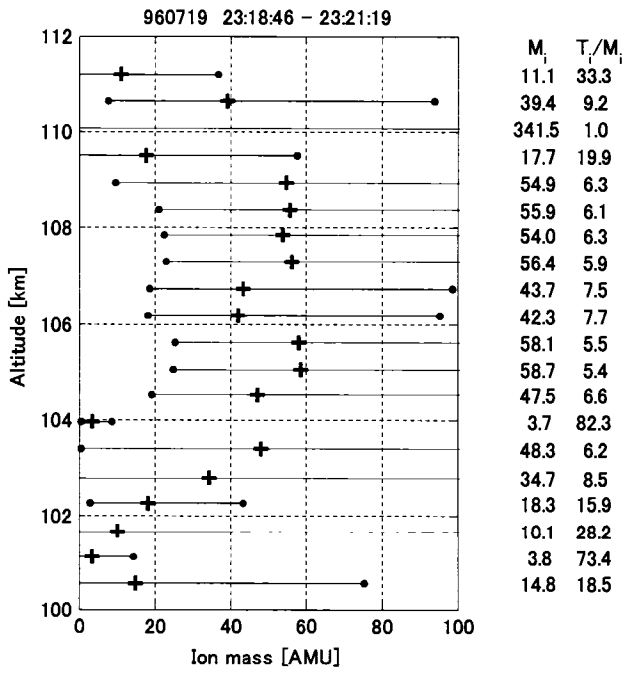

(d) Ion mass in the layer

Fig. 6.40 Ion mass estimation in the layer during 23:18-23:21UT on Jul. 19th 1996.

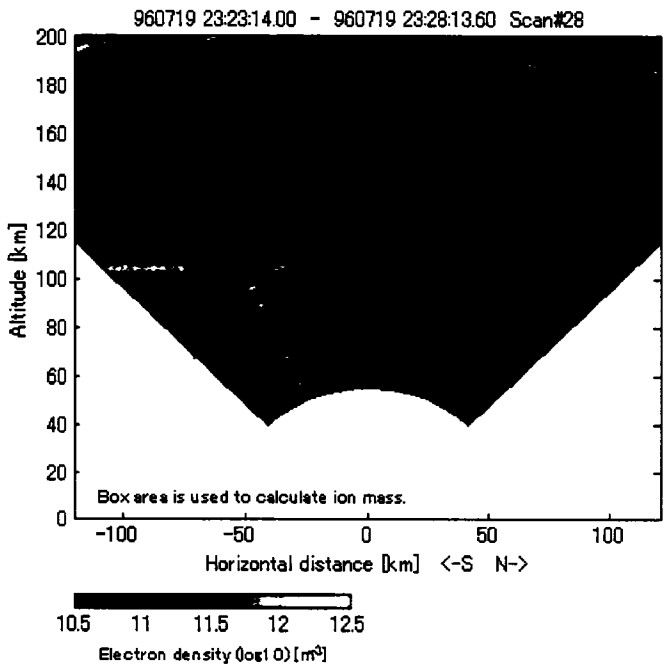

(a) Electron density

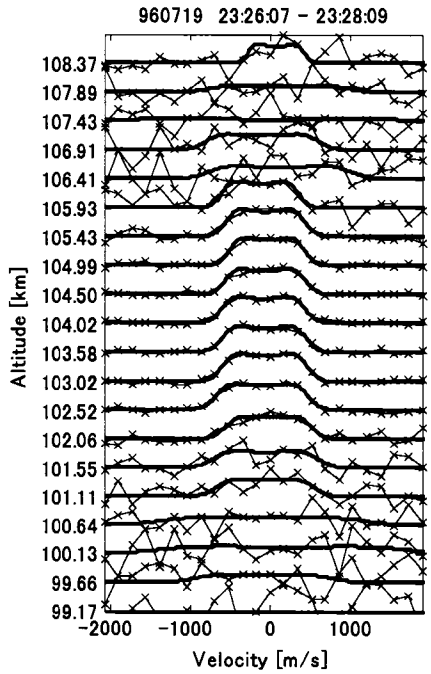

(b) Spectra

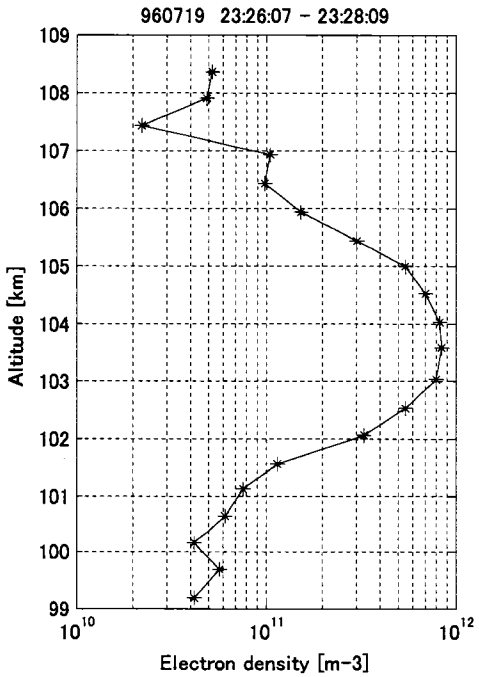

(c) Electron density in the layer

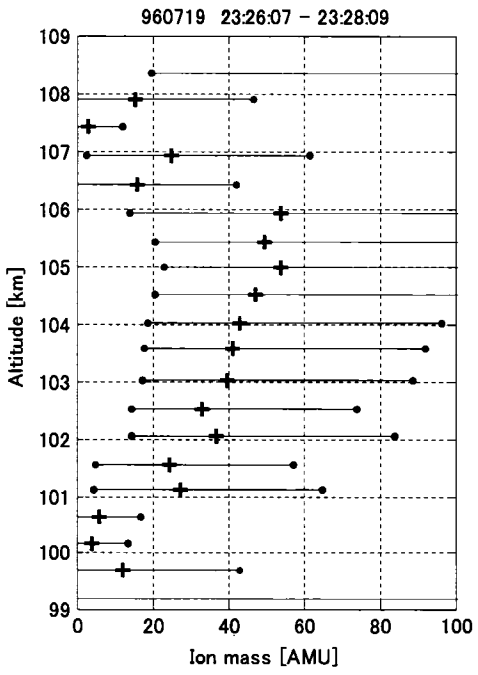

(d) Ion mass in the layer

M_i	T_i/M_i
108.3	3.4
7.2	51.3
8.1	44.9
3.4	105.6
34.4	10.3
76.6	4.5
39.7	8.7
44.3	7.7
62.5	5.4
46.6	7.1
41.1	8.0
35.0	9.2
29.1	11.0
38.3	8.3
12.5	24.9
7.7	39.7
35.4	8.5
29.5	10.1
9.2	31.7
294.7	1.0

Fig. 6.41 Ion mass estimation in the layer during 23:26-23:28UT on Jul. 19th 1996.

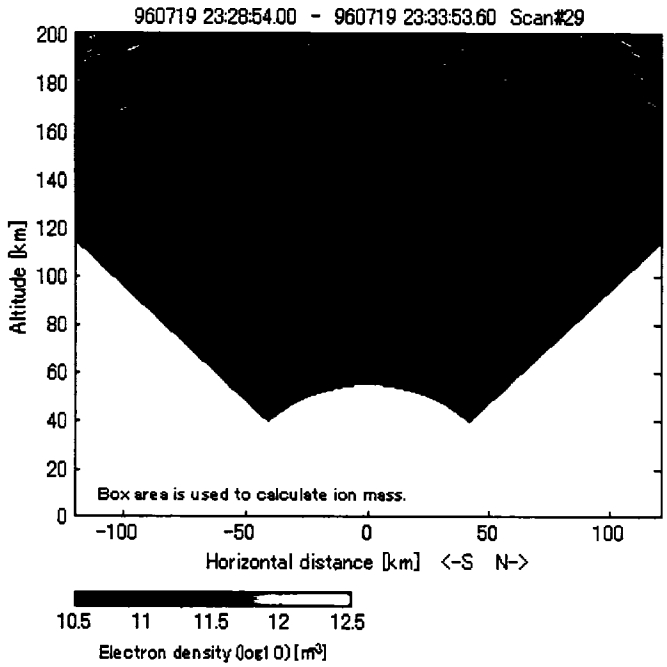

(a) Electron density

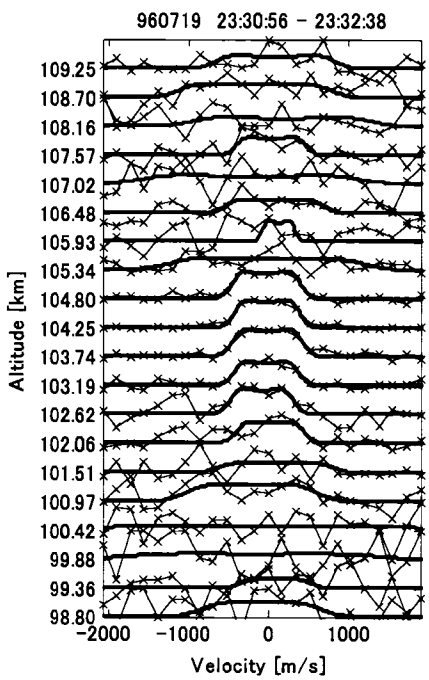

(b) Spectra

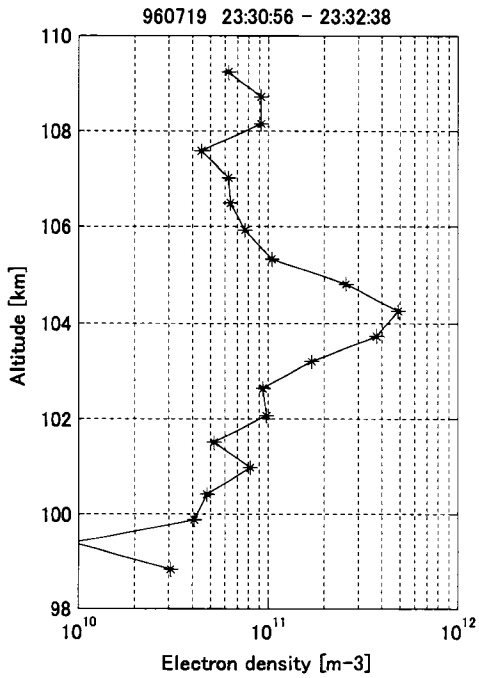

(c) Electron density in the layer

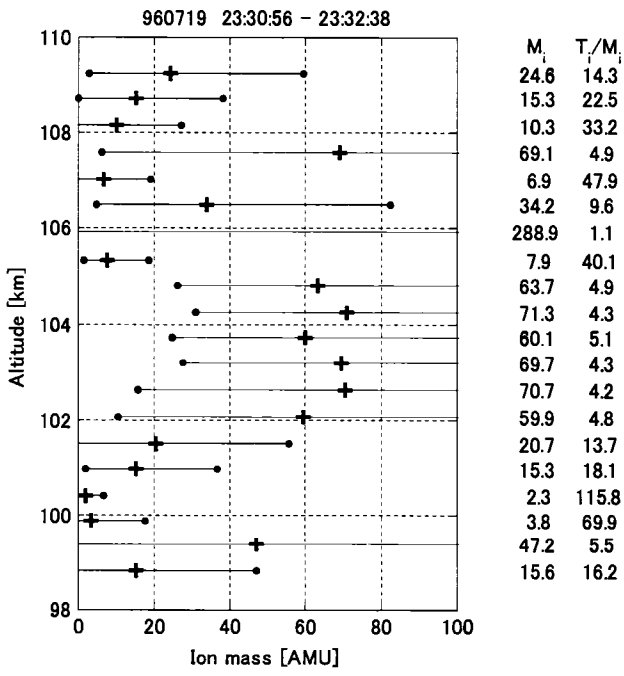

(d) Ion mass in the layer

Fig. 6.42 Ion mass estimation in the layer during 23:30-23:32UT on Jul. 19th 1996.

6.2.5 Jul. 8th 1996

A weak layer first appeared at 0:14 UT on Jul. 8th 1996. This layer strengthened and weakened several times, and then became thick at 2:13UT as shown in Fig. 6.48; a double layer appeared at 2:30UT. Since the layer thickened before the double layer appeared, this thickening may have been a precursor of double layer formation. Since the SNR of the coded short pulse mode was too low, the unmodulated long pulse mode was used for temperature estimation.

In the double layer case shown in Fig.6.50, the SNR unfortunately seems too low to discern ion mass. In other cases, it is difficult to determine the ion mass tendency. However there are some cases in which a tendency for ion mass in the top part of the layer is greater than in the bottom part can be seen, rather than a tendency of homogeneous ion mass, as shown in Figs.6.47, 6.48, and 6.49.

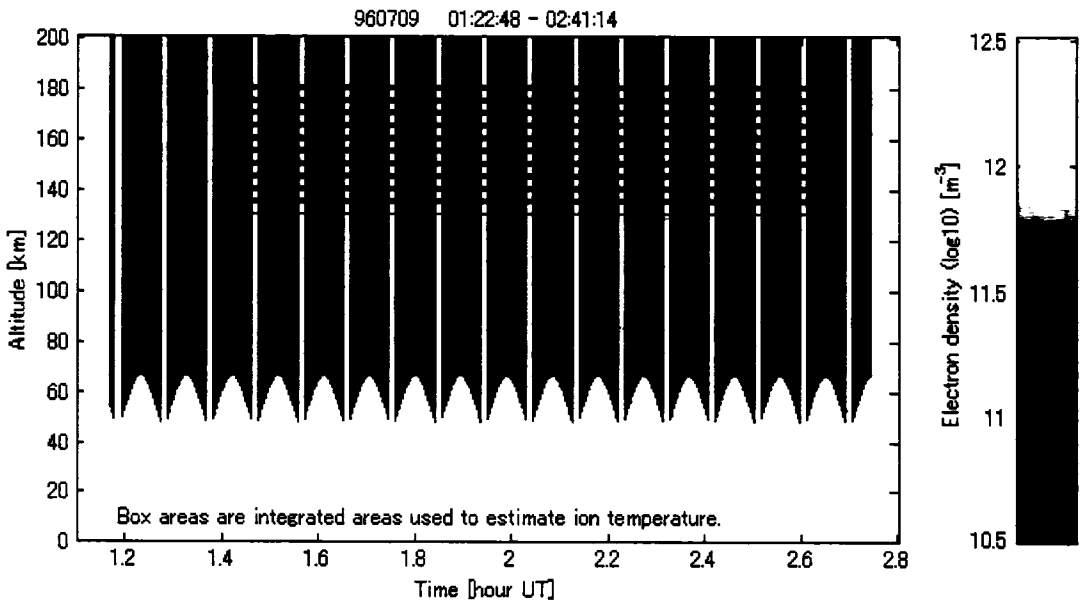

(a) Electron density

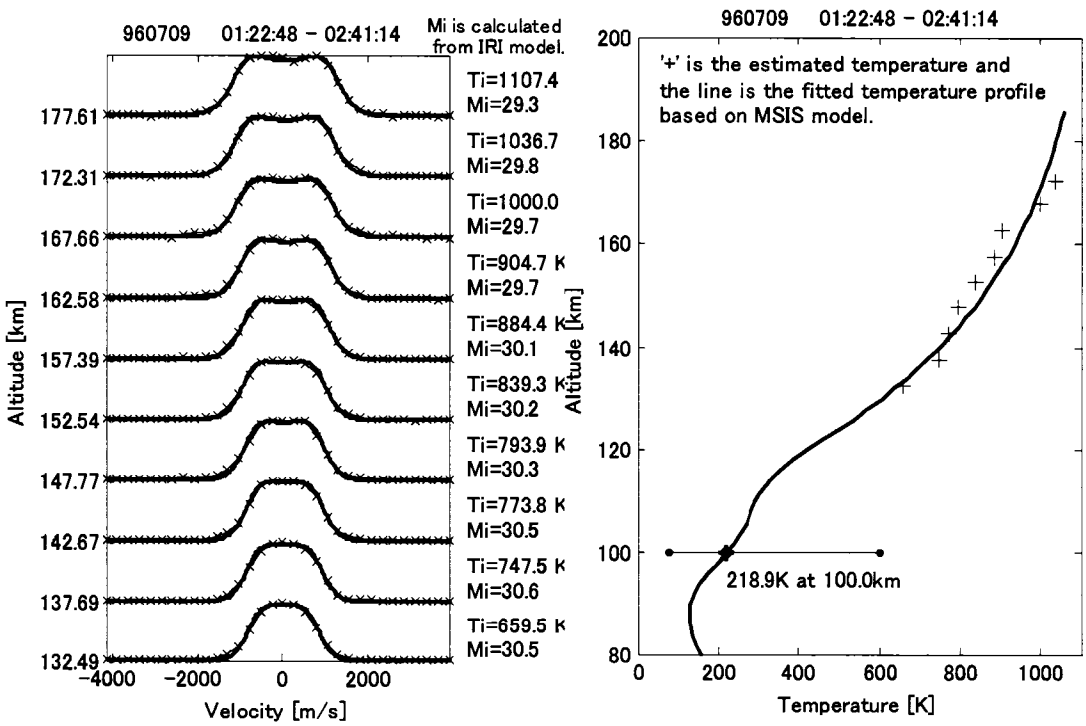

(b) Spectra (c) Ion temperature

Fig. 6.43 Ion temperature estimation using the long pulse mode on Jul. 9th 1996.

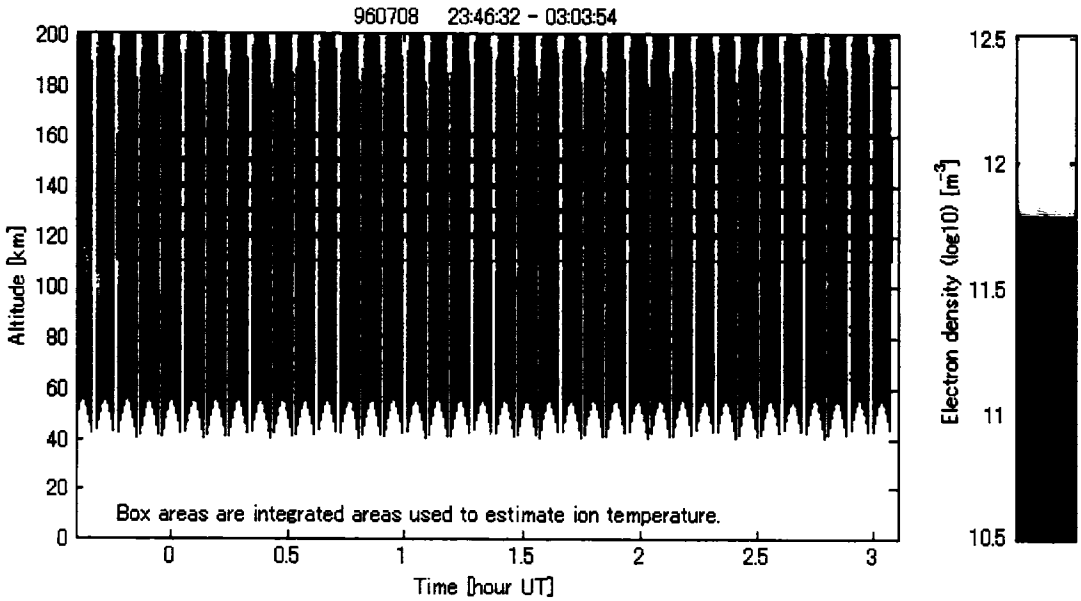

(a) Electron density

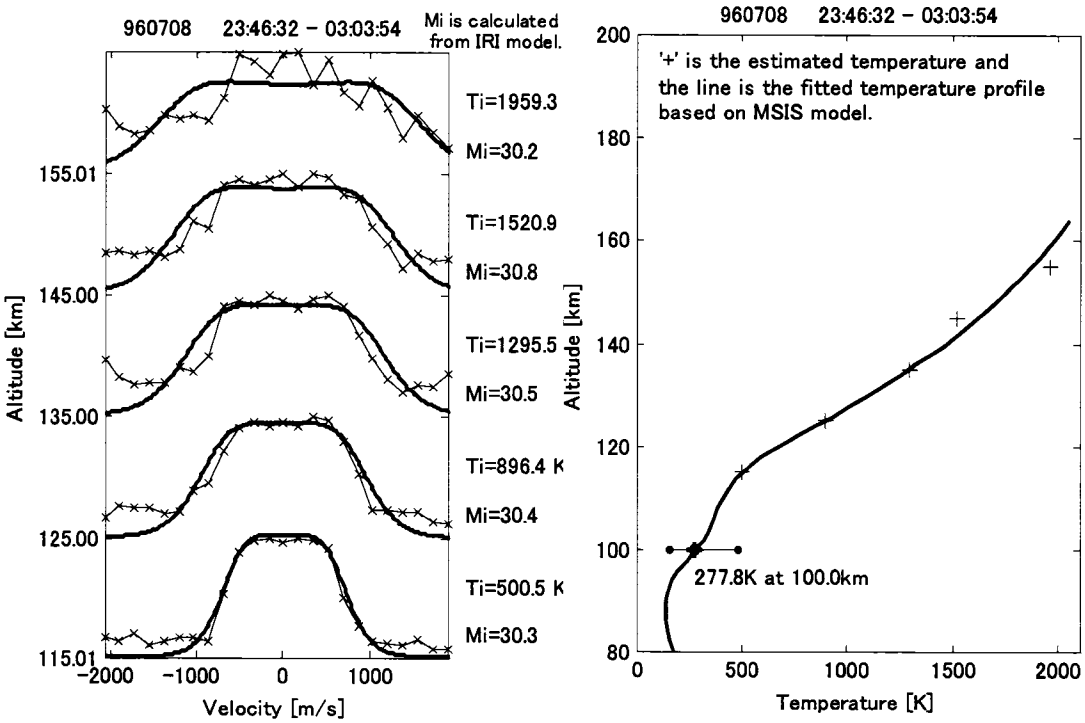

(b) Spectra (c) Ion temperature

Fig. 6.44 Ion temperature estimation using the short pulse mode on Jul. 9th 1996.

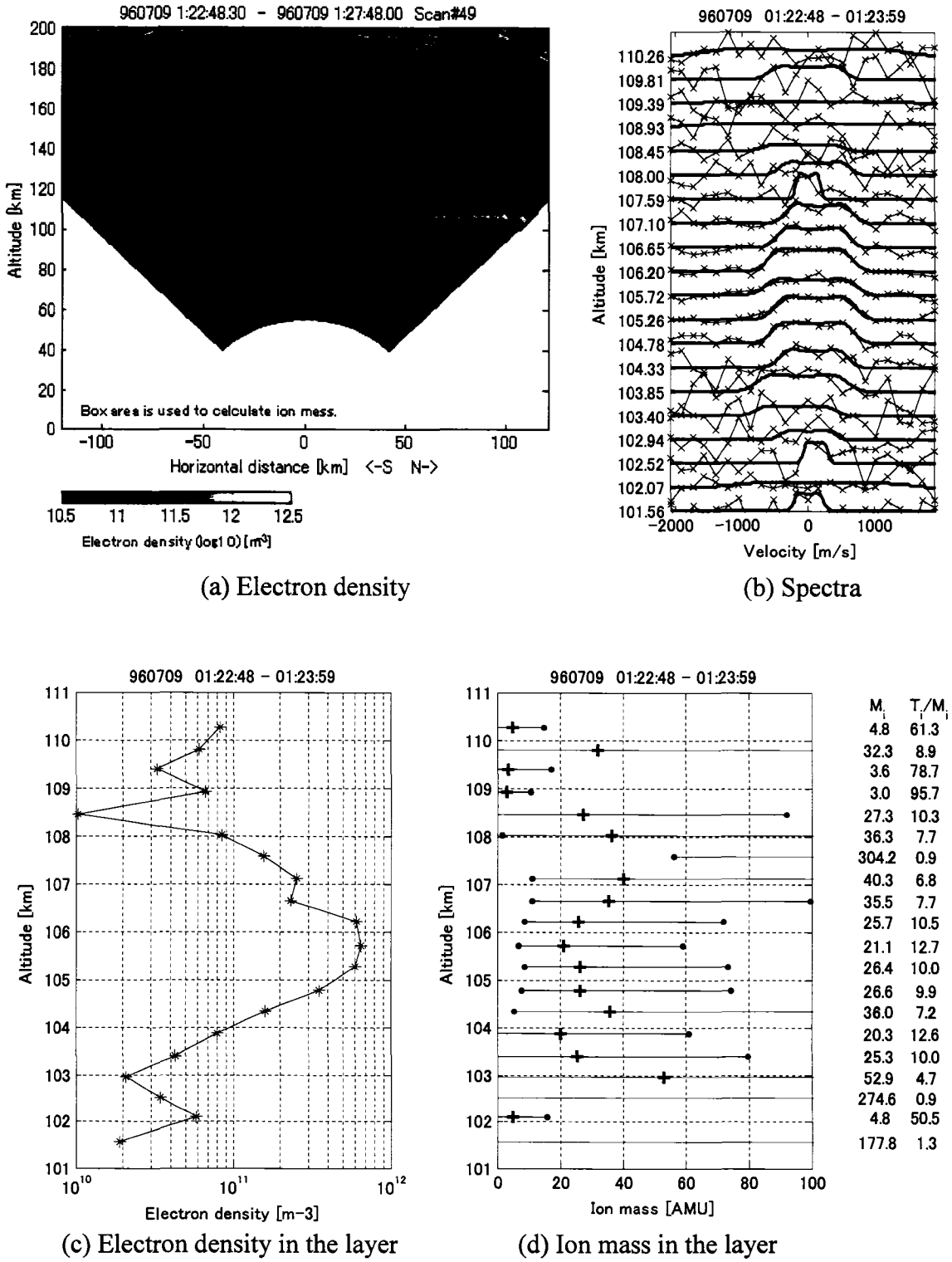

(a) Electron density (b) Spectra

(c) Electron density in the layer (d) Ion mass in the layer

Fig. 6.45 Ion mass estimation in the layer during 1:22-1:23UT on Jul. 9th 1996.

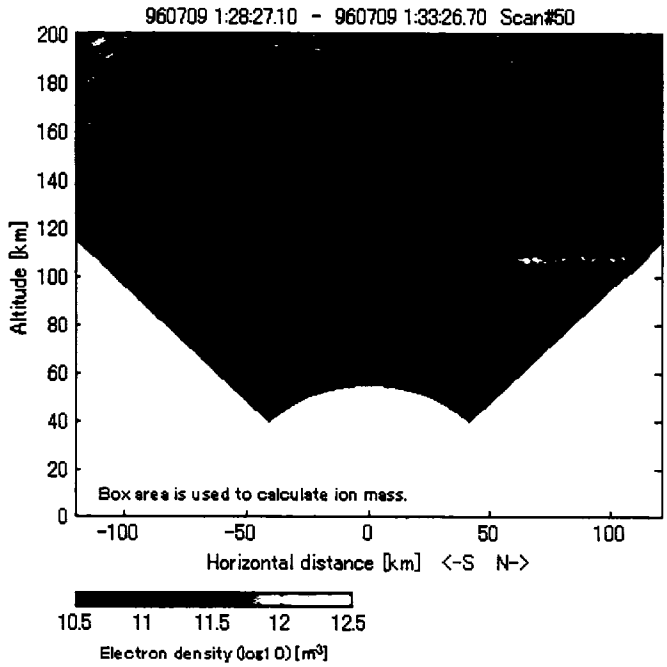

(a) Electron density

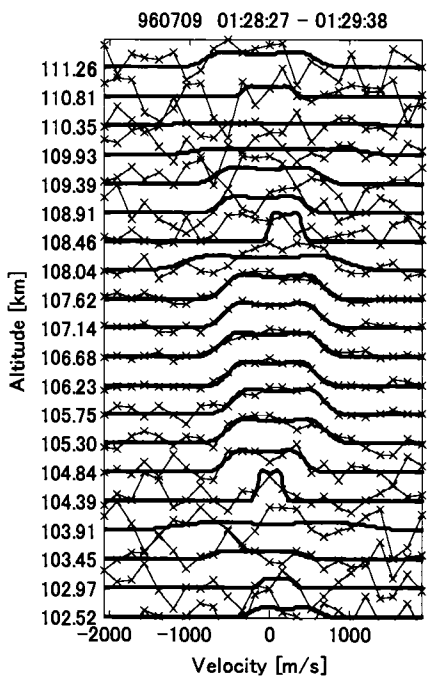

(b) Spectra

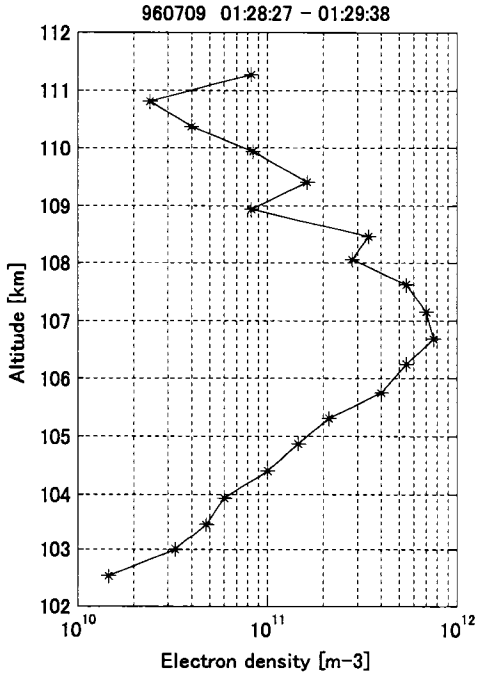

(c) Electron density in the layer

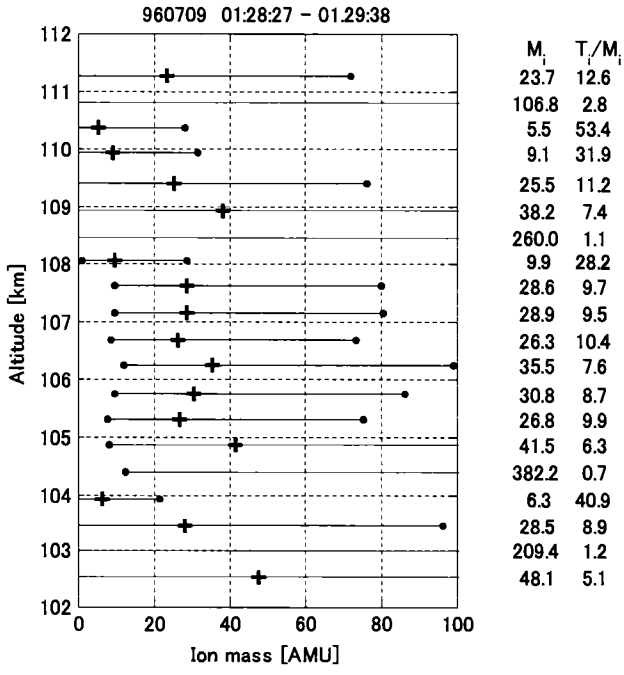

(d) Ion mass in the layer

Fig. 6.46 Ion mass estimation in the layer during 1:28-1:29UT on Jul. 9th 1996.

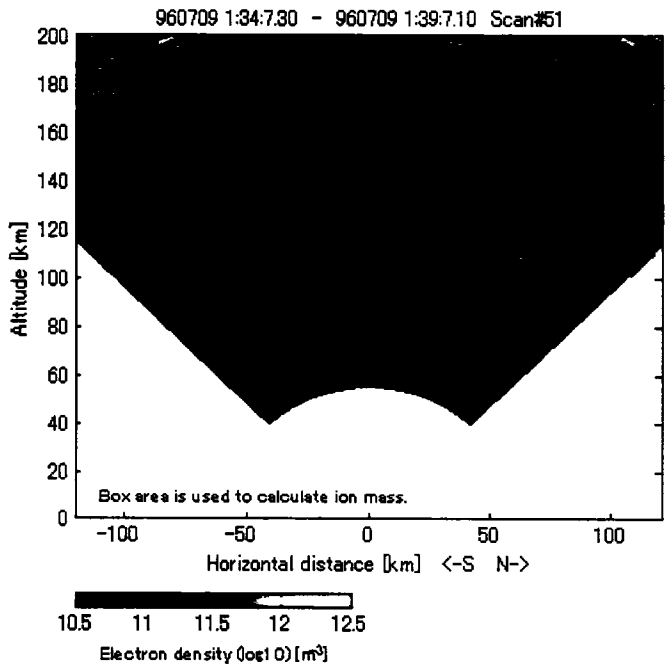

(a) Electron density

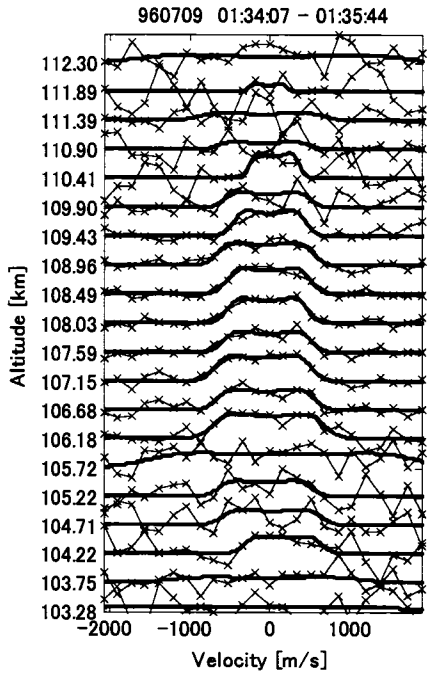

(b) Spectra

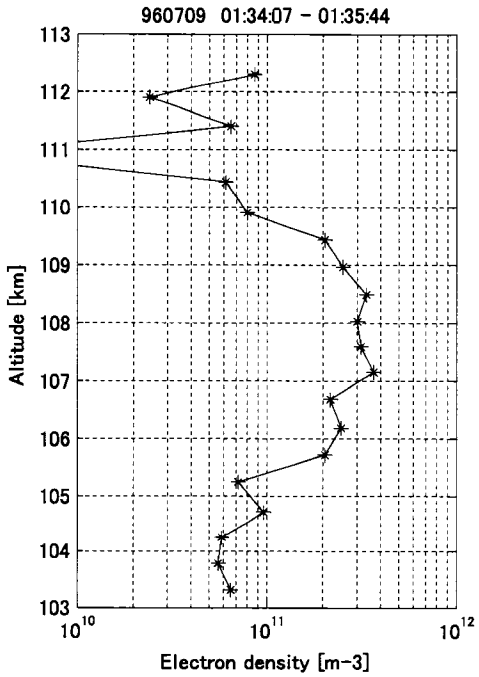

(c) Electron density in the layer

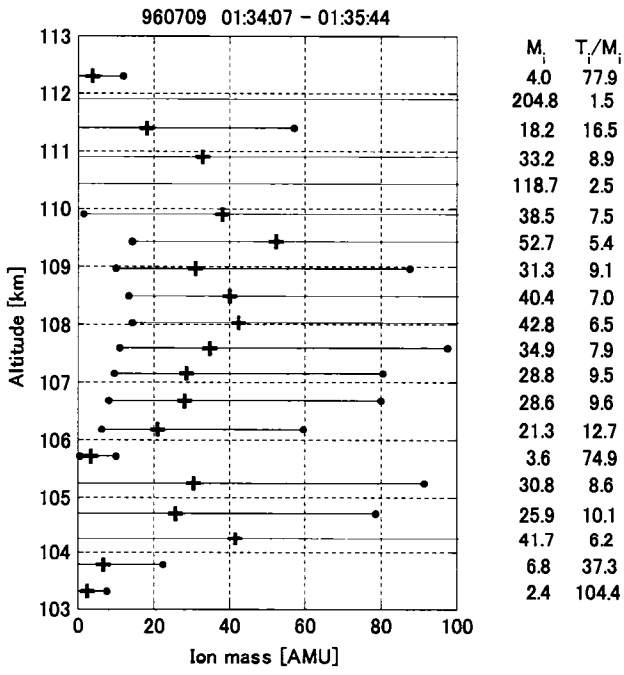

(d) Ion mass in the layer

Fig. 6.47 Ion mass estimation in the layer during 1:34-1:35UT on Jul. 9th 1996.

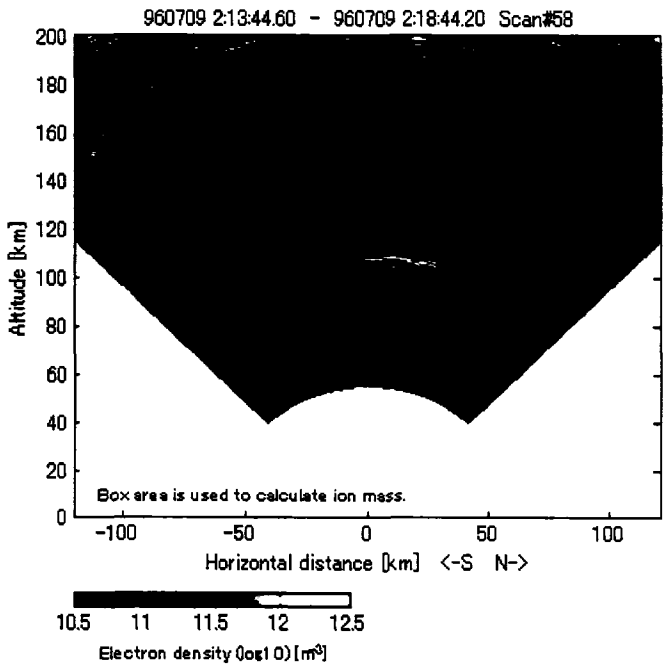

(a) Electron density

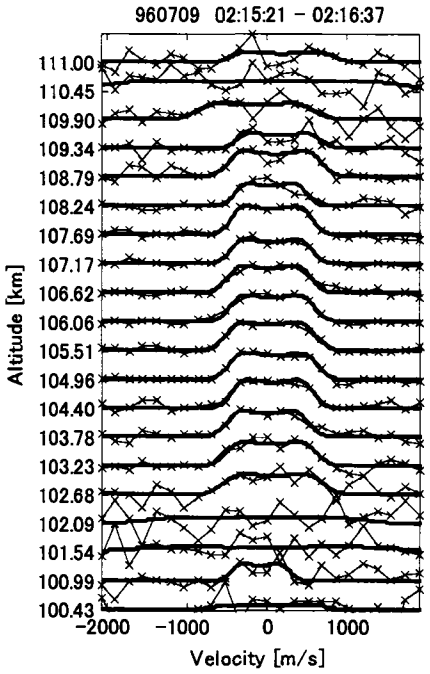

(b) Spectra

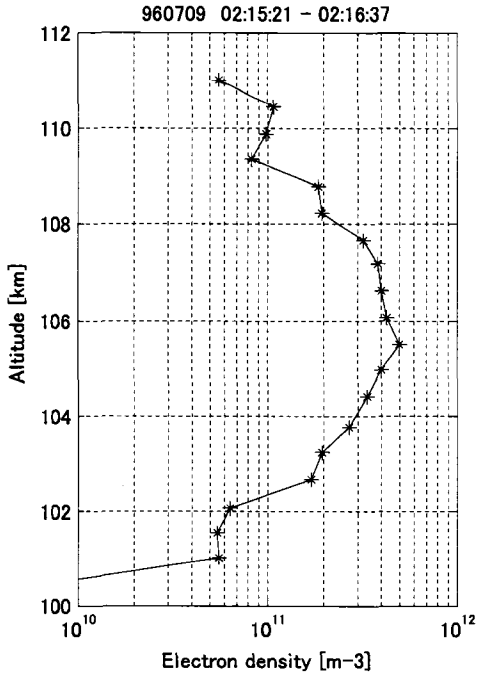

(c) Electron density in the layer

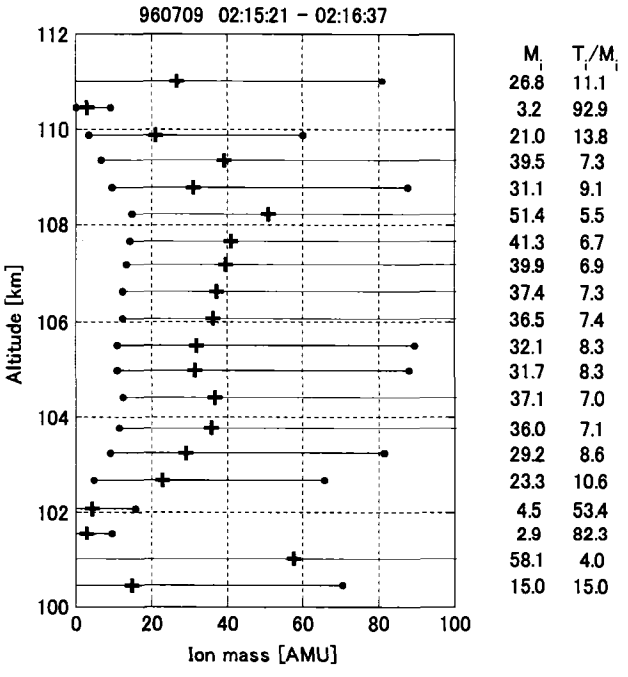

(d) Ion mass in the layer

Fig. 6.48 Ion mass estimation in the layer during 2:15-2:16UT on Jul. 9th 1996.

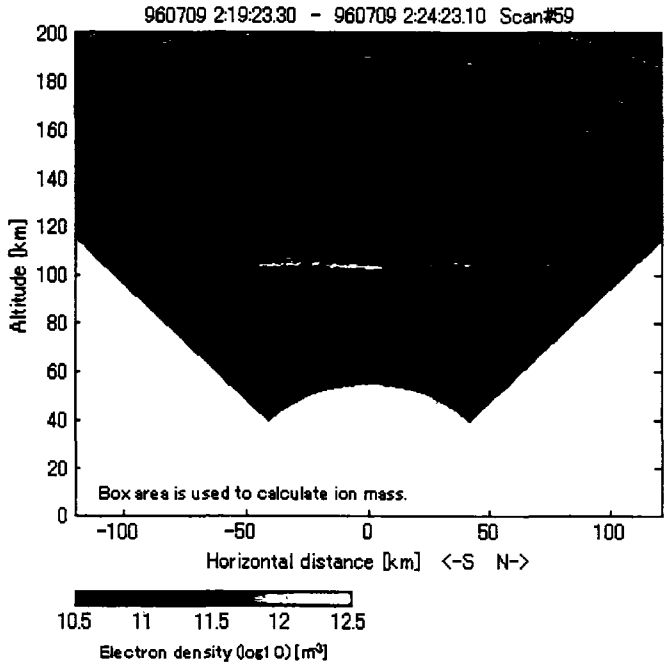

(a) Electron density

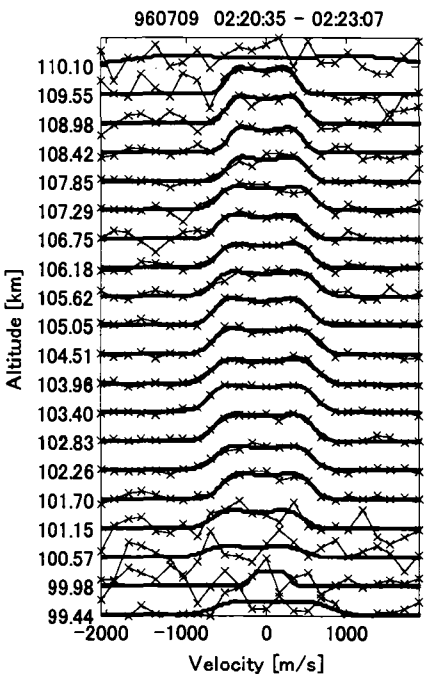

(b) Spectra

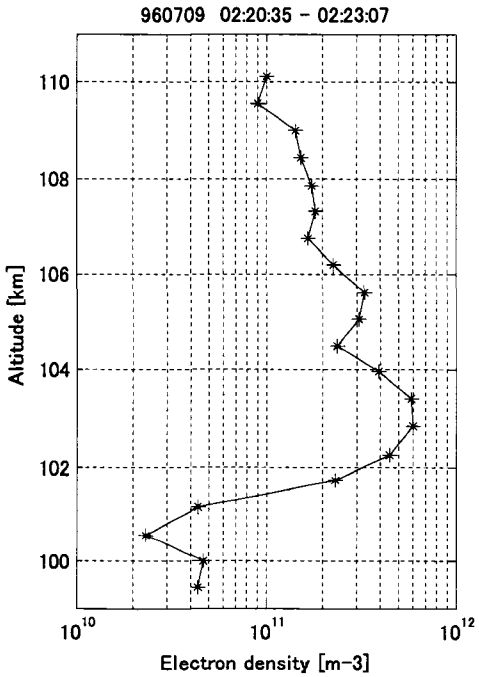

(c) Electron density in the layer

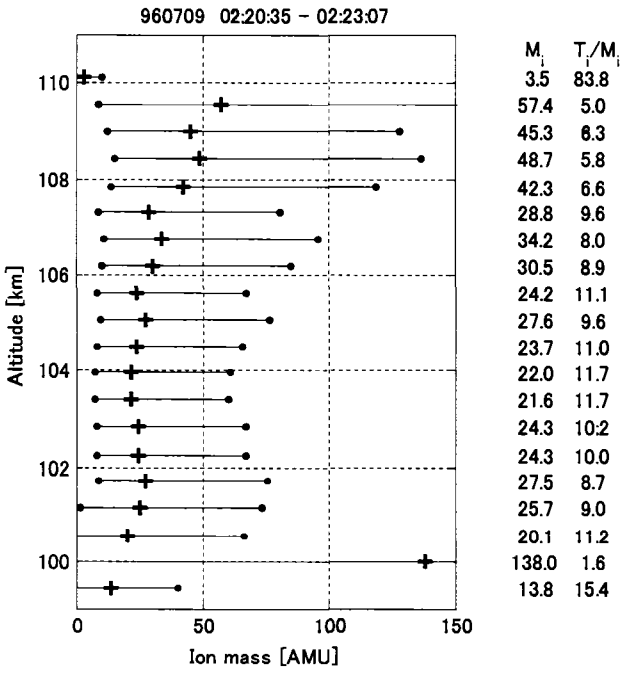

(d) Ion mass in the layer

Fig. 6.49 Ion mass estimation in the layer during 2:20-2:23UT on Jul. 9th 1996.

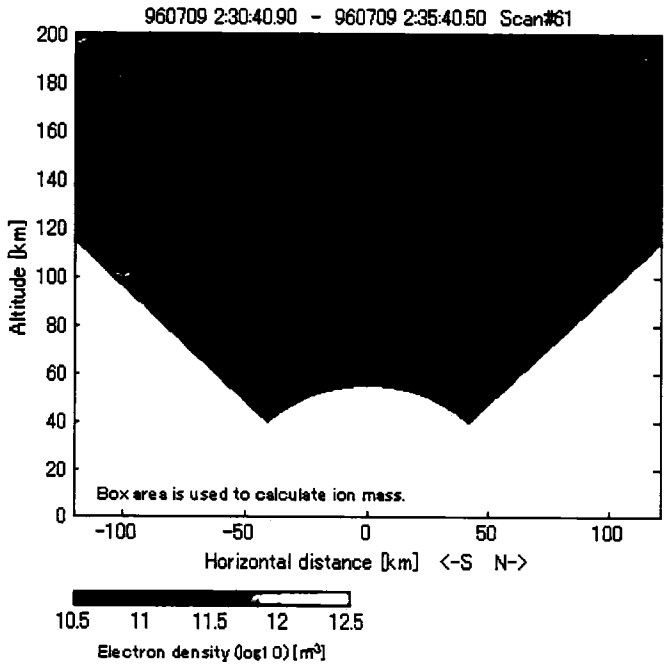

(a) Electron density

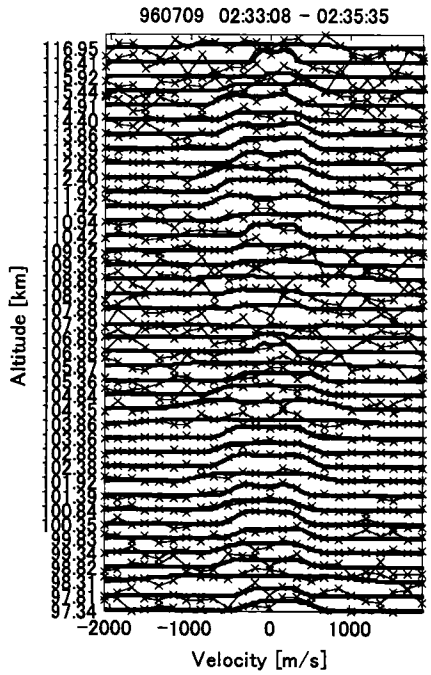

(b) Spectra

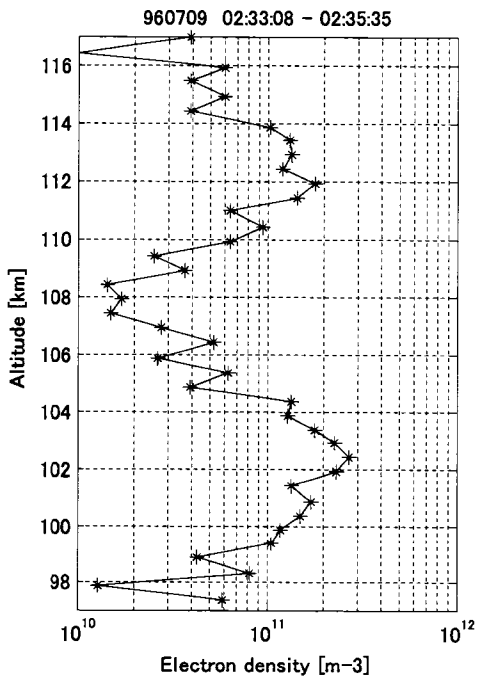

(c) Electron density in the layer

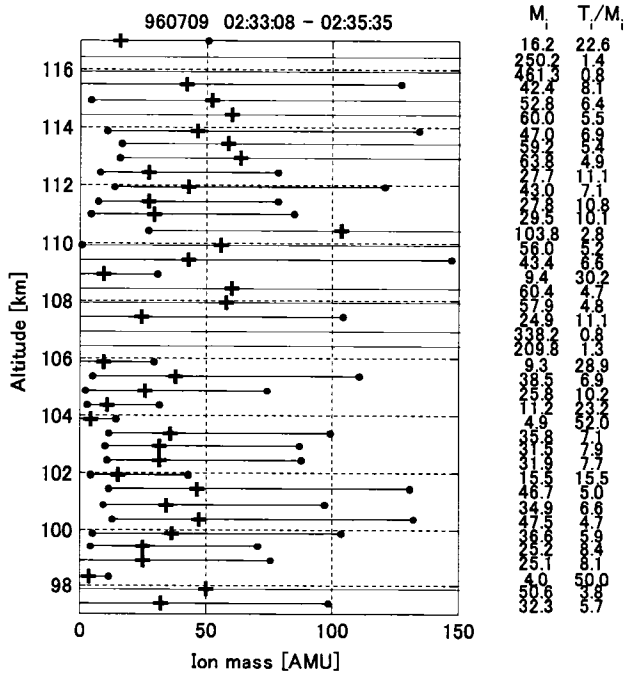

(d) Ion mass in the layer

Fig. 6.50 Ion mass estimation in the layer during 2:33-2:35UT on Jul. 9th 1996.

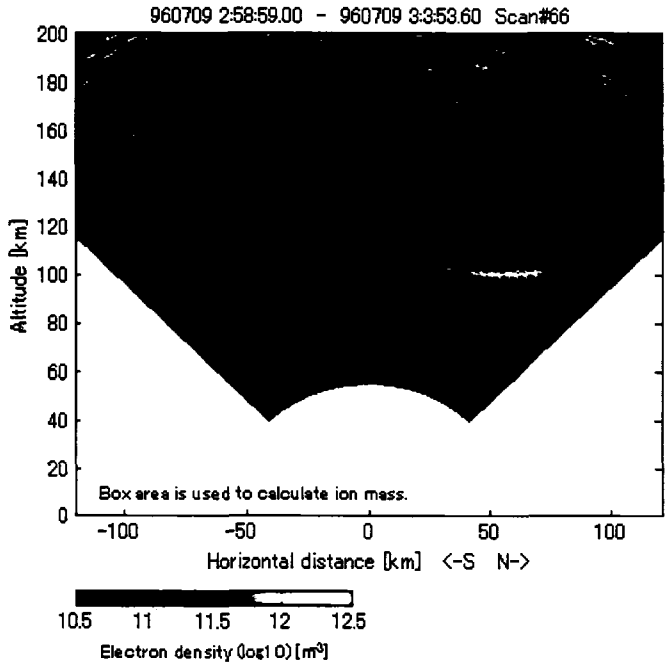

(a) Electron density

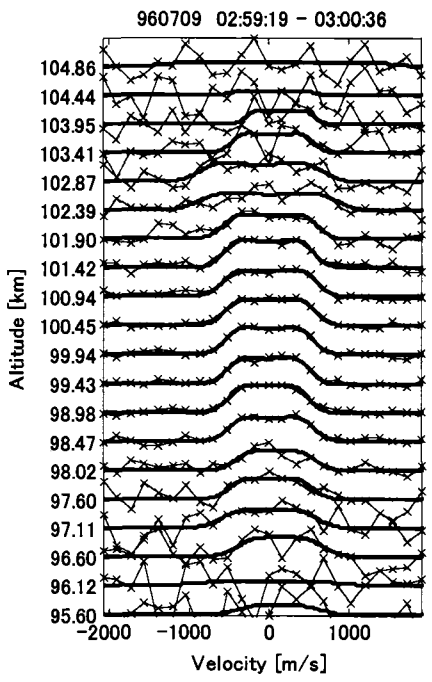

(b) Spectra

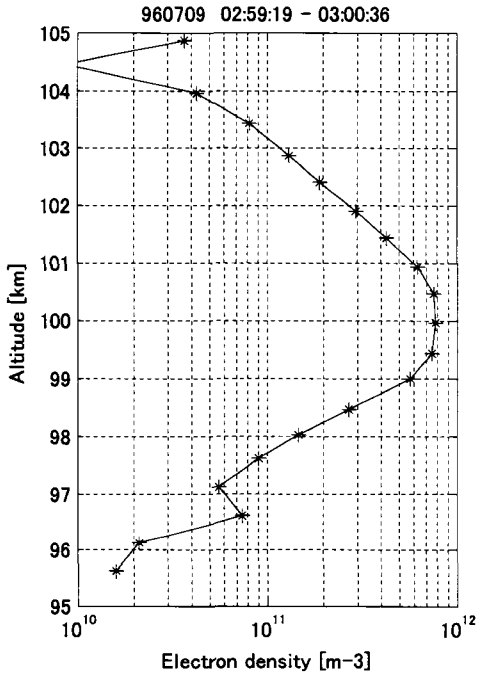

(c) Electron density in the layer

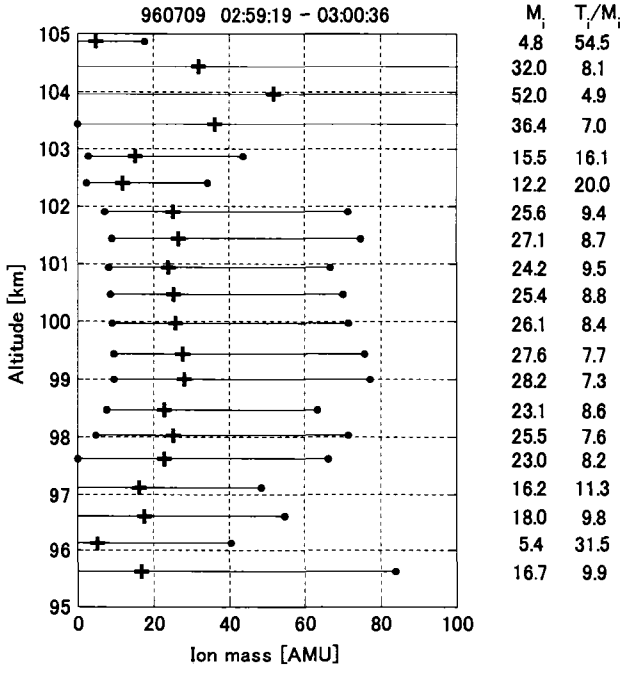

(d) Ion mass in the layer

Fig. 6.51 Ion mass estimation in the layer during 2:59-3:00UT on Jul. 9th 1996.

6.2.6 Jul. 18th -21st 1995

The sporadic layer, including double layers, appeared for three sequential nights. The temperature profile was estimated on each night using the unmodulated long pulse mode.

On Jul. 18th 1995, the first night, a significant layer appeared at 22:42UT, moving from north to south. The layer disappeared from the view of the radar at 23:04UT, and another layer appeared from the north from 23:21UT through 23:43UT. Although a double layer did not appear, ion mass seemed to exhibit a top heavy tendency.

On the second night, Jul. 19th-20th, a stepped layer, which is a bended layer occurred at slightly different altitudes on two sides with a tilted transition boundary, as is shown in Figs.6.64 and 6.65. The stepped layer became weaker at 0:42UT but was detected until 1:43UT. Similar to the explanations suggested for the tilted layer previously, two explanations can be suggested in this case: a truly stepped layer or a layer moving vertically during observation. In the case of Figs.6.64 and 6.65, it is reasonable to bet on the truly stepped layer because a similar layer pattern continued for two scans. If the steps were due to vertical motion, there would have to have been two instances of sudden motion in each scan, which seems unlikely. We lack the evidence necessary to determine why the step occurred, but it seemed that conditions on the two sides of the boundary differed, creating a difference in the layer altitude on either side of the boundary.

On the third night of Jul. 20th-21st, a double layer appeared at 0:40UT and continued through 0:56UT. After the double layer appeared to merge into a single layer, the single layer weakened and disappeared at 1:36UT. In the double layer case shown in Fig.6.71, ion mass seems to be the same in the upper layer and the lower layer. In other cases of this night, evidence is lacking that would allow us to discuss the ion mass tendency.

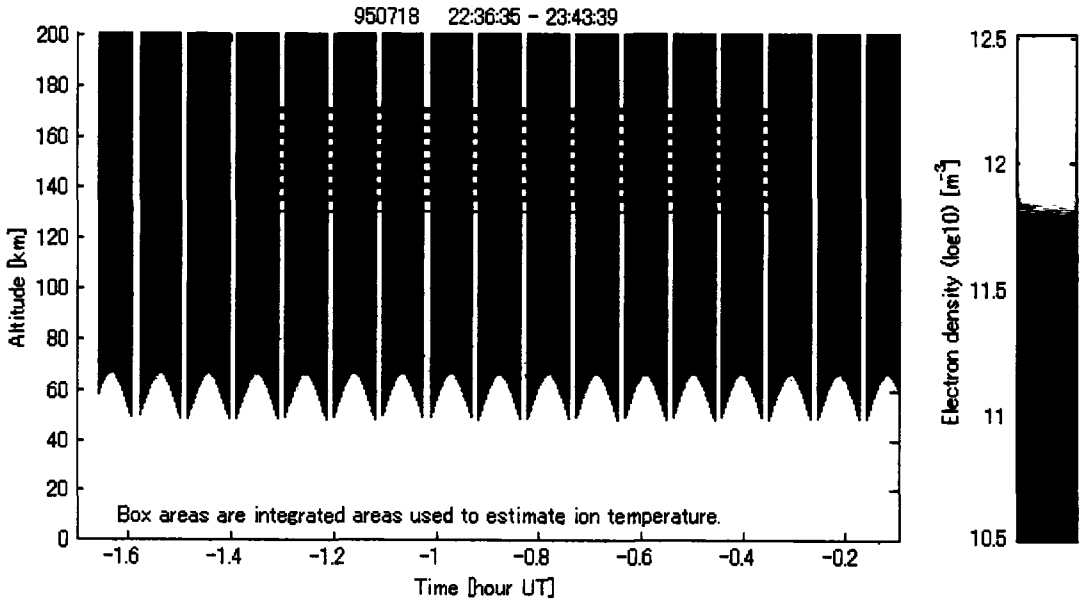

(a) Electron density

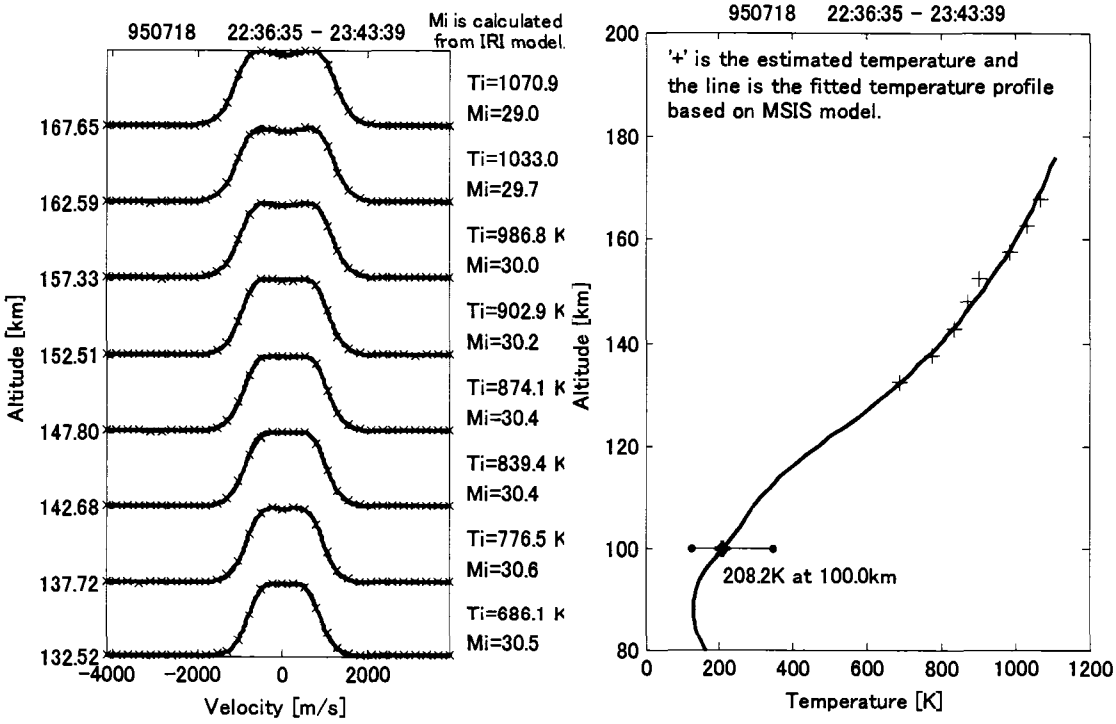

(b) Spectra (c) Ion temperature

Fig. 6.52 Ion temperature estimation using the long pulse mode on Jul. 18th 1995.

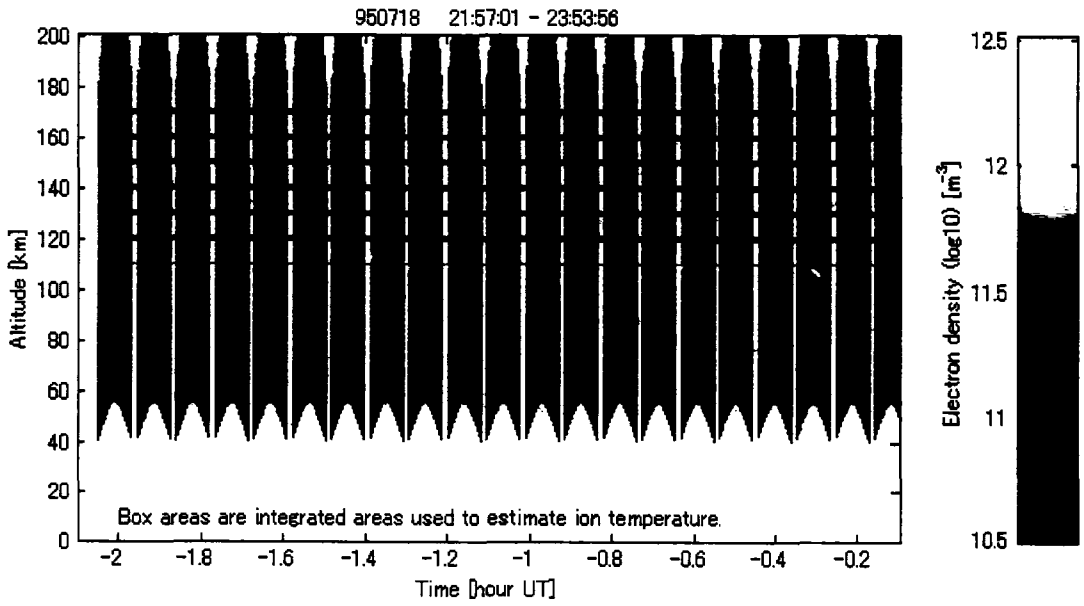

(a) Electron density

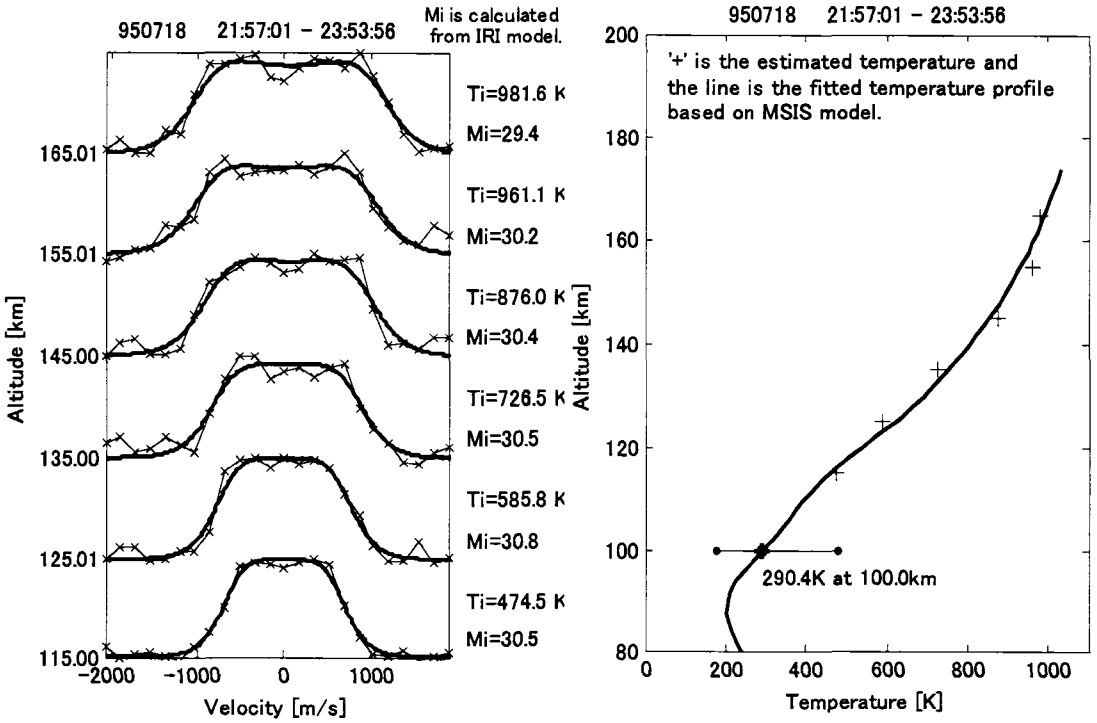

(b) Spectra (c) Ion temperature

Fig. 6.53 Ion temperature estimation using the short pulse mode on Jul. 18th 1995.

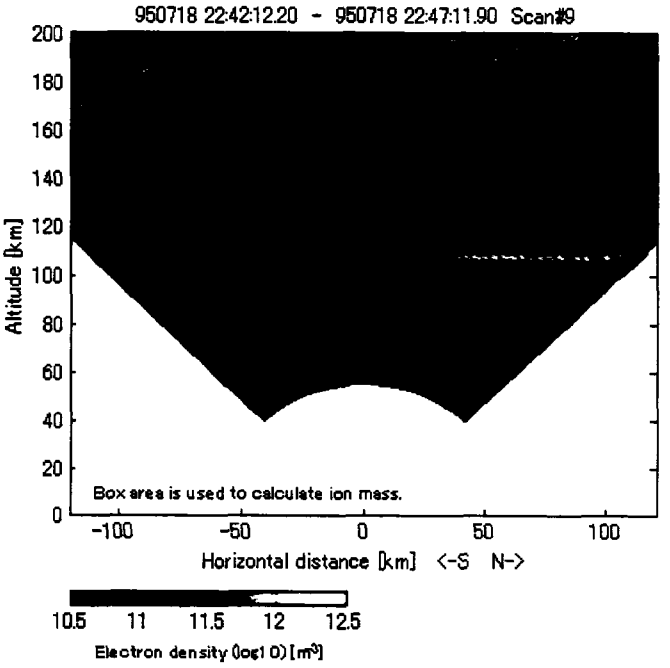

(a) Electron density

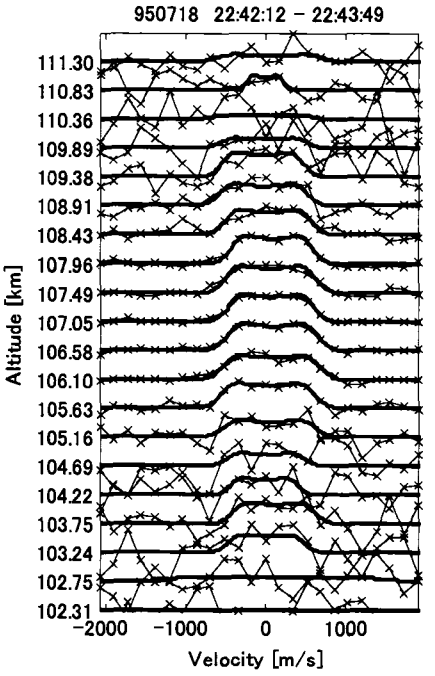

(b) Spectra

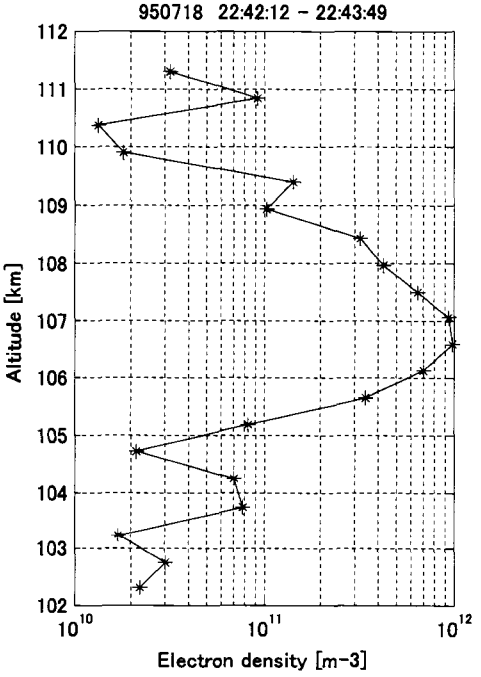

(c) Electron density in the layer

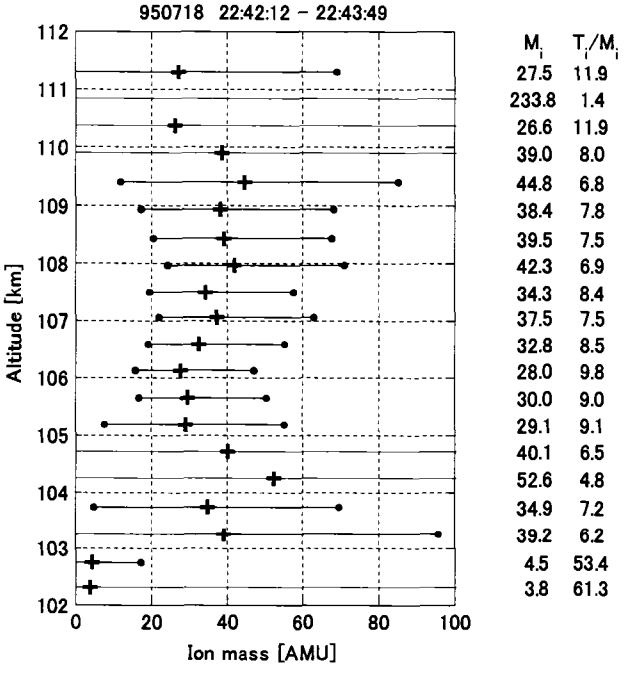

(d) Ion mass in the layer

Fig. 6.54 Ion mass estimation in the layer during 22:42-22:43UT on Jul. 18th 1995.

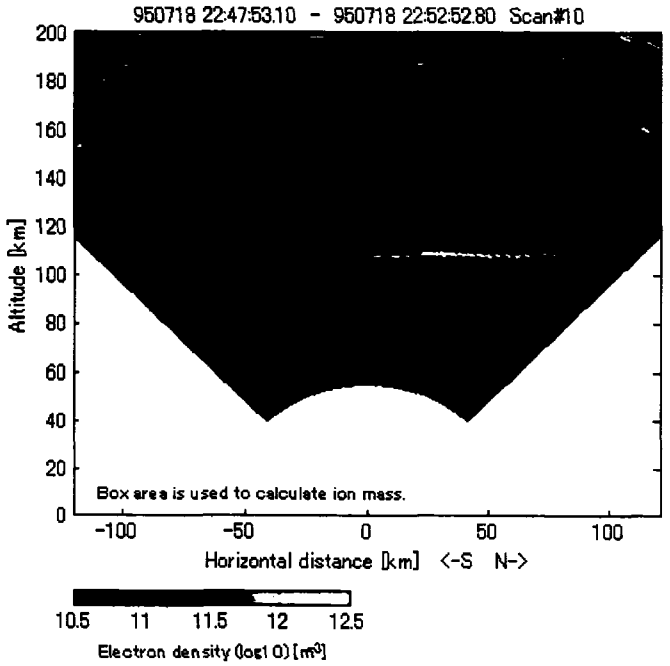

(a) Electron density

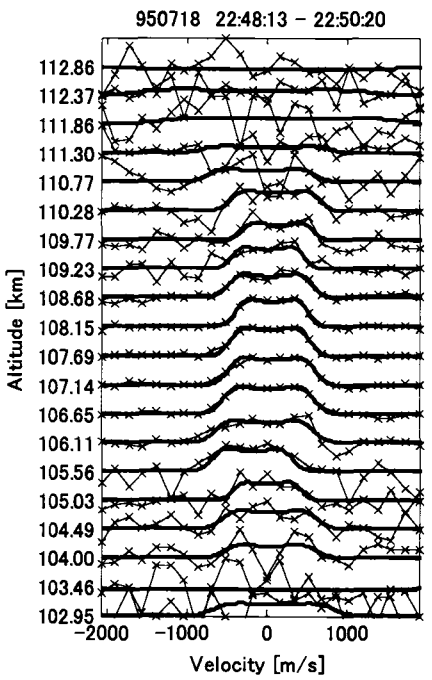

(b) Spectra

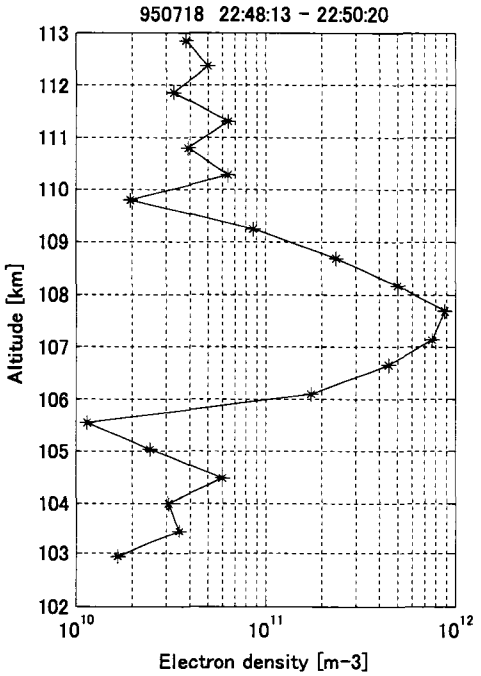

(c) Electron density in the layer

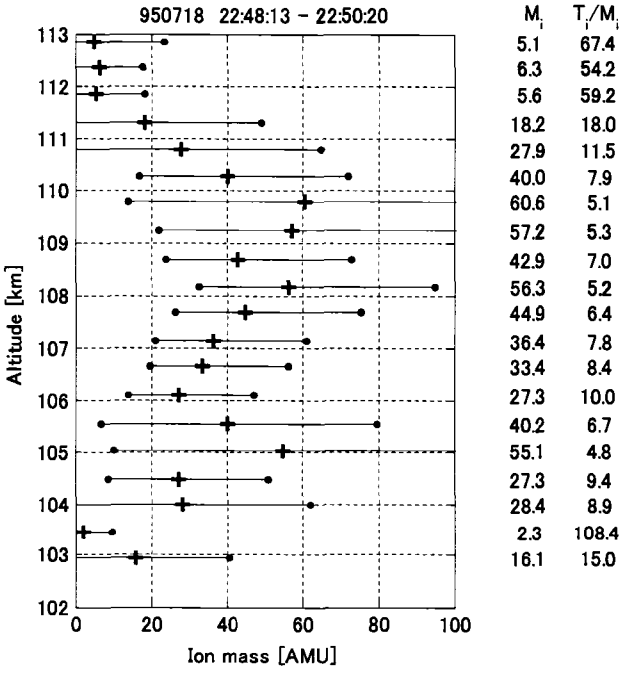

M_i	T_i/M_i
5.1	67.4
6.3	54.2
5.6	59.2
18.2	18.0
27.9	11.5
40.0	7.9
60.6	5.1
57.2	5.3
42.9	7.0
56.3	5.2
44.9	6.4
36.4	7.8
33.4	8.4
27.3	10.0
40.2	6.7
55.1	4.8
27.3	9.4
28.4	8.9
2.3	108.4
16.1	15.0

(d) Ion mass in the layer

Fig. 6.55 Ion mass estimation in the layer during 22:48-22:50UT on Jul. 18th 1995.

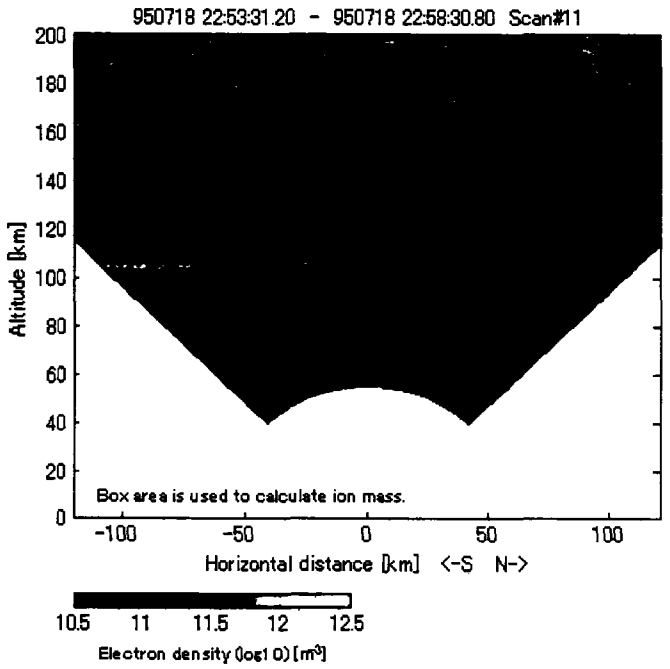

(a) Electron density

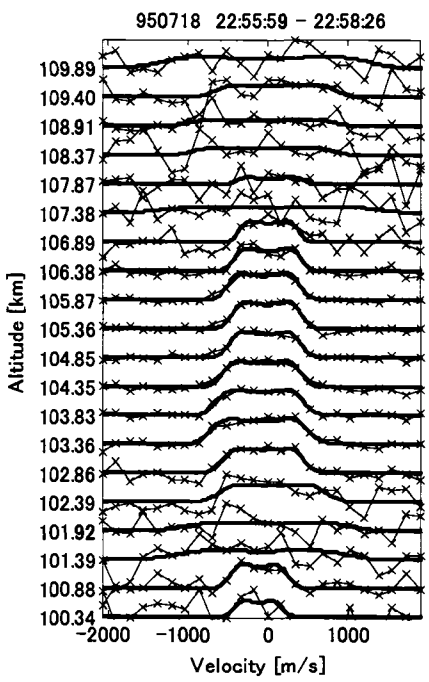

(b) Spectra

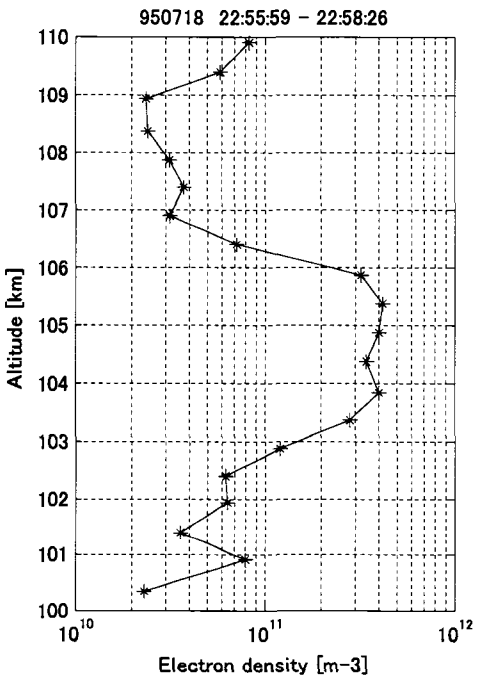

(c) Electron density in the layer

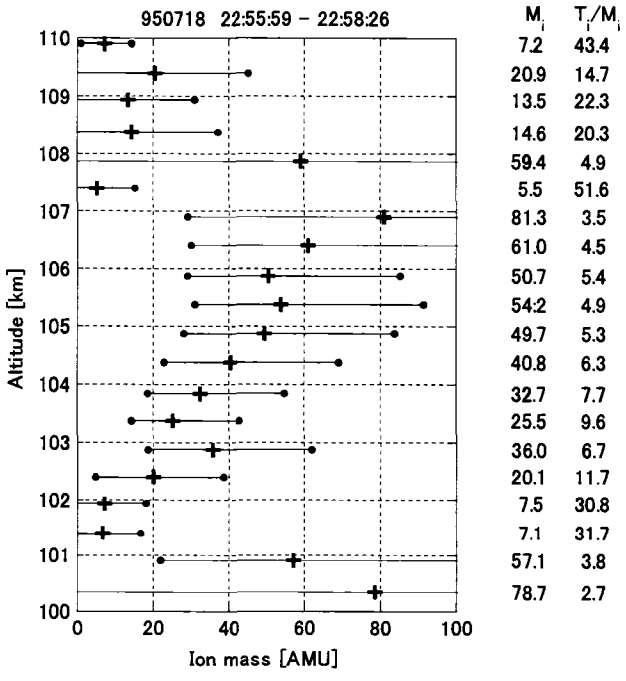

(d) Ion mass in the layer

Fig. 6.56 Ion mass estimation in the layer during 22:55-22:58UT on Jul. 18th 1995.

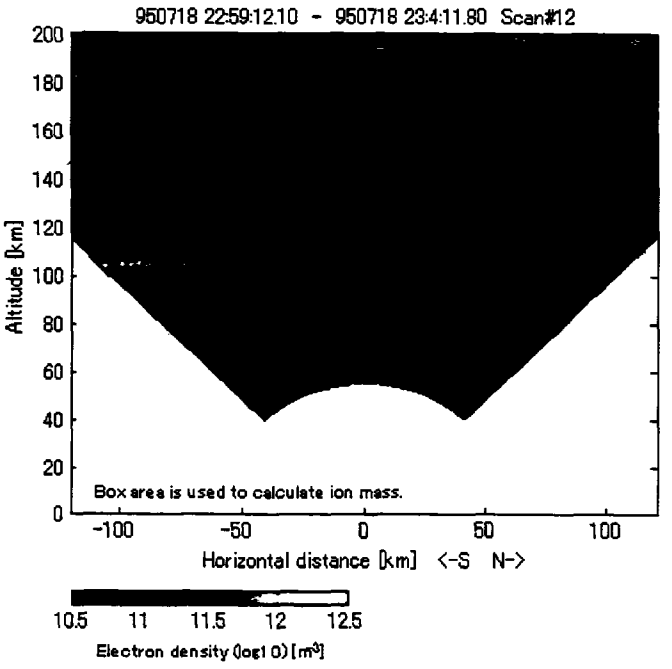

(a) Electron density

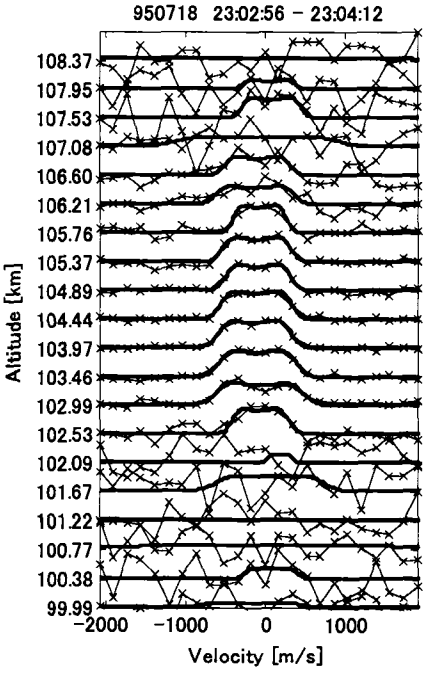

(b) Spectra

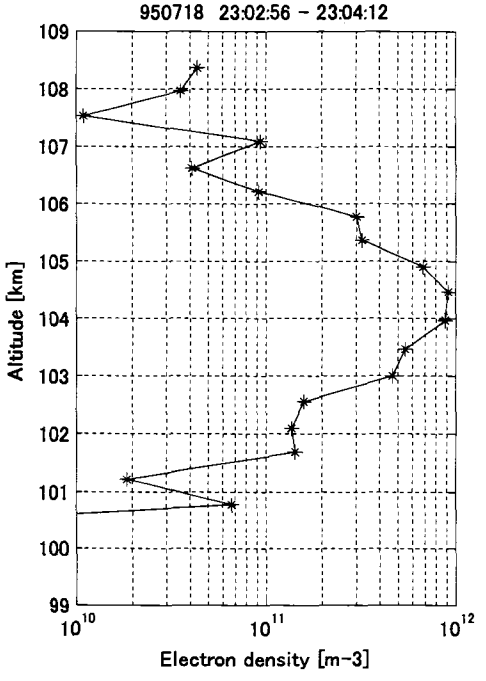

(c) Electron density in the layer

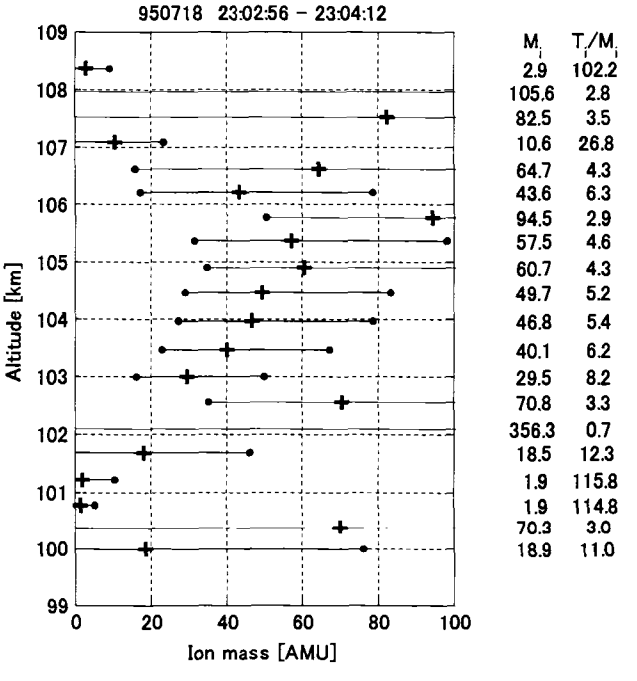

(d) Ion mass in the layer

Fig. 6.57 Ion mass estimation in the layer during 23:02-23:04UT on Jul. 18th 1995.

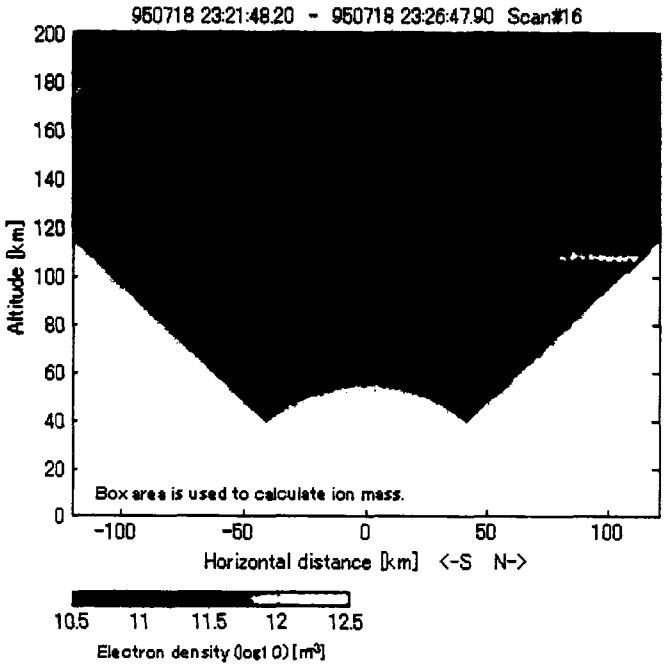

(a) Electron density

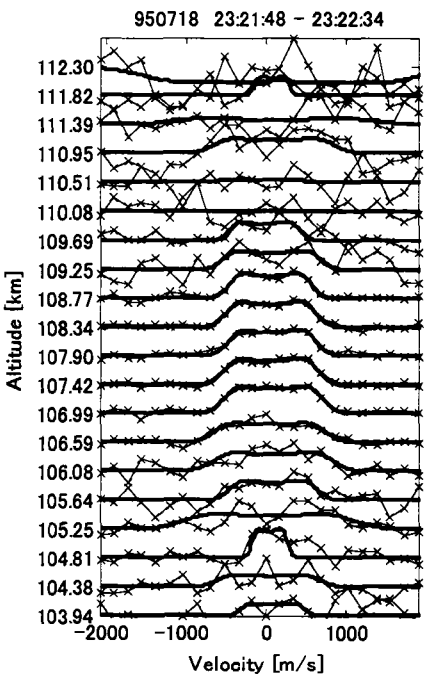

(b) Spectra

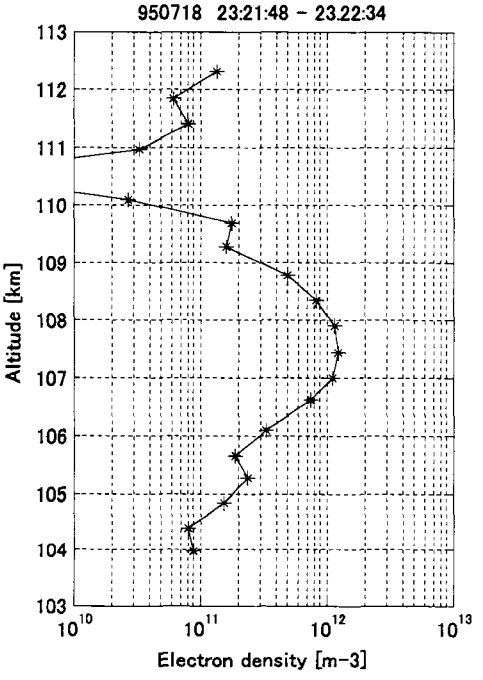

(c) Electron density in the layer

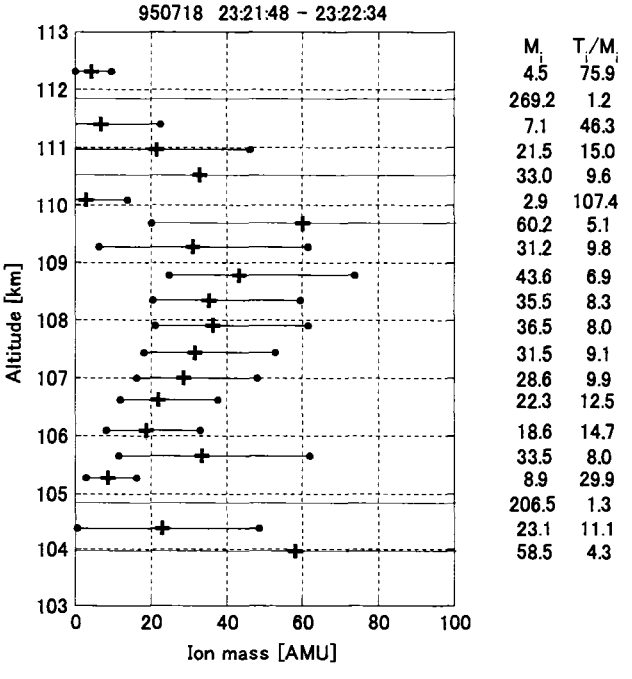

(d) Ion mass in the layer

Fig. 6.58 Ion mass estimation in the layer during 23:21-23:22UT on Jul. 18th 1995.

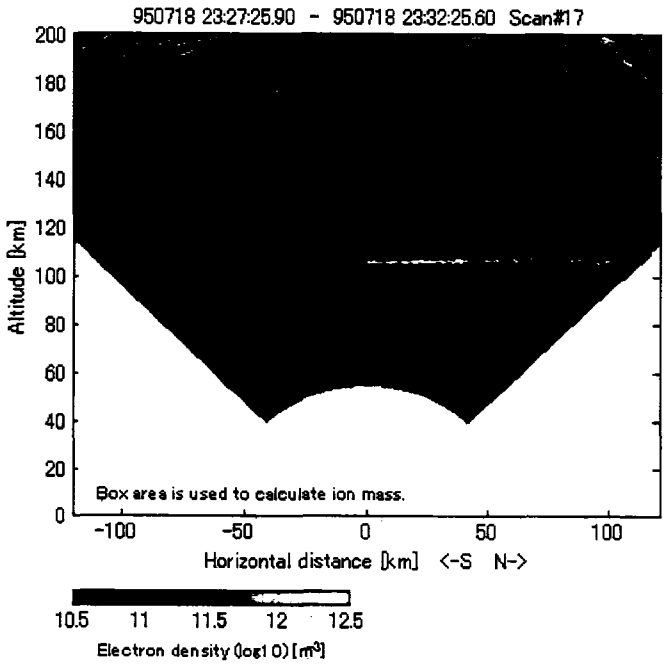

(a) Electron density

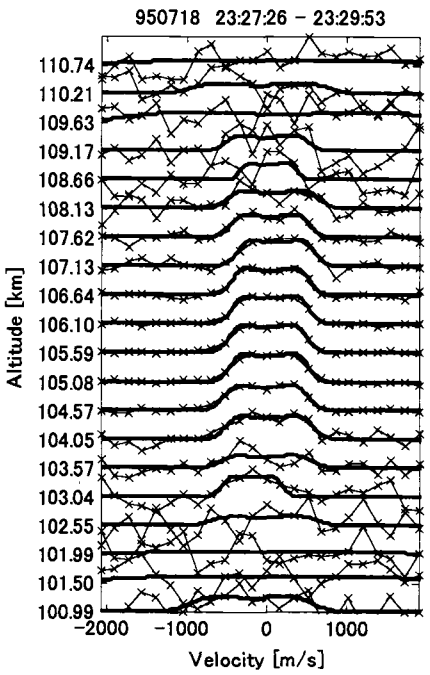

(b) Spectra

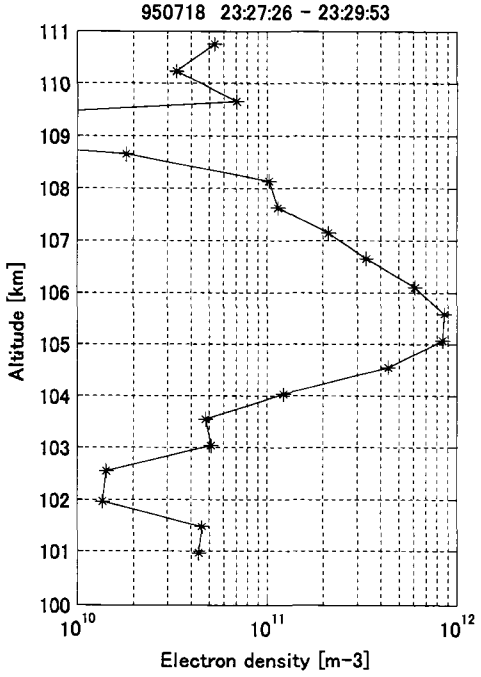

(c) Electron density in the layer

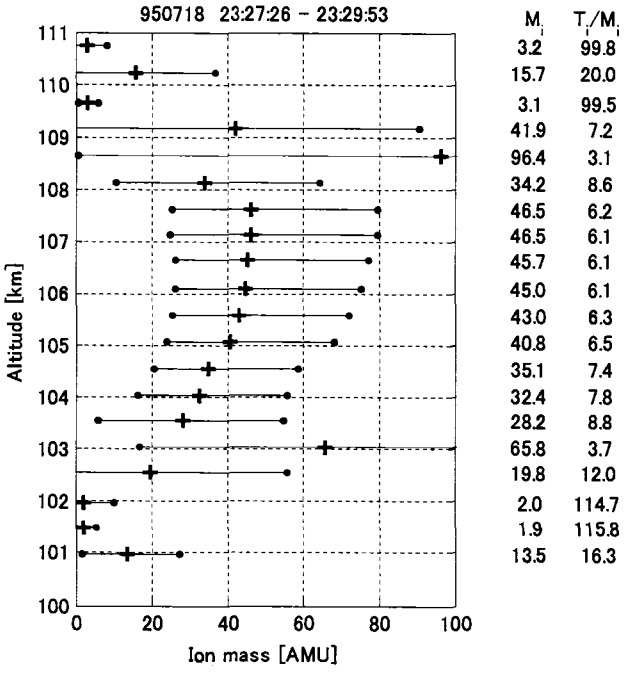

(d) Ion mass in the layer

Fig. 6.59 Ion mass estimation in the layer during 23:27-23:29UT on Jul. 18th 1995.

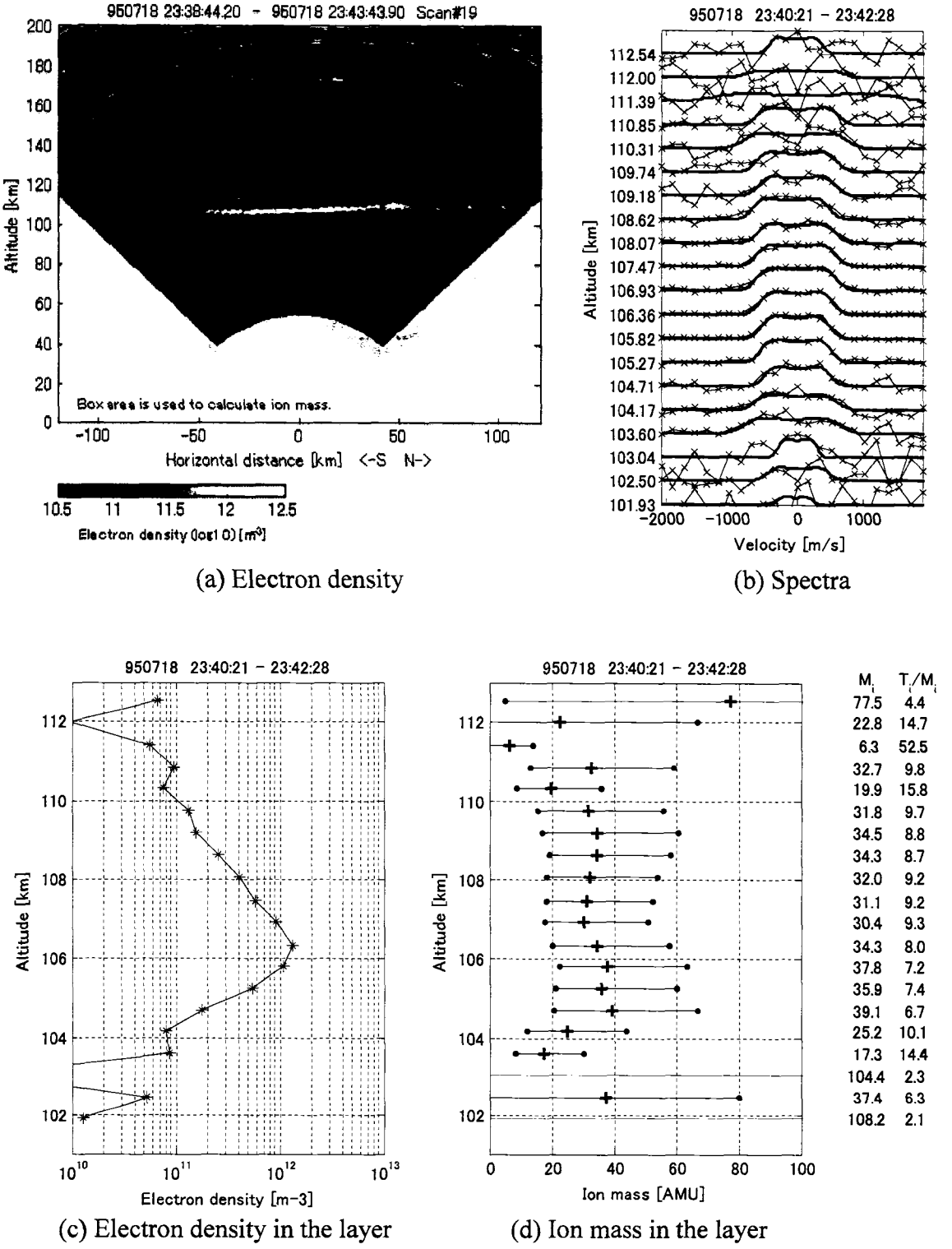

(a) Electron density (b) Spectra

(c) Electron density in the layer (d) Ion mass in the layer

Fig. 6.60 Ion mass estimation in the layer during 23:40-23:42UT on Jul. 18th 1995.

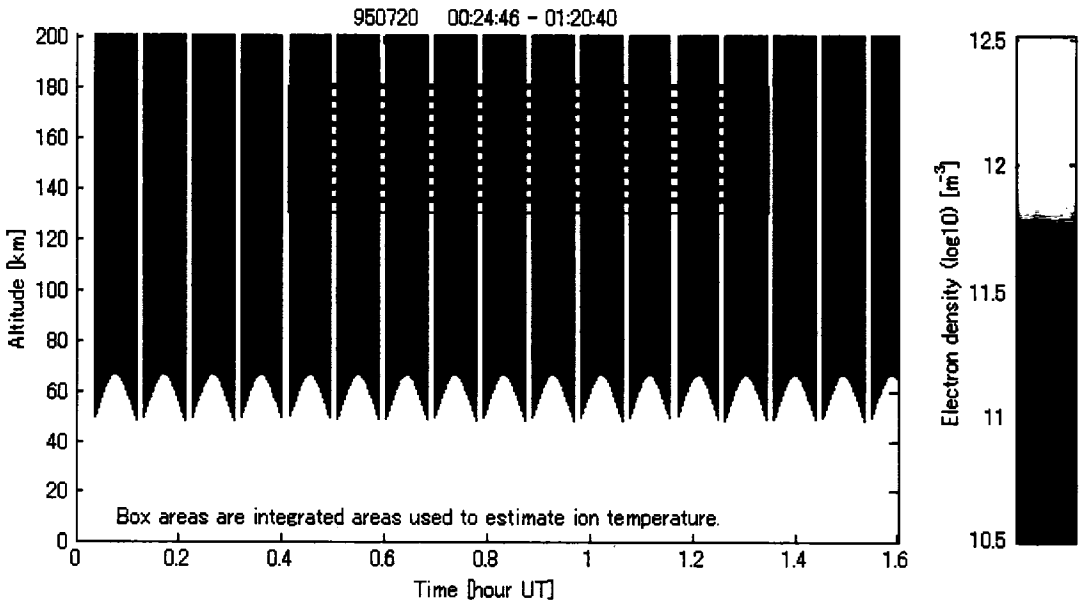

(a) Electron density

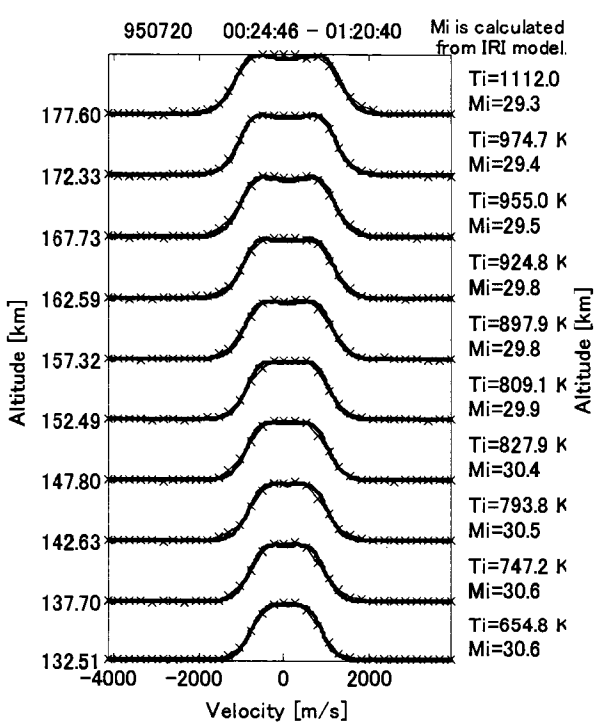

(b) Spectra

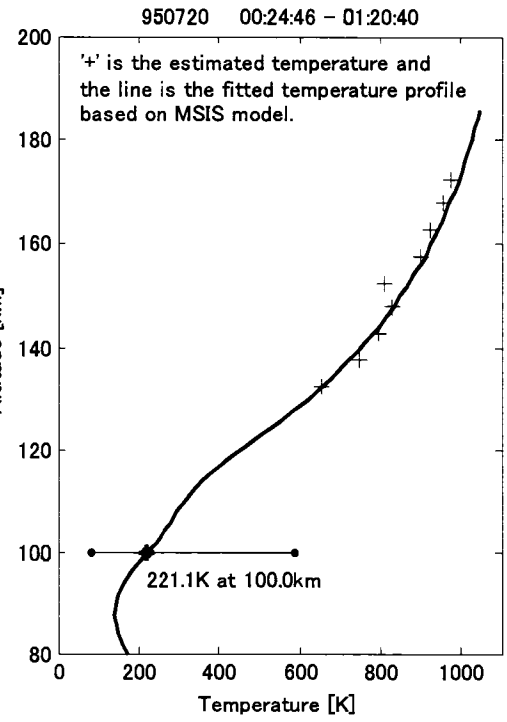

(c) Ion temperature

Fig. 6.61 Ion temperature estimation using the long pulse mode on Jul. 20th 1995.

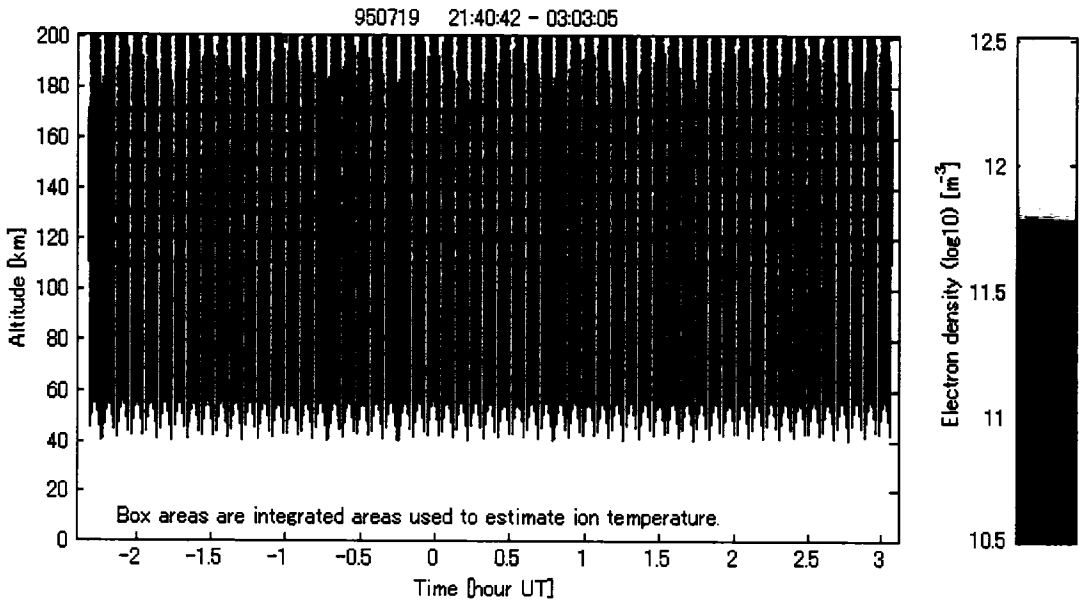

(a) Electron density

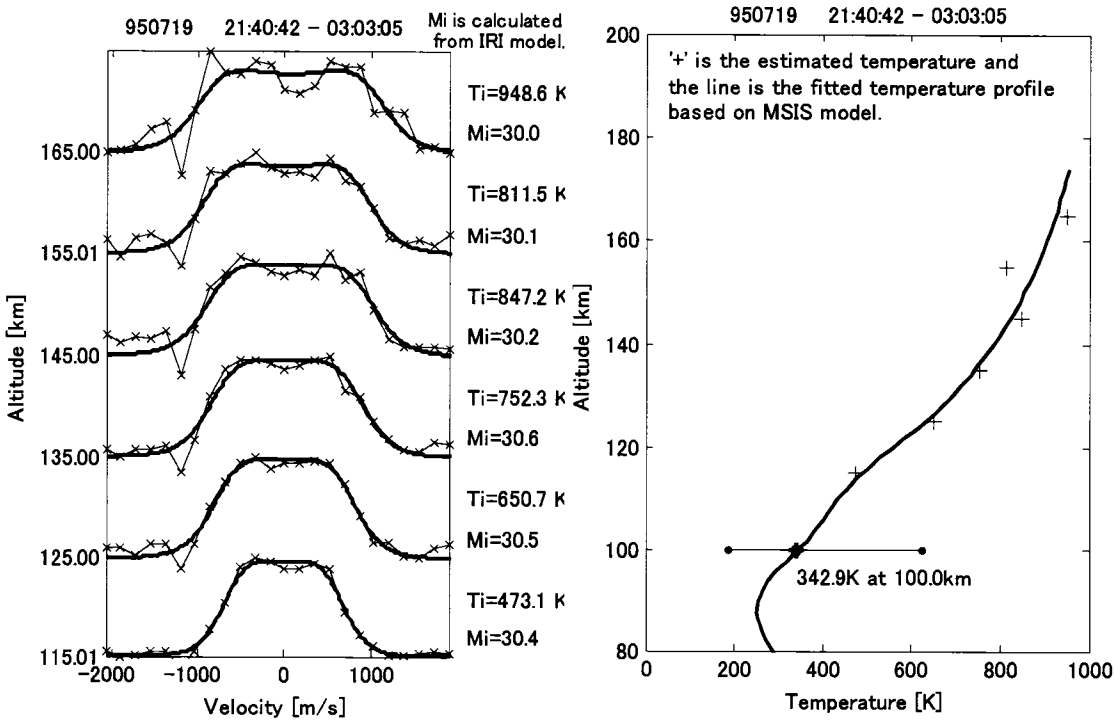

(b) Spectra (c) Ion temperature

Fig. 6.62 Ion temperature estimation using the short pulse mode on Jul. 20th 1995.

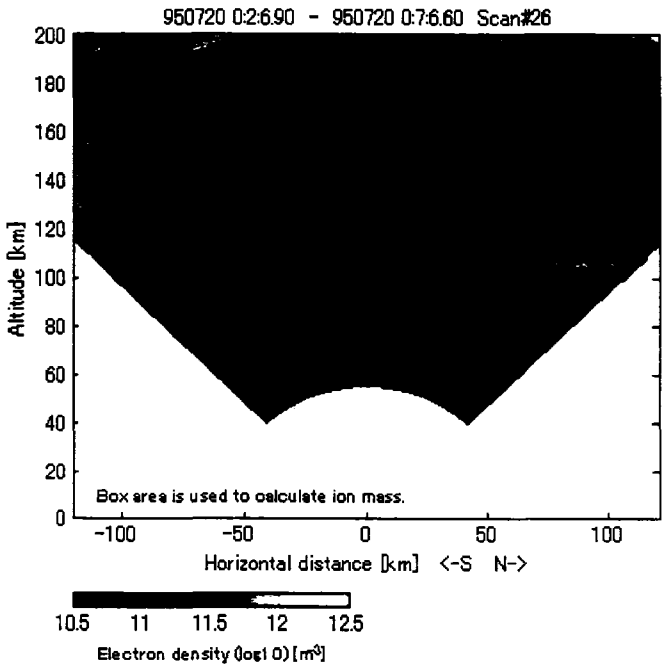

(a) Electron density

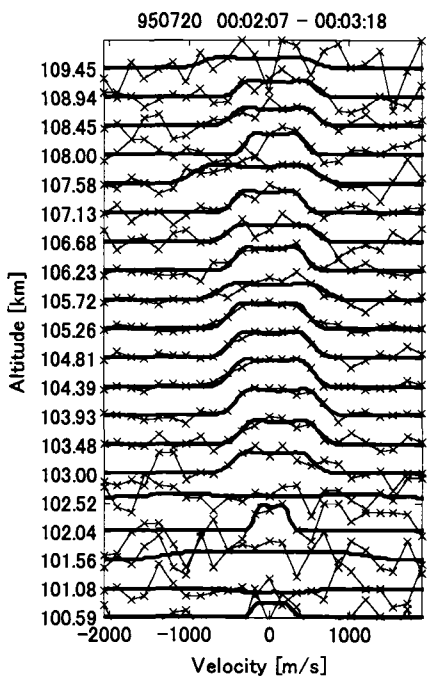

(b) Spectra

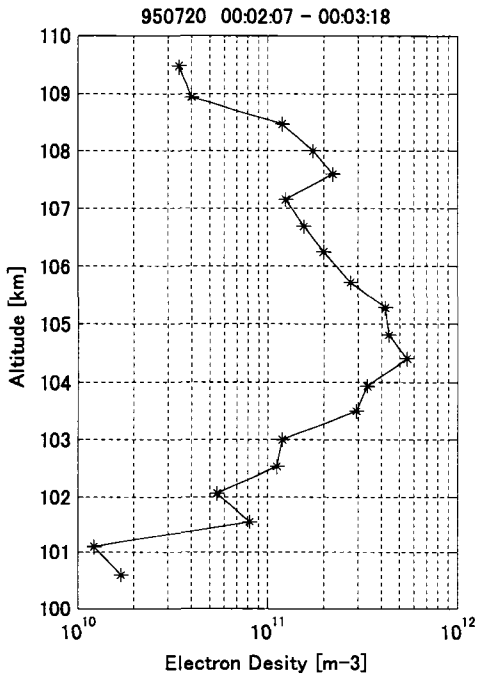

(c) Electron density in the layer

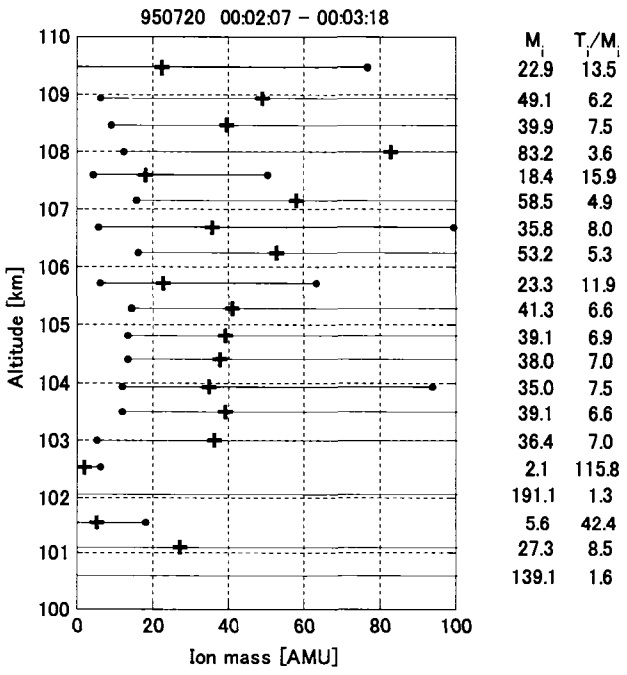

(d) Ion mass in the layer

Fig. 6.63 Ion mass estimation in the layer during 0:02-0:03UT on Jul. 20th 1995.

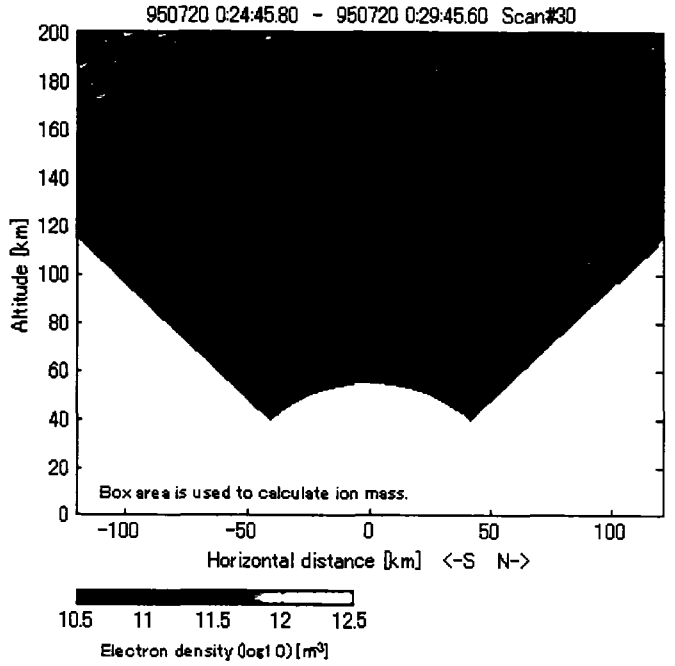

(a) Electron density

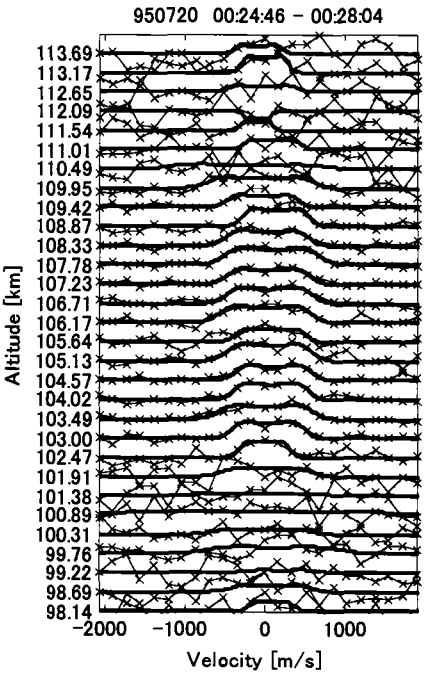

(b) Spectra

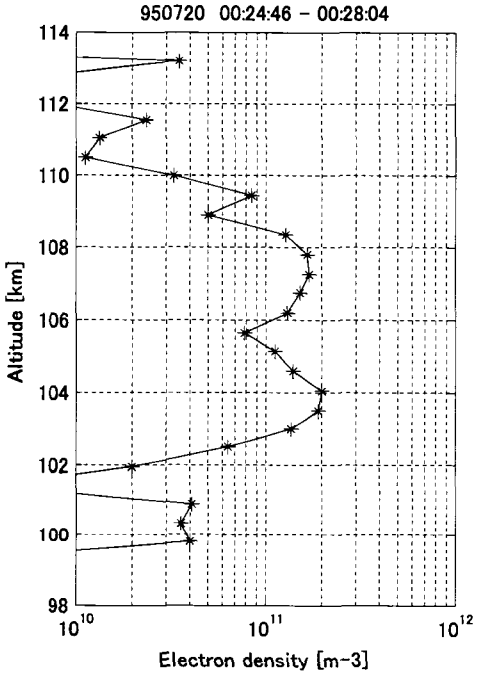

(c) Electron density in the layer

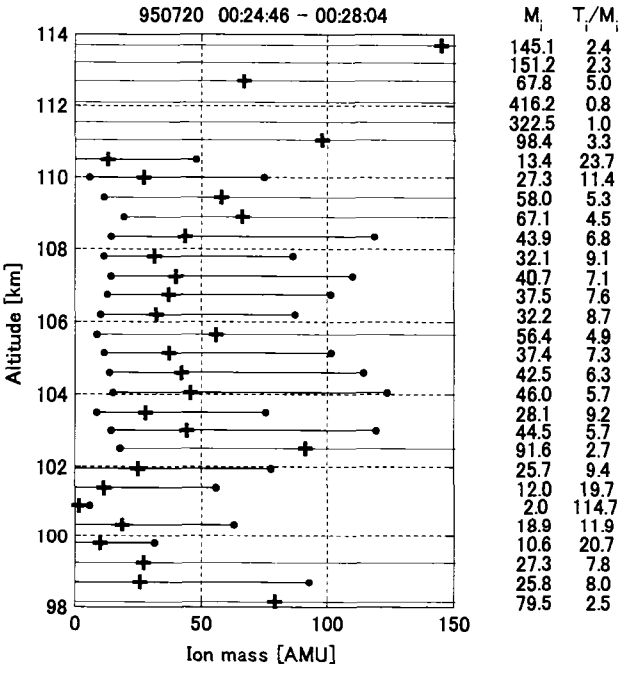

(d) Ion mass in the layer

Fig. 6.64 Ion mass estimation in the layer during 0:24-0:28UT on Jul. 20th 1995.

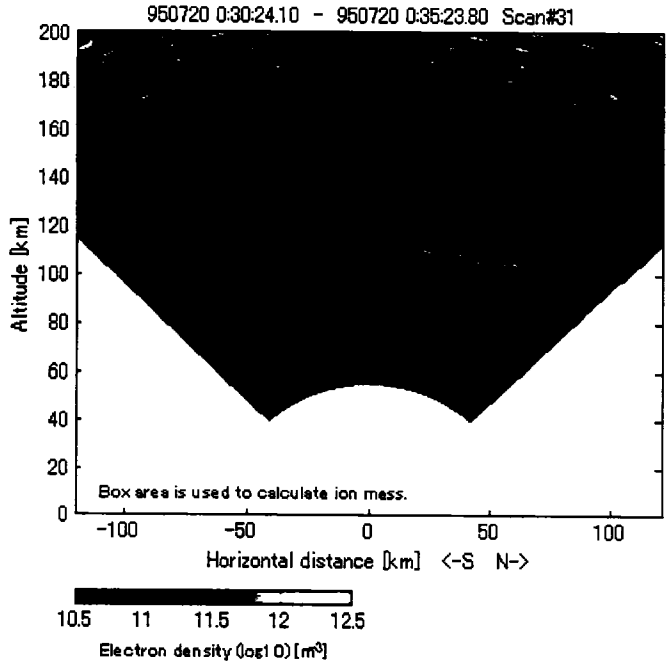

(a) Electron density

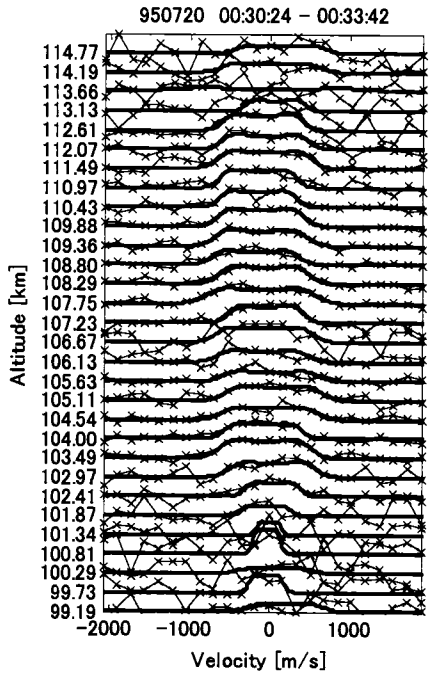

(b) Spectra

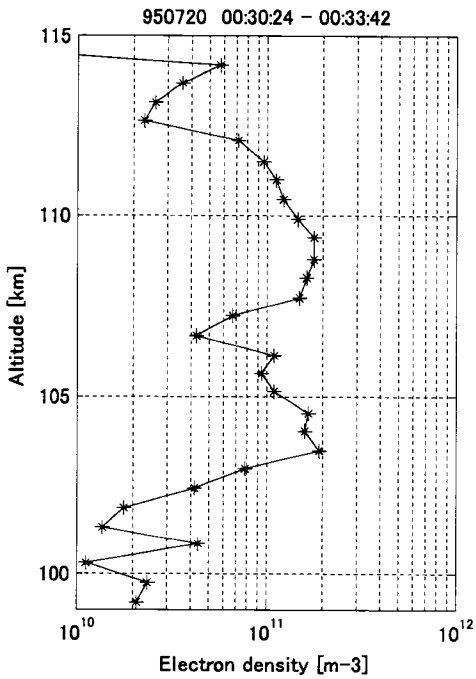

(c) Electron density in the layer

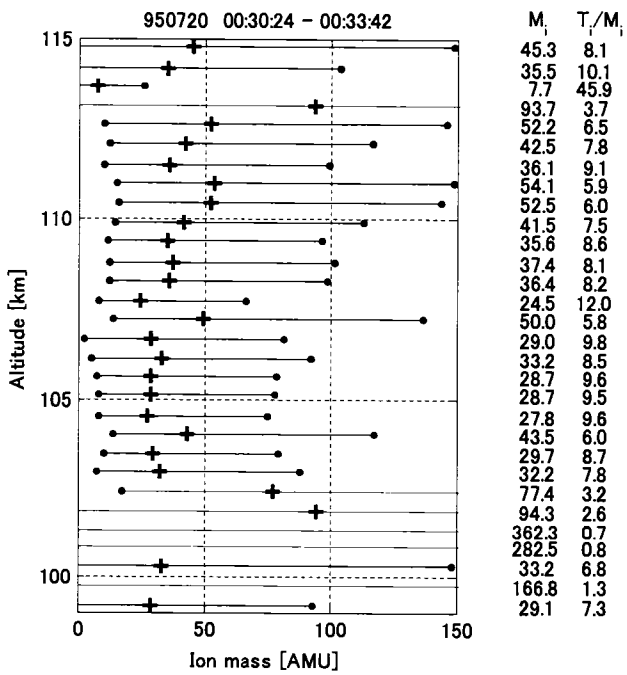

(d) Ion mass in the layer

Fig. 6.65 Ion mass estimation in the layer during 0:30-0:33UT on Jul. 20th 1995.

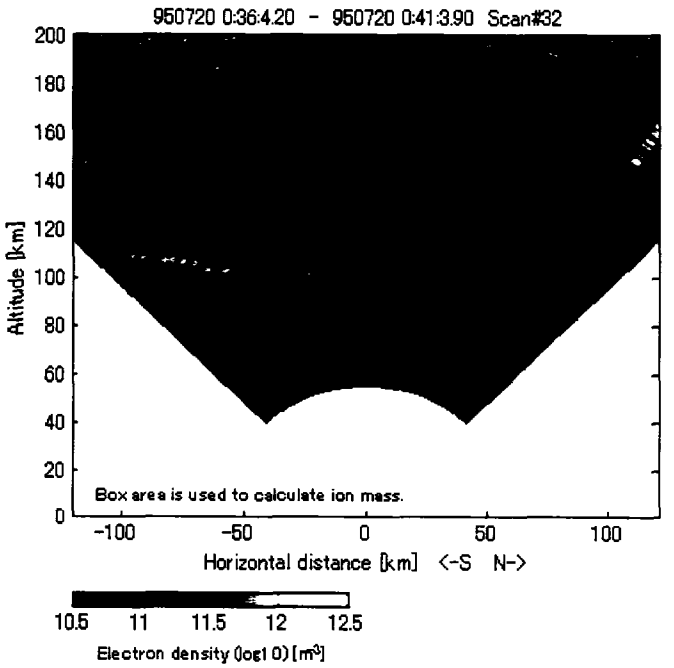

(a) Electron density

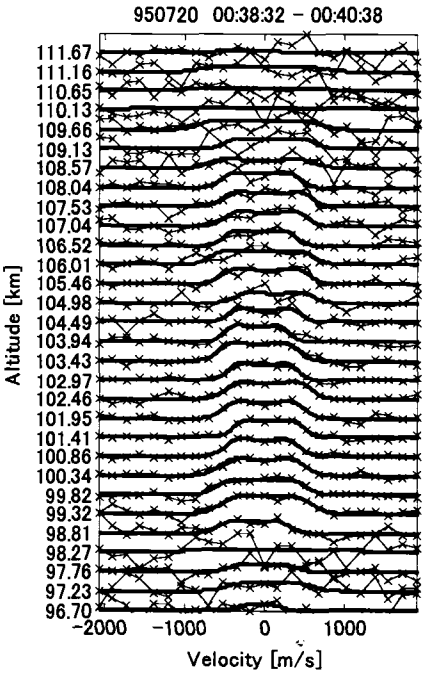

(b) Spectra

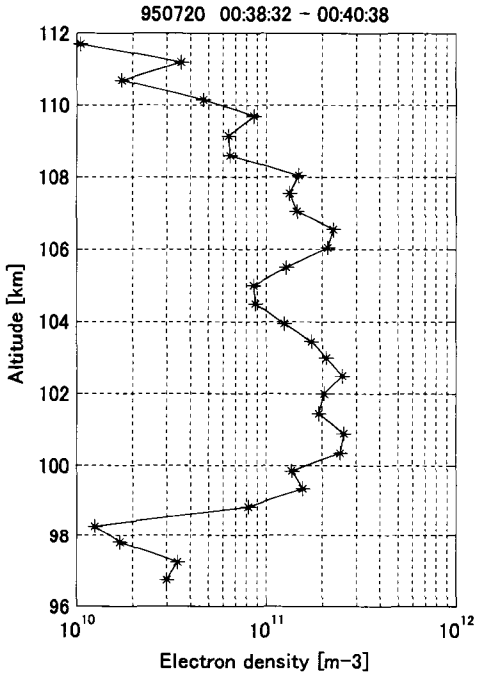

(c) Electron density in the layer

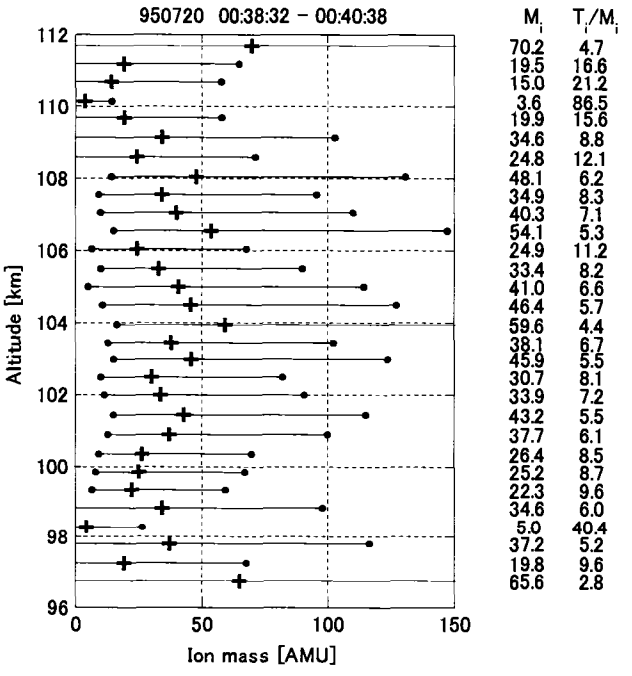

(d) Ion mass in the layer

Fig. 6.66 Ion mass estimation in the layer during 0:38-0:40UT on Jul. 20th 1995.

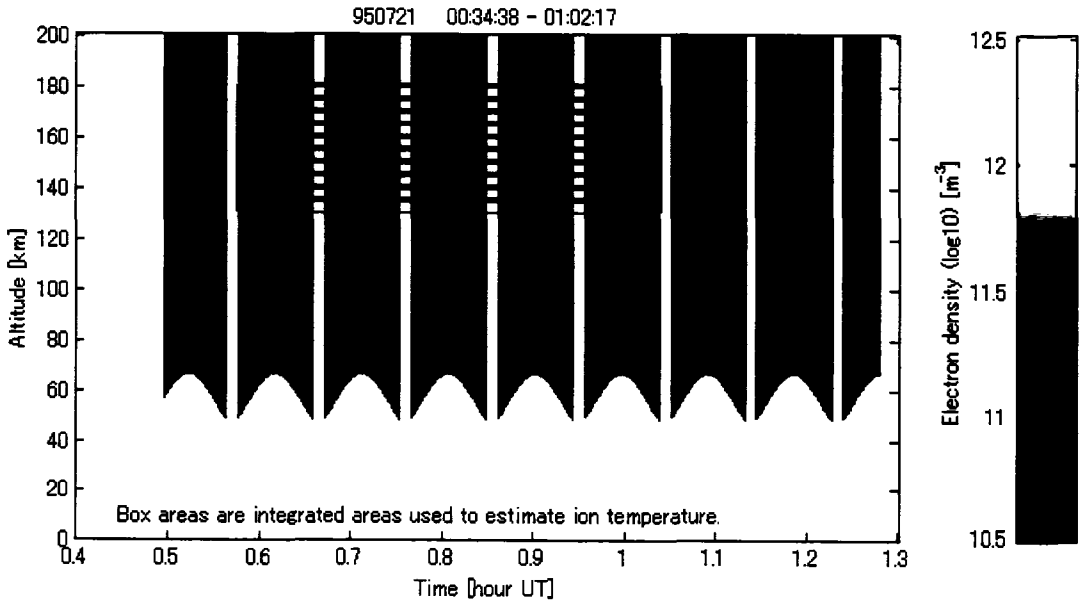

(a) Electron density

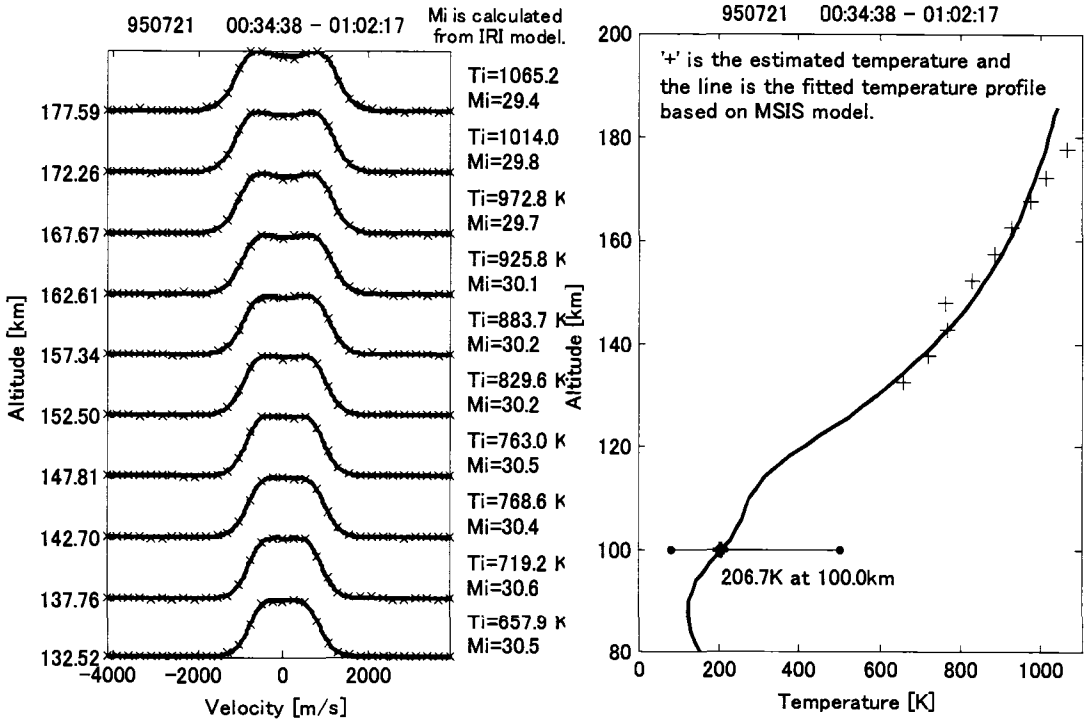

(b) Spectra (c) Ion temperature

Fig. 6.67 Ion temperature estimation using the long pulse mode on Jul. 21st 1995.

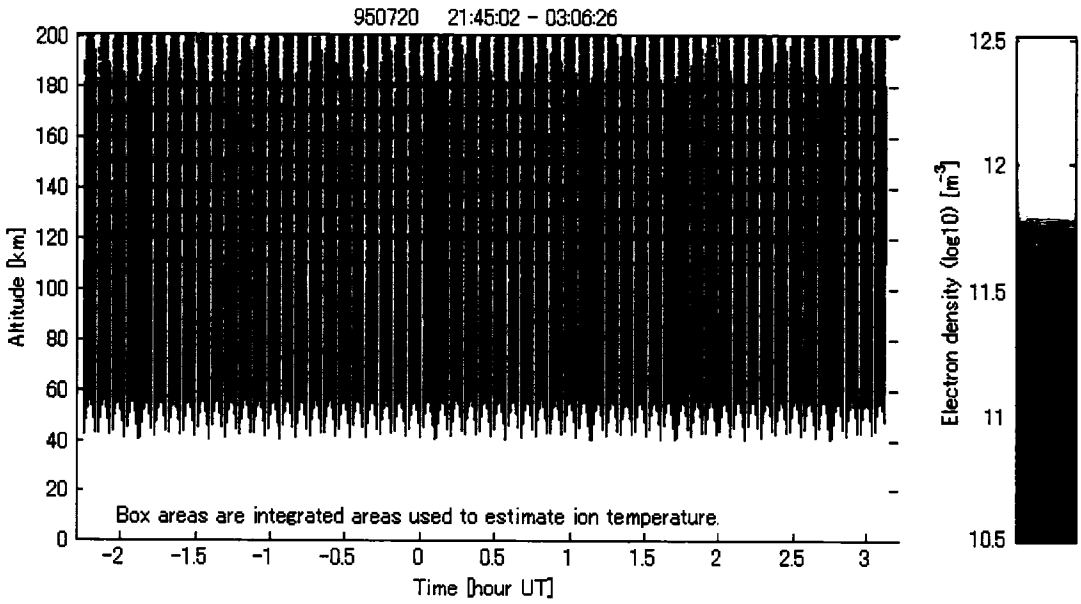

(a) Electron density

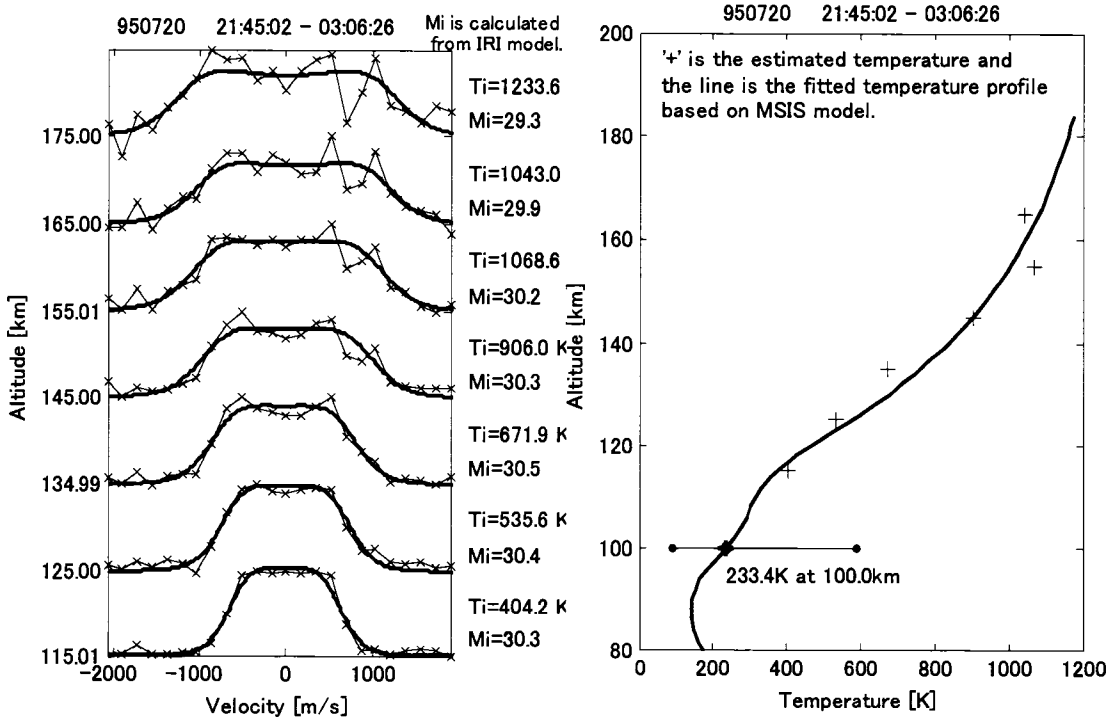

(b) Spectra

(c) Ion temperature

Fig. 6.68 Ion temperature estimation using the short pulse mode on Jul. 21st 1995.

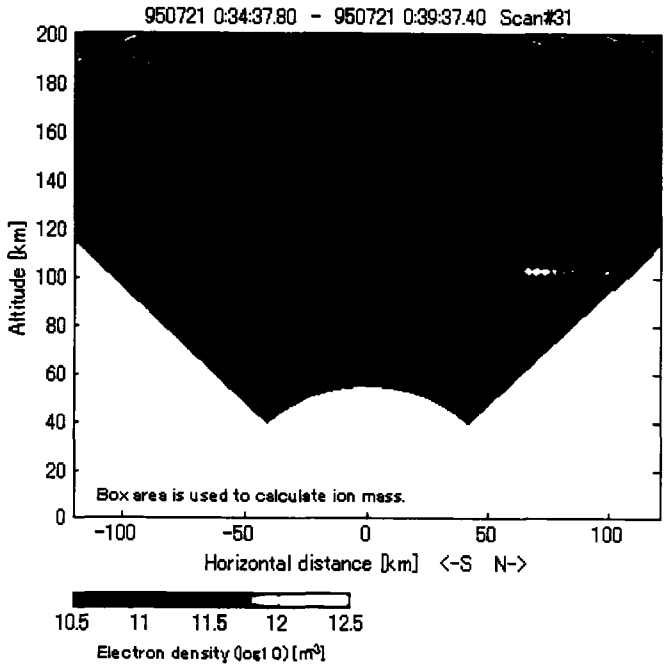

(a) Electron density

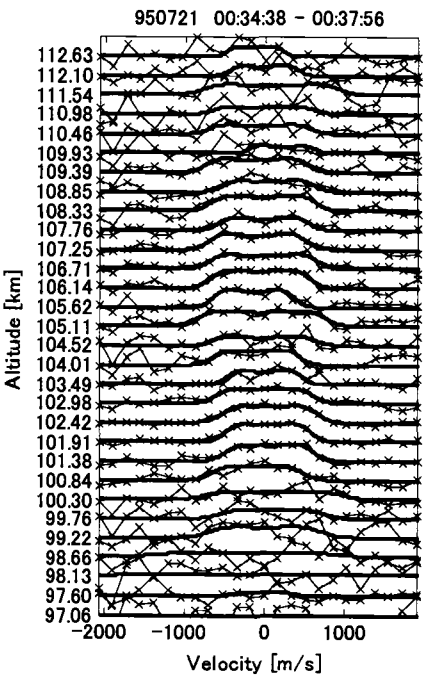

(b) Spectra

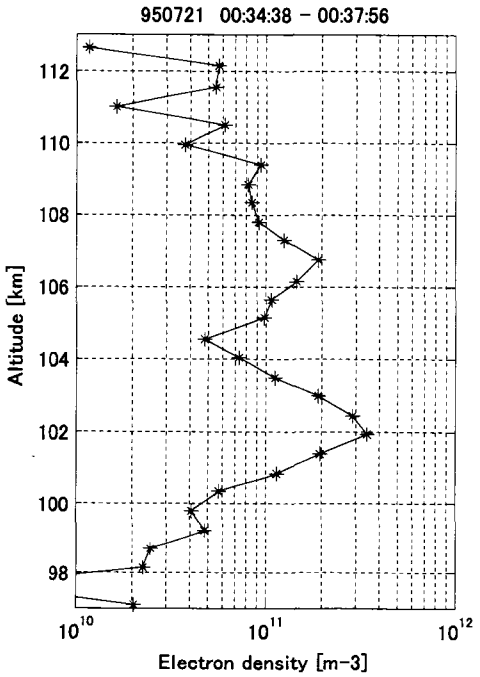

(c) Electron density in the layer

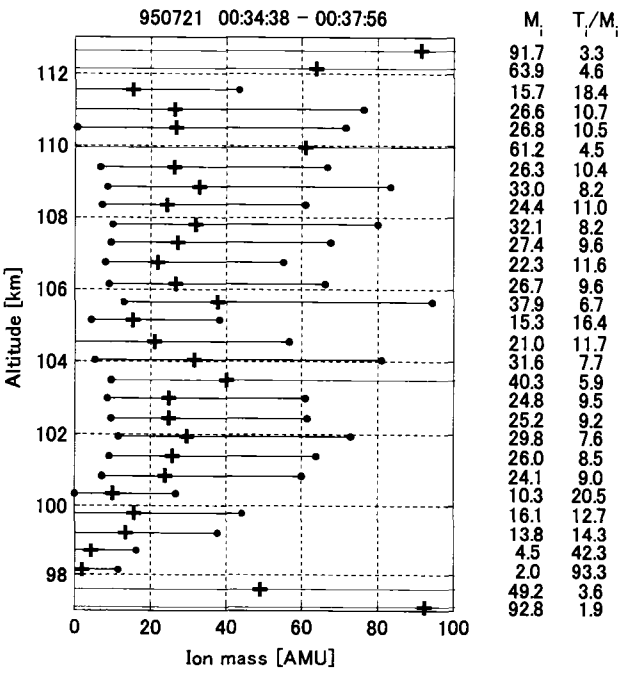

(d) Ion mass in the layer

Fig. 6.69 Ion mass estimation in the layer during 0:34-0:37UT on Jul. 21st 1995.

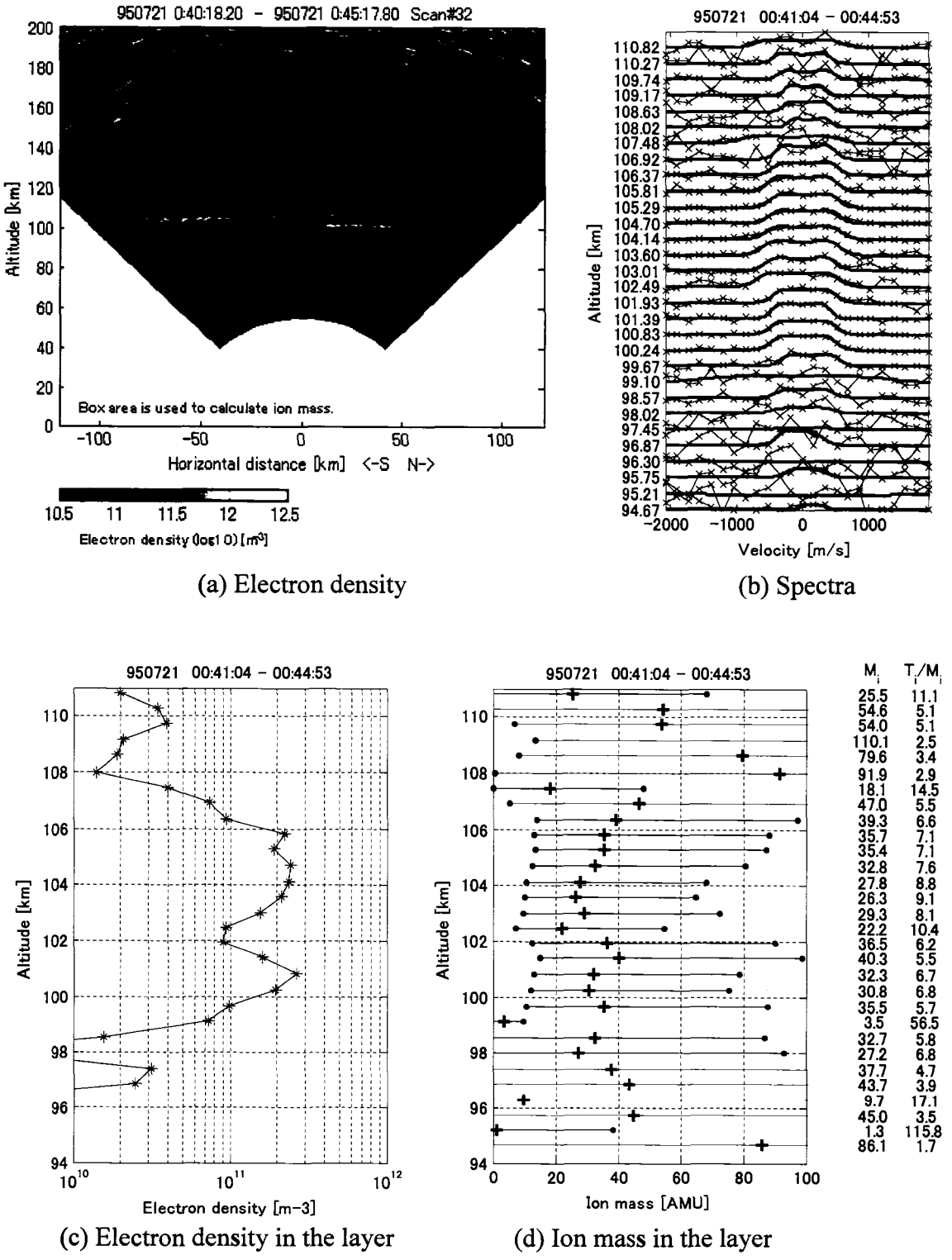

(a) Electron density (b) Spectra

(c) Electron density in the layer (d) Ion mass in the layer

Fig. 6.70 Ion mass estimation in the layer during 0:41-0:44UT on Jul. 21st 1995.

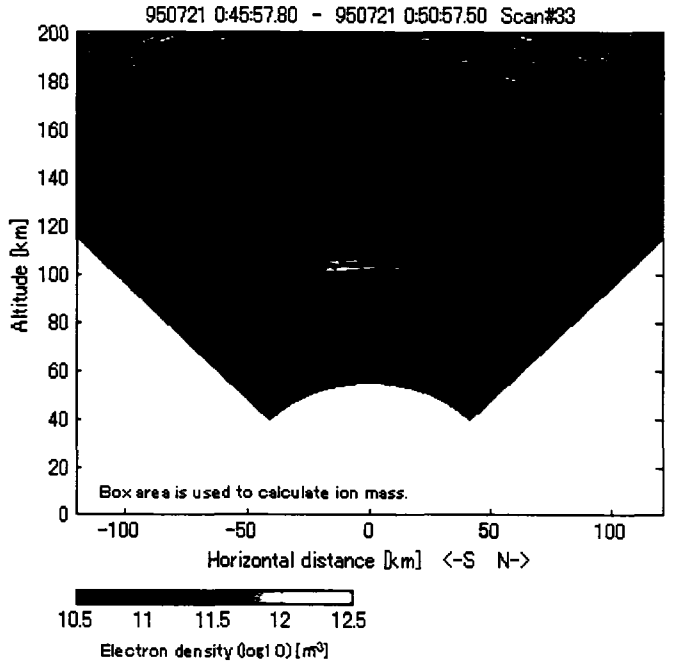

(a) Electron density

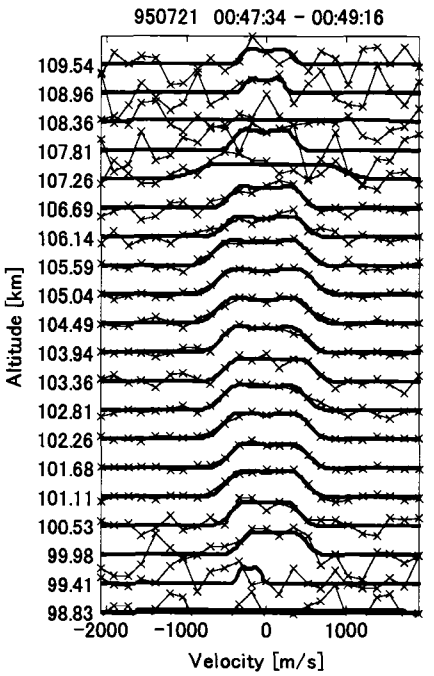

(b) Spectra

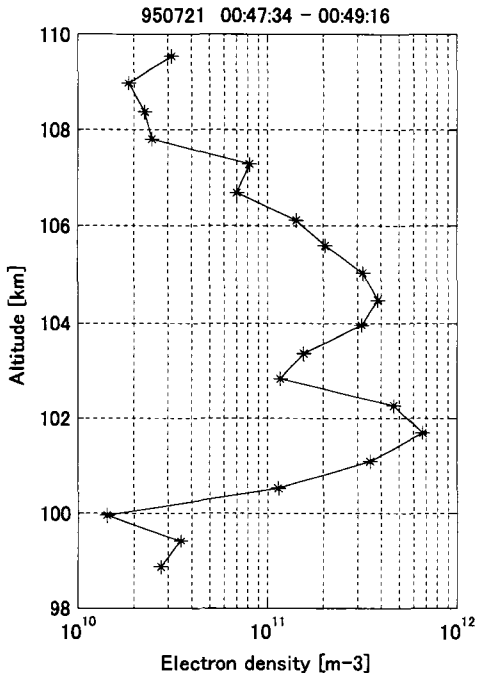

(c) Electron density in the layer

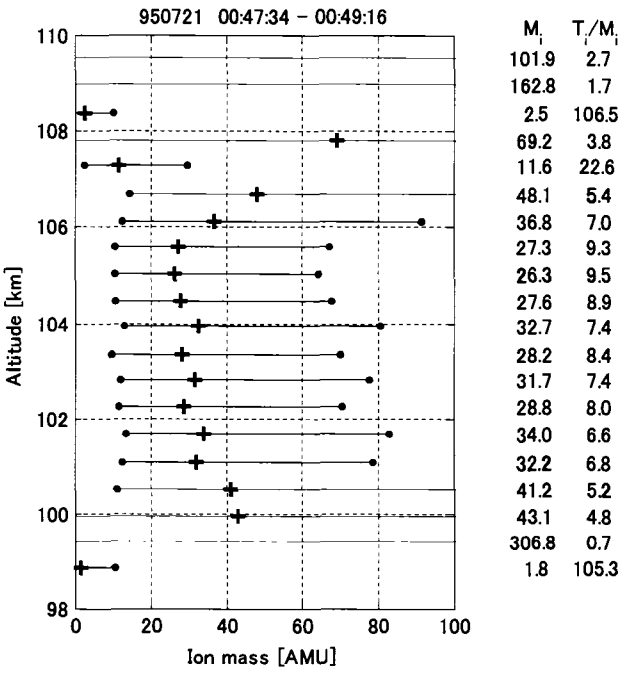

M_i	T_i/M_i
101.9	2.7
162.8	1.7
2.5	106.5
69.2	3.8
11.6	22.6
48.1	5.4
36.8	7.0
27.3	9.3
26.3	9.5
27.6	8.9
32.7	7.4
28.2	8.4
31.7	7.4
28.8	8.0
34.0	6.6
32.2	6.8
41.2	5.2
43.1	4.8
306.8	0.7
1.8	105.3

(d) Ion mass in the layer

Fig. 6.71 Ion mass estimation in the layer during 0:47-0:49UT on Jul. 21st 1995.

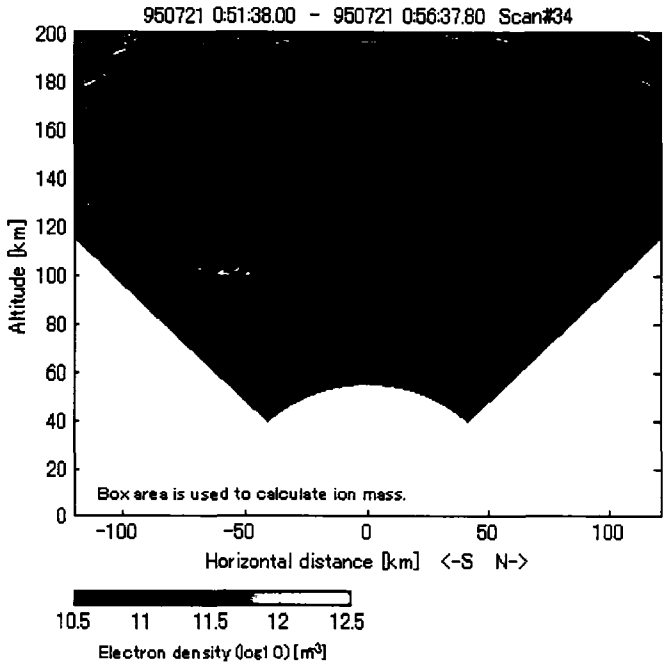

(a) Electron density

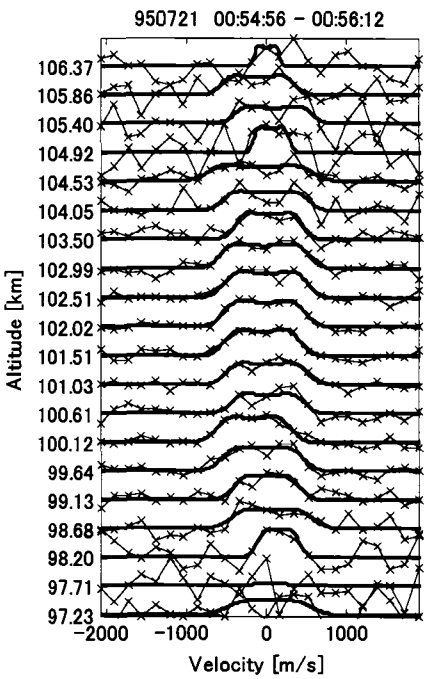

(b) Spectra

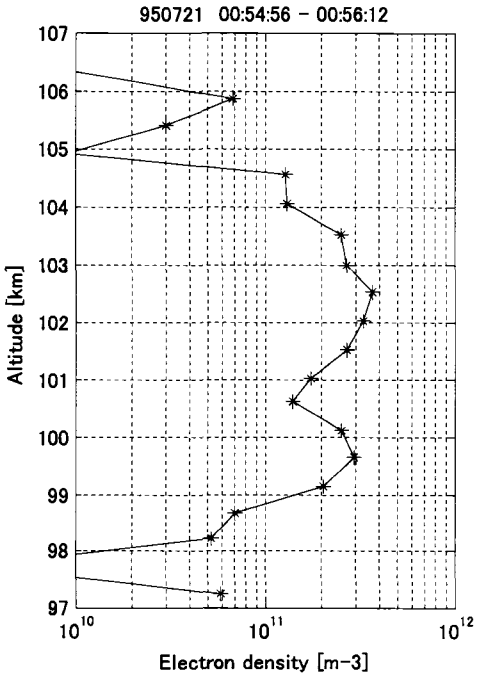

(c) Electron density in the layer

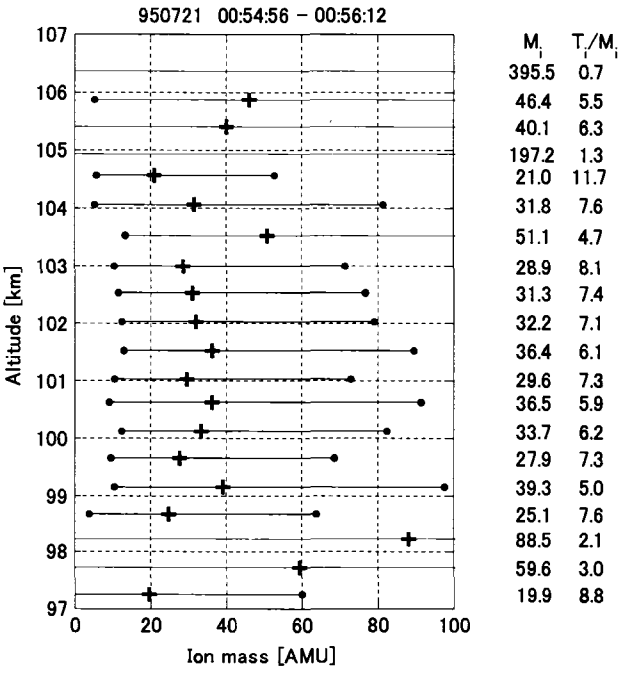

(d) Ion mass in the layer

Fig. 6.72 Ion mass estimation in the layer during 0:54-0:56UT on Jul. 21st 1995.

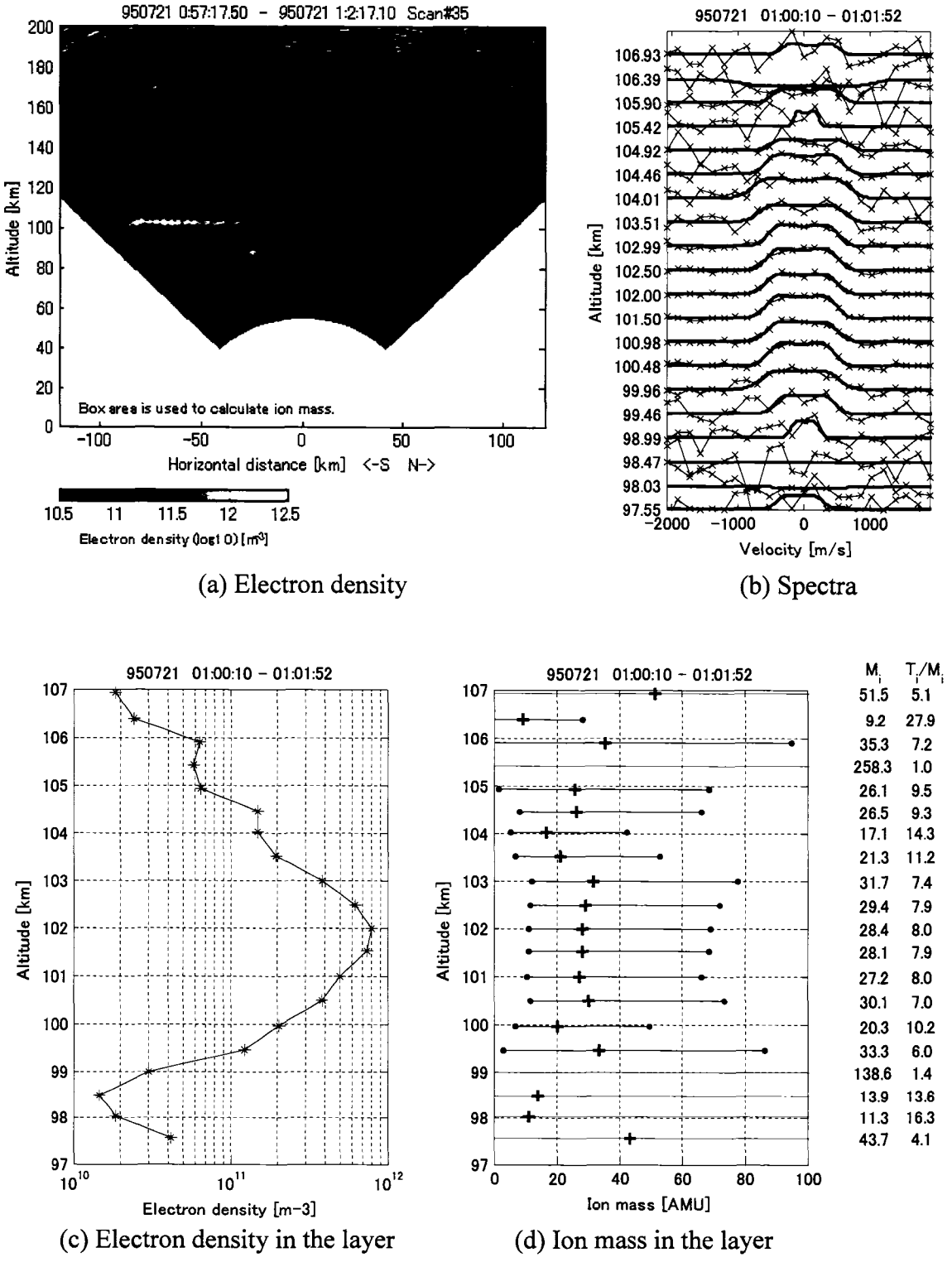

(a) Electron density (b) Spectra

(c) Electron density in the layer (d) Ion mass in the layer

Fig. 6.73 Ion mass estimation in the layer during 1:00-1:01UT on Jul. 21st 1995.

6.3 Discussion

Due to the large number of data all could not be presented here; the data in this dissertation represent a carefully selected subset of the most interesting data. Data supporting Nygren's hypothesis were presented in chapter 4. In Fig.6.3 - 6.15 (from Aug. 10th 2000) we may see a tendency for ion mass in the upper part of a layer to be greater than ion mass in the lower part of a layer. Other data exhibited a similar tendency for ion mass distribution, although temperature errors on other days were larger than on Aug. 10th 2000.

In some cases, two closely spaced layers appeared in which ion mass in the upper layer was greater than in the lower layer. In Fig.6.12, the two layers were spaced about 3 km apart. The absolute value of the ion mass in this case is not reliable, as is shown by the error bar; however we can rely on the ratio of upper layer ion mass to lower layer ion mass if the layers are close enough in altitude.

The ion mass ratio between the two layers in Fig.6.12 is 33.9/22.5 = 1.51. If we assume both layers contain only Mg^+(24AMU) and Fe^+(56AMU) and the lower layer contains mainly Mg^+, the upper layer should contain 62% Mg^+ and 38% of Fe^+ since the mean ion mass should be 36.2(=24*1.51) in the upper layer. Alternatively, if we assume the upper layer contains mainly Fe^+, the lower layer should be composed of 59% Mg^+ and 41% of Fe^+, since the mean ion mass should be 37.1(=56/1.51) in the lower layer. In either case, we can conclude that the lower layer should contain 59-100% of Mg^+ and 0-41% of Fe^+, and the upper layer should contain 0-62% of Mg^+ and 38-100% of Fe^+.

There exists a different type of double layer, which exhibits a wider altitudinal space between the two layers. In those cases, the upper layer and the lower layer sometimes appear to inhabit a different horizontal location, and the upper layer is sometimes tilted or bent as shown in Fig.6.18 and Fig.6.33.

There is a fundamental question about whether this wide spaced double layer was formed by the same mechanism as the narrow spaced double layer, which seems to be formed by the same mechanism as the top heavy single layer.

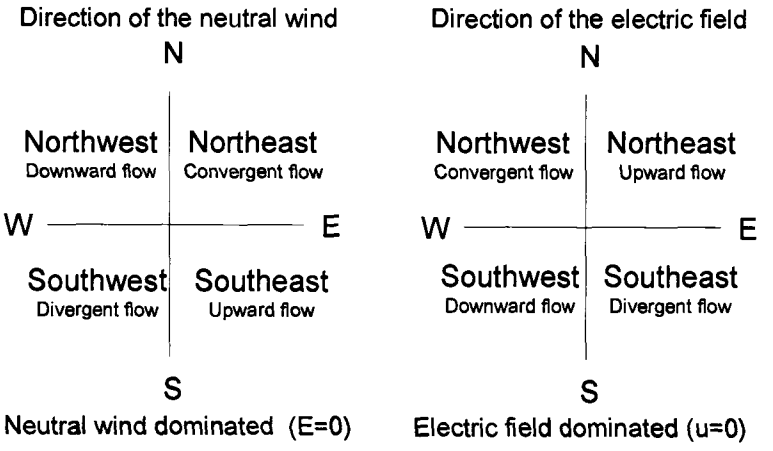

Fig. 6.74 Effects of neutral wind and electric field on vertical ion flow.

Although there are data which suggest the wide spaced double layer is formed when a single layer splits, as shown in Fig.6.33, a different mechanism might be responsible for creating the observed difference between the wide spaced and narrow spaced double layers. As we can see in Fig. 6.12(a) and other figures of most single layers, both the narrow spaced double layer and the flat single layer seem to be strictly restricted in altitude by some force, whereas the top layers of both the wide spaced double layer and the tilted layers seem to change altitude easily. The stepped layer shown in Fig.6.64 and Fig.6.65 may include elements of both altitude restriction and liberation.

In order to find the reason for restriction and liberation in layer altitude, we have to discuss the mechanism of layer formation. As mentioned in Chapter 4, there are two major factors involved in layer formation: neutral wind and electric field. As is clear from an examination of Eq.(4.1), those factors produce vertical ion flow as shown in Fig.6.74.

First we will consider a neutral wind dominated mechanism. Fig.6.75 shows a plot of vertical ion velocities versus altitude. Ion velocities were calculated using Eq. (4.1), assuming a neutral northeast wind of 50m/s; wind direction and speed were both kept uniform with altitude. As Fig.6.74 suggests, Fig. 6.75 shows that the heavy ion will concentrate in a region located several kilometers higher than the region where the light ion concentrates. However, this result was achieved by assuming a uniform neutral wind, whereas actual neutral wind varies with altitude.

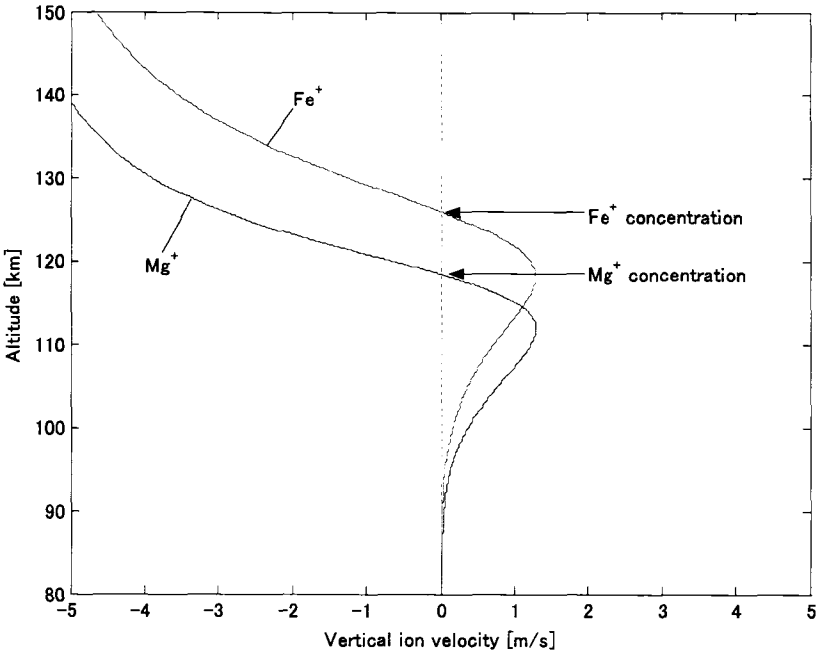

Fig. 6.75 Vertical ion velocity calculated with uniform neutral wind of 50m/s with NE. direction. B = 50000nT, geomagnetic dip angle = 80deg., and E = 0V/m.

Fig.6.76 shows a neutral wind velocity profile at 2:00UT on Aug. 10th 2000 calculated using the Horizontal Wind Model (http://nssdc.gsfc.nasa.gov/space/model/atmos/hwm.html). We can see that the direction of wind changes with small changes in altitude. Therefore, it is highly possible that the significant vertical ion flow is not convergent flow but rather flow in one direction, upward or downward, even though the direction of the neutral wind is northeast within the small region of altitude where it is widely thought convergent flow is produced.

Fig.6.77 shows vertical ion velocity calculated using the neutral wind shown in Fig.6.76. Contrary to expectation, the light ion concentrates at a higher altitude than does the heavy ion. This result shows that the ion mass profile is not always top heavy in the complex neutral wind situation, and it is also reasonable to suppose the space between two layers of the double layer may not always be narrow but may sometimes become wider.

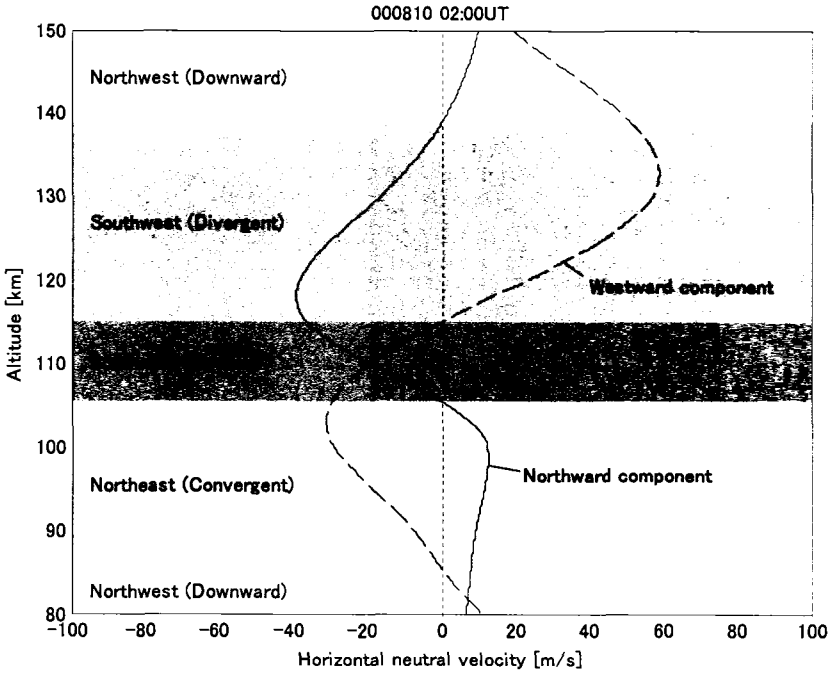

Fig. 6.76 Horizontal neutral wind velocity calculated using the Horizontal Wind Model. (http://nssdc.gsfc.nasa.gov/space/model/atmos/hwm.html)

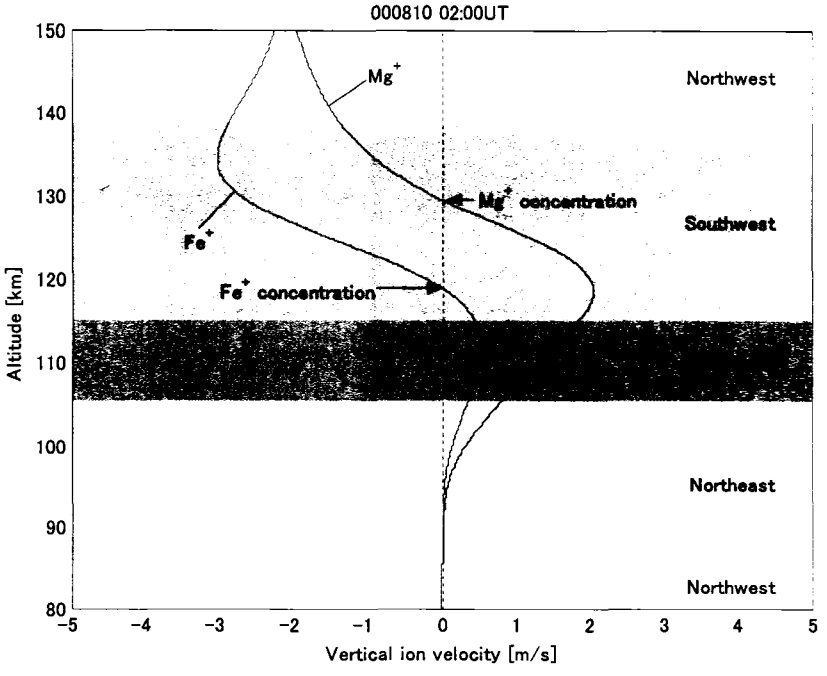

Fig. 6.77 Vertical ion velocity calculated with neutral wind as shown in Fig.6.76. Other parameters are B = 50000nT, geomagnetic dip angle = 80deg., and E = 0V/m.

Next, we will consider electric field effects. Fig.6.78 shows vertical ion velocity calculated using a uniform electric field of 50mV/m with northwest direction and with the neutral wind shown in Fig.6.76. Under these conditions, the heavy ion concentrates at a higher altitude than does the light ion. In reality the electric field may be complex and may include a vertical component, whereas the neutral wind has hardly any vertical component. It is possible that the complexity of the electric field may produce irregular layers, such as tilted or bended layers.

From the above discussion, we can conclude that whether the layer is formed by electric field or neutral wind, a uniform electric field or a uniform neutral wind with appropriate direction may produce a top heavy flat thin layer and a narrow spaced double layer. However, a nonuniform neutral wind may produce wide spaced double layers within which the ion mass of the upper layer is not always heavier than the ion mass of the lower layer. In addition, a nonuniform electric field may also produce irregular layers such as tilted, bent, and wide spaced double layers.

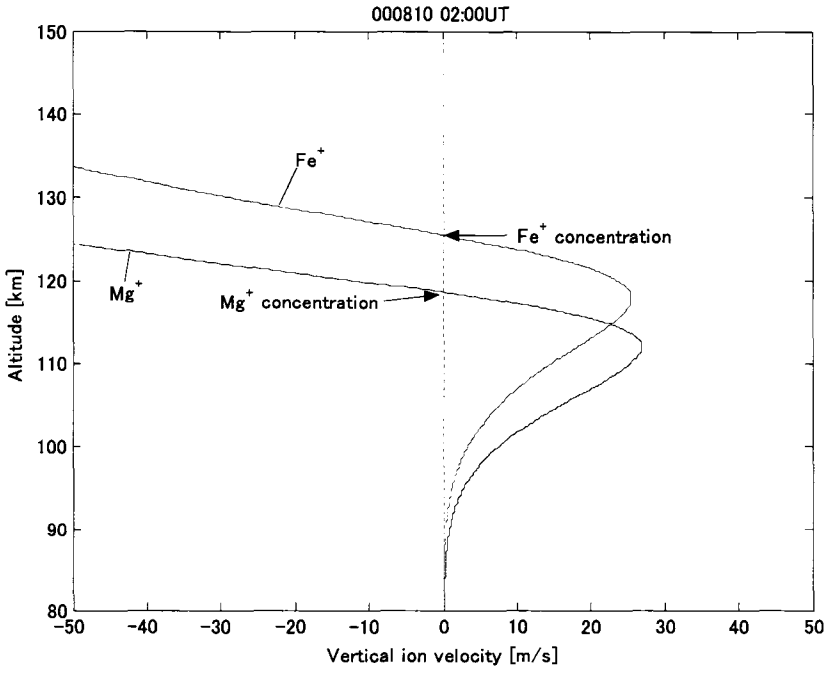

Fig. 6.78 Vertical ion velocity calculated with E = 50mV/m with NW direction. The neutral wind is as Fig.6.76, B = 50000nT, and geomagnetic dip angle = 80deg.

CHAPTER 7
SUMMARY AND CONCLUSIONS, POSSIBLE FUTURE DIRECTIONS

7.1 Summary and Conclusions

A number of incoherent-scatter radar experiments designed to observe thin sporadic ion layers have been studied with the objective of evaluating the mean ion mass within the layers and, where possible, to determine the mean ion mass as a function of altitude within the layers. This thesis represents the first extensive analysis of ion mass data utilizing a relatively large number of varied sporadic-*E* structures in the upper atmosphere. Although an extensive database was available for this work, the number of experimental periods with useful data was limited. The limited number of useful experiments is mainly due to the sporadic nature, in both space and time, of these events. Since incoherent-scatter radar systems are costly to operate, this has limited the radar operation to specific scheduled time periods which in turn limits the amount of useful data that are collected that include these sporadic events. Nevertheless there are a number of excellent case studies that have been analyzed and presented here. There are two general aspects of these data that are new; first we have events that show the altitude variation of ion mass within individual layers, and second we have examples of double layers with characteristics that have not been observed or studied by other researchers.

- Single Sporadic-*E* layers

  Some examples of these structures are shown in figures 6.5(a) through 6.10(a). These are expected structures that have been suggested from historic ionosonde records and observed with previous radar observations. The data confirm that these structures typically have peak densities of about 10^6 cm^{-3} or more, drift north to south, and have thicknesses of about one km. The observations and new analysis presented in this thesis found mean ion masses of about 20-25 amu at the bottom and about 35-40 amu at the top for most examples studied. This is turn suggests that the heavy Fe^+ ions tend to reside (in accordance with theory) at the top of the layer. Lighter ions

such as Mg^+ , Si^+, and Na^+ are therefore more prevalent near the bottom, however the data show a relatively small altitude variation of ion mass as a function of altitude. The small altitude trend in the ion mass values, and magnitudes of the ion masses, computed from the radar data are quite consistent over many experiments and is generally consistent with expectations based on mass spectrometer measurements from rocket experiments as shown for example in figures 1.3 and 1.4 where all the light ions including Si^+ are plotted.

The observations have shown these layer structures to sometimes thicken to about 2-3 km and for some examples split into two distinct layers very close in altitude. The figure 6.12(a) shows this effect. For these cases the general altitude variation of the mean ion mass is similar to the thin single layer cases. For the limited number of cases studied the twin closely spaced layers do not represent distinctly different ion masses and is contrary to our initial idea that the top layer might have predominantly heavy ions (Fe^+), whereas the lower layer would be primarily composed of lighter ions (Mg^+, Si^+, Na^+, etc). This in turn suggests that the double layers are each independently formed, and are not the result of a mass separation process in a single layer formation mechanism.

Occasionally the layers are not horizontal and an example is shown in figure 6.65(a). The altitude for convergent flow in the vertical direction depends on the electric field direction as explained in chapter 4. The topic of electric fields in the data has not been addressed in this thesis, however changes in the electric field direction over the observation distance of the layer is the most probable explanation. The conventional concept is that sporadic layers are primarily horizontal in nature, however during the course of this analysis many cases of more complex shape were discovered.

- Complex Widely-Spaced Double Layers

This thesis presents new observations of a variety of complex sporadic layers that are unexpected and not reported in the literature. It is suggested that the background

neutral wind (that is not easily measurable with adequate altitude and time resolution) is probably changing rapidly with altitude in magnitude and/or direction. The combination of neutral and ion dynamics, and their variations over altitude, are likely causes and this is a topic for future researchers. The figure 6.18(a) for example shows two layers spaced by about 10km with different horizontal gradients. The data suggest similar ion composition in both structures. Other examples of widely-spaced layers (about 10km) are shown in figures 6.19(a) and 6.20(a); the ion composition in upper and lower layers are similar, viz about 30 amu. The figures 6.33(a) and 6.34(a) are other interesting examples. The similar ion mass values in each layer again suggests that the two widely-spaced layers are formed independently where two convergent nulls in the vertical component of the ion velocity act to form two layers.

The issue of a possible systematic error in the ion mass values has been a concern. Although the there are minimal errors for the process of fitting data taken within a sporadic layer to a theoretical spectrum, it needs to be emphasized that the computations fit the data to determine the ion temperature-mass ratio. The ion temperature has been independently determined using a procedure explained in chapter 6 where a model has been fitted to radar long-pulse temperature data acquired above the layer altitude. Possible systematic errors in the procedure to determine the ion temperature will therefore possibly bias the ion mass values that are computed. This is a limitation that is intrinsic in the data and future experiments with other facilities may improve these uncertainties. Although the values computed are not inconsistent with expectations from rocket mass spectrometer data, it would not be unreasonable to associate possible systematic errors of 5-10 amu in the data values.

7.2 Possible Future Directions

The experimental work of this thesis is limited by the weak radar signal returns. This has resulted in limitations on the ability to measure the background plasma density and temperature surrounding the sporadic-*E* structures. The layers themselves are quite thin and require appropriately fine range resolution that in turn demands wide receiver bandwidths and hence results in relatively noisy signals; only the very dense layers have been useful for determining ion mass values.

The experiments used to derive data for this thesis demand both high range-resolution and high sensitivity, two demands which are difficult to satisfy simultaneously. Better sensitivity can be obtained with a longer pulse length, for example, but long pulse length compromises the range resolution. The Søndestrøm radar has a considerably smaller antenna aperture than does the large dish antenna at the Arecibo Observatory, and the maximum duty factor of the Søndestrøm radar transmitter is about 3% which is somewhat less than the EISCAT European incoherent-scatter radar. While small gains in SNR could be achieved with the Søndrestøm radar by fully utilizing the available transmitter duty factor, it is unlikely that significantly better results, or science gains, would result.

The experiments have used an unmodulated long pulse (48 km range resolution) for temperature estimation as well as a modulated pulse that provides high range resolution (600 m range resolution) for mass estimation inside thin layers. If there was another independent method to determine, or estimate, temperatures one could avoid transmitting the long pulse and thereby effectively double the number of high-resolution radar pulses in a given integration time, increasing the SNR of layer data. It is unclear how such an alternative temperature estimation could be achieved except by relying on a statistical model of atmospheric temperatures, the use of which would then introduce other uncertainties.

Another factor is range resolution. The thin-layer data in this thesis were collected using 600m range resolution corresponding to a 2MHz pulse bandwidth. The Søndestrøm radar is potentially capable of 300m range resolution; however there is a corresponding

decrease in SNR, and some initial tests with 300m resolution suggested that the potential loss of data quality was not worth the gain in resolution. In retrospect, some of the layer data have proven to have quite high SNR so that it would be feasible to duplicate some experiments at 300m resolution. Such duplication might possibly provide a better altitude profile within a layer, but that is unlikely to change the scientific conclusions of this thesis.

It is evident that while small gains would be possible with some changes in experimental procedures, there is a fundamental limitation in the overall sensitivity of the Søndrestrøm facility for these experiments. This leads us to focus our suggestions on helping to guide new radar designs that would provide better results in demanding experiments that require high resolution in poor signal-noise situations. There are two initiatives to develop new radar designs: first the US National Science Foundation initiative to develop a modular phased-array system, and second a possible new Japanese radar for installation in Antarctica.

A significant difficulty with the Søndrestrøm radar is the operating frequency (1290 MHz) which limits the radar's capability to make measurements at low densities (less than about 10^4 cm^{-3}). This difficulty arises because the condition for incoherent-scattering is that the radar wavelength must be greater than the plasma Debye length. For low background ionospheric densities that are typical of the lower ionosphere the Debye length becomes too large. Therefore a lower frequency, say 300-450 MHz, would permit measurements at lower densities (about 10^3 cm^{-3}). It is not feasible to use an operating frequency much lower than about 300 MHz because sky noise increases significantly at lower frequencies.

The possibility of adding system enhancements, viz. antenna aperture, transmitter peak pulse power and duty factor, is largely controlled by cost. Significant enhancement would be achieved with a system that featured ≈4 MW peak pulse power and ≈ 10% duty factor, coupled to a large antenna with dimensions ≈ 200x200m. Transmitter bandwidth up to 5 MHz would also permit very high range resolution for experimental situations with strong signals; this would permit measurements inside layers much thinner than have

been studied in this thesis. The new phased-array radar being installed at Poker Flat Alaska should provide significant advantages, viz lower frequency, larger antenna aperture, and more rapid beam scanning (although the scan angle is less than a dish antenna). The other hope for the future is a planned Japanese system shown in Figure 7.1.

Fig. 7.1 A possible phased-array IS radar for Antarctica.

REFERENCES

Aikin A.C., R.A. Goldberg, Metallic ions in the equatorial ionosphere. *J. Geophys. Res.* 78, 734-745, 1973.

Axford, W.I., The formation and vertical movement of dense ionized layers in the ionosphere due to neutral wind shear. *J. Geophys. Res.* 68, 769-779, 1963.

Axford, W.I., D.M. Cunnold, The windshear theory of temperate zone sporadic E. *Radio Sci.*, 1, 191-198, 1966.

Barker, R.H., Group synchronization of binary digital systems, In: Jackson, W. (ed.), Communication theory, Academic Press, New York, 273-287, 1953.

Bedey, D. F., B. J. Watkins, Diurnal occurrence of thin metallic ion layers in the high-latitude ionosphere. *Geophys. Res. Lett.*, 25, 3767-3770, 1998.

Bedey, D. F., B. J. Watkins, Simultaneous observations of thin ion layers and the ionospheric electric field over Sondrestrom. *J. Geophys. Res.*, 106, 8169-8183, 2001.

Behnke, R.A., J.F. Vickery, Radar Evidence for Fe+ in a Sporadic-E layer. *Radio Sci.*, 10, 325-327, 1975.

Bristow, W. A., B. J. Watkins, Numerical simulation of the formation of thin ionization layers at high latitudes, *Geophys. Res. Lett.*, 18, 404-407, 1991.

Bristow, W. A., B. J. Watkins, Incoherent scatter observations of thin ionization layers at Sondrestrom, *J. Atmos. Terr. Phys.*, 55, 873-894, 1993.

Dougherty, J. P., D. T. Farley, A theory of incoherent scattering of radio waves by a plasma. *Proc. Roy. Soc. London A*, 259, 79-99, 1960.

Dougherty, J. P., D. T. Farley, A theory of incoherent scattering of radio waves by a plasma (3), Scattering in a partly ionized gas. *J. Geophys. Res.*, 68, 5473-5486, 1963.

Dungey, J.W., Effect of a magnetic field on turbulence in an ionized gas. *J. Geophys. Res.*, 64, 2188-2191, 1959.

Evans, J.V., Theory and practice of ionosphere study by Thomson scatter radar. Proc. IEEE, 57, 496-530, 1969.

Farley, D. T., A theory of incoherent scattering of radio waves by a plasma (4). The effect of unequal ion and electron temperature. *J. Geophys. Res.*, 17, 4091-4098, 1966.

Farley, D. T., Incoherent scatter correlation function measurements. *Radio Sci.*, 4, 935-953, 1969.

Farley, D. T., Multiple-pulse incoherent scatter correlation function measurements. *Radio Sci.*, 7, 661-666, 1972.

Fejer, J.A., Scattering of radio waves by an ionized gas in thermal equilibrium. *Can. J. Phys.*, 38, 1114-1133, 1960.

Fried, B. D., S. D. Conte, The plasma dispersion function. New York Academic Press, New York, 1961.

Goldberg, R.A., Silicon ions below 100km: A case for Si02. *Radio Sci.*, 10, 329-334, 1975

Grebowsky, J.M., and A.C.Aikin, In Situ Measurements of Meteoritic Ions, in E.Murad and I.P.Williams (ed), *"Meteors in the Earth's Upper Atmosphere"*, Cambridge University Press, 189-214, 2002.

Huuskonen, A., T. Nygren, L. Jalonen, N. Bjorna, T. L. Hansen, A. Brekke, T. Turunen, Ion composition in sporadic E layers measured by EISCAT UHF radar. *J. Geophys. Res.*, 93, 14603-14610, 1988.

Johannesen A., D. Krankowsky, Positive-ion composition measurement in the upper mesosphere and lower thermosphere at a high latitude during summer. *J. Geophys. Res.* 77, 2888-2901, 1972.

Johannessen, A., D. Krankovwsky, Daytime positive ion composition measurement in the altitude range 73-137 km above Sardinia. *J. Atmos. Terr. Phys.*, 36, 1233-1247, 1974.

Kopp, E., On the abundance of metal ions in the lower ionosphere. *J. Geophys. Res.*, 102, 9667-9674, 1997.

Martin, P., G. Donoso, J. Zamudio-Cristi, A modified asymptotic Pade method: Application to multiple approximation for plasma dispersion function Z. *J. Math. Phys.* 21, 280-285, 1980.

Narcisi, R.S., A.D. Bailey, Mass spectrometer measurements of positive ions at altitudes from 64 to 112 kilometers. *J. Geophys. Res.* 70, 3687-3700, 1965.

Narcisi, R.S., A.D. Bailey, L. Della Lucca, Composition measurements of a sporadic-E in the night time lower ionosphere. *Space Res.* 7, 123, 1968.

Narcisi, R.S., Composition Studies of the Lower Ionosphere. In: Veriani, F. (Ed.), *Physics of the Upper Atmosphere*, Editrice Compositori Publisher, Bologna in Italy, pp. 12-59, 1971.

Nygren, T., L. Jalonen, J. Oksman, T. Turunen, The role of electric field and neutral wind direction in the formation of sporadic E-layers. *J. Atmos. Terr. Phys.*, 46, 373-381, 1984a.

Nygren, T., L. Jalonen, A. Huuskonen, T. Turunen, Density profile of sporadic E-layers containing two metal ion species, *J. Atmos. Terr. Phys.*, 46, 885-893, 1984b.

Rino, C. L., M. J. Baron, G. H. Burch, O. de la Beaujardiere, A multipulse correlator design for incoherent scatter radar, *Radio Sci.*, 9, 1117-1127, 1974.

Rummler, W. D., Introduction of a new estimator for velocity spectral parameters. *Tech Memo*. MM-68-4121-5, Bell Telephone Laboratories, Whippany, N.J., 1968.

Skolnik, M.I(Chief editor), Radar handbook 2nd ed., McGraw-Hill Publishing Company, New York, 1990.

Turunen, T., J. Silen, T. Nygren, L. Jalonen, Observation of a thin Es-Layer by the EISCAT radar. *Planet. Space Sci.*, 33, 12, 1407-1416. 1985.

Turunen, T., T. Nygren, A. Huuskonen, L. Jalonen, Incoherent scatter studies of sporadic-E using 300m resolution, *J. Atmos. Terr. Phys.*, 50, 277-287, 1988.

Whitehead, J.D., The formation of the sporadic E-layer in the temperate zones. *J. Atmos. Terr. Phys.*, 20, 49-58, 1961.

Whitehead, J.D., Mixtures of ions in the wind shear theory of sporadic E. *Radio Sci.*, 1, 198-203, 1966.

Young, J.M., C.Y. Johnson, J.C. Holmes, Positive ion composition of a temperate-latitude sporadic E layer as observed during a rocket flight. *J. Geophys. Res.* 72, 1473-1479, 1967.

Zamlutti, C. J., Design of Barker coded multiple pulse experiments, *J. Atmos. Terr. Phys.*, 42, 975-982, 1980.

Zamlutti, C. J., D. T. Farley, Incoherent scatter multiple-pulse measurements at Arecibo, *Radio Sci.*, 10, 573-580, 1975.

Zbinden, P.A., M.A. Hildago, P. Eberhardt, and J. Geiss, Mass spectrometer measurements of the positive ion composition in the *D*- and *E*-regions of the ionosphere. *Planet. Space Sci.*, 23, 1621-1642, 1973.

APPENDIX
CALCULATION OF PLASMA DISPERSION FUNCTION

A.1 Definition and Properties of Plasma Dispersion Function

The plasma dispersion function is defined as

$$\begin{aligned} G(z) &= 2e^{-z^2}\int_{i\infty} e^{p^2}dp \\ &= 2ie^{-z^2}\int_z^{\infty} e^{-q^2}dq \\ &= \sqrt{\pi}\int_{-\infty}^{\infty}\frac{e^{-s^2}ds}{s+z}. \end{aligned} \tag{A.1}$$

Note that the sign of z is opposite from the function mentioned in Fried and Conte(1961). This function has the following properties:

1) $$\begin{aligned} G(-z^*) &= \sqrt{\pi}\int_{-\infty}^{\infty}\frac{e^{-s^2}ds}{s-z^*} = \sqrt{\pi}\int_{\infty}^{-\infty}\frac{e^{-t^2}(-dt)}{(-t)-z^*} = -\left[\sqrt{\pi}\int_{-\infty}^{\infty}\frac{e^{-t^2}dt}{t+z}\right]^* \\ &= -G^*(z) \end{aligned} \tag{A.2}$$

2) $$\begin{aligned} G(z)+G(-z) &= 2ie^{-z^2}\int_z^{\infty}e^{-q^2}dq + 2ie^{-z^2}\int_z^{-\infty}e^{-r^2}(-dr) = 2ie^{-z^2}\int_{-\infty}^{\infty}e^{-q^2}dq \\ &= 2i\sqrt{\pi}e^{-z^2} \end{aligned} \tag{A.3}$$

Using the above properties, we can calculate a whole complex z plane using a quadrant as,

2^{nd} quadrant: $G(-z) = 2i\sqrt{\pi}e^{-z^2} - G(z)$ (A.4)

3^{rd} quadrant: $G(-z^*) = -G^*(z)$ (A.5)

4^{th} quadrant: $G(z^*) = -G^*(-z) = 2i\sqrt{\pi}e^{-(z^*)^2} + G^*(z).$ (A.6)

Usually a quadrant of z plane is calculated using an approximation function. However, we will try to calculate by executing a complex numerical integration. The approximation function will be discussed later.

A.2 Calculation by Numerical Integration

A.2.1 Suitable Expression for Numerical Integration

As mentioned above, we need only a quarter of a z plane to calculate the whole z plane. Therefore we can assume $z = x - iy$ $(x \geq 0, y \geq 0)$ for numerical integration.

$$G(x-iy) = 2ie^{-(x-iy)^2} \int_{y+ix}^{\infty} e^{-q^2} dq \qquad \text{for } (x \geq 0, y \geq 0). \tag{A.7}$$

In the complex integration, we can take any root for q from $y+ix$ to ∞. Then, we take the integration root as $q = r + ixy/r$. When q moves from $y+ix$ to ∞, r moves from y to ∞.

$$\begin{aligned} G(x-iy) &= 2ie^{-(x-iy)^2} \int_{y}^{\infty} e^{-(r+ixy/r)^2} \left(dr - ixy\frac{dr}{r^2} \right) \\ &= 2e^{-x^2+y^2} \left\{ xy \int_{y}^{\infty} e^{-r^2+(xy/r)^2} \frac{dr}{r^2} + i \int_{y}^{\infty} e^{-r^2+(xy/r)^2} dr \right\} \end{aligned} \tag{A.8}$$

Note that both the real part $e^{-r^2+(xy/r)^2}/r^2$ and the imaginary part $e^{-r^2+(xy/r)^2}$ of functions to integrate are monotonic decreasing positive functions, which makes easy to manage integration errors.

A.2.2 Numerical Integration Error Management

Here we discuss how to manage the error of sectional numerical integration. As mentioned above, functions we want to integrate are monotonic decreasing positive functions. For a monotonic decreasing positive function $f(r)$, we will find the following relationship as shown on Fig.A.1:

$$\sum_{k=1}^{K} f(r_k)\Delta r_k \leq \int_{0}^{r_K} f(r)dr \leq \sum_{k=1}^{K} f(r_{k-1})\Delta r_k \tag{A.9}$$

where $\Delta r_k = r_k - r_{k-1}$ is the size of integral section or the integral step.

We define the numerical integration error as

$$E_{num} = \left| \frac{\sum_{k=1}^{K} f(r_{k-1})\Delta r_k - \sum_{k=1}^{K} f(r_k)\Delta r_k}{\int_{0}^{r_K} f(r)dr} \right|. \tag{A.10}$$

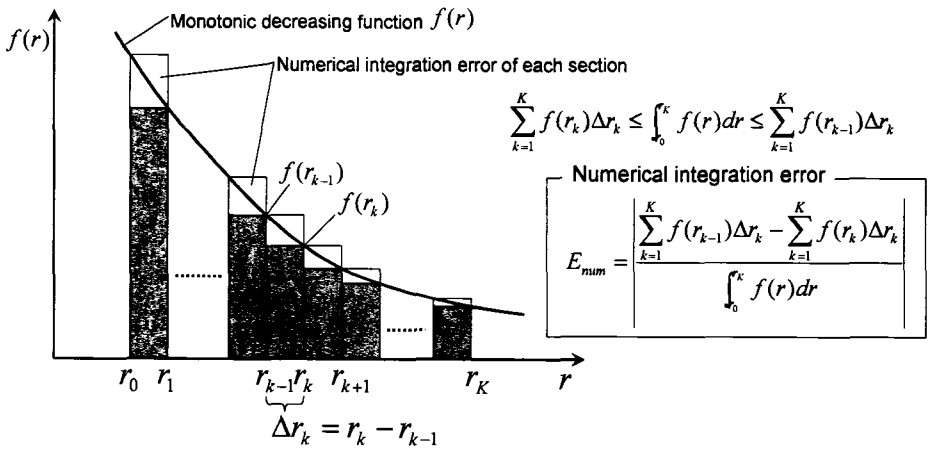

Fig. A.1 Explanation of numerical integration error of the plasma dispersion function.

If the error of each section of the summation is less than a certain error E_{num} as shown in the next equation, the total error of the summed values is also ensured to be less than E_{num}:

$$\left| \frac{f(r_{k-1})\Delta r_k - f(r_k)\Delta r_k}{\int_{r_{k-1}}^{r_k} f(r)dr} \right| \le E_{num} \qquad (k = 1, 2, \ldots, K). \qquad \text{(A.11)}$$

The integral step Δr_k is expected to be small enough in order to reduce the integration error, therefore the integration in the denominator of the above equation can be replaced by $f(r_k)\Delta r_k$ as:

$$\left| \frac{f(r_{k-1})\Delta r_k - f(r_k)\Delta r_k}{f(r_k)\Delta r_k} \right| \le E_{num} \qquad (k = 1, 2, \ldots, K). \qquad \text{(A.12)}$$

In order to manage the numerical integration error, we have to determine the integral step Δr_k $(k = 1, 2, \ldots, K)$ which ensures the integration error is less than a certain value of E_{num}. There are two methods to determine Δr_k which satisfy (A.12). One method is a repetitious method, in which integral summation is begun from $k = 1$ and the integral step Δr_k is updated recursively during the computation as:

$$\Delta r_{k+1} = \left| \frac{f(r_k) E_{num}}{f(r_{k-1}) - f(r_k)} \right| \Delta r_k \qquad (k = 1, 2, \ldots, K). \tag{A.13}$$

This equation is quite reasonable by itself. If the denominator is a large value, which means the gradient of the function is large, the next integral step Δr_{k+1} will be set to a small value. On the other hand, if the denominator is a small value, which means the gradient of the function is small, Δr_{k+1} will be set to a large value. Due to this property, the numerical integration error can be managed by inserting (A.13) in the repetitious computation. However, we should note that if the function becomes completely flat $\left(f(r_{k-1}) = f(r_k)\right)$, this method will fail since the denominator of (A.13) becomes zero. It can be used only for integration of a monotonic decreasing function or a monotonic increasing function. In addition, this method also can not be used in the case of a function which takes both positive and negative values in the integration area. Only positive or negative functions can be applied. The real part and the imaginary part of (A.8), which is our objective function, satisfy those conditions.

The other method to determine Δr_k is a direct method, in which Δr_k is obtained by replacing $\{f(r_{k-1}) - f(r_k)\}/\Delta r_k$ with $df(r_k)/dr$ in (A.12):

$$\left| \frac{df(r_k)/dr}{f(r_k)} \right| \Delta r_k = E_{num} \qquad (k = 1, 2, \ldots, K). \tag{A.14}$$

Using the relationship $df/f = d(\log f)$,

$$\left| \frac{d(\log f(r_k))}{dr} \right| \Delta r_k = E_{num} \qquad (k = 1, 2, \ldots, K). \tag{A.15}$$

Here, think about the meaning of Δr_k. Δr_k is the movement of r per unit k, thus $\Delta r_k = dr/dk$, although k is an integer therefore this thought is a kind of logical. Substituting it into (A.15),

$$\left| d(\log f(r_k)) \right| = E_{num} dk. \tag{A.16}$$

Integrating both side of the equation,

$$\left|\log f(r_k)\right| = E_{num}k + C \qquad (k = 1, 2, \ldots, K) \qquad \text{(A.17)}$$

where C is a constant. Solving the above equation by r_k, we obtain r_k expressed with k. For example, think about $f(r) = e^{-r^2+(xy/r)^2}$ which is the imaginary part of (A.8). (A.17) becomes

$$\left|-r_k^2 + (xy/r_k)^2\right| = E_{num}k + C \qquad (k = 1, 2, \ldots, K). \qquad \text{(A.18)}$$

We can expect $r_k^2 > (xy/r_k)^2$ because integration will be carried out toward infinity. Then,

$$r_k^2 - (E_{num}k + C) - (xy/r_k)^2 = 0 \qquad (k = 1, 2, \ldots, K). \qquad \text{(A.19)}$$

Solving this equation by r_k,

$$r_k = \sqrt{\frac{E_{num}k + C + \sqrt{(E_{num}k + C)^2 + 4(xy)^2}}{2}} \qquad (k = 1, 2, \ldots, K). \qquad \text{(A.20)}$$

Since $r_0 = y$ at $k = 0$, $C = y^2 - x^2$. Then,

$$r_k = \sqrt{\frac{E_{num}k + y^2 - x^2 + \sqrt{(E_{num}k + y^2 - x^2)^2 + 4(xy)^2}}{2}} \quad (k = 1, 2, \ldots, K). \quad \text{(A.21)}$$

As shown in the above, we can calculate r_k from k directly for the given integration error E_{num} without repetitious computation. All r_k $(k = 1, 2, \ldots, K)$ can be calculated independently; in consequence, this method is good for parallel processing. However, unfortunately it is difficult to apply this method for the real part of (A.8) since (A.17) for the real part cannot be solved analytically. The repetitious method can be used more generally. Executing numerical integration using those integral steps, the numerical integration errors are ensured to be less than certain values.

A.2.3 Consideration of Finite Integration Error

Equation (A.8) demands integrations for r from y to infinity, however we can stop the integrations at finite value since both of real part and imaginary part are monotonic decreasing positive functions and go to zero. Here we will discuss the error caused by integrations stopped at a finite value a for r.

As shown on Fig.A.2, we define the finite integration error as:

$$E_{fin}(a) = \frac{\int_a^\infty f(r)dr}{\int_y^a f(r)dr}. \tag{A.22}$$

Think about the imaginary part of (A.8). The function we need to integrate is $f(r) = e^{-r^2+(xy/r)^2}$. This function is similar to the Gaussian function so that we will compare the finite integration error of the function to integrate with that of the Gaussian function. The relationship between the function to integrate and the Gaussian function is:

$$f(r) = e^{-r^2+(xy/r)^2} \le Ce^{-(r-y)^2} \text{ when } y \le r \le a \tag{A.23}$$

where $C = e^{-a^2+(xy/a)^2+(a-y)^2}$. Then,

$$\int_y^a f(r)dr > C\int_y^a e^{-(r-y)^2}dr = C\int_0^{a-y} e^{-s^2}ds. \tag{A.24}$$

In the same way,

$$f(r) = e^{-r^2+(xy/r)^2} \le Ce^{-(r-y)^2} \text{ when } a \le r \tag{A.25}$$

and

$$\int_a^\infty f(r)dr < C\int_a^\infty e^{-(r-y)^2}dr = C\int_{a-y}^\infty e^{-s^2}ds. \tag{A.26}$$

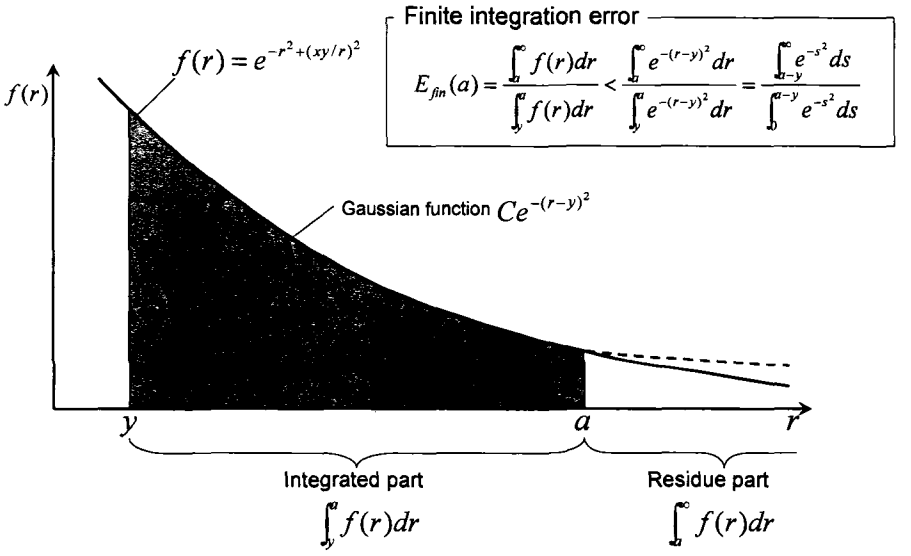

Fig.A.2 Explanation of finite integration error of the plasma dispersion function.

Using (A.24) and (A.26), the finite integration error is given by

$$E_{fin}(a) = \frac{\int_a^\infty e^{-r^2+(xy/r)^2}\,dr}{\int_y^a e^{-r^2+(xy/r)^2}\,dr} < \frac{\int_{a-y}^\infty e^{-s^2}\,ds}{\int_0^{a-y} e^{-s^2}\,ds}. \qquad \text{(A.27)}$$

Now we can estimate the finite integration error at a given finite value a using the error function and the complementary error function, which are definite integration of the Gaussian function. The table of those functions can be found in the statistical text books easily. Table A.1 shows, for example, if $a-y$ is set to 4, the finite integration error will be less than 1.54×10^{-8}. For another example, if $a-y$ is set to 3, the finite integration error will be less than 2.21×10^{-5}.

In the above, we have discussed the finite integration error of the imaginary part of (A.8). The finite integration error of the real part of (A.8) also can be estimated in the same way. In conclusion, integration areas for both the real part and imaginary part of (A.8) can be set to $a = y+4$ for general purpose, which yields the finite integration errors of less than 1.54×10^{-8}, since the numerical integration error is usually much larger than the finite integration error because of computational power limitation.

Fig. A.3 and A.4 show, respectively, the real part and the imaginary part of the plasma dispersion function, calculated with ensured numerical integration errors of 0.1 % and the integration area set to $a = y+4$. Note that the true integration error may be less than the ensured error.

Table A.1 Finite integration error of the plasma dispersion function.

$t = a-y$	Error function: $\frac{2}{\sqrt{\pi}}\int_0 e^{-s^2}\,ds$	Complementary error function: $\frac{2}{\sqrt{\pi}}\int e^{-s^2}\,ds$	Finite integration error: $E_{fin}(a) < \int e^{-s^2}\,ds \Big/ \int_0 e^{-s^2}\,ds$
0	0	1	---
1	0.842701	1.572992e-1	1.866608e-1
2	0.995322	4.677735e-3	4.699719e-3
3	0.999978	2.209050e-5	2.209098e-5
4	1.000000	1.541726e-8	1.541726e-8
5	1.000000	1.537460e-12	1.537460e-12

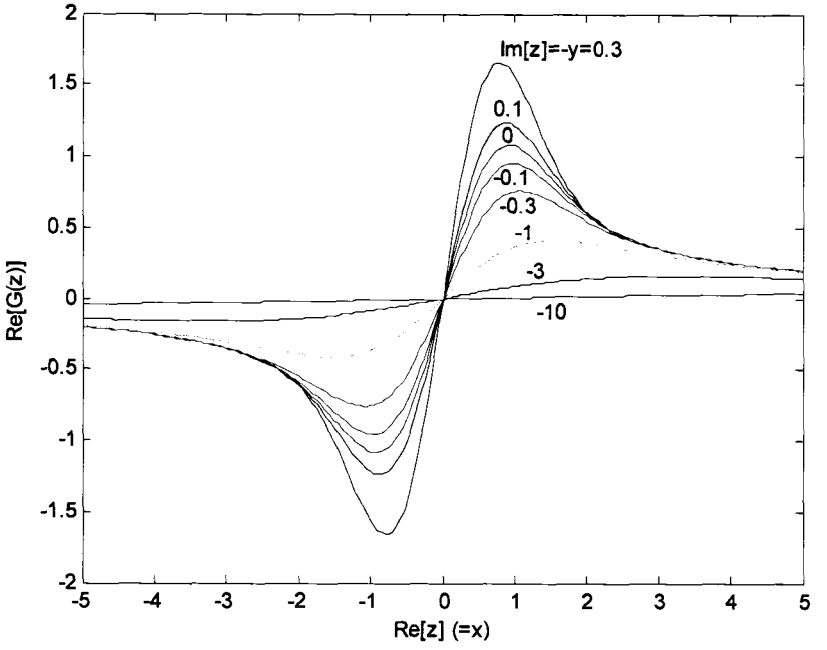

Fig A.3 The real part of the plasma dispersion function calculated by numerical integration. The numerical integration error is ensured to be less than 0.1%.

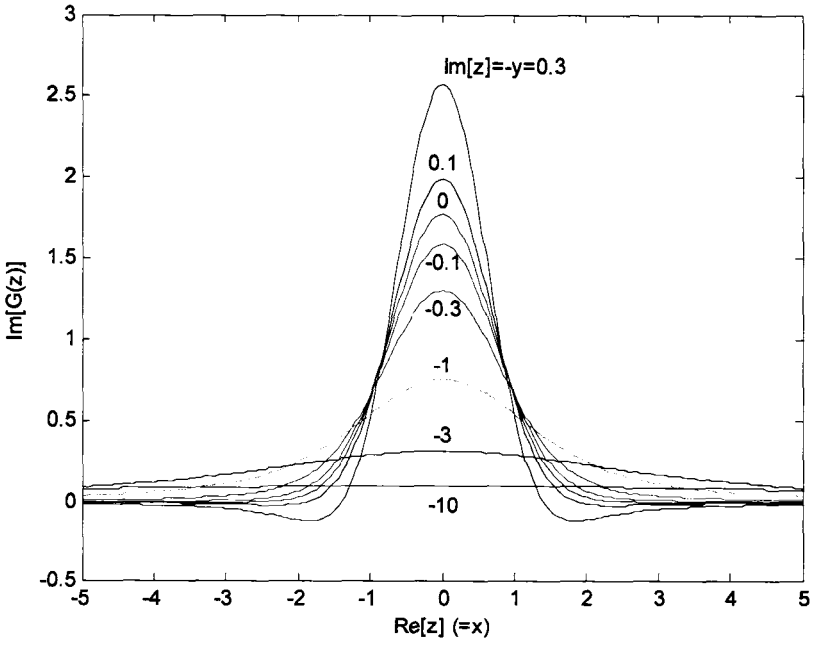

Fig A.4 The imaginary part of the plasma dispersion function calculated by numerical integration. The numerical integration error is ensured to be less than 0.1%.

A.3 Approximation Function of Plasma Dispersion Function

Numerical integration can be executed to obtain several plots for testing. However, in order to obtain hundreds or thousands of plots for spectrum fitting, this process is slow, even using the latest powerful computers. For such applications, the approximation function is still useful. Martin et al.(1980) proposed a polynomial fractional approximation for the plasma dispersion function:

$$G(z) \approx G_{ap}(z) = \frac{\sum_{n=0}^{N-1} p_n z^n}{1+\sum_{n=1}^{N} q_n z^n}. \tag{A.28}$$

In order to obtain the values p_n $(n = 0, 1, \ldots, N-1)$ and q_n $(n = 1, 2, \ldots, N)$, the above fractional expression should be expanded to the following forms:

$$G_{ap}(z) = p_0 + (p_1 - p_0 q_1)s + (p_2 - p_0 q_2 - p_1 q_1 + p_0 q_1^2)s^2 + \cdots, \tag{A.29}$$

$$\begin{aligned} G_{ap}(z) = {} & \frac{p_{N-1}}{q_N}\frac{1}{s} + \frac{p_{N-1}}{q_N}\left(\frac{p_{N-2}}{p_{N-1}} - \frac{q_{N-1}}{q_N}\right)\frac{1}{s^2} \qquad \frac{1}{s^3} + \cdots. \\ & + \frac{p_{N-1}}{q_N}\left(\frac{p_{N-3}}{p_{N-1}} - \frac{q_{N-2}}{q_N} - \frac{p_{N-2}q_{N-1}}{p_{N-1}q_N} + \frac{q_{N-1}^2}{q_N^2}\right)\frac{1}{s^3} + \cdots. \end{aligned} \tag{A.30}$$

The plasma dispersion function also can be expanded to a form similar to that of the Maclaurin expansion:

for small value of z,

$$G(z) = i\sqrt{\pi} + 2z - i\sqrt{\pi}z^2 - \frac{4}{3}z^3 + \frac{i\sqrt{\pi}}{2}z^4 + \frac{8}{15}z^5 + \cdots \tag{A.31}$$

and for large value of z,

$$G(z) = 2i\sqrt{\pi}e^{-z^2} + \frac{1}{z} + \frac{1}{2z^3} + \frac{3}{4z^5} + \frac{15}{8z^7} + \cdots \qquad \text{for } \mathrm{Im}[z] > 0 \tag{A.32a}$$

$$G(z) = i\sqrt{\pi}e^{-z^2} + \frac{1}{z} + \frac{1}{2z^3} + \frac{3}{4z^5} + \frac{15}{8z^7} + \cdots \qquad \text{for } \mathrm{Im}[z] = 0 \tag{A.32b}$$

$$G(z) = \frac{1}{z} + \frac{1}{2z^3} + \frac{3}{4z^5} + \frac{15}{8z^7} + \cdots \qquad \text{for } \mathrm{Im}[z] < 0. \tag{A.32c}$$

As will be mentioned later, the approximation function we will obtain is valid only for $\mathrm{Im}[z] < 0$; therefore we will use (A.31) and (A.32c). Comparing (A.29) to (A.31), and (A.30) to (A.32c), we can obtain p_i and q_i. However actual calculations should be carried out using the following expression in order to avoid poles at which the function goes to infinity.

$$G_{ap}(z) = \sum_{k=1}^{N} \frac{b_k}{z - a_k} \tag{A.33}$$

Coefficients a_k and b_k for an 8-pole approximation function are shown in Table A.2. Note that all poles exist on the right half of the complex z plane; therefore we can use this approximation function only for $\mathrm{Im}[z] \le 0$. We use the properties of the plasma dispersion function expressed in (A.6) to obtain $\mathrm{Im}[z] > 0$. We also should note that the symmetrical property of (A.2) is automatically satisfied in this approximation function since the poles are symmetrical with $\mathrm{Re}[z] = 0$.

Fig A.5 shows the error trajectory of the approximation function using coefficients from Table A.2 for Re[z] varying from 0 to 5 and Im[z] varying 0, -0.1, -0.3, and -1. The approximation error is calculated as:

$$E_{ap} = \left(G_{ap}(z) - G(z)\right) \Big/ \left|G(z)\right| \tag{A.34}$$

where $G(z)$ is the numerical integrated function. The error is calculated only for $\mathrm{Re}[z] \ge 0$ and $\mathrm{Im}[z] \le 0$ since other parts of the z plane are calculated using the properties of the plasma dispersion function. Fig A.5 shows the approximation error of less than 0.0015%. However, the ensured numerical integration error was set to 0.1% to calculate numerical integrated function, whereas the actual numerical integration error becomes smaller; therefore we cannot distinguish the actual approximation error from the numerical integration error. However, in total, we can trust the approximation function as well as the numerical integrated function.

Table A.2 Coefficients for 8-pole approximate plasma dispersion function. (calculated by C. Price, UAF, 5/89.)

k	a_k	b_k
1	2.259469521588466 +1.486997599578438 i	2.352801477487318 3E-02 -1.8025870760874432E-02 i
2	-2.259469521588466 +1.486997599578438 i	2.352801477487318 3E-02 +1.8025870760874432E-02 i
3	1.474133304429912 +1.655294955417770 i	0.2477795854098427 +0.6505154887878118 i
4	-1.474133304429912 +1.655294955417770 i	0.2477795854098427 -0.6505154887878118 i
5	0.8421162988640557 +1.763048001627204 i	-3.699956189280012 -0.1397385912387920 i
6	-0.8421162988640557 +1.763048001627204 i	-3.699956189280012 +0.1397385912387920 i
7	0.2745040671197318 +1.815989290036745 i	3.928648589094993 -6.764414500230631 i
8	-0.2745040671197318 +1.815989290036745 i	3.928648589094993 +6.764414500230631 i

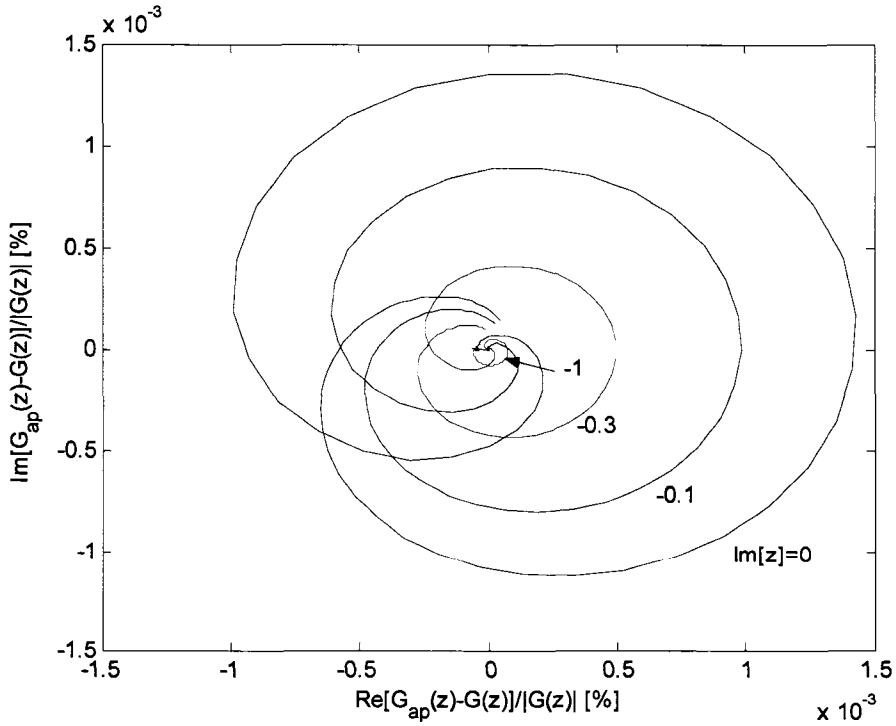

Fig. A.5 The error trajectory of 8-pole approximate plasma dispersion function. The real part of z varies from 0 to 5.